HAL
open science

Long-range transfer of spin information using individual electrons

Benoit Bertrand

To cite this version:

Benoit Bertrand. Long-range transfer of spin information using individual electrons. Condensed Matter [cond-mat]. Université Grenoble Alpes, 2015. English. NNT : 2015GREAY020 . tel-01212493

HAL Id: tel-01212493

https://theses.hal.science/tel-01212493v1

Submitted on 6 Oct 2015

HAL is a multi-disciplinary open access archive for the deposit and dissemination of scientific research documents, whether they are published or not. The documents may come from teaching and research institutions in France or abroad, or from public or private research centers.

L'archive ouverte pluridisciplinaire **HAL**, est destinée au dépôt et à la diffusion de documents scientifiques de niveau recherche, publiés ou non, émanant des établissements d'enseignement et de recherche français ou étrangers, des laboratoires publics ou privés.

UNIVERSITÉ DE GRENOBLE

THÈSE

Pour obtenir le grade de

DOCTEUR DE L'UNIVERSITÉ DE GRENOBLE

Spécialité : **Physique de la matière condensée et du rayonnement**

Arrêté ministériel : 7 août 2006

Présentée par

Benoit Bertrand

Thèse dirigée par **Tristan Meunier**

préparée au sein **de l'Institut Néel - CNRS**
et de **l'École doctorale de Physique**

Long-range transfer of spin information using individual electrons

Thèse soutenue publiquement le **13 mars 2015**,
devant le jury composé de :

H. Bluhm
Professeur, RWTH Aachen University, Rapporteur
F. Pierre
Directeur de recherche, LPN - CNRS, Rapporteur
T. Ouisse
Professeur, Grenoble INP Phelma, Président
J.-M. George
Directeur de recherche, Unité Mixte de Physique CNRS/Thales, Examinateur
M. Sanquer
Directeur de recherche, SPSMS - CEA INAC, Examinateur
T. Meunier
Chargé de recherche, Institut Néel - CNRS, Directeur de thèse

Abstract

A growing interest is emerging towards the use of electron spins to carry information. It promises applications in spintronics for instance, to realize non-volatile devices with reduced power consumption. For this purpose, significant efforts are made to generate and transport spin-polarized electrons in semiconductors. Another promising application is the use of single electron spins isolated in quantum dots for quantum information processing.

In this thesis, we explore the possibility to transport single electron spins between distant quantum dots as a mean to transfer quantum information. This is a promising way to interconnect different nodes of a quantum nanoprocessor. The principle is to generate a surface acoustic wave (SAW) in order to induce dynamical quantum dots propagating in the sample.

The injection of a single electron from a static to a dynamical quantum dot has first been characterized, studying in particular the influence of the SAW amplitude and the confining potential. The control of the single electron transfer at a nanosecond timescale has been achieved thanks to a fast engineering of the confinement potential. Next, we demonstrate the preparation of a coherent spin superposition in an isolated double quantum dot, in a position compatible with the SAW transfer. We show that such an isolated system offers more liberty in terms of control. A new scheme for coherent spin manipulation taking advantage of this feature has been implemented and proved to have reduced noise sensitivity. Finally, transfer of information encoded in a single or two-electron spin magnetization has been achieved. The transfer fidelity reaches 30 %. A mechanism responsible for this partial loss of spin information has been identified, and a way to circumvent it is proposed.

Abstract - Français

Utiliser le degré de liberté de spin de l'électron pour coder de l'information est aujourd'hui un vaste sujet de recherche, motivé par les nombreuses applications qui peuvent en découler. La spintronique, par exemple, tente d'en tirer profit pour développer des dispositifs non-volatiles et moins coûteux en énergie. Dans cette perspective, d'importants efforts sont faits pour générer des courants d'électrons polarisés en spin dans des semiconducteurs. Un autre exemple d'application est la manipulation de spins d'électrons uniques, isolés dans des boîtes quantiques, permettant de réaliser un traitement quantique de l'information.

L'objectif de cette thèse est d'étendre le concept de transfert de spin à l'échelle de l'électron unique. Pour cela, nous cherchons à accomplir le transport cohérent d'un spin d'électron entre deux boîtes quantiques. Cela permettrait de transférer de l'information entre les différents nœuds d'un nanoprocesseur quantique. Le principe utilisé repose la génération de boîtes quantiques en mouvement à partir d'une onde acoustique de surface (OAS).

L'étude de l'injection d'un électron dans une boîte quantique en mouvement a tout d'abord été effectuée. Le déclenchement à la nanoseconde du transfert a été démontré grâce à un contrôle rapide du potentiel de confinement. Dans un deuxième temps, la préparation d'une superposition cohérente d'états de spin a été réalisée à l'aide d'une double boîte quantique isolée, dans une position compatible avec le transfert par OAS. Enfin, le transport d'information d'aimantation, en utilisant le spin d'une paire ou d'un unique électron, a été accompli avec une fidélité atteignant 30 %. Un mécanisme pouvant expliquer cette perte partielle d'information a été identifié et un moyen de l'empêcher est proposé.

Contents

Introduction **1**

1 State of the art of the control over a single electron and its spin **5**
1.1 Isolating a single electron in a quantum dot . . . 5
1.1.1 Fabrication of lateral quantum dots . . . 5
Two-dimensional electron gas . . . 5
Lateral confinement . . . 7
1.1.2 Model of a quantum dot . . . 8
1.1.3 Charge sensing of a quantum dot . . . 10
1.2 Spin states in a single quantum dot . . . 13
1.2.1 One-electron spin states . . . 13
1.2.2 Two-electron spin states in a single quantum dot . . . 13
1.2.3 Spin readout techniques . . . 14
Energy selective readout . . . 15
Tunnel-rate selective readout . . . 15
1.3 Spin states in a double quantum dot . . . 17
1.3.1 Two-electron spin states in a double quantum dot . . . 17
1.3.2 Spin Blockade readout . . . 20
1.4 Couplings to the environment . . . 22
1.4.1 Relaxation, dephasing and decoherence . . . 22
1.4.2 Spin-Orbit interaction . . . 23
1.4.3 Hyperfine interaction . . . 26
Singlet-triplet mixing by nuclear spins in a double quantum dot . . . 28
1.5 Coherent spin manipulations . . . 28
1.5.1 Single-spin rotation . . . 28
1.5.2 Two-spin exchange . . . 30
1.6 Transport of a single electron with moving quantum dots . . . 32
1.6.1 Surface acoustic waves moving quantum dots . . . 32
Generation of surface acoustic waves . . . 33
Dynamical quantum dots . . . 35
1.6.2 On-demand single electron transfer between static quantum dots . . . 37

2 Experimental setup **39**
2.1 Introduction . . . 39
2.2 Cryogenics . . . 39
2.3 Electronics . . . 42
2.3.1 Voltage sources . . . 42
2.3.2 High frequency signals . . . 43
Nanosecond gate voltage pulses . . . 43
SAW burst generation . . . 43
2.3.3 Measurement . . . 46
2.3.4 Control software . . . 47

3 Injection of a single electron from a static to a dynamical quantum dot **49**
3.1 Introduction . . . 49
3.2 Electron transfer regimes . . . 49
3.3 Influence of the static potential shape on the electron emission . . . 52
3.4 Influence of the SAW parameters on the electron emission . . . 56
3.5 Nanosecond electron emission from the source dot . . . 60
3.6 Conclusion . . . 64

4 Coherent spin manipulations in an isolated double quantum dot **67**
4.1 Introduction . . . 67
4.2 Observation of a double dot behavior in the metastable position . . . 67
4.2.1 Potential numerical simulations . . . 67
4.2.2 Additional patterns in standard stability diagrams . . . 69
4.2.3 Metastability diagrams with fixed number of electrons . . . 70
4.3 Spin measurement and relaxation in metastable position . . . 74
4.4 Coherent spin manipulations in a metastable double quantum dot . . . 78
4.4.1 Mapping of the spin mixing regions . . . 78
4.4.2 Coherent oscillations on a sweet spot . . . 83

5 Transfer of individual electron spins **89**
5.1 Introduction . . . 89
5.2 Two-electron spin state transfer . . . 89
5.2.1 Two-electron transfer . . . 89
5.2.2 Calibration of the spin detection . . . 93
5.2.3 Spin measurement after transfer . . . 95
5.3 Single electron spin transfer . . . 102
5.3.1 Adaptation of the spin readout technique to single-electron states . . . 102
Spin initialization . . . 102
Magnetic field influence . . . 103
Temperature influence . . . 103
Tunnel rates study . . . 104
5.3.2 Spin measurement after transfer . . . 106
5.3.3 SAW impact on the electron spin . . . 110

5.4 Conclusion 112

Conclusion and perspectives **113**

Bibliography **117**

Appendix **137**

A Frequency dependence of the transfer efficiency **137**

B Extending nanosecond triggering to the reception dot and time of flight measurements **139**

C Probing the excited states of the metastable double quantum dot **149**

D Observation of long relaxation times in metastable position **153**

E Spin-blockade readout in metastable position **155**

F SAW influence on the spin of the system **159**

G French summary **165**

Introduction

Over the last decades, the constant miniaturization of electronic and photonic components have led to an impressive improvement in computing power. The fabrication of nanometer size devices has become common and current developments in silicon technology are reaching the atomic scale [Fue12]. At such a small scale, quantum mechanics is necessary to understand device properties. For some people, these appearing quantum phenomena constitute an additional difficulty towards further scale reduction. On the contrary, it is for some others an incredible opportunity to access more powerful information processing.

Feynman was one of the first to introduce this idea and proposed an abstract model showing how a quantum system could be used to do computation [Fey82]. He suggested that such a machine could be particularly efficient for quantum mechanics simulations. This is of significant interest since a classical computer suffers from the exponentially growing complexity with the number of particles contained in a quantum system. The Feynman's conjecture was confirmed more than one decade later with the proof that universal quantum simulators can be built from quantum mechanical systems [Llo96]. It promises a large number of potential applications in the study of many-body problems in physics and chemistry [Geo14].

A further milestone in the development of quantum computing was then the discovery of the Shor's algorithm for prime number factoring [Sho94]. The major impact it could have on today's cryptography protocols gave rise to a tremendous interest even outside the physics community. Some other algorithms taking advantage of the potential of quantum computing have later been proposed. A famous one is for instance the Grover's algorithm [Gro96], that allows for searching an unsorted database faster than a conventional computer.

For the physical realization of such quantum information processing, any system is not suitable. DiVincenzo proposed a set of five requirements for the implementation of quantum computation [DiV00]. These criteria are the following:

1. *A scalable physical system with well characterized qubits.* A quantum bit or qubit is a quantum mechanical two-level system, as the two spin states of a spin $\frac{1}{2}$ particle for instance. These two states are usually denoted $|0\rangle$ and $|1\rangle$. The essential difference compared to a classical bit is that a qubit can be a superposition of these two states. A general state can therefore be written as $a|0\rangle + b|1\rangle$, where a and b are complex numbers. This is the essence of the quantum computing speed-up. All the parameters of these qubits (state energies and the different coupling mechanisms involved) have to be known with high accuracy.

2. *The ability to initialize the state of the qubits.* Before the start of a computation, the system has to be initialized with a known value. Therefore, it must be possible to prepare each qubit in at least one particular state. Most of the time, a simple solution consists in preparing the qubit to its ground states by cooling down the system.
3. *Low decoherence relative to the gate operation time.* Decoherence is the mechanism by which the classical limit emerges from a quantum system. As a result, this decoherence time should be as long as possible compared to the computation time in order to take advantage of the quantum properties of the system. One could worry that long computations are thus made impossible. However, some error correction codes can be applied to quantum computation [Sho95; Ste96] in order to counteract the effect of decoherence. One of the less stringent approach for error correction, known as *surface codes* [Bra98; Den02; Fow12], gives estimated permissible error rate on the order of 10^{-2}, which sounds experimentally accessible[1].
4. *A universal set of quantum gates.* In principle, it has to be possible to produce any unitary operation involving arbitrary numbers of qubits, but this sounds unrealistic from an experimental point of view. However, it has been shown [Bar95] that any unitary operation can be decomposed into one and two-qubit gates, that are much more accessible for experimentalists. Again, the errors on these transformations should be as small as possible, and at least below 10^{-2} for surface codes implementation.
5. *The ability to measure specific qubits.* Measuring a qubit without disturbing the rest of the system is necessary both for the management of error correction codes and, not surprisingly, to readout the outcome of a computation. What is considered as an ideal measurement performed on a state $\rho = p\,|0\rangle\langle 0| + (1-p)\,|1\rangle\langle 1| + \alpha\,|0\rangle\langle 1| + \alpha^*\,|1\rangle\langle 0|$ should yield to the outcome 0 with probability p and 1 with probability $(1-p)$ independently of α, the state of neighbor qubits or any other parameter of the system. In general, a measurement scheme has not a perfect efficiency and errors may occur. However, the reliability of the procedure can be increased by repeating the same computation several times.

Experimentally, it is not easy to find a system that fulfills all these requirements. A typical problem is that a qubit should be extremely well isolated from its environment in order to manage long coherence times. But reciprocally, one should also have some means to couple to it in order to manipulate the stored information, and these traits tend to be in opposition. In the search for a "perfect" qubit (that is both easy to control and hard to alter), a large number of physical systems have been examined by researchers, each having their own advantages and drawbacks. An extensive review of all the studied implementations would be too long. We can name just a few examples like trapped ions [Cir95; Haf08; Roo99], superconducting circuits using Josephson junctions [Jef14; Koc07; Nak99], nuclear spins controlled with Nuclear Magnetic Resonance (NMR) techniques

1 However, the price to pay for this high error tolerance is that surface code implementation involves much higher numbers of physical qubits (see discussion in [Fow12]).

[Ger97; Jon11], Nitrogen Vacancy (NV) centers in diamonds [Jel04; Ken02], and electron spins trapped in semiconductor quantum dots [Kop06; Los98; Pet05]. Even with a given system, many different implementations of a qubit are possible. In the case of spin-based computing for instance, single-electron [Los98; PL08], two-electron [Fol09; Han07b; Pet05; Tay05] or three-electron spins [Lai10; Med13] have been proposed as qubits.

In the frame of this thesis, we will consider the case of confined electron spins as a medium for quantum information. Exciting progress has recently been achieved in this research field. First, the use of isotopically purified materials offers an extremely small coupling of the isolated spins to their environment, resulting in extremely promising coherence times around a second [BG13; Tyr12]. In addition, the confinement of single-electron spins in lithographically-defined quantum dots allows for a controlled coupling between neighbor spins that can be precisely engineered. This provides means for achieving relatively easily spin manipulations, and the "universal set of quantum gates" has been demonstrated [Kop06; Pet05]. Another main advantage of this scheme lies in its potential scalability. Indeed, the fabrication of the quantum dots that are used to isolate single electron spins involves very similar technology to the one employed in the microelectronic industry. This is especially true with the recent switch to silicon Metal-Oxide-Semiconductor (MOS) structures [Ang07; Vel14]. Therefore, developing qubits in semiconductors sounds like a very promising route to realize scalable quantum information devices.

Since the basic requirements for spin-based quantum computing have been demonstrated, a trend in this research field is now trying to fabricate and to control devices containing more and more qubits. To that purpose, a first track that is followed is the development of large arrays of quantum dots [Del14; Tha12], where coupling between neighbor spins (and possibly on a further extent [Bra13; Meh14; San14]) could be controlled. However, the large number of parameters to tune and the direct capacitive coupling between the different parts of such devices make its design and manipulation significantly more complicated.

Reducing the complexity of the device tuning could be a first means towards the manipulation of large arrays of quantum dots. In this perspective, we propose a way to tackle a specific issue that is the coupling of the system to electron reservoirs. Usually, the number of electrons in a quantum dot array is fixed (with typically one electron per quantum dot) and should not vary. This requirement implies large constraints on the range of parameters that can be used and is detrimental for the full control of the system. As a solution, we investigated the possibility to work with quantum dots in a metastable configuration, completely isolated from the electron reservoirs. It presents the great advantage that the number of electrons in the system cannot vary, allowing for a much wider range of tuning parameters to be explored.

A second possibility for a facilitated control of a large qubit number could be to further space the different nodes of quantum dot arrays. One can imagine for instance a chip with quantum dots widely spaced from each others, where some long distance coupling would then be necessary in order to mediate the entanglement between the different nodes of the device. However, the very small coupling to the environment that makes the strength of spin-based qubits becomes a large impediment in that case. Some schemes have been proposed consisting in the interconnection of the different nodes of the device with cavity resonators [Bur06; Chi04; Tri08], similarly to what has been developed in

superconducting qubits [Maj07; Sil07]. It has been investigated in many groups now [Del11; Fre12; Pet12], but achieving sufficient coupling through this way seems very challenging. It exists other proposals for achieving distant spins coupling, such as the use of floating electrodes mediating electrostatic [Tri12] or magnetic [Tri13] coupling. No experimental realization of such a scheme has been done until now.

In our case, we investigate a quite different approach, inspired from the research in spintronics. Researchers in this field are developing devices aiming at spin-based information processing and storage. In that context, the generation and utilization of spin-polarized currents in semiconductors is intensively investigated to convey spin information [Bra12]. We consider a similar development at the single-electron level, in order to directly displace the qubits on a chip and transfer the information. The main advantage is that no conversion of spin information to another propagating medium would be necessary. However it must be found a way to achieve spin-preserving transfer of single electrons between different quantum dots of a device. This implies to keep a single electron isolated from any other one during its transport in order to prevent any spin mixing.

Although displacing electrons is one of the most common tasks for physicists, the control of the displacement of a single electron is quite challenging. Nevertheless, the transfer of a single electron between distant quantum dots has been achieved in 2011 [Her11; McN11]. In these works, two quantum dots separated by a few micrometers are connected by an empty one-dimensional channel along which a single electron can propagate. In order to overcome localization of the single electron in the channel, a surface acoustic wave (SAW) is excited. The potential modulation induced by the SAW when passing through the device results in the formation of moving quantum dots that can transfer the electron between the two quantum dots. This process allows to transfer single electrons over a few micrometers on a nanosecond timescale, that is faster than spin coherence time. In addition the electron remains confined during its transfer, which enhances the spin coherence length compared to the free displacement case [Dya72; Sto05; Sto08]. As a result, the information encoded on the electron spin should be preserved.

During this PhD work, described in the next chapters, I investigated the possibility to transport spin information encoded in individual electrons using such SAW-assisted electron transfer. In chapter 1, the basics of electronics at the single electron level are reviewed: the means of isolating a single electron in a quantum dot is first explained; the different methods to readout an electron spin and the procedures to coherently manipulate it are then described; finally, the on-demand transfer of an electron between distant quantum dots is discussed. In chapter 2, the experimental set-up that was used for the measurements is presented. In chapter 3, the electron injection process from a static to a SAW-defined moving quantum dot is investigated. In particular, we demonstrate that we can reach a regime where a single electron can be controllably injected in a specific moving quantum dot with unity probability. Next in chapter 4, coherent spin manipulations are demonstrated using a double quantum dot in metastable position. Such coherent manipulations are immediately compatible with a SAW electron transfer. These two chapters are important milestones towards the achievement of coherent transfer of a single electron spin. Finally in chapter 5, the first experiments of spin information transfer using individual electrons are presented.

CHAPTER 1

State of the art of the control over a single electron and its spin

In this chapter, a review of the electronics at the single electron level is done. In particular, we will discuss the way a single electron can be trapped in a quantum dot. It will then be explained how the spin state of the trapped electron can be measured and how it can be coherently manipulated. Finally, the on-demand transfer of a single electron between distant quantum dots is presented. This introduces all the basic concepts necessary to understand the work accomplished in this thesis.

1.1 Isolating a single electron in a quantum dot

A quantum dot is an artificially structured system that behaves as a potential trap. It can be filled with electrons (or reciprocally with holes) and confines them in a small region of space (on the order of the Fermi wavelength of the electrons). It is usually coupled via tunnel barriers to reservoirs with which it can exchange electrons.

It exists a large variety of systems that have been studied in which quantum dots can be formed, such as single molecules trapped between electrodes [Par02], nanoparticles of noble-metal [Pet01], superconducting [Ral95; VD01] or ferromagnetic materials [Gue99], self-assembled quantum dots [Kle96], semiconductor lateral [Kou97] or vertical dots [Kou01], and also semiconducting nanowires or carbon nanotubes [Bjo04; Dek99; McE00].

The work presented in this thesis has been done on lateral quantum dots realized in a GaAs/AlGaAs heterostructure. These dots are electrostatically defined with negative voltages applied on nanometer gates and have the advantage of being tunable to a large extent. In this section, we will first discuss the fabrication of such quantum dots. Their basic properties will then be recalled and the technique used to probe the charge of a quantum dot will be presented.

1.1.1 Fabrication of lateral quantum dots

Two-dimensional electron gas

The fabrication of lateral quantum dots starts with a junction between two semiconductors of different gap, called heterostructure. One of the most widely used for several decades is made from GaAs and AlGaAs. A difference in band gap combined with a low lattice

mismatch ($< 0.05\%$) between the two materials allows for band engineering (see for instance [Dav98] for further details). A quantum well can be formed at the interface between the two semiconductors in which electrons accumulate (see Fig. 1.1). The well has a typical width smaller than the electrons wavelength, implying that their motion becomes quantized in the direction perpendicular to the interface at cryogenic temperatures. Under these conditions, the confinement is so tight ($\sim 16\,\mathrm{meV}$) that only the first of these quantized levels is occupied. The electron system in the well can therefore be considered as purely two-dimensional. As will be detailed in the following, very high quality devices can be achieved using these kind of structures. One of the main applications is the realization of high electron mobility transistors (HEMTs), but for physicists it constitutes above all an extraordinary test bed for exploring fundamental physics in two dimensions.

The fabrication of very high quality heterostructures relies on molecular beam epitaxy (MBE). This technique allows to deposit very thin films, which are grown layer by layer at an atomic scale. It results in extremely regular interfaces and very abrupt composition gradients in the growth direction. The quality of the obtained interface is much higher than the oxide grown Si/SiO_2 interface of the metal-oxide-semiconductor (MOS) devices for instance. Another key ingredient to obtain high quality structures lies in the spatial separation between the AlGaAs/GaAs interface and the doping impurities providing the electrons forming the 2DEG. Indeed, ionized impurities are responsible for a major part of the electron scattering events. Putting them far from the plane where the electrons accumulate results in less irregularities in the potential they feel and a reduced scattering rate.

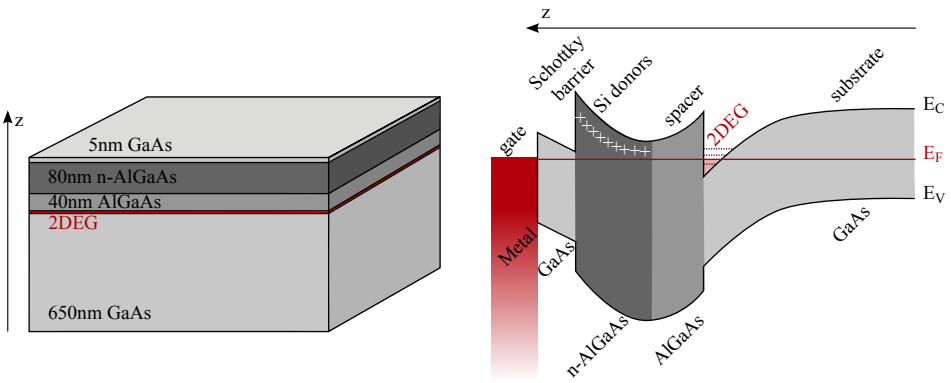

Figure 1.1: **(left)** Schematic of the $Al_{0.34}Ga_{0.66}As/GaAs$ heterostructure used to fabricate the device studied in this work. **(right)** Schematic of the band structure as a function of depth below the surface of the wafer. The substitution of part of the gallium atoms by aluminum atoms allows to reach a higher band gap than for pure GaAs. This is used to tailor the conduction band of the structure. The electrons of the 2DEG are provided by the silicon-doped (negative doping) AlGaAs layer. A 40 nm undoped AlGaAs layer is used as a spacer to further separate the electrons from the donors. The electric field coming from the ionized Si atoms is responsible for the bending of the bands, which results in the confinement of the electrons at the interface between the two materials.

The AlGaAs heterostructures used during my Ph.D. have been grown by our collaborator A.D. Wieck from the Ruhr-University Bochum. The two-dimensional electron gas has a mobility μ_e of $1.5 \times 10^6\,\mathrm{cm^2V^{-1}s^{-1}}$ and an electron density n_e of $1.35 \times 10^{15}\,\mathrm{m^{-2}}$. We can deduce from this the mean free path of an electron:

$$l_e = v_F \tau_e = \sqrt{2\pi n_e}\frac{\hbar\mu_e}{e} = 9\,\mu\mathrm{m} \tag{1.1}$$

where v_F is the speed of the electrons at the Fermi energy and τ_e is the momentum relaxation time. Therefore there should be on average only one impurity every few microns in the 2DEG. This relatively large distance allows to define micron-sized structures that are free of these defects. In our case, this is of importance to ensure the full tunability of the quantum dots that will be defined in the structure and to avoid defects on the path used for the electron transport.

Lateral confinement

As we have seen, the AlGaAs/GaAs heterostructure provides an excellent confinement along the growth direction. In order to obtain a quantum dot, the confinement along the other two directions of space remains to be achieved. In lateral quantum dots, the confinement is ensured by metallic gates deposited on the surface of the heterostructure[1]. The metal-semiconductor contact that is formed exhibits a Schottky behavior which allows to apply a relatively large negative voltage on a gate without having current flowing from it to the 2DEG. Therefore the equivalent of a capacitor is formed, with the two conducting plates being the metal gate and the 2DEG. Changing the voltage applied on a gate modulates the charge density of the electron gas underneath. It can be entirely depleted by this way, giving rise to a tunnel barrier that splits the 2DEG. If several of these gates are used, it is possible to completely isolate some regions of the 2DEG (see Fig. 1.2).

The relevant length scales at which the potential seen by the electrons has to be shaped in order to start observing quantum effects is given by the Fermi wavelength:

$$\lambda_F = \sqrt{\frac{2\pi}{n_e}} = 70\mathrm{nm} \tag{1.2}$$

This is a relatively high value for the Fermi wavelength (it is around a hundred times larger than in metals for instance). In particular, it is wider than the resolution of the electron beam lithography technique that is used to deposit the thinnest parts of the metal gates[2]. Therefore it will be possible to confine the electrons in patterns smaller than the Fermi wavelength and so to create quantum dots.

Many different gates are necessary to form a quantum dot. The characteristics of each resulting tunnel barrier as well as the shape and size of the dot can thus be precisely defined by properly tuning the voltages applied on the different gates. This is the origin of

1 Alternatively, confinement can also be realized by etching of the structure.

2 The typical resolution of EBL is around 2 nm. The main restriction arises from the lift-off step which is limited to ~ 20 nm.

the exceptional tunability of this kind of quantum dots.

1.1.2 Model of a quantum dot

The small size of the quantum dots has two impacts on the energy scales involved. First, as it has been said, the electrons are confined into a region smaller than the Fermi wavelength and therefore their wave-like behavior becomes preponderant. It induces the appearance of discrete energy levels equivalent to the orbitals in an atom [Kou01]. Because of the Pauli principle, it is forbidden for two electrons to occupy the same quantum state. Taking into account the spin degeneracy, there can be only two electrons per orbital. Higher energy orbitals will therefore be occupied when filling the quantum dot with more and more electrons. The typical order of magnitude for the energy between orbital states can be estimated by

$$\Delta E_{orb} \sim \frac{\hbar^2}{2m^*}\left(\frac{\pi}{L}\right)^2 \tag{1.3}$$

where $m^* = 0.067m_0$ is the effective mass of an electron in GaAs, and L is the dimension of the quantum dot. For $L \sim 100\,\text{nm}$, that gives an energy scale around half a milli-electronvolt, equivalent to a temperature of a few kelvins. As a comparison, the base temperature reached by a dilution refrigerator is several orders of magnitude smaller (a few tens of milli-kelvins) and therefore makes possible the experimental observation of these distinct energy levels.

The second consequence of the small dot size is the large energy cost for adding an extra electron into a quantum dot because of Coulomb repulsion. This electrostatic energy is called the charging energy. It is one of the largest energy associated with this system. As shown in [Wie02] and [Han07a], this energy contribution gives rise to a regular structure

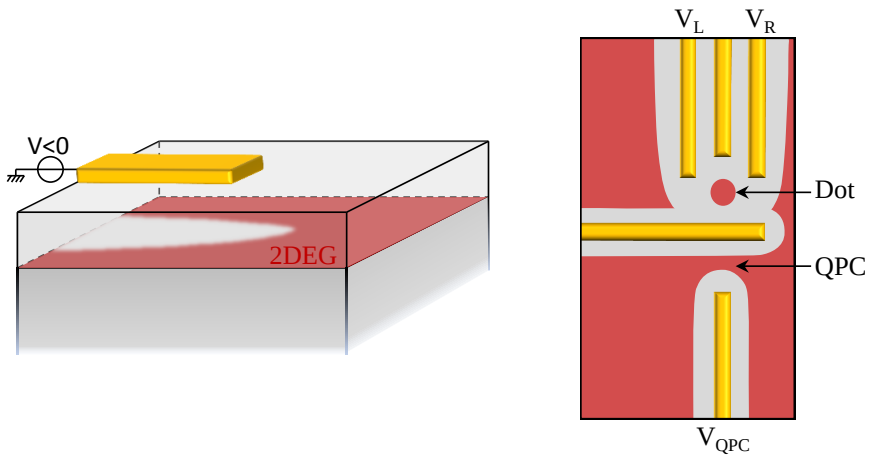

Figure 1.2: **(left)** 3D schematic illustrating the depletion of the 2DEG by a metal gate deposited on the surface of the wafer. Electrons are represented as the red layer. **(right)** Schematic of the use of multiple gates to confine the electron gas in the two dimensions of the 2DEG and form a quantum dot. The design presented here is similar to the one that is used for the sample. The lowest gate serves for the charge sensing of the dot (see 1.1.3).

in the energy spectrum, such as the "Coulomb Diamond" structure in single quantum dots.

This is well described by the constant interaction (CI) model [Kou97; VH92; Wan11]. This model is based on two assumptions. First, the Coulomb interactions are parametrized by a single capacitance corresponding to the sum of the capacitances between the dot and its environment (neighbor reservoirs and gates, see Fig. 1.3). The second assumption is that the single-particle energy-level spectrum is independent of these Coulomb interactions and therefore of the number of electrons.

From these assumptions, the expression of the electrostatic energy of the system can be derived. The typical picture used to model a quantum dot is represented on Fig. 1.3. The dot is represented as an island coupled to two electron reservoirs (a source S and a drain D) with which electrons can be exchanged. The tunnel barriers separating the dot from the reservoirs are modeled as "leaking" capacitors. In addition, the dot is also coupled to a gate G that can be used to vary the dot chemical potential. The electrostatic energy of the quantum dot is then given by:

$$U = \frac{1}{2}CV^2 \tag{1.4}$$

where $C = C_G + C_S + C_D$ is the sum of all the contributions to the dot capacitance, and V is the voltage of the island. If N electrons are contained in the quantum dot, the opposite charge lies on the surrounding capacitors. This can be written as:

$$-Ne = C_G(V - V_G) + C_S(V - V_S) + C_D(V - V_D) \tag{1.5}$$

Finally by combining the equations 1.4 and 1.5, one obtains:

$$U(N) = \frac{(-Ne + C_G V_G + C_S V_S + C_D V_D)^2}{2C} \tag{1.6}$$

This corresponds to the electrostatic energy of the quantum dot. In order to have the total energy, one should also take into account the energy cost for the occupation of the different orbitals of the quantum dot. We simply write this contribution as

$$\sum_{n=1}^{N} E_n \tag{1.7}$$

where the E_n are the single-particle orbital energies of the quantum dot.

As the number of electrons in a quantum dot can vary, the relevant term to look at is not the energy of the dot but rather its electrochemical potential. It is defined as the energy required to add the Nth electron to the island. In the case where the two reservoirs are grounded ($V_S = V_D = 0$), the calculation leads to

$$\mu(N) = U(N) - U(N-1) = (N - \frac{1}{2})E_C + E_N + \frac{C_G}{C}V_G \tag{1.8}$$

where $E_C = \frac{e^2}{C}$ is the charging energy of the system; E_N is the cost in orbital energy for the addition of a new electron to the dot; $\frac{C_G}{C}$ gives the conversion factor from gate voltage

into energy, also called the α-factor or gate lever arm.

The order of magnitude of the charging energy can be estimated through geometrical considerations. The quantum dot can be seen as a charge disk of radius R. In this case, the self capacitance is known to vary as

$$C = 8\varepsilon_0\varepsilon_r R \tag{1.9}$$

where ε_0 is the vacuum permittivity and ε_r the relative permittivity of GaAs. For a radius of 50 nm, the resulting capacitance is around 50 aF leading to a charging energy of 3.5 meV[1]. This is an order of magnitude larger compared to the estimation of the orbital energy, confirming that this is the dominant energy scale of the system.

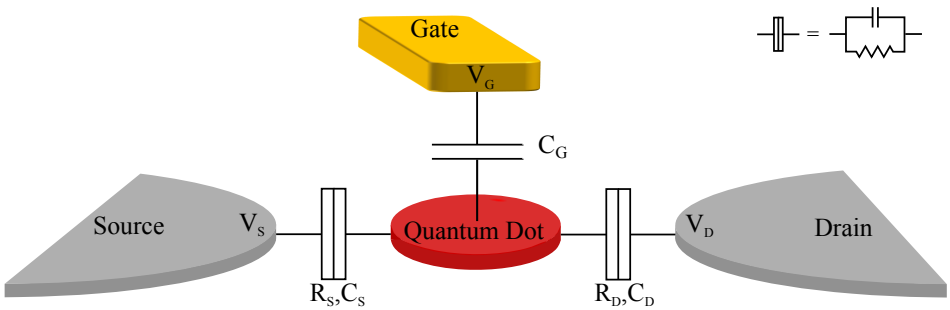

Figure 1.3: Scheme of the Quantum dot description used in the CI model. N electrons are contained in an island capacitively coupled to its environment (source, drain and gate). Electrons can be exchanged with the source and drain contacts.

1.1.3 Charge sensing of a quantum dot

Different methods can be used to probe the charge state of a quantum dot. A first one consists in measuring the current flowing through the quantum dot. Depending on the relative position between the source, drain and dot chemical potential, the current can be allowed or blocked (Coulomb Blockade mechanism). Since no work relying on this technique is presented in this thesis, we will not describe it into details. Further information can be found in [Kou01; Wie02].

A second method to determine the charge state of a quantum dot system consists in using a local charge sensor [Fie93], such as a quantum point contact (QPC). A QPC is a small one-dimensional constriction (see Fig. 1.2 for instance). It can be viewed as the equivalent for electrons of a waveguide in optics. In 1988, it has been observed that the conductance G_{QPC} through a QPC is quantized [Wee88; Wha88]. At the transition between two conductance plateaus, G_{QPC} becomes very sensitive to the electrostatic environment. When a QPC is located very close to a quantum dot, it can even be sensitive to the charge state of the dot. This has been exploited to determine the absolute number of electrons in

1 This is an upper estimation for the charging energy since the presence of the metal gates and the adjacent 2DEG increases the dot capacitance.

single [Spr02] and coupled lateral quantum dots [Elz03].

This technique constitutes a major technological improvement mainly due to its non-invasive nature, which enabled many experiments that could not be performed using standard transport measurements. A first advantage arises for establishing the proof that the single-electron regime is reached. Indeed, reducing the number of electrons in a quantum dot usually implies shaping thick tunnel barriers between the dot and its electron reservoir. At some point, it will no longer be possible to detect a current flowing through the quantum dot, and transport measurement becomes insensitive. On the contrary, QPC-based charge sensing will not be affected by this effect. Another advantage in the case of a quantum dot connected to only one reservoir is that charge sensing using a QPC is still possible whereas transport measurement will be impossible to set up.

We will now discuss in more details the characteristics and the way to process the signal of a QPC. The part of the sample on which a dot has been defined is shown on Fig. 1.4 (see inset of the bottom right diagram). On the left part, one can recognize a structure similar to the one presented on Fig. 1.2. The quantum dot is defined by the four blue gates, and the lower red gate defines the QPC. The two green gates prevent any coupling with an electron reservoir on the right side of the dot. We have thus here a single lead quantum dot.

The top left plot of Fig. 1.4 shows a typical measurement of the QPC current when varying the voltage applied on V_{QPC}. As V_{QPC} is set more and more negative, the constriction where the current is forced to pass gets more and more pinched and the measured current is reduced. Plateaus start appearing when pinching is almost complete, revealing the quantized nature of G_{QPC}. The setting point for the sensor to be efficient is highlighted in red. As it has been said, the QPC current is highly affected by a change in the electrostatic environment at this position.

Once the QPC is tuned to this specific position, one can now vary the voltage applied on a gate defining the quantum dot. Figure 1.4 represents the evolution of G_{QPC} when sweeping the voltage applied on gate V_L. The general trend of the curve (lower current for more negative V_L) is the effect of direct capacitive coupling between the gate voltage that is swept and the QPC. On top of that, small jumps in the current are observed. Each of them is the result of the tunneling of an electron from the dot to the reservoir. Indeed as V_L is swept more negative, the dot chemical potential is progressively raised, and at some point the number of electrons in the dot will be reduced.

All the information we need is then contained in these jumps of the QPC current. A switch to a larger (resp. smaller) current will mean less (resp. more) electrons in the dot. It is therefore more clever to look at the derivative of the signal: one will get rid of the trend imposed by the direct capacitive coupling to the gates, and the changes in the dot occupation will be highlighted (see bottom left plot of Fig. 1.4).

It is now possible to perform a characterization of the charge state of a quantum dot by studying G_{QPC} as a function of the gate voltages applied to V_L and V_R. This so-called charge stability diagram constitutes usually the first step of an experiment on a quantum dot. An example of such a diagram is shown on the bottom right plot of Fig. 1.4. The voltages applied on gate V_L and V_R are respectively swept and stepped, while the current of the QPC is recorded and numerically derived. The lines that can be seen on the diagram

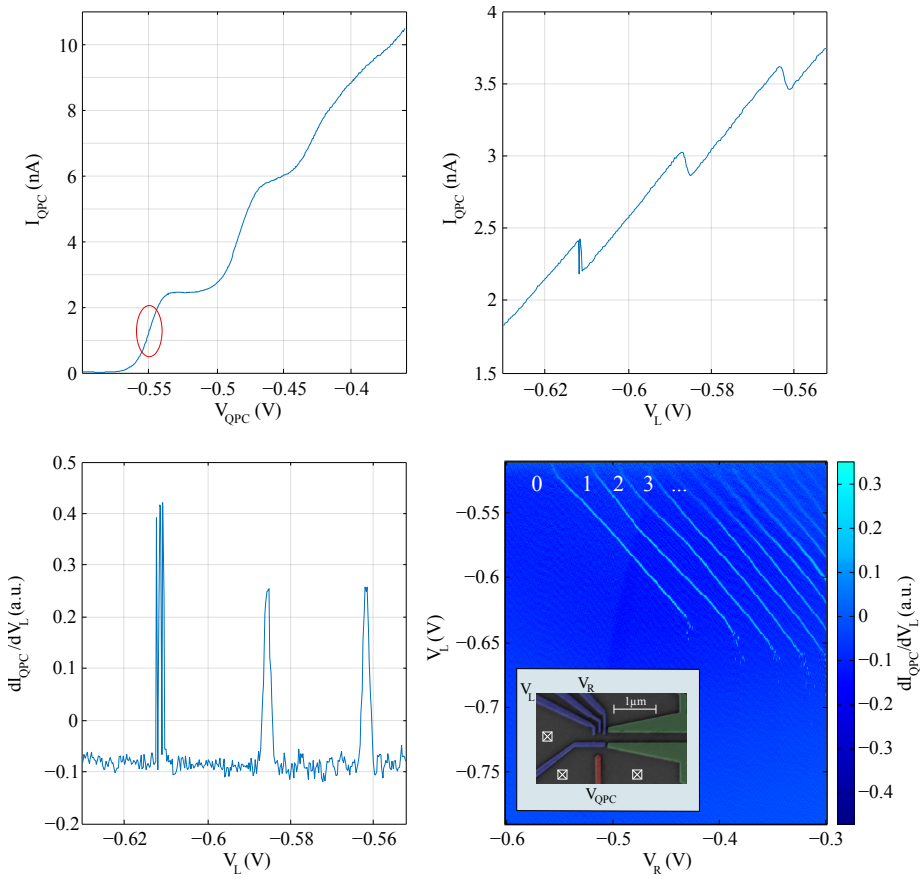

Figure 1.4: (top left) Pinching of the QPC and observation of a few conductance plateaus. The bias applied between the two ohmic contacts of the QPC is around 30 µV. The position to use for optimal sensitivity is circled in red. **(top right)** Observation of steps in the QPC current indicating a change in the number of electrons contained in the quantum dot. **(bottom left)** Derivative of the top right plot. The derivative is achieved numerically. A smoothing function (moving averaged) is first applied to the signal to improve the quality of the result. **(bottom right)** Charge stability diagram of the quantum dot. V_L is swept (going to more negative values) while V_R is stepped. QPC current is averaged for 3 ms for each data point. (inset) SEM picture of the part of the sample of interest. Ohmic contacts are indicated by the white squares.

correspond to the peaks in the QPC current derivative, and therefore stand for changes in the number of electrons in the dot. On the left of the diagram, there is no charge degeneracy line anymore, indicating that the dot has been completely emptied. It is then possible to deduce how many electrons are in the dot for each part of the diagram (it is labeled in white on the diagram for the first regions).

It can also be seen that the degeneracy lines are disappearing for the most negative values of V_L. In this region, the tunnel coupling between the dot and its reservoir becomes too weak (typically $< 1\,\mathrm{kHz}$). One obtains an isolated dot and no change in the electron number can be observed anymore (within the measurement timescale). Using this feature, it has been shown that a quantum dot with very large tunnel barriers can trap electrons for minutes or even hours in nonequilibrium conditions [Coo00]. A further study of this isolated dot configuration will be the subject of chapter 4. On the contrary, the lines are broadened on the top right part of the diagram. This is the result of a very strong tunnel coupling (which typically overcomes the temperature broadening around $\sim 1\,\mathrm{GHz}$). This change of the tunnel coupling over many orders of magnitude emphasizes the great tunability of these systems.

1.2 Spin states in a single quantum dot

We have seen in section 1.1 how to confine a single or a few electrons into a quantum dot, and how the charge of the dot can be probed and controlled. However, we are also interested in the spin state of the system. In this section, the different spin states that are found for a single or a two-electron system will be described as well as the techniques used to measure them.

1.2.1 One-electron spin states

This is the simplest case that can be faced. The two eigenstates for the electron spin are spin up ($|\uparrow\rangle$) or spin down ($|\downarrow\rangle$). In the absence of magnetic field, these two states are degenerated. When a magnetic field is applied, all the orbitals of the dot split into Zeeman doublets. The relative shift of the energy levels is given by the Zeeman energy, $E_Z = g\mu_B B$, where $\mu_B = 9.27 \cdot 10^{-24}\mathrm{J/T}$ is the Bohr magneton, and g is the effective Landé factor. In bulk GaAs, the value of g is -0.44, which results in an energy splitting around $25\,\mu\mathrm{eV/T}$. Because of its negative sign, the lowest energy state corresponds to the electron spin pointing up, *i.e.* parallel to the magnetic field, and the excited state to the spin pointing down, *i.e.* anti-parallel to the magnetic field.

1.2.2 Two-electron spin states in a single quantum dot

We consider now the case of two electrons in a single quantum dot. In this case, the two electrons will be indistinguishable, and it is now necessary to construct a wavefunction describing both particles. For fermions, the overall wavefunction (product of an orbital part and a spin part) must be anti-symmetric with respect to exchange of the particles. Therefore the states must have a symmetric orbital part and an anti-symmetric spin part or *vice versa*. If we restrict the discussion to the two lowest orbitals of a quantum dot (a ground orbital $|g\rangle$ and an excited orbital $|e\rangle$), only a few authorized states can be constructed.

At zero magnetic field, the ground state of a two-electron dot is always a singlet state (total spin number $S = 0$) with the two electrons occupying the lowest orbital [Ash76]. It can be written

$$|S\rangle = |gg\rangle \otimes \frac{|\uparrow\downarrow\rangle - |\downarrow\uparrow\rangle}{\sqrt{2}} \tag{1.10}$$

This is the only state where the electrons are allowed to both occupy the lowest orbital. It can be noted that the orbital part is symmetric while the spin part is anti-symmetric.

For the next possible states, at least one electron has to occupy the excited orbital. Three states called the spin triplets (with total spin number $S = 1$) can be written, which have a symmetric spin part. They are referred as follows:

$$|T_+\rangle = \frac{|ge\rangle - |eg\rangle}{\sqrt{2}} \otimes |\uparrow\uparrow\rangle \qquad (m_s = +1) \tag{1.11a}$$

$$|T_0\rangle = \frac{|ge\rangle - |eg\rangle}{\sqrt{2}} \otimes \frac{|\uparrow\downarrow\rangle + |\downarrow\uparrow\rangle}{\sqrt{2}} \qquad (m_s = 0) \tag{1.11b}$$

$$|T_-\rangle = \frac{|ge\rangle - |eg\rangle}{\sqrt{2}} \otimes |\downarrow\downarrow\rangle \qquad (m_s = -1) \tag{1.11c}$$

At zero magnetic field, they all have the same energy. This degeneracy is lifted by the Zeeman energy in finite magnetic field because of their different quantum number m_s (corresponding to the spin z component).

Finally, the last two states that can be found using only two orbitals are excited singlets with one or both electrons occupying the higher energy orbital:

$$\text{first excited singlet} : \frac{|ge\rangle + |eg\rangle}{\sqrt{2}} \otimes \frac{|\uparrow\downarrow\rangle - |\downarrow\uparrow\rangle}{\sqrt{2}} \tag{1.12a}$$

$$\text{second excited singlet} : |ee\rangle \otimes \frac{|\uparrow\downarrow\rangle - |\downarrow\uparrow\rangle}{\sqrt{2}} \tag{1.12b}$$

Even though the triplets and the first excited singlet all have one electron on each orbital, the energy of the excited singlet is higher (at zero magnetic field). Indeed, given the orbital part associated with the excited singlet, the two electrons tends to be at the same position while they tend to avoid each other for the anti-symmetric orbital of the triplets. When adding to this description the effect of the Coulomb interaction between the electrons, the energy of the excited singlet will therefore be further lifted up.

1.2.3 Spin readout techniques

The magnetic moment associated with the spin of a single electron is extremely small and it is very challenging to measure it directly (but has been achieved in [Rug04]). On the contrary we have seen in section 1.1.3 that it is relatively easy to measure the charge state of a quantum dot. The procedure to allow for single spin measurements relies therefore on the engineering of a spin dependent tunneling. This is called a spin-to-charge conversion. In the following, two different procedures realizing spin-to-charge conversion are presented.

Energy selective readout

This method requires an energy difference between the spin states that are involved. It has been used to probe the state of either a single [Elz04] or a two-electron spin [Meu06a]. We will generalize the principle of the measurement by talking about the excited $|E\rangle$ and the ground $|G\rangle$ spin state of the system. In the case of a single electron spin, $|G\rangle$ corresponds to $|\uparrow\rangle$ and $|E\rangle$ to $|\downarrow\rangle$. For the case of a two-electron spin state, $|G\rangle$ will stand for the singlet ground state $|S\rangle$ and $|E\rangle$ represents any of the three triplet states.

We consider a quantum dot coupled to a reservoir and with its charge state monitored by a QPC. The position of the quantum dot chemical potential relative to the Fermi level of the reservoir (E_F) can easily be adjusted by changing gate voltages. The principle of the measurement is to set the dot chemical potential such that E_F lies between the ground and the excited spin states. If the system is initially in $|G\rangle$, (see bottom left sketch of Fig. 1.5), we are in the most energetically favorable configuration and nothing happens. In contrast, in the case where the system is in $|E\rangle$ (see top left sketch of Fig. 1.5), it will be possible for an electron of the dot to relax to the reservoir. A new electron can next enter the quantum dot to occupy the $|G\rangle$ state. Temporarily, the quantum dot has contained one electron less. This change in the dot electron number can be observed on the QPC signal. The right plot of Fig. 1.5 shows two typical traces obtained for a dot containing an excited spin state (blue) and a ground spin state (green). For the green curve, the QPC current does not vary, meaning that the number of electrons in the dot remains constant. For the blue curve, it can be observed a sudden jump of I_{QPC} to a more positive value revealing that an electron tunneled off the dot. Then the current switches back to its initial value, indicating that a new electron tunneled into the dot.

This technique enables to measure a spin state in a single-shot manner. This is especially valuable for applications in quantum information processing. However it also suffers from several limitations. The first one is that for a clear readout, the energy splitting between the spin states must be larger than the thermal energy of the electrons in the reservoir. Thus for a single spin, the readout will be effective only for very large magnetic fields ($g\mu_B B >> k_B T$). A second limitation arises from the trade-off on the tunnel coupling rate that must be done. On the one hand if the tunneling time is too large compared to the spin relaxation time, the spin can relax before a tunneling event occurs and the measurement of an excited state will fail. On the other hand if the tunneling time is faster than the measurement bandwidth, the time spent by the dot with $N-1$ electrons can be too short to be detected. Finally this technique requires a precise positioning of the spin levels with respect to the Fermi level of the reservoir. As a consequence it is very sensitive to background charge fluctuations, which can be a major issue if the sample is not perfectly stable.

Tunnel-rate selective readout

An alternative solution that has been developed is tunnel-rate selective readout. The main ingredient necessary for this technique is a spin-dependent tunnel rate. It has been pioneered in 2005 by Hanson *et al.* [Han05]. Similarly to the previous method, changes in gate voltages allow to control the position of the dot chemical potential. It is set such that both the ground and excited spin states lie above the Fermi energy of the reservoir (see

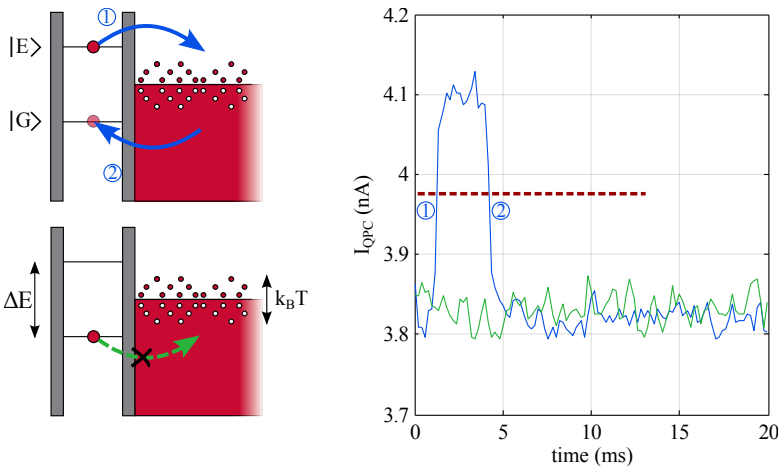

Figure 1.5: Principle of energy-selective readout. **(left)** Schematics of a quantum dot in a readout position. The top sketch corresponds to the case of an excited spin state present in the dot. Tunneling to the reservoir is energetically possible and a new electron can tunnel onto the dot to occupy the ground state. The bottom sketch corresponds to a ground spin state in the dot. Tunneling to the reservoir is not possible. **(right)** Typical QPC current traces obtained in energy-selective readout position (two-electron spin measurement). The blue curve corresponds to a excited spin state and the green curve to a ground spin state. A threshold (red dotted line) can be defined to distinguish between the two kinds of traces.

left sketch of Fig. 1.6). Regardless of the initial spin state, an electron will tunnel off the quantum dot. However if the tunnel rate for an excited state (Γ_E) is much larger than for the ground state (Γ_G), then at a suitably chosen time the dot will have a large probability to be already empty if the spin state was $|E\rangle$, but a large probability to be still occupied if the spin state is $|G\rangle$. An example of measurement is presented on the right plot of Fig. 1.6.

The main advantage of this scheme is its robustness against charge switches, since no precise positioning of the dot levels with respect to the lead is required: both levels simply have to be above E_F. Also, switches have a small influence on the tunnel rates themselves, as they tend to shift the whole potential landscape up or down, rather than modulating a single tunnel barrier [Jun04]. Of course, the measurement visibility will depend on the difference in tunnel rates that can be achieved[1].

For two-electron spin states, a difference of tunnel rates is often present. In the singlet state, the two electrons occupy the ground orbital whereas for a triplet state, one of the electrons is in the first excited orbital. As higher orbitals of a dot have more weight near the edges of the confining potential, the coupling to the reservoir is generally stronger for a triplet state than for a singlet. Nevertheless, this is strongly dependent on the precise dot configuration, and in some cases the rates will be too similar to use this procedure.

A difference in tunnel rate for spin-up and spin-down electrons has also been measured [Ama08c; Hou13; Yam14], usually more pronounced at larger magnetic field. However

1 Similarly to the energy selective readout, the relaxation rate can also affect the measurement visibility.

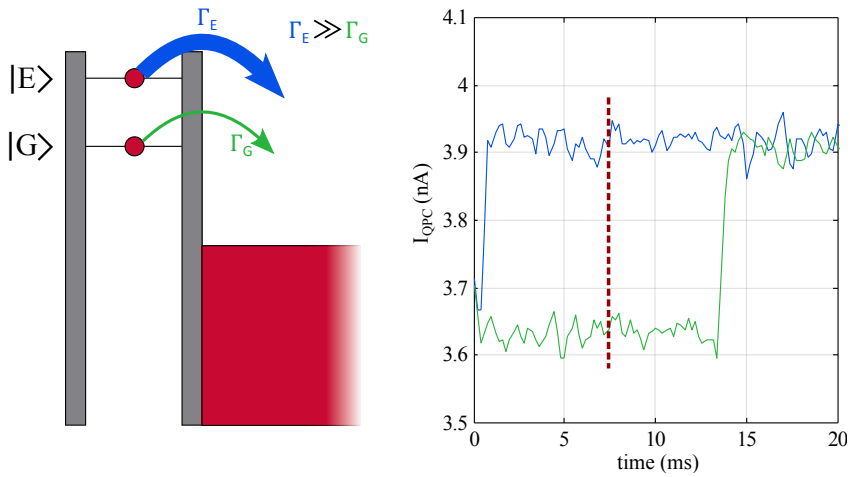

Figure 1.6: (left) Illustration of the principle of tunnel-rate selective readout. The ground and excited spin states are set above the Fermi level of the reservoir. The figure corresponds to the case where the tunneling rate of the excited state is much larger than the ground state. **(right)** Typical QPC traces obtained in tunnel-rate readout configuration (two-electron spin measurement). The blue curve corresponds to an excited spin state and the green to a ground spin state. A threshold can be defined to distinguish between the two kinds of events (red dotted line).

there is for the moment no clear explanation to understand this behavior. Contrary to the two-electron case, it is observed that the ground state is more strongly coupled to the reservoir than the excited state, which is not preventing tunnel rate selective readout in principle. Nevertheless, the effect remains modest, and the spin-selectivity achieved does not allow for clean single-shot spin measurement. In principle, a much larger spin-selectivity is possible in a perpendicular magnetic field, *i.e.* in the quantum Hall regime (see [Cio00; Cio02]).

The main drawback of the two readout schemes we have described is that an electron (and therefore the spin) is lost after tunneling to the reservoir. It would be preferable to have a measurement protocol that leaves the spin state unaffected. That would allow a so-called quantum nondestructive (QND) measurement. One thing that can be done is to re-initialize the spin to the state it was before the electron tunneling [Meu06b]. Another solution would be to be able to keep trace of the electron after its tunneling. Instead of having an electron tunneling to a reservoir, it is possible to have it tunneling to a second dot where it can remain isolated. This is the purpose of the Pauli spin blockade readout in double quantum dots, and it will be the object of section 1.3.2.

1.3 Spin states in a double quantum dot

1.3.1 Two-electron spin states in a double quantum dot

We consider now two coupled quantum dots (with a tunnel coupling t_c), and we will restrict the study to the case of two-electron systems. On a first approximation, we can

consider the case of $t_c = 0$. An electron is either on the left or on the right minimum of potential. When working with two electrons, three different charge configurations are then encountered: the two electrons can be located on the left (resp. right) minimum or there can be one electron in each minimum of the double dot. In the following, the different charge configurations will be labeled (2,0), (1,1) or (0,2), where the (i,j) notation refers to i electrons located in the left minimum and j electrons in the right minimum.

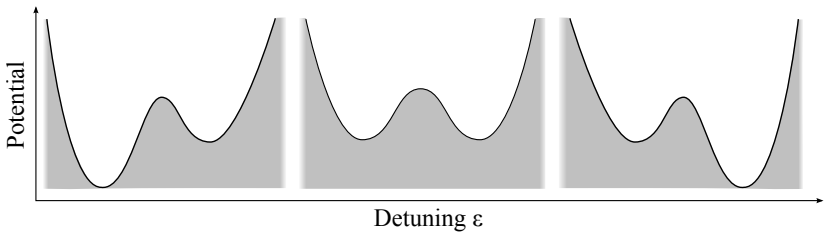

Figure 1.7: Evolution of the double quantum dot potential shape as a function of detuning. A (2,0), (1,1) and (0,2) charge configuration is more favorable for the left, middle and right case respectively.

When the double dot potential is symmetric, the (1,1) configuration is the most favorable in energy since the Coulomb interaction between the electrons is minimized (the cost of the charging energy is reduced). It is then possible to change the charge configuration of the double dot by making one side more favorable in energy. The energy difference between the two minima is called the detuning of the double dot and is noted ε. An illustration of the shape of the potential profile for different values of this parameter is represented on Fig. 1.7. For large values of detuning, the energy cost of Coulomb interaction can be overcome so that the two electrons will be in the same minimum of potential. In this case, the eigenstates will be equivalent to those of a single quantum dot. The ground state at zero magnetic field is the singlet state with the two electrons occupying the lowest orbital. The triplet states are higher in energy since one electron must occupy a higher energy orbital. In the case of a (1,1) charge state, it is still possible to define the singlet and triplet states. Only the orbital part will be modified to construct symmetric or anti-symmetric combinations of each single-dot orbital state. It has to be noted that it is no longer necessary to have an electron occupying a higher energy orbital to form a triplet, and in the absence of magnetic field, all spin states are degenerate.

This discussion can be summarized on the energy diagram represented on the top plot of Fig. 1.8. When the detuning is changed by a value ε, it is considered that the left dot chemical potential has been raised by $\frac{\varepsilon}{2}$ and the one of the right dot has been lowered by the same amount. As a result, the energy of a (1,1) state is constant for any value of detuning while the energy of the (2,0) and (0,2) states are linearly shifted with detuning. Since we do not consider any magnetic field for the moment, the three triplet states are degenerate and are simply labeled $|T\rangle$.

We can now start to take into account the tunnel coupling t_c between the dots (see also [Wie02] or [CT77]). Since a tunneling process is spin conservative, only the states with similar spin part will be coupled. We will focus more specifically on the case of the $|S(1,1)\rangle$

and $|S(0,2)\rangle$ states. We define the origin of the ε axis as the crossing point of these two unperturbed states (see Fig. 1.8). In the $\{|S(0,2)\rangle, |S(1,1)\rangle\}$ basis, the Hamiltonian can then be written as

$$H = \begin{pmatrix} -\varepsilon & t_c \\ {t_c}^* & 0 \end{pmatrix} \tag{1.13}$$

The new eigenstates are now the analogous of bonding ($|\psi_B\rangle$) and anti-bonding ($|\psi_A\rangle$) orbitals in a molecule. They are given by

$$|\psi_B\rangle = \frac{1}{\sqrt{(t_c)^2 + (\Omega_-)^2}} \begin{pmatrix} \Omega_- \\ t_c \end{pmatrix} \tag{1.14a}$$

$$|\psi_A\rangle = \frac{1}{\sqrt{(t_c)^2 + (\Omega_+)^2}} \begin{pmatrix} \Omega_+ \\ t_c \end{pmatrix} \tag{1.14b}$$

where $\Omega_\pm = -\frac{\varepsilon \pm \sqrt{\varepsilon^2 + (2t)^2}}{2}$. Their respective energies are

$$E_B = \frac{-\varepsilon - \sqrt{\varepsilon^2 + (2t_c)^2}}{2} = \Omega_- \tag{1.15a}$$

$$E_A = \frac{-\varepsilon + \sqrt{\varepsilon^2 + (2t_c)^2}}{2} = \Omega_+ \tag{1.15b}$$

For $\varepsilon = 0$, the bonding and antibonding states are the symmetric and anti-symmetric superposition of $|S(0,2)\rangle$ and $|S(1,1)\rangle$, with an energy splitting of $2t_c$. It can also be verified that for $|\varepsilon| \gg t_c$, the two eigenstates tend towards the $|S(0,2)\rangle$ and $|S(1,1)\rangle$ states with respective energies of $-\varepsilon + \frac{{t_c}^2}{\varepsilon}$ and $-\frac{{t_c}^2}{\varepsilon}$. A similar behavior will be observed at each level crossing involving two states with identical spin parts. The resulting energy diagram is represented on the center plot of Fig. 1.8.

The two-spin system can be described by the Heisenberg Hamiltonian $H = J\vec{S}_1.\vec{S}_2$, where $\vec{S}_i$ is the electron-spin operator. In this mapping procedure, J corresponds to the energy difference between the lowest energy singlet and the $|T_0\rangle$ triplet state. It will depend on the tunnel coupling t_c and the single-dot charging energy E_C. In the position where the two dots are aligned, $J = 4{t_c}^2/E_C$ in the Hubbard approximation [Bur99; Hu00; Los98]. This is consistent with the result we obtained on the above calculation. This exchange interaction can therefore be modulated from very small to very large values either by modifying the interdot tunnel coupling or by changing the detuning of the system.

Finally, if a finite magnetic field is now applied to the system, the degeneracy between the triplet states is lifted. The states T_+ (resp. T_-) is shifted down (resp. up) by the Zeeman energy ΔE_Z. This is commonly used to work in the S and T_0 subspace with no risk of feeling the influence of the other triplet states.

As it has already been discussed, triplet states are much higher in energy (usually a few hundreds of µeV) for the (0,2) and (2,0) configurations. Consequently the avoided crossing of the triplets are pushed relatively far away from the singlet anticrossing. This induces a

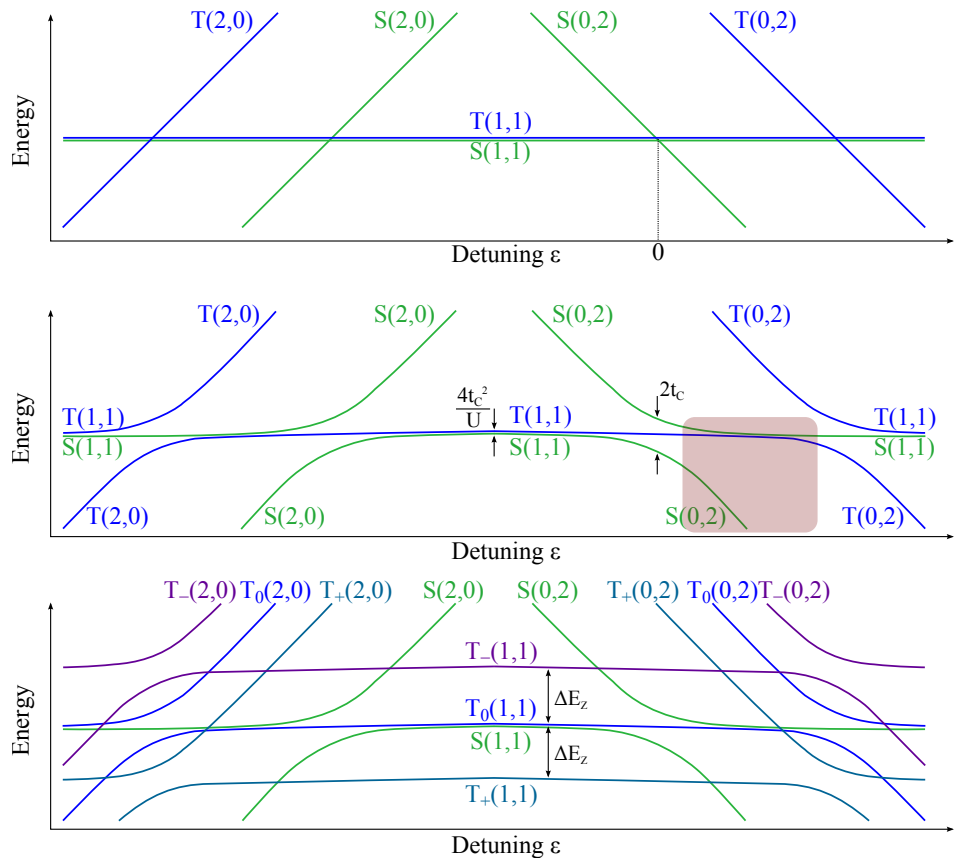

Figure 1.8: Energy diagrams of the different spin states in a double quantum dot as a function of detuning ε, for different values of the interdot tunnel coupling t_c and magnetic field B_0. **(top)** $t_c = 0$ and $B_0 = 0$ **(middle)** $t_c \neq 0$ and $B_0 = 0$ **(bottom)** $t_c \neq 0$ and $B_0 \neq 0$.

range of detuning where the lowest energy state for a singlet is in a (0,2) (or (2,0)) charge configuration while it is energetically favorable for the triplets states to be in a (1,1) charge configuration. This is highlighted by the red region on the energy diagram. This specific position can therefore be used for spin readout of the system [Eng04] (see section 1.3.2).

1.3.2 Spin Blockade readout

This effect was first observed in experiments on vertically coupled quantum dots [Ono02] and later applied to lateral quantum dots [Joh05b]. It was originally probed with transport measurement across a double dot system. We will not discuss extensively about spin blockade here but only give its basic principle and how to use it for spin readout.

We consider a two-electron system in a double dot initially in a (1,1) configuration (for simplicity, the magnetic field is assumed to be zero). The double dot detuning is then increased (see arrows on the bottom left energy diagram of Fig. 1.9). Basically, it consists in tuning the system to the position where it is energetically favorable for a singlet state to be in a (0,2) charge configuration whereas it is favorable for a triplet state to

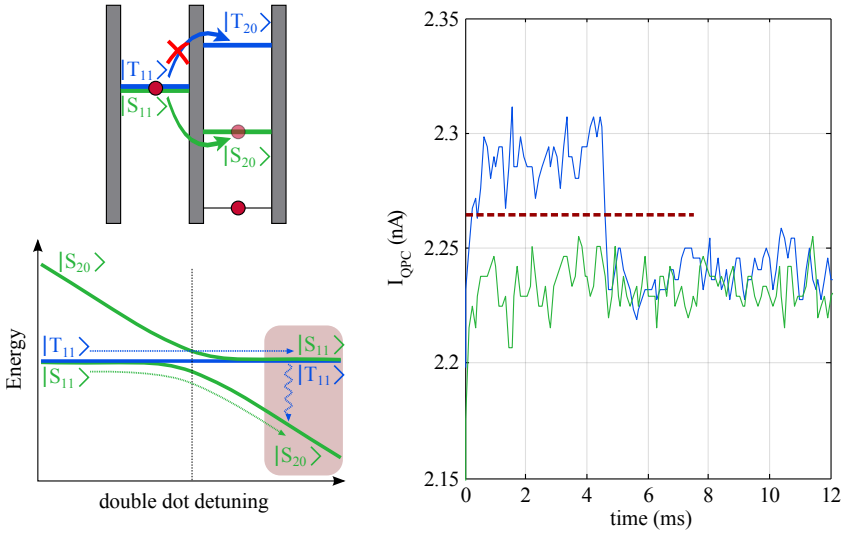

Figure 1.9: (top left) Schematics of a double quantum dot in a spin blockade configuration. It is favorable for a singlet to be in a (2,0) configuration whereas a triplet remains in a (1,1) configuration. **(bottom left)** Corresponding energy diagram. Spin blockade position is highlighted in red. **(right)** Typical QPC current traces obtained in spin blockade readout configuration. The blue curve corresponds to a triplet and the green to a singlet. A threshold can be defined to distinguish between the two kinds of events (red dotted line).

remain in a (1,1) configuration (see top left diagram of Fig. 1.9 and the red regions on the energy diagram). If the electrons were initially forming a singlet state $|S(1,1)\rangle$, the electron in the left dot can tunnel to the right dot to form the $|S(0,2)\rangle$ state (since tunneling is spin-preserving). On the contrary, if electrons were initially forming one of the triplet states $|T(1,1)\rangle$, the electron in the left dot will be blocked because $|T(2,0)\rangle$ is too high in energy, and the system remains in the (1,1) charge configuration. This blockaded position will be held until the electron spin relaxes to the singlet state, which requires a spin flip and can be as long as a few milliseconds. From a standard QPC charge measurement, it is therefore possible to distinguish between the two different situations and deduce the spin state of the system. An example of QPC measurement is shown on the right graph of Fig. 1.9. At $t = 0\,\text{ms}$, the system is pulsed from the (1,1) region to the measurement position. For the singlet state (green curve) the tunneling to the (0,2) region occurs faster than the measurement bandwidth and cannot be observed. A constant current corresponding to the (0,2) charge state is measured. For the triplet states (blue curve), the QPC current remains at a higher value (corresponding to the (1,1) charge state) for a few milliseconds before reaching the (0,2) configuration.

When such direct observation through QPC charge sensing is possible, single-shot spin readout can be achieved. Successive spin measurements of the same two electrons can therefore be performed (see for instance [Bar09] or [Pra12]). In principle a non-destructive measurement of the spin state can be set up since no exchange with a reservoir is required

anymore.

1.4 Couplings to the environment

1.4.1 Relaxation, dephasing and decoherence

Until now we have considered a quantum system, a single or two-electron spin, without taking into account its interaction with the environment. In GaAs/AlGaAs lateral quantum dots, two main interactions are encountered: spin-orbit and hyperfine interactions. If control over these interactions is achieved, they can provide means of coherent spin manipulations [Fol09; Now07] and prove to be very useful. However if this is not the case, they will disturb the quantum system and result in the loss of the stored information.

Meeting the accuracy thresholds for fault tolerant quantum computation in any physical system is very challenging, and consists most of the time in reducing the detrimental effects of such uncontrolled interactions. In that sense, a detailed understanding of the processes that lead to information losses is of direct interest. They are by now well understood for GaAs/AlGaAs quantum dots, and we will describe the main features in the following.

Let us first introduce a convenient way to picture these processes by using the Bloch sphere representation (see [Nie10] and left sketch of Fig. 1.10). Mathematically, the physical state $|\psi\rangle$ of a two-level system, is written as:

$$|\psi\rangle = \alpha\,|0\rangle + \beta\,|1\rangle \tag{1.16}$$

where $|0\rangle$ and $|1\rangle$ are respectively the ground and excited states of the two-level system, and α and β are complex numbers satisfying the normalization criterion $|\alpha|^2 + |\beta|^2 = 1$. This normalization makes it natural to think of $|\psi\rangle$ as a point on a sphere (referred to as the Bloch sphere) of radius 1. The state $|\psi\rangle$ can be rewritten using spherical coordinates as

$$|\psi\rangle = \cos\left(\frac{\theta}{2}\right)|1\rangle + \sin\left(\frac{\theta}{2}\right)e^{i\phi}\,|0\rangle \tag{1.17}$$

where the poles of the Bloch sphere correspond to the eigenstates $|0\rangle$ and $|1\rangle$ of the system.

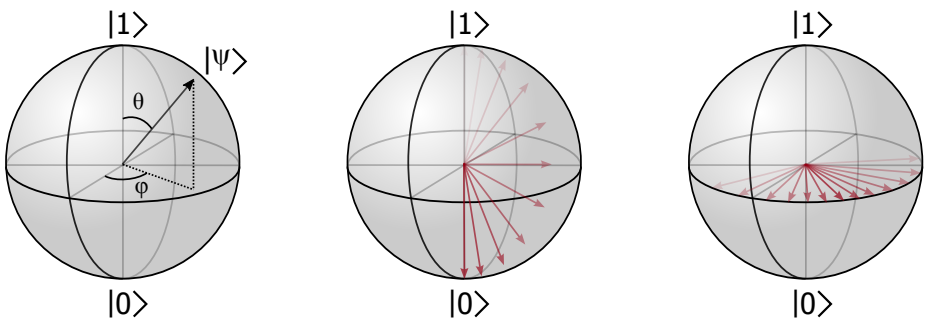

Figure 1.10: (left) Representation of a quantum state on a Bloch sphere. The angles are defined in equation 1.17. **(middle)** Illustration of a relaxation process. **(right)** Illustration of a decoherence process.

The information that is stored into the qubit can be viewed as the position of the state on this Bloch sphere. The mechanisms we want to identify are thus processes that affect the position of the state on the sphere. The coupling of the qubit to its environment leads to two kind of processes.

First, a system in an arbitrary superposition will relax over time into its ground state[1]. On the Bloch sphere, it can be viewed as a collapse of the state towards the pole corresponding to the ground state (see center sketch of Fig. 1.10). During this process, characterized by a timescale called T_1, the qubit exchanges energy with its environment. For an electron spin in a GaAs dot, the energy will be dissipated mainly to the phonon bath [Meu07].

The second process consists in a loss of phase information. In contrast with relaxation, this dephasing occurs without energy exchange, *i.e.* the latitude on the Bloch sphere remains constant (see right sketch of Fig. 1.10). Phase noise can be separated into two types, dephasing (described by a timescale called T_2^*) and decoherence (T_2 timescale). Dephasing corresponds to how fast an ensemble of qubits[2] loses phase information. It occurs when members of this ensemble experience different conditions, for instance varying local magnetic or electric fields. This will imply slightly different Hamiltonians for each qubit, resulting in a distribution of phases across the ensemble. Contrary to relaxation or decoherence, the effect of dephasing can be mitigated through clever qubit manipulation using so-called dynamical decoupling techniques. This will allow to cancel out static or slow variations in the Hamiltonian across the ensemble, restoring coherence. The simplest and most familiar of these techniques is the Hahn Echo [Hah50]. Decoherence corresponds to how fast an individual qubit loses its phase information. Experimentally, a lower bound can be estimated through the longest coherence time T_2 that is achievable with dynamical decoupling techniques. Mechanisms responsible for decoherence can be for instance entanglement with the environment, or classical noise that occurs too rapidly to be corrected by dynamical decoupling sequence. This sets $T_2 \geq T_2^*$ as a bound on the dephasing time, while the relaxation rate by definition limits the coherence time to be $T_2 \leq 2T_1$.

In the following, we will consider more precisely the spin-orbit and hyperfine interactions and show how they can induce relaxation and dephasing of an electron spin.

1.4.2 Spin-Orbit interaction

The spin of an electron moving with a momentum $\mathbf{p}$ in an electric field $\mathbf{E}$ experiences an internal magnetic field proportional to $\mathbf{E} \times \mathbf{p}$. As a consequence, the spin of the electron couples to its momentum. This is the case *e.g.* for an electron "orbiting" around a positively charged nucleus. It is well known that atomic spectra are strongly affected by the spin-orbit coupling. In solids, the electrons also experience electric fields coming from the charged atoms in the lattice and from the band structure. Two major contributions to spin-orbit coupling are known and present in GaAs/AlGaAs heterostructures.

1 Except for temperatures higher than the qubit level splitting, for which the system will evolve into an incoherent statistical mixture of $|0\rangle$ and $|1\rangle$ states in thermal equilibrium with the environment.

2 This is true for single qubit as well. The repetition of an experiment with time fluctuating environment is equivalent to the case of an ensemble of qubits in space fluctuating experimental conditions.

The first one is known as the Dresselhaus spin-orbit interaction [Dre55; Par55]. It occurs in crystals that exhibit bulk inversion asymmetry (BIA), which is the case of the Zinc Blende structure of GaAs. For two-dimensional systems, the Dresselhaus spin-orbit Hamiltonian can be written as

$$H_{SO,D} = \beta(-p_x\sigma_x + p_y\sigma_y) \tag{1.18}$$

where β is a constant depending on the material properties and on $\langle {p_z}^2 \rangle$.

Secondly, the electric fields coming from asymmetric confining potentials can also give rise to a spin-orbit contribution. This contribution, due to so-called structural inversion asymmetry (SIA), is known as the Rashba term [Byc84; Ras60]. In our system, the triangular shape of the confinement at the GaAs/AlGaAs interface allows for such an effect (see Fig. 1.1). In two-dimensional systems with a confinement along the z-axis, we have

$$H_{SO,R} = \alpha(p_x\sigma_y - p_y\sigma_x) \tag{1.19}$$

where α is a constant depending on the material and the value of the confining electric field.

In 2DEG, the contribution of both terms are comparable and they have to be added to picture the whole spin-orbit interaction. It can be noted that the strength of the spin-orbit will be sensitive to the direction of the electron momentum (the terms can tend to sum or cancel each other, see [Gol08]).

To understand the effect of this interaction, it is often pictured as the occurrence of an effective magnetic field (B_{SO}) that will be directly proportional to the electron momentum. The faster the electron moves, the larger is B_{SO} and the faster the spin will precess around. However as the dependence with momentum is linear, the spin will always rotate the same amount over a given distance. A convenient way to quantify the magnitude of the spin-orbit interaction is therefore by defining the spin-orbit length l_{SO}. It corresponds to the length after which a spin has undergone a π-rotation when moving under the influence of the spin-orbit interaction. This has been measured in 2DEG [Zum02] and is on the order of $l_{SO} = 1$ to $10\,\mu\text{m}$. As the size of quantum dots is much smaller ($l_{dot} \sim 100\,\text{nm}$), it is reasonable to expect that spin-orbit interaction weakly affects the electron spin states in a quantum dot (the coupling is scaling as l_{dot}/l_{SO}).

We will now consider more quantitatively the case of a single electron in a quantum dot. Its average motion is zero and $\langle p_x \rangle = \langle p_y \rangle = 0$. As the spin-orbit Hamiltonian H_{SO} only consists of terms of the form $p_{x,y}\sigma_{x,y}$ for both the Rashba and Dresselhaus contributions, this implies that

$$\langle \phi_n \uparrow | H_{SO} | \phi_n \downarrow \rangle \propto \langle \phi_n | p_{x,y} | \phi_n \rangle \langle \uparrow | \sigma_{x,y} | \downarrow \rangle = 0 \tag{1.20}$$

where ϕ_n stands for the orbital part of the state. Therefore, there is no direct coupling between the two spin states of the same dot orbital. Spin-orbit interaction will be effective only to couple states having both different orbital and spin parts [Kha00]. The perturbed eigenstates can be written as an admixture of different states using first order perturbation

theory [Han07a]:

$$|\phi_n \uparrow\rangle^{(1)} = |\phi_n \uparrow\rangle + \sum_{n' \neq n} \frac{\langle \phi_{n'} \downarrow| H_{SO} |\phi_n \uparrow\rangle}{E_{n'} - E_n - \Delta E_Z} |\phi_{n'} \downarrow\rangle \tag{1.21a}$$

$$|\phi_n \downarrow\rangle^{(1)} = |\phi_n \downarrow\rangle + \sum_{n' \neq n} \frac{\langle \phi_{n'} \uparrow| H_{SO} |\phi_n \downarrow\rangle}{E_{n'} - E_n - \Delta E_Z} |\phi_{n'} \uparrow\rangle \tag{1.21b}$$

where E_n is the energy of the orbital ϕ_n and ΔE_Z is the Zeeman splitting of unperturbed states.

The situation is a bit different for a two-electron state in a quantum dot. We have seen that the two electrons can be on the ground orbital to form a singlet state, but one electron must occupy a higher energy orbital to form a triplet because of Pauli principle. Therefore, singlet and triplet states have both different orbital and spin parts, and it results in direct coupling of some of the states through spin-orbit interaction (for instance between the $|T_\pm\rangle$ and $|S\rangle$ states or between $|T_0\rangle$ and $|T_\pm\rangle$). It can be noted however that no coupling is present (to the lowest order) between $|S\rangle$ and $|T_0\rangle$ or between $|T_+\rangle$ and $|T_-\rangle$. Rigorously, a similar reasoning than for the single electron case needs to be included since the first order corrections are generally non-negligible, and the new perturbed states can be written down. A detailed discussion can be found in [Gol08].

In any case, pure spin states are no longer the eigenstates of the system. An important consequence is that these pseudo-spin states will allow coupling of an electron spin to electric fields. This opens a channel for any source of electric noise to induce spin relaxation or decoherence. In that sense spin-orbit interaction is detrimental for the preservation of a spin state. In GaAs quantum dots, there exist various sources of electric noise. For instance, there can be noise from the gate potentials (such as Nyquist noise [Mar05]), background charge fluctuations [Jun04], charge fluctuations caused by electrons passing through the QPC [Bor06] or the electric-field fluctuations created by the lattice phonons. This latter source is often the major cause of spin relaxation and has been extensively studied in [Gol04; Kha01; Kha00; Woo02].

The relaxation rate depends on two factors:

- First, the phonon density of states at the energy ΔE corresponding to the difference between the initial and final state (energy conservation is ensured by emission of a phonon). This scales as ΔE^2.
- Second, the strength of the pseudo-spin state coupling to the phonons. This is most of the time given by the coupling to acoustic phonons via piezoelectric effect, and scales as ΔE^3.

In the end a relaxation rate dependency of ΔE^5 is expected [Kha01] and it is consistent with experimental observations [Ama08b; Elz04].

However as we said, such coupling can also have some advantages. The benefit is that it is possible to control spin transitions by use of electric fields only (which are much easier to produce than local magnetic fields), either coherently as proposed by [Deb05; Fli06; Lev03]. This will be briefly introduced in section 1.5.

1.4.3 Hyperfine interaction

Hyperfine interaction is well known in atomic physics: the magnetic moments of the electrons bound to a nucleus interact with the magnetic moment of that nucleus. This leads to the so-called hyperfine structure, consisting of a small splitting of an atom energy levels. In a quantum dot, an electron is confined on a much larger scale than in a single atom and can therefore interact with many nuclear spins of the host material (see Fig. 1.11). The nuclei of Gallium, Arsenic, and Aluminum all possess non-zero spins. Given the typical size of a quantum dot, the number N of nuclei that the electron overlaps can be estimated around 10^6. These nuclear spins interact with the electron spin through the contact hyperfine interaction, and following [Pag77], it can be written as

$$H_{HF} = \frac{8\pi}{3}\frac{\mu_0}{4\pi} g_0 \mu_B \hbar \sum_j \gamma_{n,j} \mathbf{I}_j.\mathbf{S} |\psi(\mathbf{r}_j)|^2 \tag{1.22}$$

where μ_0 is the vacuum permeability, g_0 is the free electron g-factor, $\gamma_{n,j}$ is the gyromagnetic ratio of the nuclear spin j at the position $\mathbf{r}_j$, $\mathbf{I}_j$ is the operator of this nuclear spin, $\mathbf{S}$ is the electron spin operator, and ψ is the electron wave function.

Instead of treating individually the contribution of each spin, a semi-classical description consists in treating the ensemble of nuclear spins as an apparent magnetic field B_N. The interaction can then be re-written as

$$H_{HF} = g^* \mu_B \mathbf{B_N}.\mathbf{S} = \hbar \gamma_e \mathbf{B_N}.\mathbf{S} \tag{1.23}$$

where g^* is the effective electron g-factor, γ_e is the gyromagnetic ratio of the electron spin and $\mathbf{B_N}$ is given by

$$\mathbf{B_N} = \frac{2\mu_0}{3}\frac{g_0}{g^*}\hbar \sum_j \gamma_{n,j} \mathbf{I}_j |\psi(\mathbf{r}_j)|^2 \tag{1.24}$$

This effective field is referred to as the Overhauser field. If the nuclear spins were all polarized, B_N would be expected around 5 T. However, the thermal energy in experimental conditions ($k_B T \sim 10\,\mu$eV for a temperature of 100 mK) is much larger than the splitting between energy levels of nuclear spins ($g^* \mu_B B \sim$ a few 10 neV for a 1 T external field applied). The nuclear spins are therefore in a high temperature regime and their spin polarization fluctuates. This allows us to consider the Overhauser field as a classical random variable exhibiting a Gaussian distribution centered on zero and with a typical width of $\Delta B \sim \frac{B_{N,max}}{\sqrt{N}} = 5\,$mT for $N = 10^6$.[1] The statistical distribution of the nuclear field has been measured in different kind of systems (optical [Bra05; Dut05] and electrical dots [Joh05c; Kop05]) and it varies from 1 to a few 10 mT. The timescale of these fluctuations is around 1 s or more in the z direction, and around $10 - 100\,\mu$s in transverse direction [Bar09; Rei08; Tay07]. It is thus a good approximation to consider the Overhauser field

1 The fact that the electron is confined to a quantum dot limits the number N of nuclear spins interacting with the electron and thus enhances the effect of the hyperfine interaction. It is contrasting in that sense with the case of spin-orbit interaction.

as constant during a single experiment, but subject to fluctuations between successive repetitions of the same measurement.

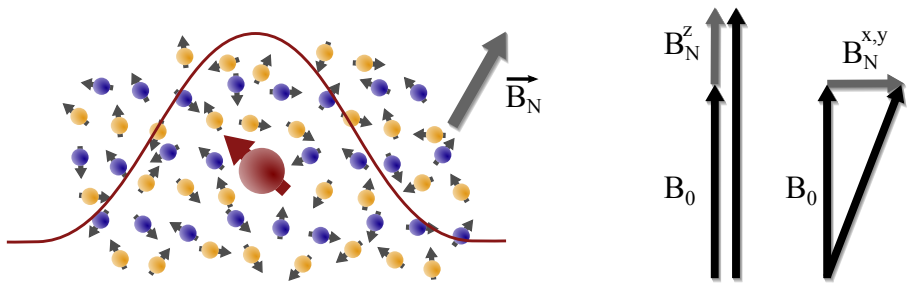

Figure 1.11: (left) The spin of an electron is coupled to $N \sim 10^6$ nuclear spins. The contribution of this ensemble of spins is modeled as an effective magnetic field $\mathbf{B_N}$ that adds up to the static magnetic field B_0 (applied by convention along the z direction). **(right)** The z component of this effective field adds up to the static magnetic field and will affect the precession frequency. The x and y components can affect the precession axis, depending on the magnitude of B_0.

This varying effective field has a major impact on the temporal evolution of the electron spin. In presence of an external magnetic field B_0 (applied by convention along the z direction), an electron spin will precess at the Larmor frequency $\omega = \gamma_e B_0$ around the field direction. The Overhauser field adds up to the external field, and therefore the z component of the nuclear field will directly affect the spin precession frequency. An additional 5 mT along the z component of the magnetic field will induce a 30 MHz shift of the precession frequency, resulting in a π additional phase after only 16 ns.

The impact of the x and y component of the nuclear field will depend on the external field applied. If $B_0 >> B_N^{x,y}$, it will slightly tilt the total field axis but will not affect its magnitude on the first order. For instance, with simply 100 mT of external field applied, an additional 5 mT along the x or y component will result in an additional π phase after 0.65 µs. On the contrary, if no external field is applied, the axis of precession can be in the xy plane and the electron spin will alternately be changed from spin up to spin down.

At any given time, the nuclear field thus assumes a random and unknown value and orientation, and this randomness in the nuclear field directly leads to a randomness in the electron-spin time evolution. During free evolution, the electron spin will thus pick up a random phase depending on the value of the nuclear field. Averaging over many realization will result in a decay of the coherent evolution. The shape of the decay (exponential, Gaussian, power law, etc.) is determined by the distribution of nuclear field values. For a longitudinal nuclear field B_N^z that is randomly drawn from a Gaussian distribution of nuclear fields with standard deviation ΔB_N^z (*e.g.*, when every nuclear spin had equal probabilities for being up or down), the decay would be Gaussian as well [Mer02], *i.e.* of the form $\exp\left(-\left(\frac{t}{\mathrm{T}_2^*}\right)^2\right)$ where

$$\mathrm{T}_2^* = \frac{\hbar\sqrt{2}}{g\mu_B\sqrt{\Delta B_N{}^z}} \tag{1.25}$$

For $\Delta B_N^z = 5\,\mathrm{mT}$, T_2^* would be as short as 7 ns.

Interesting developments on feedback mechanisms have been demonstrated that reduce the randomness of the nuclear fields, resulting in T_2^* extended by a factor of 10 [Blu10]. Dynamic nuclear decoupling using a series of echo pulses further extends the coherence time (extended by a factor of almost 10^4), and T_2 larger than 200 µs have been observed [Blu11].

Singlet-triplet mixing by nuclear spins in a double quantum dot

The effect of the hyperfine interaction in the case of two electrons separated in a double quantum dot can be studied in more details [Jou06; Tay07]. Each part of the double dot will experience a different effective magnetic field, respectively B_N^L and B_N^R for the left and right parts of the double dot. In that case, the Hamiltonian of eq. 1.23 can be rewritten as:

$$H_{HF} = g^* \mu_B \left(\mathbf{B_N^L}.\mathbf{S^L} + \mathbf{B_N^R}.\mathbf{S^R}\right) \tag{1.26a}$$

$$= \frac{g^* \mu_B}{2} \left[\left(\mathbf{B_N^L} + \mathbf{B_N^R}\right).\left(\mathbf{S^L} + \mathbf{S^R}\right) + \left(\mathbf{B_N^L} - \mathbf{B_N^R}\right).\left(\mathbf{S^L} - \mathbf{S^R}\right)\right] \tag{1.26b}$$

where $\mathbf{S^{L(R)}}$ is the spin operator of the left (right) electron. The effective nuclear field has been decomposed in a symmetric and an anti-symmetric part. The symmetric part simply adds vectorially to the external field B_0, and will have the same effect as what we explained just before. On the other hand, the anti-symmetric part is responsible for some coupling between the $|T(1,1)\rangle$ and the $|S(1,1)\rangle$ spin states. For the coupling between $|T_\pm(1,1)\rangle$ and $|S(1,1)\rangle$, only the in-plane components of the nuclear field gradient (noted $\Delta\mathbf{B_N} = \mathbf{B_N^L} - \mathbf{B_N^R}$) play a role, giving coupling terms of the form $g^*\mu_B \frac{\Delta B_N^x \pm i \Delta B_N^y}{\sqrt{2}}$. The longitudinal component of the nuclear field gradient couples the states $|T_0(1,1)\rangle$ and $|S(1,1)\rangle$ with a strength $g^*\mu_B \Delta B_N^z$. These coupling terms are generally on the order of 100 neV, and will be mostly relevant when spin states are degenerate. The conservation of the total angular momentum requires spin exchange between the electrons and nuclei.

1.5 Coherent spin manipulations

The key element towards possible use in spintronics and spin-based quantum information processing is the ability to control the state of a single electron spin in a quantum dot. By control, it is meant inducing transitions between the spin-up and spin-down states of a localized electron spin and to prepare arbitrary superpositions of these two states. For application in quantum logics, it is also required to realize two-qubit operations. In the following, we will briefly describe the principle of pioneering experiments that have been achieved towards these objectives.

1.5.1 Single-spin rotation

The most commonly used technique for inducing spin flips is electron spin resonance (ESR) [Poo96]. Its concept is very similar to the one of nuclear magnetic resonance (NMR). Electron spins are rotated by applying a transverse oscillating magnetic field B_{AC} that is resonant with the spin precession frequency in an external magnetic field B_{ext}. This

technique is well developed to probe and manipulate ensembles of spins, but the control of a single one is very challenging because of the coupling strength. It has been realized for the first time in 2006 [Kop06]. In order to address a single electron spin trapped in a quantum dot, a microfabricated coplanar stripline was precisely placed above the quantum dot. The application of RF-bursts to the stripline induces a local oscillating magnetic field that allows for the spin rotation. The fastest demonstrated rotations are about 10 MHz although in principle much faster rotations should be possible. The great advantage of this method is that a change of the relative phase of B_{AC} from one RF burst to the next allows to change the spin rotation axis. This permits a complete control of a single electron spin qubit.

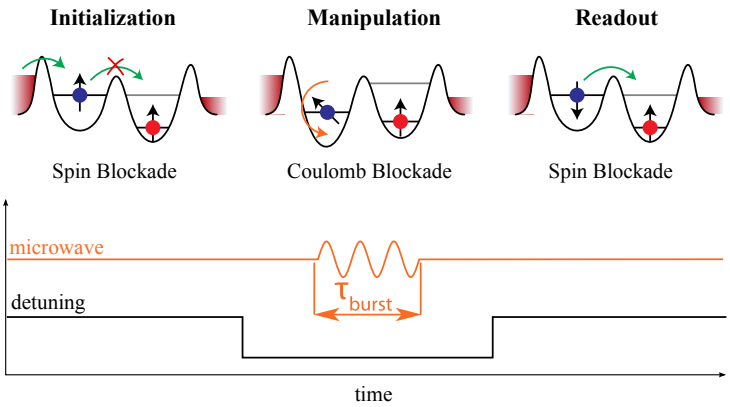

Figure 1.12: Measurement scheme used to probe single-spin manipulation. A spin up is initialized by setting the dot in a spin blockade configuration. The dot is then set in a protected position during the application of the microwave pulse aimed at rotating the spin. The readout is done by setting back the system in spin blockade configuration.

However, this method remains difficult to set up and might be hard to scale up since it involves fabrication of extra control lines on the sample (*e.g.* for the striplines). AC electric fields are easier to localize and can be generated simply by adding an excitation to one of the gates that is used to define the dot. Electric fields do not directly couple to spins but we have seen in section 1.4 that this becomes possible with the help of spin-orbit interaction. If an AC electric field moves the electron back and forth inside its quantum dot, the electron spin will feel an oscillating effective magnetic field B_{SO}. When this is done resonantly with the spin precession frequency, it will induce as well a rotation of the spin [Gol06]. This variant of ESR is known as electric-dipole spin resonance (EDSR). It has been demonstrated experimentally in 2007 [Now07]. However, the rather low spin-orbit coupling in GaAs is here a limitation, and the best frequencies obtained for Rabi oscillations were only of a few megahertz.

Further improvements can be done using materials with stronger spin-orbit interaction (InAs [NP10] or InSb [Ber13] for instance). Alternatively, a position-dependent Zeeman energy can be engineered: if an electron moves back and forth, this will be equivalent to having an oscillating magnetic field [Tok06]. This can be achieved by different means. A micromagnet can be deposited to induce a slanted magnetic field [PL08], a position

dependent g-tensor can be engineered [Kat03], or this can be achieve through hyperfine interaction [Lai07]. The price to pay for these options is often a higher complexity in the device fabrication or in the manipulation.

1.5.2 Two-spin exchange

Another kind of demonstrated spin manipulation is the exchange of a quantum of spin between two adjacent electrons. This constitutes a two-qubit gate, and is usually called exchange gate or SWAP gate. It was first realized by Petta *et al.* [Pet05] with two electrons trapped in a double quantum dot. Swap operations down to just a few hundreds of picoseconds have been demonstrated.

The basic principle for the spin manipulation done here relies on the use of adiabatic and non-adiabatic change of basis. We will first briefly present this concept before explaining in more details the sequence used for manipulations.

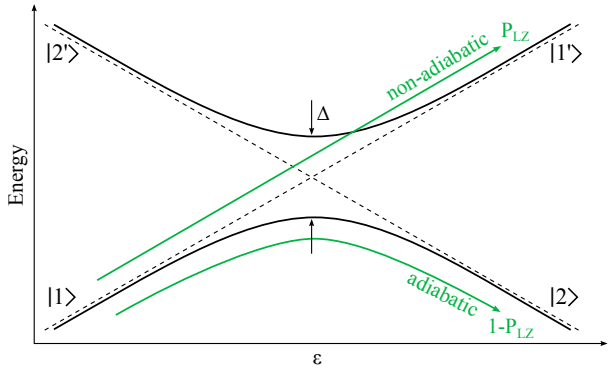

Figure 1.13: Illustration of an avoided crossing. The coupling between the states $|1\rangle$ and $|2\rangle$ opens a gap of typical energy Δ. The Landau-Zener probability (see equation 1.29) defines if the passage through such a crossing will be adiabatic or non-adiabatic.

We consider the following Hamiltonian, written in a basis $\{|1\rangle, |2\rangle\}$:

$$H = \begin{pmatrix} \frac{\varepsilon}{2} & \frac{\Delta}{2} \\ \frac{\Delta}{2}^* & -\frac{\varepsilon}{2} \end{pmatrix} \tag{1.27}$$

The evolution of the eigenstate energies as a function of the parameter ε is shown on Fig. 1.13. The dashed lines represent the case of $\Delta = 0$, *i.e.* when there is no coupling between the states $|1\rangle$ and $|2\rangle$. In the presence of finite coupling terms, an avoided crossing arises and opens a gap Δ (see continuous lines).

We consider the case of a state initially prepared in $|1\rangle$, with the parameter ε linearly increased with time so that the system is swept through the avoided crossing. The question is to know towards which state it will evolve. For a fast sweep, the system has no time to "feel" the interaction and ends up in the $|1'\rangle$ state. On the contrary, for a slow enough sweep, the interaction has to be taken into account and the state will end up in $|2\rangle$. Therefore, the final state after such a process depends on the experimental timescales. On the one hand, the typical timescale associated to the interaction is given by $\hbar/\Delta$. On the other

hand, the typical timescale for the passage through the crossing is given by $\Delta/\frac{dE}{dt}$. The transition between the two regimes will thus depend on the ratio between these two values. The Landau-Zener theory [Lan32; Zen32] tells us that this is given by an exponential law that can be written

$$P_{LZ} = e^{-2\pi\Gamma}, \text{with } \Gamma = \frac{\Delta^2}{\hbar\frac{dE}{dt}} \tag{1.28}$$

where P_{LZ} is the probability to end up in the $|1'\rangle$ state, *i.e.* the probability of a non-adiabatic passage. Finally, if the system is brought in a non-adiabatic way right at the crossing point it will also remain in state $|1\rangle$, but this is no longer an eigenstate of the system at this position. This will induce coherent oscillations between the $|1\rangle$ and $|2\rangle$ states such that

$$P_{|1\rangle}(t) = \cos^2\left(\frac{\Delta}{2\hbar}t\right) \tag{1.29}$$

where $P_{|1\rangle}$ is the probability to measure the system in the state $|1\rangle$.

We have now the tools to describe the principle of the spin exchange experiment. The first part of the sequence consists in initializing the system in the $|\downarrow\uparrow\rangle$ state. The idea is to take advantage of the nuclear field gradient between the two parts of the double dot induced by the hyperfine interaction. In a configuration where $J \ll g^*\mu_B\Delta B_z$, the eigenstates of the system will no longer be $|S\rangle$ and $|T_0\rangle$ but $|\downarrow\uparrow\rangle$ and $|\uparrow\downarrow\rangle$. Such a configuration can be obtained deep in the (1,1) charge configuration where the electrons are well separated. The initialization in the $|\downarrow\uparrow\rangle$ state is then achieved thanks to a slow adiabatic ramp to this configuration. Here are the detailed steps of the initialization procedure:

- To begin, the system is prepared with both electrons on the same dot in the singlet ground state $|S\rangle$ (see point A on Fig. 1.14). It can easily be done by waiting for the system to relax.
- The double dot detuning is then pulsed to point B (see Fig. 1.14) to pass the crossing between the $|S\rangle$ and $|T_+\rangle$ states non-adiabatically (within $\sim$ 1 ns). The system therefore remains on the singlet branch after this step.
- Next, the detuning is gently swept towards more negative values (within $\sim$ 1 µs) up to a position where the exchange interaction J becomes negligible (point C on Fig. 1.14). The system will thus adiabatically follow its ground state and end up in the $|\downarrow\uparrow\rangle$ state[1].

Once this state is prepared, the exchange pulse can be applied. It consists of a non-adiabatic pulse (with duration varying between a few 100 ps and a few 10 ns) to a region where $J \gg g^*\mu_B\Delta B_z$, and so where the eigenstates of the system are $|S\rangle$ and $|T_0\rangle$ (point D on Fig. 1.14). As we have seen, this will induce a rotation of the state between $|\downarrow\uparrow\rangle$ and $|\uparrow\downarrow\rangle$ (see corresponding Bloch sphere on Fig. 1.14). The speed of this rotation will be proportional to J. For the right choice of this pulse duration, the spins will be completely

1 In fact it could also be the $|\uparrow\downarrow\rangle$ state, depending on the sign of the magnetic field gradient between both dots. However, this will have no impact on the output of the measurement

exchanged and the SWAP operation is performed. For a duration half as long, the spins will evolve from $|\uparrow\downarrow\rangle$ to an entangled state (*e.g.* $\frac{1}{\sqrt{2}}(|\uparrow\downarrow\rangle - i\,|\downarrow\uparrow\rangle)$). This is called a $\sqrt{SWAP}$ operation.

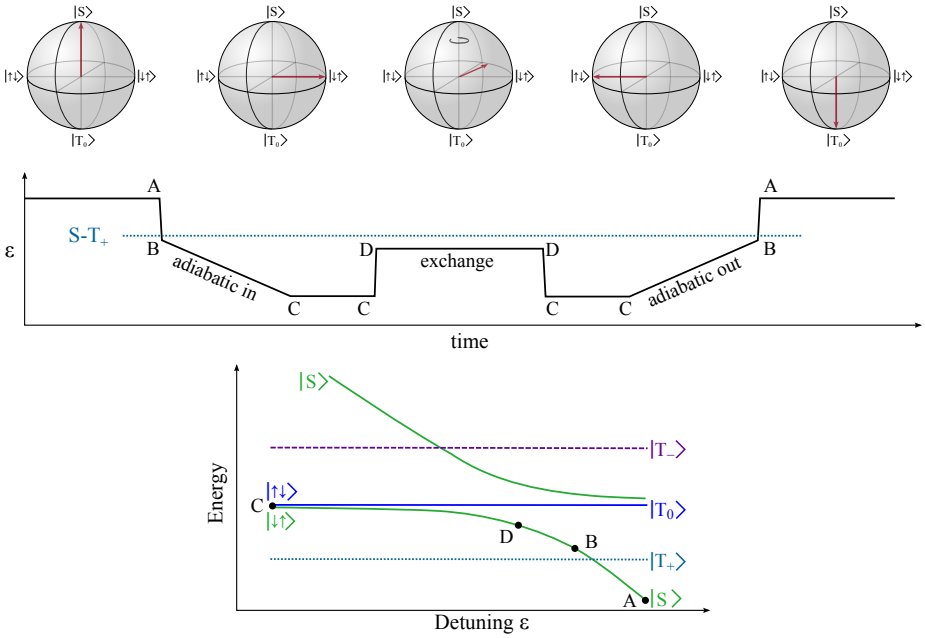

Figure 1.14: (top) Representation of the spin state evolution on a Bloch sphere during a swap experiment. **(middle)** Description of the sequence used to realize a SWAP experiment. **(bottom)** Energy diagram with reference to the specific positions indicated on the sequence description.

After such a rotation, it is not possible to directly readout the spin state obtained. Indeed, we have seen that the only measurement schemes available enable us to distinguish between $|S\rangle$ and $|T\rangle$ states. Therefore, a mirror sequence of the initialization one is performed in order to convert $|\downarrow\uparrow\rangle$ back into $|S\rangle$ and $|\uparrow\downarrow\rangle$ into $|T\rangle$.

Now that the essential building blocks for universal quantum computation have been demonstrated with spins in quantum dots, the focus is on integrating all the elements in one device and on extending the number of controlled qubits. To that purpose, transferring quantum information between distant nodes (*i.e.* quantum dots in our case) is of great interest. An option is to coherently transport individual electron spins, and the envisaged principle is introduced in the next section.

1.6 Transport of a single electron with moving quantum dots

1.6.1 Surface acoustic waves moving quantum dots

A surface acoustic wave is a type of mechanical wave which travels along the surface of a solid material. This special type of waves was discovered in 1885 by Lord Rayleigh and is often named after him. Rayleigh pointed out that SAWs could explain some seismological

signals due to an earthquake that were not previously understood [Ray85].

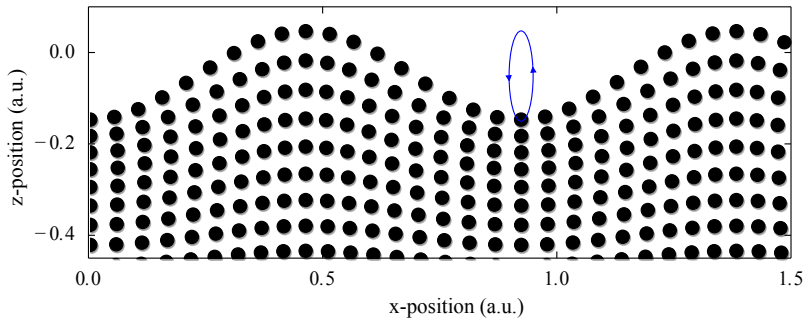

Figure 1.15: Position of the atoms of a material during the propagation of a surface acoustic wave (taken from [Bau14]). The deformation of the material extends on a depth corresponding roughly to the SAW wavelength.

Figure 1.15 shows a SAW traveling along the plane surface of a solid material. As the wave passes, each atom of the material follows out an elliptical path, repeating this path for every period of the wave. The motion amplitude of the atoms is getting smaller as one looks deeper into the material. In fact it is exponentially decaying away from the surface with a typical length corresponding to the wavelength of the SAW. In the simplest case (an isotropic material), the atoms move in the so-called sagittal plane, *i.e.* the plane which includes the surface normal and the propagation direction.

Nowadays, these acoustic waves are often used in electronic devices. At first sight it seems odd to use an acoustic wave for an electronic application, but these waves have some particular properties that make them very attractive for specialized purposes[1]. In our case, we are interested in their potential applications for electronics at the single-electron level, and we will develop this aspect in the following.

Generation of surface acoustic waves

The first prerequisite to use surface acoustic waves is to have a way to control their emission. The most convenient would be to be able to trigger it from an electrical input signal. The conversion process (electric to acoustic, or reciprocally acoustic to electric) is called transduction, and is ensured by piezoelectricity. The piezoelectric effect offers a coupling between electrical and mechanical disturbances. As a consequence, the application of an electric field to a piezoelectric material induces mechanical stresses and strains. Conversely, a mechanical stress gives rise to an electric field, and hence a voltage. A surface acoustic wave propagating on a piezoelectric material will therefore have an electric field associated to it.

A basic SAW emitter consists of an interdigital transducer (IDT) on a piezoelectric substrate. The IDT consists of interleaved metal electrodes alternately connected to two

1 Among all the possible applications, we can cite the use for sensors, delay lines, pulse compression filters, and the realization of band-pass filters for cellular telephones [Mor10].

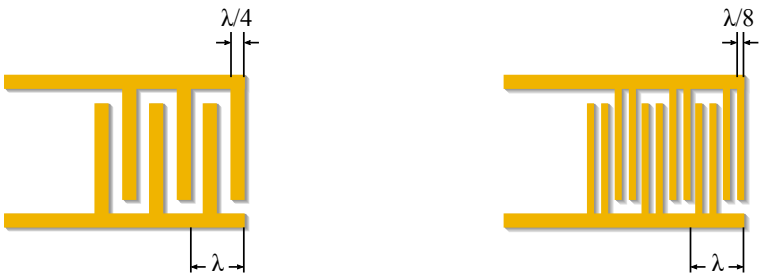

Figure 1.16: Basic geometries of Inter-Digital Transducers. **(left)** So-called "single finger" IDT. The alternation of the metal gates results in a $\lambda/4$ modulation of the surface properties. **(right)** So-called "double finger" or "split finger" IDT. This geometry permits a doubling of the surface properties modulation.

contacts (see left sketch of Fig. 1.16). When a voltage is applied between these two contacts, electric fields are induced in the gaps between the electrodes, and via the piezoelectric effect this induces mechanical stresses. If an oscillating voltage is applied, each pair of fingers will thus generate a surface wave. When the frequency of the signal applied to the IDT is chosen such that the SAW wavelength equals the transducer pitch, the waves generated by subsequent finger pairs are all in phase and therefore reinforce each other. This resonant condition can be written as

$$f = \frac{c_{SAW}}{\lambda_{IDT}} \tag{1.30}$$

where c_{SAW} is the propagation speed of SAWs in the material and λ_{IDT} is the period of the IDT. As the piezoelectric effect is relatively weak in GaAs, a large number of electrodes can be used to obtain higher amplitude waves. The price to pay will be a longer rise time for the amplitude.

This basic geometry is not ideal for several reasons and some improvements can be made. First, with the geometry we described, the IDT has electrodes alternating with a $\frac{\lambda}{2}$ periodicity. This results in a $\frac{\lambda}{4}$ modulation of the surface properties, which will form the equivalent of a Bragg mirror [Oka10] for the acoustic wave. Hence this basic design intrinsically exhibits a cavity effect. This enhances the insertion losses of the IDT and is also detrimental for the rise time of the SAW amplitude. A possible improvement is to use a split-finger IDT [Bri72; DV72], as shown on the right sketch of Fig. 1.16. The doubling of the surface properties modulation enables to avoid the Bragg reflections at the resonant frequency. It should also lead in principle to a slightly higher conversion efficiency between electrical and mechanical power. The drawback is that the realization of a split-finger IDT is more challenging in terms of nanofabrication (since fingers twice as thin compared to standard IDTs must be done to work at similar frequency).

Another point is that with such symmetric designs, IDTs are emitting waves on two directions (which is responsible for 3 dB conversion loss). It could be possible to add a Bragg grating (or use more complex IDT geometries) to make the IDT unidirectional [Mor10]. On top of it, it should also be possible to use curved fingers in order to focus the

wave at the point of interest on the sample [Lim03].

For the sample used in this thesis, basic single-finger IDTs have been used, but double-finger IDTs should be available for the upcoming samples.

Dynamical quantum dots

As a surface acoustic wave has an associated electric field, a coupling to the charge carriers of the material emerges. This leads to what is called acoustoelectric effects [Wei57], where currents (or voltages) are induced as a result of energy and momentum transfer from the SAW to the carriers.

In 1996, Shilton *et al.* investigated on the acoustoelectric effects in a 2DEG and studied more specifically the acoustic charge transport through a quantum point contact [Shi96a; Shi96b]. For sufficiently negative voltages applied on the split-gate electrodes (see Fig. 1.17), the constriction is completely pinched-off, meaning that the top of the resulting potential barrier gets above the Fermi level of the reservoirs. A bias-driven current flow is therefore prohibited. However for sufficiently powerful SAW applied, an acoustoelectric current was measured and in addition, it was found to be quantized in units of ef (where e is the electron charge and f the SAW frequency). This was attributed to the trapping of a single or few electrons in the traveling minima of the SAW potential (see Fig. 1.17). Such charge packets are then transferred across the potential barrier of the QPC as the wave propagates. The number of electrons residing in each of the wave minima depends on the potential barrier defined by the QPC and the SAW amplitude.

This experiment showed that the equivalent of quantum dots can be formed, with the gate potential ensuring the confinement in the direction perpendicular to the wave propagation and the SAW potential ensuring the confinement in the direction of propagation. In addition, the SAW propagation provides to these dots a dynamical aspect that led to the term of moving or dynamical quantum dots.

Many different proposals taking advantage of such moving quantum dots have emerged since then:

- First, it is envisaged to use the quantization of the SAW-induced single-electron transport in order to define a quantum standard of current [Cun99; Cun00; Zim03]. The existence of such a standard would be a great advancement enabling the closure of the quantum metrology triangle (definition of electrical units of current, voltage and resistance)[1].
- The SAW induced moving quantum dots could also be used as a key component towards an on-demand single photon source [Fod00]. The idea is to bring moving quantum dots transporting single electrons into a p-type region, where the electrons can recombine with holes and emit single photons. Such single-photon sources are of high interest for optical quantum information processing [Kni01] and quantum cryptography [Bev02].

1 Very similar options have been developed where static dots are used instead, and where the pumping effect is obtained by modulation of the dot tunnel barriers, either by SAW [Fle03] or by gigahertz signals directly applied on gates [Blu07; Ros14]

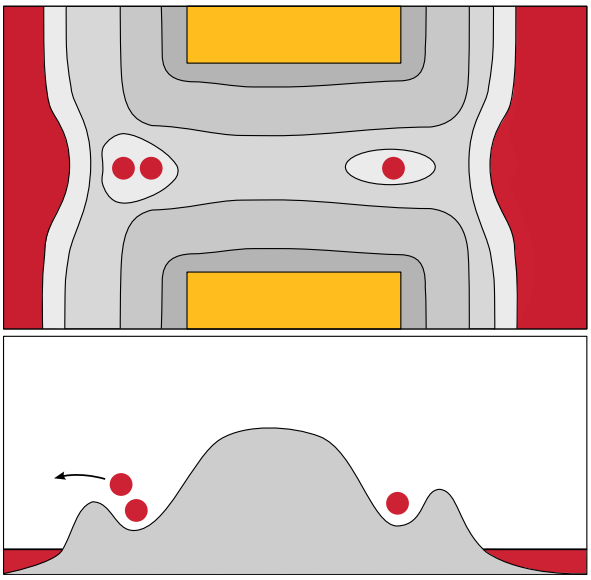

Figure 1.17: Schematics of the mechanism responsible for the formation of moving quantum dots, adapted from [Shi96a]. **(top)** top view of the potential induced by a split gate under SAW irradiation. The split gate is represented by the two yellow rectangles. The red parts on the left and right correspond to the electron reservoirs, and the red circles represent electrons. **(bottom)** Slice of the potential across the split gate potential barrier. The number of electrons confined in a minimum of the wave is progressively emptied as it arrives to the barrier. Under good conditions n electrons will remain in each wave minimum resulting in a quantized current.

- Another interesting proposal [Bar00; Fur04; Gum04] suggests using the spins of single electrons trapped in moving quantum dots as quantum bits, where successive gate operations are performed while the SAW propagates (the name of "flying qubits" is often used).
- Finally, these moving quantum dots could also be used as communication medium between logical quantum nodes, by directly transporting spins of single electrons between static dots. Compared to the previous proposal, it has the advantage that all the basic spin manipulations are already commonly achieved in static dot systems.

Considering the application of moving quantum dots to spin-based quantum information processing, a legitimate question that remains is to know whether coherence is compatible with this transport.

A first encouraging point can be made from the dynamical quantum dots characterization that has been done in [Ast07]. It was measured that the energy spectrum of the dynamical dots they used was comparable to what is measured in usual static few-electron quantum dots. This suggests that static and dynamical dots can be made to have similar properties, and so dynamical dots should be suitable to transport a single electron and its spin. Then more recently, a first evidence of coherent charge dynamics has been obtained [Kat09]. Regarding spin, one of the best achievements so far is the work of [Sto05]. In this paper, it

is presented coherent spin transport in dynamical quantum dots over lengths exceeding 100 µm. However, it was achieved using ensemble of photo-generated carriers. A later work [Sto08] showed that the coherence time of the electron spins is independent of the number of charges transported within a dynamical dot, suggesting the possibility of coherent long-range transport of single electron spins.

1.6.2 On-demand single electron transfer between static quantum dots

A last major advancement has recently been done by [Her11] and [McN11]. In these two papers, it is demonstrated the controlled transfer of a single electron between two static dots by the use of SAW-defined moving quantum dots. This proves that transfer between static and moving quantum dots can be achieved and could constitute a major advancement towards interconnection of distant nodes of a spin-based quantum information nanoprocessor. In the following, we will describe in more details the principle of these experiments.

Two quantum dots are defined and are connected by a channel of a few micrometers (see top picture of Fig. 1.18). The voltage applied on the two gates defining the channel is set negative enough to fully deplete the 2DEG between the two static dots. In this way, the path between the dots is free of electrons. This prevents any electron interaction that could induce a loss of spin information.

The first step consists in the initialization of the system (see bottom left panel of Fig. 1.18). The source dot (left) is coupled to its reservoir in order to be loaded with a single electron. Similarly, the reception dot (right) is also coupled to its reservoir but one makes sure that it is completely emptied. This position cannot directly be used for the transfer for two reasons. First, if the dots are too coupled to the reservoir, the modulation of potential induced by the SAW passage could repeatedly cause population and depopulation of the quantum dots [Kat07]. Second, the potential of the channel usually lies several milli-electronvolt above the Fermi level. As a result, there is a large potential gradient between the dot and the channel. It prevents the formation of moving quantum dots and thus the electron transport.

To solve these issues, the solution consists in applying a very negative voltage on the gates V_L and V_L' to reach the so-called transfer position (see bottom left panel of Fig. 1.18). In this position, the source dot electron is trapped in a metastable position where the influence of the reservoir can be disregarded. Therefore exchange of electrons with the reservoirs during the application of the SAW burst will be prevented. Moreover, transfer of the electron through the channel is facilitated since the dot chemical potentials are lifted up closer to the channel one.

To achieve the electron transfer, a SAW burst is applied. This will induce moving quantum dots traveling along the channel, similarly to the experiments of Shilton *et al.* previously described. The electron of the source dot will be captured by a dynamical quantum dot and brought to the reception dot.

The efficiency of this transfer procedure can be determined by looking at the charge of each dot before and after the application of a SAW burst. Typical QPC traces are represented on the bottom right panel of Fig. 1.18. The correspondence between the measured currents and the electron number in the dots are labeled on the graphs. The top

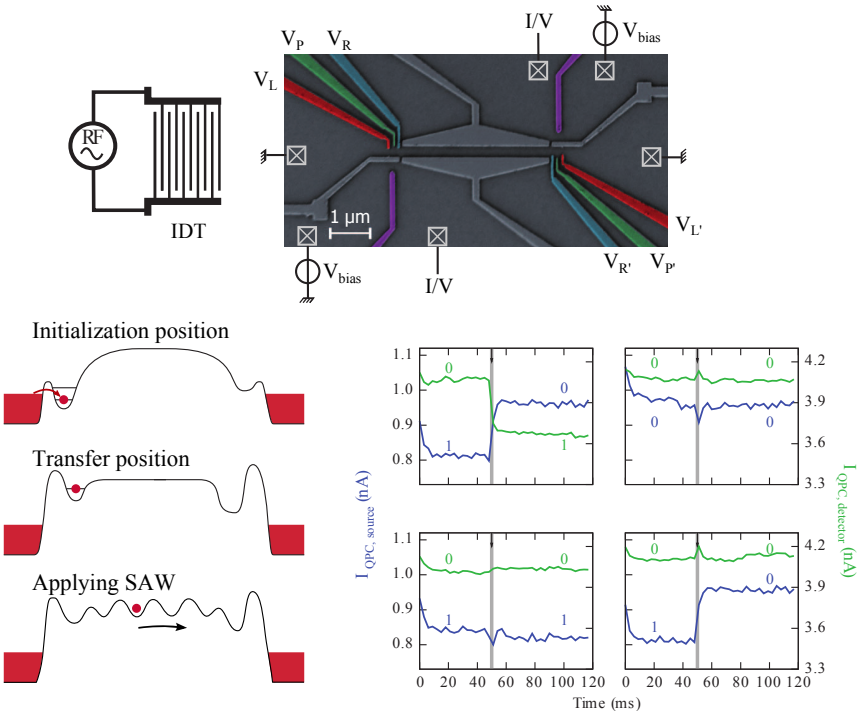

Figure 1.18: (top) Scanning Electron Microscope (SEM) image of the sample. The two large gates define a 1D channel connecting two quantum dots located on each side. Each purple gate defines a QPC used to monitor the charge of a dot. The IDT is located 2 mm away from the sample. **(bottom left)** Sketch of the potential shape for the different steps used for the transfer of a single electron. First an electron is loaded to the source quantum dot. Large barriers are then induced between the dots and their reservoirs and the chemical potential of each dot is raised close to the channel one. Application of a SAW burst finally allows the transfer of the electron through a moving quantum dot. **(bottom right)** Typical QPC current measurements observed during transfer experiment. The vertical gray line indicates the time at which is applied the SAW burst. The corresponding charge states of each dot are precised on the plots.

left plot shows the current traces corresponding to a successful transfer: one electron is removed from the source dot and added in the reception dot. In the best configuration, this is observed more than 90 % of the cases. It can be checked that if no electron is initially present on the source dot, no electron arrives to the reception dot (see top right plot). This can be reproduced over many runs with almost perfect correlations between sending and reception events. It permits to confirm that this is indeed the same electron that is sent and received. Two sources of failure have been identified: either the electron is not sent from the source dot (bottom left plot) or not received in the reception dot (bottom right plot). These errors are both smaller than 5 %.

This definitely proves that a single electron can efficiently be transferred between two static quantum dots using this procedure. The last remaining point is to demonstrate that spin can also be preserved, and this is the purpose of the work presented in this thesis.

CHAPTER 2

Experimental setup

2.1 Introduction

As it has been seen in section 1.1, the typical energy scale in lateral quantum dots is relatively small. For instance, the energy splitting between spin states that we want to probe is on the order of 0.1 meV. Regarding temperature, this energy is equivalent to 1 K. It will therefore be necessary to reach a much smaller temperature, on the order of 100 mK or less to conveniently observe this effect. Such temperature range is commonly achieved using dilution refrigerators. This will be the object of the first part of this chapter.

Regarding the electronics used for the experiment, the precision of the voltages used on the system must be also small compared to this energy scale. By considering a gate lever arm α (ratio for the conversion from a gate voltage into energy) equal to 20 (being the typical order of magnitude of the gate lever arm), it means that the voltage sources should have $\sim 1\,\mu$V stability in order to minimize detrimental fluctuations. In addition, the typical signal extracted from this kind of systems is relatively small (QPC current variations are on the order of a few 100 pA). Therefore all the acquisition chain has to be engineered in order to be able to detect such small signals. The second section of this chapter will be dedicated to describe the electronics used to address and probe the system.

2.2 Cryogenics

We first briefly review the basic principle of a dilution refrigerator which allows for a temperature around 10 mK and for specific details we refer the reader to [Lou74; Pob07].

Below 0.87 K, the dilution of ^{3}He into ^{4}He is an endothermic process[1]. The idea is thus to impose a flow of pre-cooled ^{3}He that will dilute in ^{4}He.

In practice, the dilution unit is surrounded by 4 K liquid helium[2]. Since the dilution temperature should go below 4 K, it is isolated from the helium bath by vacuum. It is then organized around different stages that are presented in Fig. 2.1. We will quickly describe them going from higher to lower temperatures.

1 which cooling power scales with T^2
2 in the case of a "wet" dilution fridge

- The inlet of ^{3}He is first pre-cooled by the 4 K bath of liquid helium.
- The ^{3}He flow is further cooled to 1.5 K by the 1 K-pot. This stage is a pumped reservoir of ^{4}He which is continuously refilled from the helium bath.
- The two following stages allow to transfer heat from the ^{3}He inlet to the cold ^{3}He outlet. First the continuous heat exchanger allows to go below 100 mK and then the step heat exchangers allow to go down to a few millikelvins.
- The ^{3}He flow finally reaches the mixing chamber where the dilution process takes place.

The fridge used for the work presented in this thesis has a base temperature around 20 mK. The available cooling power is on the order of 1 mW at 100 mK and gets approximately an order of magnitude larger for each stage presented in Fig. 2.1 (cold plate, still and 1 K pot).

In order to connect the room temperature electronics of the setup to the sample, different cables are going down the dilution fridge. Many precautions have to be taken in order to bring as little heat as possible to the sample. It is especially true for the electrons temperature, which exceeds most of the time that of the cryostat because of the insufficient thermal contact and the external noise which produces parasitic heating. Therefore, a careful choice of the materials is needed and a thorough thermal anchoring to every stage of the fridge is achieved. We detail in the following the different techniques used depending on the type of line.

We first consider the DC lines. In that case, long Thermocoax™ coaxial cables are used. The dielectric (MgO or Al_2O_3) is quite dissipative for high frequency signals (it exhibits a low-pass filter behavior with cutoff frequency around ~ 100 MHz [Zor95]). This allows to dissipate into heat the high frequency noise. If these modes were not dissipated, they would be directly coupled to the sample and the electron temperature would rise. The heat load is then absorbed by the fridge at its different stages thanks to the thermal anchoring of both the inner- and outer-conductor of the coaxial lines.

For the high frequency lines, this technique is no longer possible since we want the RF signals to reach the sample. In order to preserve a relatively low electron temperature, the usual technique is to attenuate the signal along the line. Attenuators, from XMA Corp., are placed at 1 K (-20 dB) and at the mixing chamber (-10 dB). The price to pay as a counterpart will be a limited amplitude of the pulses reaching the sample. For the generator we use (a Tektronix 5014B Arbitrary Waveform Generator) the maximal amplitude is 4.5 V peak-peak. With a 30 dB attenuation, the pulse amplitude reachable at the sample will be only around 140 mV.

In the case of the IDT feed line, less precautions are needed. Since the bandwidth of the IDT is only a few megahertz and the signal does not couple directly to the electrons, the noise amplitude actually reaching the electrons via the piezoelectric effect is limited. We thus chose to apply only 6 dB of attenuation at 1 K. For the study of metastable double dots (see chapter 4) this was even reduced to 1 dB attenuation.

The final temperature of the cryostat measured close to the sample was around 50 mK for all the experiments. In order to estimate the final electron temperature on the sample,

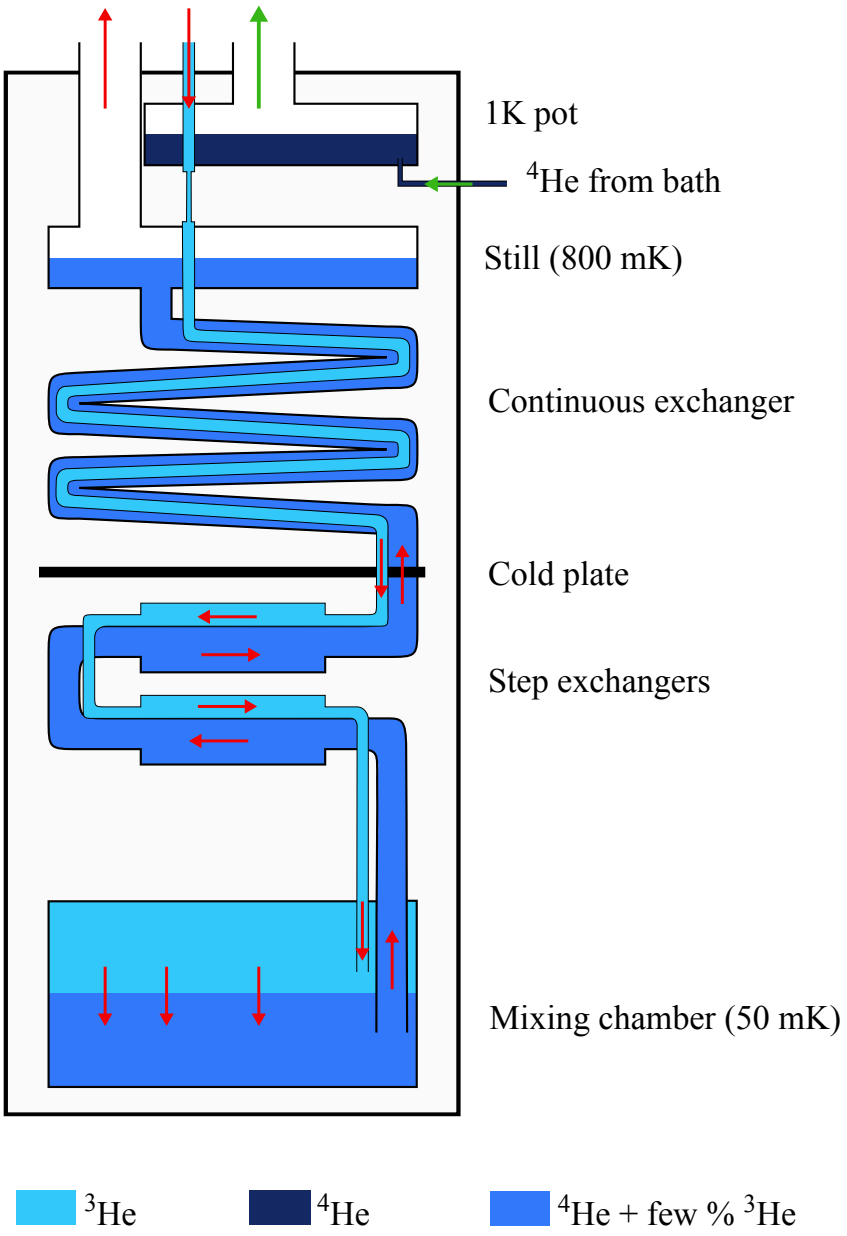

Figure 2.1: The ^{3}He flow is first cooled to 4 K by the helium bath. The 1 K-pot cools it further to 1.5 K. This one pumps liquid ^{4}He from the 4 K helium bath around. Further cooling is ensured by the counter-flowing ^{3}He. The dilution (cooling process) happens in the mixing chamber. The outermost limit designs the inner vacuum chamber (IVC), which thermally isolates the dilution from the 4 K liquid ^{4}He bath around.

a simple experiment can be done. The principle is to monitor the time-averaged population of one of the quantum dots as a function of its energy (see [Sch04]).

A quantum dot has thus been formed by polarizing a few gates on the sample, and its charge is monitored using a nearby QPC. The voltage of a gate (V_G) is varied to change the number of charges contained in the dot. The QPC current is averaged for the different values of V_G. The resulting signal is plotted on Fig. 2.2 (the linear trend has been removed and signal has been normalized to the corresponding number of electrons for clarity).

The signal is fitted with a Fermi-Dirac step function. The conversion from gate voltage to energy is done by using the gate lever arm α (which typical value has been measured around 20):

$$f(E) = \frac{1}{1 + \exp\left(\frac{E-E_0}{k_B T}\right)} = \frac{1}{1 + \exp\left(\frac{e(V-V_0)}{\alpha k_B T}\right)} \tag{2.1}$$

The output of the fit gives an electron temperature of 103 mK ± 5 mK. This should be sufficient for the experiment we want to perform.

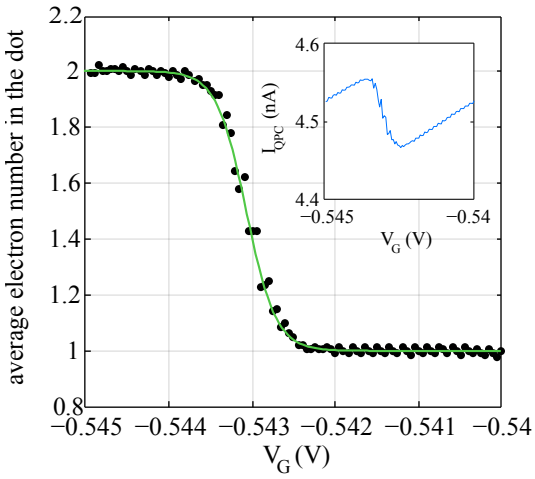

Figure 2.2: Electron temperature estimation from time-averaged quantum dot population. **(inset)** Time averaged QPC current as a function of gate voltage. A linear trend is present because of the cross-talk between the QPC and V_G. Each data point corresponds to an average time of ~ 2.7 s. The tunnel barrier between the dot and the reservoir is on the order of ~ 1 kHz coupling. **(main)** Detrended and normalized signal as a function of V_G. The signal is fitted with a Fermi-Dirac function (green line) and an α factor equal to 20 (see Eq. 2.1). The output of the fit gives an electron temperature of 103 mK and $V_0 = -0.543$ V. The temperature of the fridge was around 50 mK.

2.3 Electronics

2.3.1 Voltage sources

The sample that has been used for the work presented here is defined by twelve electrostatic gates and six ohmic contacts. This constitutes many parameters to vary, and thus a need for a large number of independent voltage sources. In our case, a specific requirement for

these sources is the possibility to vary the different voltages applied on a fast time scale (microsecond). Of course a fine resolution, low noise and high stability characteristics are also welcome.

The first reason for this is that because of the large number of gates on the sample, the parameter space to be explored is imposing. Characterization of the sample will thus be faster if the different voltages can quickly be changed. Secondly, this would facilitate the preparation of the metastable configurations that are required for the electron transfer.

The main voltage sources used in our experiment are based on a commercial digital-to-analog converter (DAC) chip (Linear Technology LTC2604). This chip is embedded on a home-made printed circuit board (PCB) including low-voltage power-line filtering and a low-noise amplification stage of the output. Optical isolation of the system allows to reduce problems related to ground loops and resulting 50 Hz noise. Each PCB hosts in the end eight voltage sources.

Each source has a 16 bits resolution for an operating range of $-5\,\mathrm{V}$ to $5\,\mathrm{V}$ (resulting in a $153\,\mu\mathrm{V}$ minimal voltage step). The typical noise is around $25\,\mathrm{nV\,Hz^{-1/2}}$. A voltage can be changed every $16\,\mu\mathrm{s}$, and the rise time for the voltage is slew rate limited to $300\,\mathrm{mV\,\mu s^{-1}}$. The sources have a thermal drift of $0.25\,\mathrm{ppm/^{\circ}C}$, and they exhibit a drift smaller than $10\,\mu\mathrm{V}$ in ten hours.

Finally, two low-pass filters (with cut off frequencies of 120 MHz, and 1.9 MHz) have been put at the output of the voltage sources. By considering the present bandwidth (1.9 MHz), the voltage noise due to the source can be estimated around $35\,\mu\mathrm{V}$.

2.3.2 High frequency signals

Nanosecond gate voltage pulses

As we have seen just above, a DAC device is used to set the base voltages of each gate of the sample and enables microsecond manipulations. However this is not always sufficient and some experiments will require to apply nanosecond pulses to the gates.

These high-frequency pulses are generated with a Tektronix 5014B arbitrary waveform generator (AWG). It allows to generate arbitrary 14-bit signals, with a peak-peak amplitude up to 4.5 V. The sampling rate goes up to 1.2 GHz, but its rise time (10 % to 90 %) is limited to 950 ps.

In order to add these RF signals to the relevant gates, some homemade bias tees are used. A bias tee is a device with two inputs, one for the DC and one for the RF voltages (see Fig. 2.3). Its output gives the sum of these two voltages. In our case, it is simply composed of a resistor and a capacitance, in order to form either a high pass or a low pass filter depending on the input port.

SAW burst generation

We consider now the generation of the SAW bursts. A oscillating signal at the resonant frequency of the IDT has to be generated for a short and controllable time. The initial setup that was used to produce such signal is described on Fig. 2.4.

A continuous-wave generator (Agilent E8257D) is used to generate the SAW excitation at the resonant frequency. In order to get a fast gating of this signal, the output of the continuous wave generator is sent through a mixer (Marki M8-0420LS). A gate signal of

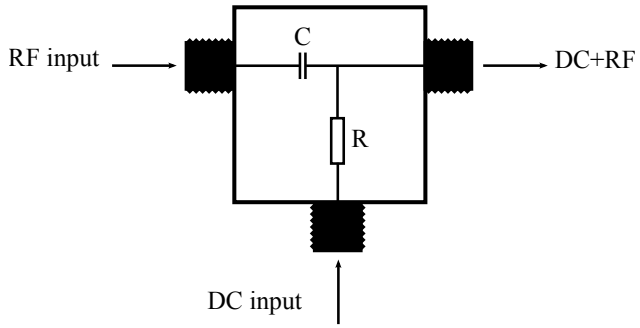

Figure 2.3: The RF input is coming from an AWG channel through a RF coaxial line. The DC input is coming from a DAC voltage source through a Thermocoax cable. The output goes to the sample and is the sum of both contribution. The values used for each component are $R = 5\,\mathrm{k\Omega}$ and $C_{DC} = 0.15\,\mathrm{nF}$. It gives cutoff frequencies around 200 kHz.

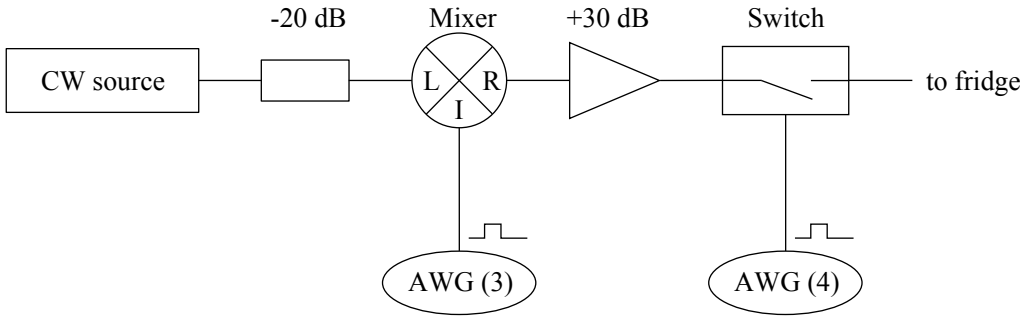

Figure 2.4: Description of the primary setup used for SAW bursts generation. In order to get a fast gating of the SAW excitation, the output of the continuous wave generator is sent through a mixer, Marki M8-0420LS, and two cascaded RF transistors (Switch), Skyworks AS186-302LF. The signal is amplified between the two stages, since the mixer can only work at a limited power. The switch, slower (rated 30 ns), allows more power (around 30 dBm). The command signal is generated by a Tektronix 5014B (AWG).

the desired duration is generated by the AWG and sent to the other input of the mixer. The burst obtained at the output of the mixer has a 10 % to 90 % rise time slightly above 1 ns. A problem was that a high power is usually required to excite the SAW but the mixer can only work at a limited power. The signal is therefore attenuated before the mixer and re-amplified afterwards.

The switch (Skyworks AS186-302LF) that is finally used is required for its on/off ratio of 80 dB that prevents power from being continuously shined through the line. Another AWG channel is required to gate it. Because of its slower rise time (30 ns from 10 % to 90 %), the switch is triggered 30 ns in advance compared to the mixer in order to obtain sharp pulses.

This setup was satisfying for intermediate power values and has been used for the first experiments performed on the sample. However, some limitations emerged for the highest power values. The output of the SAW burst generation line is presented on the left plot of

Fig. 2.5 for 18 dBm applied on the source. It can clearly be seen that the envelope of the burst is characterized by a rise time around 15 to 20 ns. In addition, the final amplitude of the signal is saturating. This has been studied in more details on the right plot of Fig. 2.5. The steady-state amplitude of the burst has been measured for different powers applied on the source. It is compared to the expected amplitude taking into account the attenuation or gain of each element of the setup. As can be seen, the maximal amplitude that can be achieved is saturating around 2 V.

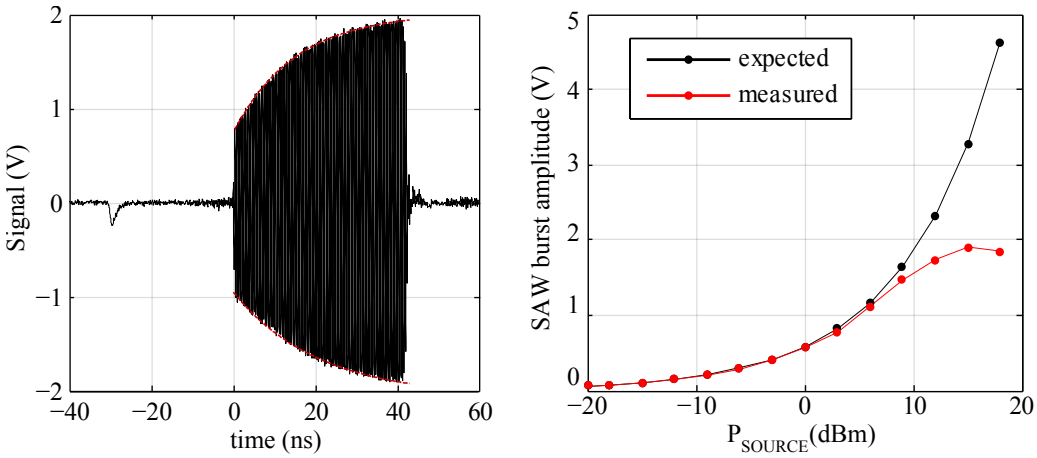

Figure 2.5: (left) Shape of the SAW burst generated with the earliest setup. Signal is recorded with a Lecroy WaveMaster 830Zi, with a 30 GHz bandwidth and a 80 GS/s sampling rate. An 18 dBm power is used on the source. The envelop is fitted with a 15 ns (resp. 20 ns) characteristic time for its top (resp. bottom) part. Such non-negligible rise times are observed for powers of −10 dBm and more). The bump in the signal at $t = -30$ ns is attributed to the gating of the switch. The RF switch is turned on from −30 ns to 40 ns and the mixer is gated from 0 ns to 40 ns. **(right)** Amplitude of the generated signal as a function of the power applied on the source. The black curve corresponds to the expected amplitude taking into the attenuation or gain of the different elements of the chain. The red curve corresponds to the actual amplitude measured. A saturation occurs at 2 V amplitude. This is attributed to saturations of the amplifier and the switch.

In order to solve these issues, a new signal generator (Rohde-Schwarz SMB 106A) has been used instead of the continuous-wave generator. This signal generator is able to internally generate the type of burst we need to use. In its pulse generation mode, it is claimed an on/off ratio > 80 dB and a rise time (10 % to 90 %) < 5 ns typically. This has led to a great simplification of the setup (see top left sketch on Fig. 2.6). A single AWG channel is now required to gate the microwave circuit, and the output of the source is directly connected to the RF line of the fridge. It can be seen on the right plot of Fig. 2.6 that there is no longer any issue regarding the rise time of the burst. The steady-state amplitude is reached within less than 1 ns. It can also be noted that the reached amplitude is larger than the saturation value of the previous setup.

It must be kept in mind that the signal shown on Fig. 2.5 and 2.6 is the signal that is sent to the IDT. The actual shape of the SAW should be the convolution of this signal

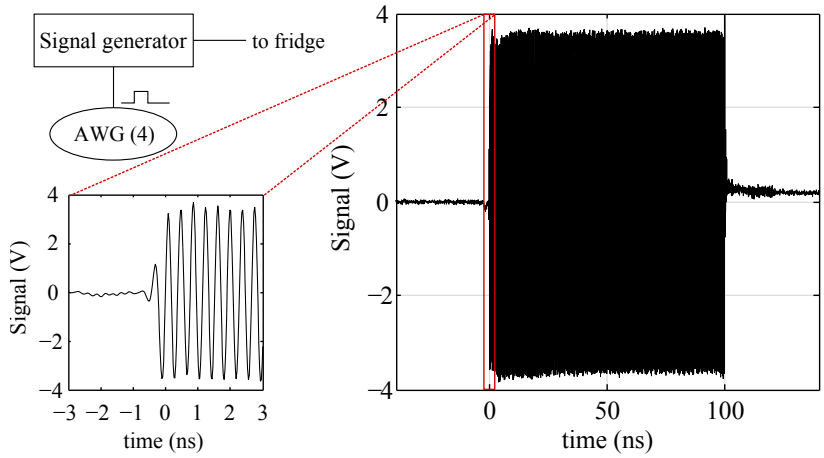

Figure 2.6: (top left) Sketch of the new setup used for SAW bursts generation. The AWG is used to gate the signal generator which internally manage the RF switching. **(right)** Example of a burst generated with this new setup (21 dBm used on the source). Amplitude can be varied within the generator specifications (−120 dBm to 30 dBm) without saturation. **(bottom left)** Close-up on the rising part of the burst. The full amplitude is reached within a nanosecond.

with the response function of the IDT. Typically, one can expect a 27 ns gate function for the IDT (because of its 70 pairs of fingers).

2.3.3 Measurement

All the information relative to the experiment is obtained by measuring the current that is flowing through the QPCs designed on the structure.

These currents are pre-amplified thanks to homemade current-to-voltage (I/V) converters, based on a Texas Instruments TLC2201 operational amplifier. The bandwidth of the I/V converters starts from DC and goes from 0.8 kHz to 1.4 kHz while the gain is changed from $10^6\,\mathrm{V\,A^{-1}}$ to $10^9\,\mathrm{V\,A^{-1}}$.

For standard measurements, the output voltage is then directly measured by two Keithley K2000. The averaging time per sample is 2 ms, with a sampling rate of 3 ms per sample (*i.e.* the K2000 have a down time of 1 ms).

For faster measurements, the I/V converters are set to a $10^7\,\mathrm{V\,A^{-1}}$ gain and an amplification stage of gain 100 is added. This amplification stage relies on an Analog Devices AD620 operational amplifier. The strong common-mode rejection ratio of this chip allows to decouple the grounds of the experiment from the one of the measurement device used afterwards.

After this amplification, the signal is then RC filtered ($R = 517\,\Omega$ and $C = 100\,\mathrm{nF}$ for a cutoff frequency around 3 kHz) before being sampled by a LeCroy WaveRunner 6050A. Further software filtering (moving average) is applied to the signal. The rise time of the amplification chain is around $\tau = 150\,\mu\mathrm{s}$.

2.3.4 Control software

This software is built in two major parts: one is embedded in the FPGA chip in order to realize the microsecond control of the voltage sources and to trigger the AWG and the voltmeters. The other part of software is a Labview program running on the host computer of the experiment. This computer is linked to the FPGA via an Ethernet network.

The major feature of the Labview program is the possibility to create so-called "fast-sequences". It allows to control the voltage sources to achieve arbitrary voltage shifts, and manages the triggering of the different instruments of the setup. This allows for instance to realize complex trajectories along the stability diagrams of the dot.

The complete experiment is implemented by building a list of orders that will be executed sequentially. Different types of orders are possible:

- shifting the output of a voltage source by a certain amount (a 16 µs time lapse is waited between two of these orders, corresponding to the DAC limitation).
- waiting a certain amount of time. This time delay can be varied between 1 µs and 35 h. The resolution is on the order of 1 µs, and progressively increases for the largest delays.
- triggering one of the measurement instruments or the AWG. This allows to synchronize the nanosecond voltage pulses and the SAW burst (which are controlled by the AWG) with the rest of the experiment.
- jumping to another slot of the sequence. This can be useful to implement some loops for instance.

Once such a sequence has been written, it is possible to repeat it while stepping some parameters (or in the same conditions for averaging). Up to three nested loops are available to explore different configurations of the device.

CHAPTER 3

Injection of a single electron from a static to a dynamical quantum dot

3.1 Introduction

The transfer of a single electron between two distant quantum dots by a SAW has been proven to be a very efficient process [Her11; McN11]. This is promising in the development of electronic circuits at the single electron level. In particular it could be an elegant way to transfer quantum information between nodes of a spin-based quantum nanoprocessor. However, the preservation of the electron spin coherence during such a transfer remains to be proven and represents a real experimental challenge. In this context, having a precise knowledge of the processes involved in the electron injection mechanism would be of great interest. Especially, the injection mechanism from a static quantum dot to a dynamical quantum dot needs to be clarified.

For example, the experiments of SAW-assisted single electron transfer achieved up to now have been done using SAW bursts of a hundred nanoseconds or more. It corresponds to the formation of several hundreds of dynamical quantum dots. In principle the electron can be transferred in any of these dynamical dots and the resulting uncertainty on the electron emission time is large compared to the spin coherence time. This constitutes a major impediment to achieve and probe coherent spin transfer.

The work presented in this chapter aims at having a better understanding on how an electron is transferred from a static into a moving quantum dot. The underlying motivation is to investigate and come up with solutions about possible processes that could be detrimental for the preservation of the electron spin. In particular, the control of the electron injection to a specific moving quantum dot has been achieved with a probability close to unity.

3.2 Electron transfer regimes

Charge transport through a one-dimensional channel [Kat06] and depopulation of a static quantum dot [Kat07] by a SAW excitation have already been studied. Two different mechanisms allowing an electron to overcome a potential barrier under SAW irradiation are suggested in these works.

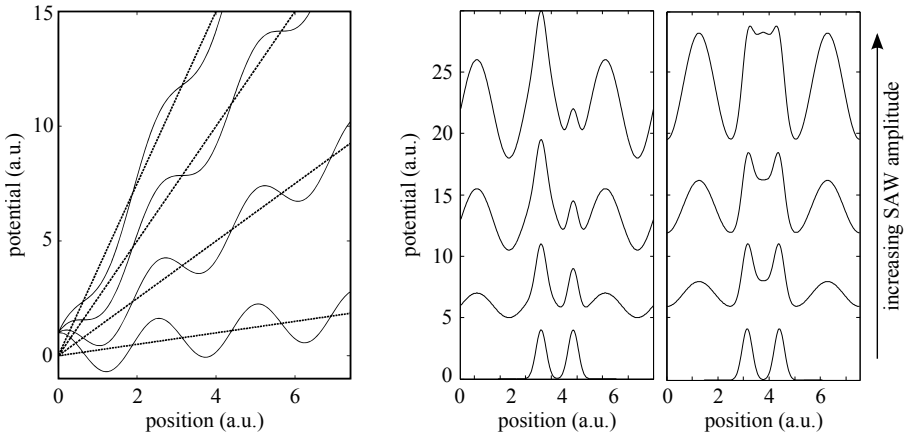

Figure 3.1: (left) Illustration of interplay between ∇_{SAW}^{max} and ∇_{pot}^{max} in the formation of moving quantum dots. Different static potential are represented as the dashed lines. The resulting potential with the SAW potential modulation superimposed is shown as the continuous lines. Moving quantum dots are defined only when ∇_{SAW}^{max} is larger than the static potential slope. **(center and right)** Illustration of the mechanism inducing SAW-assisted depopulation of a static quantum dot. A SAW with increasing amplitude (from bottom to top) is added to the static potential of a quantum dot. Both modulation of the tunnel barriers **(center)** and the dot chemical potential **(right)** can facilitate the electron tunneling-off.

On the first case, an electron crosses a wide potential barrier being transported by a SAW-defined moving quantum dot. The ability to transport electrons in such a way relies on the difference between the maximum gradient of the SAW potential modulation (∇_{SAW}^{max}) and the maximum gradient of the static potential (∇_{pot}^{max}). This is illustrated on the left plot of Fig. 3.1. As long as ∇_{SAW}^{max} overcomes ∇_{pot}^{max}, a moving quantum dot can be defined. The larger is the gradient difference, the deeper are the generated moving quantum dots. When the two parameters begin to be comparable, the moving quantum dots are defined with relatively small barriers and it becomes possible for an electron to tunnel off the moving quantum dot, implying a regime of stochastic transfer. Finally if there is a point in the static potential that is steeper than the SAW potential (∇_{pot}^{max} larger than ∇_{SAW}^{max}), the electron confinement is no longer ensured at this point and the electron will be back-scattered with certainty.

Usually the potential barriers that define a quantum dot are rather steep. Therefore, a very large SAW amplitude is required to allow this first mechanism. The second mechanism, more effective in this case, is direct tunneling through the quantum dot barrier facilitated by the SAW. Indeed, the SAW burst excitation (for relevant wavelength and amplitude) periodically lowers the height of the dot barriers and modulates the dot chemical potential, resulting in an increased tunneling probability. A sketch of the SAW influence on a dot potential is shown on the right part of Fig. 3.1 for different wave amplitudes. Raising the SAW amplitude reduces the dot tunnel barriers and so enhances the tunneling probability. Of course this is only happening once per wave period. Extending the SAW duration will increase the number of attempts for an electron to tunnel-off and will therefore lead to

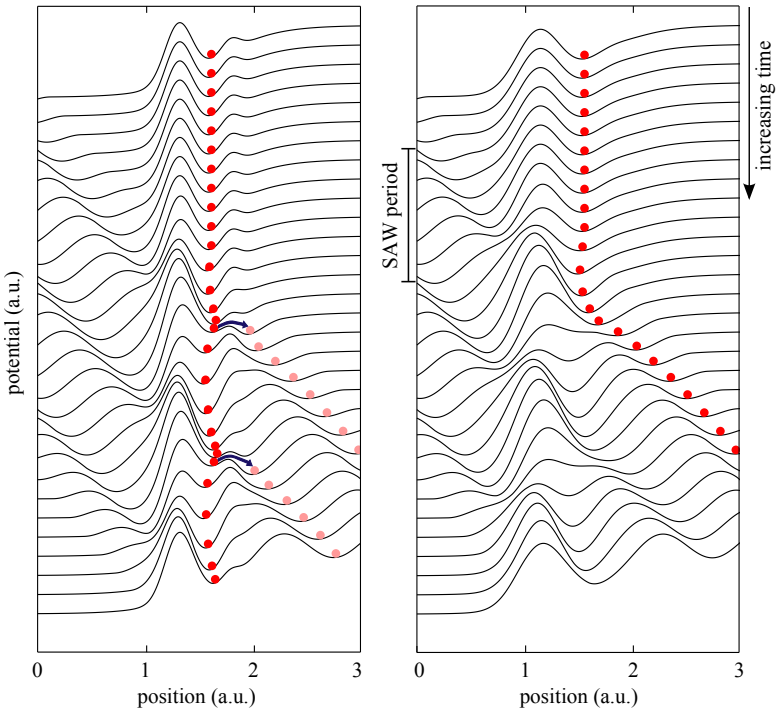

Figure 3.2: Illustration of different possible regimes of electron transfer. The potential of the sample added with SAW modulation is drawn for different times as the SAW is propagating. The curves are offset for clarity, with increasing time going from up to down. An electron initially trapped in the static quantum dot is represented as a red dot. **(left)** Example of a stochastic regime: a tunneling event is required to inject the electron to a moving quantum dot and there is a small transfer probability for each wave minimum. Such stochastic regime can also emerge because of electron back-scattering, as explained in the main text. **(right)** A moving quantum dot adiabatically drags the electron and carries it away.

a larger escape probability. It can be noted that for reasonable SAW amplitudes, this mechanism will also imply a stochastic process.

In our system, the electron must be extracted from the source quantum dot and transported in a dynamical dot along the one-dimensional depleted channel. It is likely that both mechanisms we have presented are involved. In that case, preventing the stochastic processes that could emerge should lead to a better efficiency of the transfer procedure. It would also avoid any jitter on the emission time of the electron. This is illustrated on Fig. 3.2. Two possible shapes of the static potential are pictured. Their evolution while a SAW propagates along the sample are pictured for regular time intervals (going from the top to the bottom of the plots). On the left graph, the static dot potential confines too strongly the electron. The bottom of the quantum dot remains at any time a local minimum of potential. No direct transfer of the electron is possible without crossing a tunnel barrier; a SAW-assisted dot depopulation should therefore be involved. This is most favorable each time a SAW maximum coincides with the minimum of the dot, and is thus repeated once

every SAW period (see arrows on the figure). It is no longer the case for a static potential such as the one on the right graph. Here, the local minimum of potential is following the minimum of the SAW, and the electron can "adiabatically" be transferred.

It is now clear that the shape of the static potential as well as the SAW amplitude are crucial parameters in the electron injection from a static to a moving quantum dot. This can easily be tuned, and finding a regime where the transfer becomes adiabatic constitutes a first path to improve the transfer efficiency.

3.3 Influence of the static potential shape on the electron emission

In order to study the influence of the static potential shape on the electron transfer, the idea will be to vary the gate voltages used for the source dot transfer position. We will start by precisely describing the successive steps used to prepare an electron at the transfer position.

- First, the source quantum dot is coupled to its reservoir, in a position where one electron can be loaded. A charge stability diagram of the source dot is shown on Fig. 3.3. This loading position is labeled L_1 on the diagram. The tunnel coupling to the reservoir in this position is estimated between 10 kHz and 100 kHz.
- Once initialized with an electron, a negative voltage pulse (with $\sim 1\,\mu s$ rise time) is applied on the gate V_L to rapidly bring the dot to an intermediate metastable position indicated by the point I on Fig. 3.3. At this position, the tunnel barrier between the quantum dot and the reservoir is large enough to keep the electron in the dot for hundreds of milliseconds. This time is sufficient to readout the charge state of the dot before transfer[1] and make sure that the electron has not been lost during the microsecond pulse.
- The voltages on the dot gates have then to be set much more negative to achieve the electron transfer. This is done by applying an additional microsecond pulse to the gates V_L and V_R to further lift the dot potential. On Fig. 3.3, it corresponds to a pulse from I to T. This position T is hold only for a short time (20 µs) during which the SAW burst is applied[2].
- The system is then set back to point I. A new charge measurement is performed in order to learn whether the electron has left the dot or not.

A similar sequence is applied to the reception dot in order to capture the transferred electron, except that the dot is initialized with 0 electron. This is described in details in appendix B.

1 A measure of the QPC current for a fraction of millisecond is usually sufficient. The data showed in this chapter were usually averaged for a few tens of milliseconds to improve the signal quality.

2 In principle it would be possible to directly reach the transfer position and readout the dot charge there before and after the SAW burst. However, it has been observed that the stability of the sample was improved by limiting the time spent with very negative voltages applied. The use of an intermediate metastable position for the charge readout is therefore more convenient.

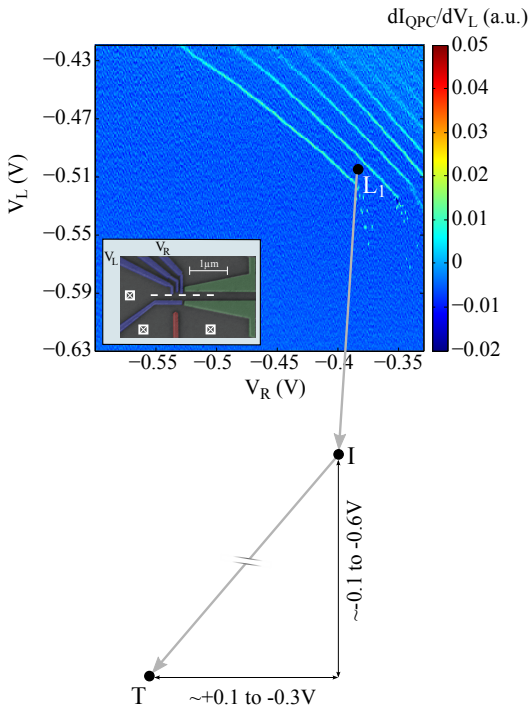

Figure 3.3: (main) Stability diagram of the source quantum dot. One electron is loaded into the quantum dot in point L_1 before pulsing the dot potential to point I within 1 µs. This point I is the reference point where charge measurement is performed before and after the SAW burst. A further negative pulse is applied (1 µs rise time and held for 20 µs) to reach the transfer position T. **(inset)** SEM picture of the source quantum dot showing the two gate voltages varied.

The V_R and V_L voltages of the position T define the static potential seen by the electron during the injection process. In the following experiments, we investigated the role of the static potential by varying these two parameters. Several mappings are presented on Fig. 3.4. The x and y axis correspond to the relative position of T in the (V_R,V_L) space, using the position I as a reference. The color corresponds to the variation ΔI_{QPC} of the source dot QPC current before and after the voltage pulse (each data point corresponds to the outcome of a single transfer realization).

First, the experimental sequence is performed with no SAW burst applied, and the resulting data is presented on the top left mapping. Two very distinct regions are observed on this figure. The top left corner (in yellow, with $\Delta I_{QPC} > 0$) corresponds to the escape of the electron from the source dot. The other region (in blue, $\Delta I_{QPC} = 0$) corresponds to the situation where the electron remains in the source dot. Since no SAW is applied, no electron transfer is possible and therefore the yellow region is necessarily a signature that

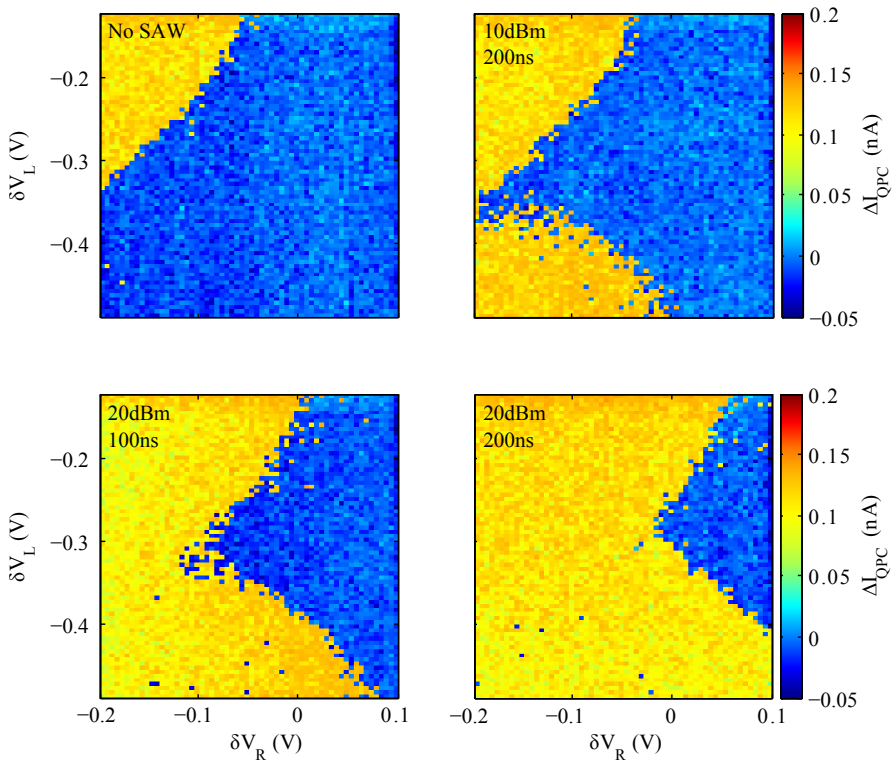

Figure 3.4: Mappings of the quantum dot charge variation with respect to the transfer position used. Different SAW parameters are used for the top four mappings. **(top left)** No SAW is applied. **(top right)** a 10 dBm (1 V) SAW burst of 200 ns is applied. **(bottom left)** a 20 dBm (3.16 V) SAW burst of 100 ns is applied. **(bottom right)** a 20 dBm (3.16 V) SAW burst of 200 ns is applied. The values of power and amplitude given correspond to the value set on the RF source. The QPC current is averaged for 5 ms before and after the pulse (while being in position I on Fig. 3.3). The color corresponds to the difference between the two values. Each data point corresponds to a single-shot realization.

the electron has tunneled to the reservoir[1].

The other three mappings on Fig. 3.4 (top right, middle left and middle right figures) correspond to the situation where SAW bursts are applied with different power and duration. The same region corresponding to the electron tunneling to the reservoir is retrieved on the top left corner of each diagram. In addition, a new region corresponding to the electron loss is present on the bottom left corner. This region is attributed to the SAW transfer of

1 It can be understood as follows: for the less negative voltages on V_L, the tunnel barrier between the dot and the reservoir is relatively thin, while a strongly negative voltage on V_R lifts up the dot chemical potential. At some point, the dot/reservoir barrier becomes too thin to prevent the electron tunneling. This is consistent with the slope of the boundary between the two regions: if V_L is pushed more negative, the dot/reservoir barrier is thickened, preventing the electron loss, and V_R has to be set more negative to lift further up the dot chemical potential and counteract this effect.

the electron. It corresponds to the most negative values applied on both gates, and so the highest chemical potential reached for the electron in the quantum dot. In this position the dot and channel chemical potentials are most likely aligned. Therefore the potential gradient between the dot and the channel is greatly reduced, making the SAW transfer achievable. The fact that a more negative pulse on V_R is facilitating the electron emission suggests that the chemical potential of the dot is here a more relevant parameter than the tunnel barrier between the dot and the channel. Indeed, an increase of V_R is both raising the dot chemical potential (which should facilitate the electron transfer) and making the dot/channel tunnel barrier thicker (which should oppose to the electron transfer).

In order to confirm this interpretation, we looked at correlations between the source dot depopulation and the population of the reception dot after transfer. This is presented on Fig. 3.5. These mappings were obtained on another run of experiments (different cool down and sample tuning). On the left graph is plotted ΔI_{QPC} of the source QPC for varying transfer positions of the source dot. The right graph corresponds to ΔI_{QPC} of the reception QPC that has been measured simultaneously. Positive current shifts (red region on the source dot data) refer to the events where the electron has been removed, whereas negative current shifts (blue region on the reception dot data) refer to the events where an electron has been received. On the upper part of the mappings, the loss of an electron on the source dot is never correlated with a reception event on the other dot. On the contrary, the correlation is almost perfect for the lower part. This is entirely consistent with our interpretation.

These mappings are a good illustration of the crucial influence of the potential shape on the injection mechanism. It constitutes a very fast and efficient way to determine the transfer position where the electron extraction from the source quantum dot is the easiest. However, we have seen that the potential shape is not the only relevant parameter and

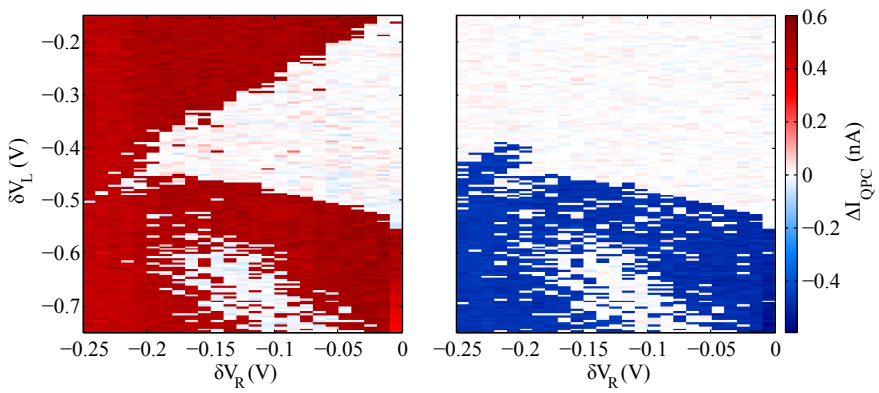

Figure 3.5: Simultaneous signal of the charge variation in the source **(left)** and reception **(right)** quantum dots for varying transfer positions of the source dot. The source (resp. reception) dot is initialized with one (resp. 0) electron. A 15 dBm SAW burst is applied for 70 ns. The variation of the QPC currents before and after the SAW burst is displayed. Each data point corresponds to a single-shot realization.

the SAW amplitude should also play an important role in the electron transfer. This dependence with the SAW parameters can be seen on the mappings of Fig. 3.4: all the "electron loss" regions become larger (shifted to less negative values of δV_R) for a higher SAW power or for a longer SAW duration.

In the next section, the study of the electron emission efficiency as a function of the SAW parameters is done more thoroughly and a model accounting for the SAW burst amplitude and its duration is described.

3.4 Influence of the SAW parameters on the electron emission

In this section the influence of the different SAW parameters on the transfer efficiency is examined in further details. We will consider especially the influence of the SAW power and duration[1]. The first one changes the wave amplitude and therefore the maximum gradient of the SAW modulation. As already discussed, a larger amplitude will thus allow the moving quantum dots to be better defined and overcome steeper static potential gradients. For its part, the SAW duration defines the number of possible attempts for transfer (one per period) and therefore also influences the transfer efficiency if a tunnel process is involved. It also allows the SAW burst to reach a higher amplitude when working with burst of duration comparable to the IDT rise time.

The relative influence of these two parameters on the electron emission efficiency has been studied. To that purpose, the following experiment is realized:

- The source quantum dot is coupled to its reservoir in order to load one electron.
- The system is then brought to the intermediate position I (see Fig. 3.3) within a microsecond. Charge readout of the source dot is performed.
- The source dot is then pulsed to its transfer position for 20 µs while the SAW burst is applied. We make sure to be in the regime where SAW-assisted transfer is possible (see Fig. 3.5).
- The dot is finally set back to point I, and a new charge measurement is performed in order to learn whether the electron has left the dot or not.

This measurement is repeated 500 times for varying SAW amplitude and duration. The transfer position has not been varied.

The result is plotted on the top left panel of Fig. 3.6. For small SAW amplitude and duration, the burst has no impact and the electron remains in the source quantum dot (blue region in the bottom left corner). On the contrary the probability to emit the electron is reaching unity for a large amplitude and duration (red region in the top right corner). To understand more specifically the influence of each parameter, we analyze two slices (horizontal and vertical) indicated by the dashed white lines. They are represented on the two bottom graphs of Fig. 3.6. We first concentrate on the SAW amplitude dependence of

1 A study of the SAW excitation frequency is presented in appendix A. The following results have been obtained at the optimal frequency value, found to be 2.6322 GHz.

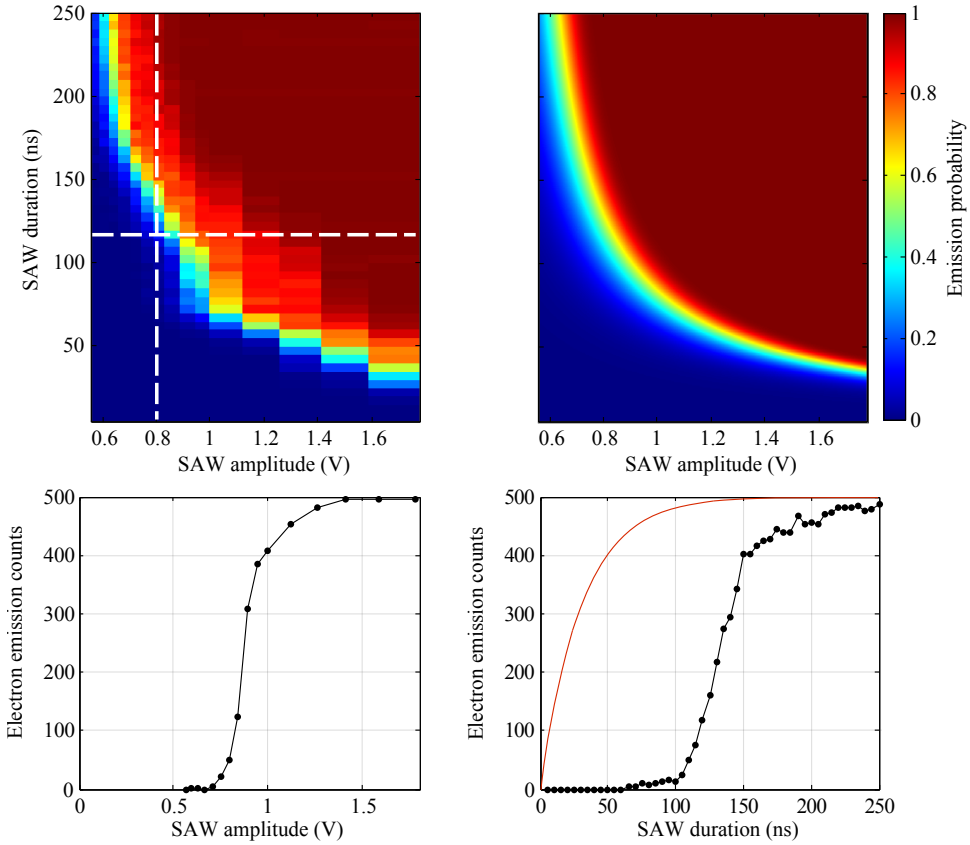

Figure 3.6: (top left) Influence of SAW parameters on the electron emission probability. The x and y axis correspond respectively to the RF signal amplitude and duration sent to the IDT. The color corresponds to the probability that the electron left the source dot after the passage of the SAW burst. For each data point the experiment has been repeated 500 times. **(top right)** Result of the fitting computation using the model described in the main text. The fit parameters found are $\tau_{IDT} = 63.3\,\text{ns}$, $A_{Th} = 0.979\,\text{V}$ and $\delta A = 0.0623\,\text{V}$. **(bottom left)** Slice of the top left figure along the x axis (horizontal white dashed line) representing the counts of emitted electrons as a function of the SAW amplitude (the SAW duration is fixed to 110 ns). **(bottom right)** Slice of the top left figure along the y axis (vertical white dashed line) representing the number of emitted electrons as a function of the duration of the SAW burst (the SAW amplitude is fixed to 0.794 V). A model assuming a constant wave amplitude is plotted (continuous red line).

the electron emission probability (bottom left plot). We can see that no electron leaves the dot for a too weak amplitude. Around 0.8 V, the transfer rate suddenly increases to finally reach 1. This behavior suggests that a threshold amplitude A_{Th} has to be passed to allow for the electron transfer.

We now examine the SAW duration dependence of the electron emission probability (bottom right plot of Fig. 3.6). A similar threshold behavior is also observed here. The electron emission probability remains close to 0 until 100 ns of SAW irradiation, and then rapidly rises close to unity. Such behavior is not consistent with a mere increase of the attempt number for the electron capture. In that case, the emission probability should immediately start rising (see red curve on the bottom right plot of Fig. 3.6). The observed behavior is however consistent with a bandwidth limitation of the IDT[1]: the SAW excitation needs some time to get established and reach the threshold amplitude A_{Th}.

To model the injection process, we consider a simple situation where a tunneling event enabled by the SAW modulation of a barrier is required to transfer the electron (as seen on the right plot of Fig. 3.2). We define p as the probability per period of the wave that this tunneling event occurs. In order to model the threshold behavior, p is assumed to depend on the SAW amplitude A as a Fermi-Dirac step function:

$$p(A) = \frac{1}{1 + \exp\left(\frac{A_{Th} - A}{\delta A}\right)} \tag{3.1}$$

For $A \ll A_{Th}$, $p(A)$ is almost zero and the electron transfer is not possible. When A is approaching the threshold value A_{Th}, $p(A)$ is finite and the transfer mechanism is stochastic. The extent of this regime is given by the parameter δA. Finally, for $A \gg A_{Th}$, $p(A)$ is nearly one and a single SAW period should be required to ensure the electron transfer. This is illustrated on the lower panel of Fig. 3.7.

As a time dependence for the SAW amplitude, it is used an RC low-pass step response, written as:

$$A(t) = A_0 \left(1 - \exp\left(-\frac{t}{\tau_{IDT}}\right)\right) \tag{3.2}$$

where A_0 is the continuous wave amplitude and τ_{IDT} the IDT rise time. This is illustrated on the top panel of Fig. 3.7. Each curve represents the amplitude evolution for different values of A_0. An horizontal red line represents the threshold that has to be crossed to have the electron transferred by the SAW. For a too small value of A_0, the threshold is never crossed and applying a longer SAW duration will have no effect. For a sufficiently large A_0, the threshold can be crossed. Typically, the larger A_0 the sooner the threshold is reached. It can be noted that a passage through a regime of stochastic transfer cannot be avoided.

Combining all these elements, the probability for the electron to be transferred after n

1 The contribution of the 70 finger pairs (of 1 µm pitch) of the IDT have to sum up to reach the maximum amplitude of the burst. This imposes a lower bound of $70\,\mu\text{m}/c_{SAW} = 30\,\text{ns}$ for the IDT rise time.

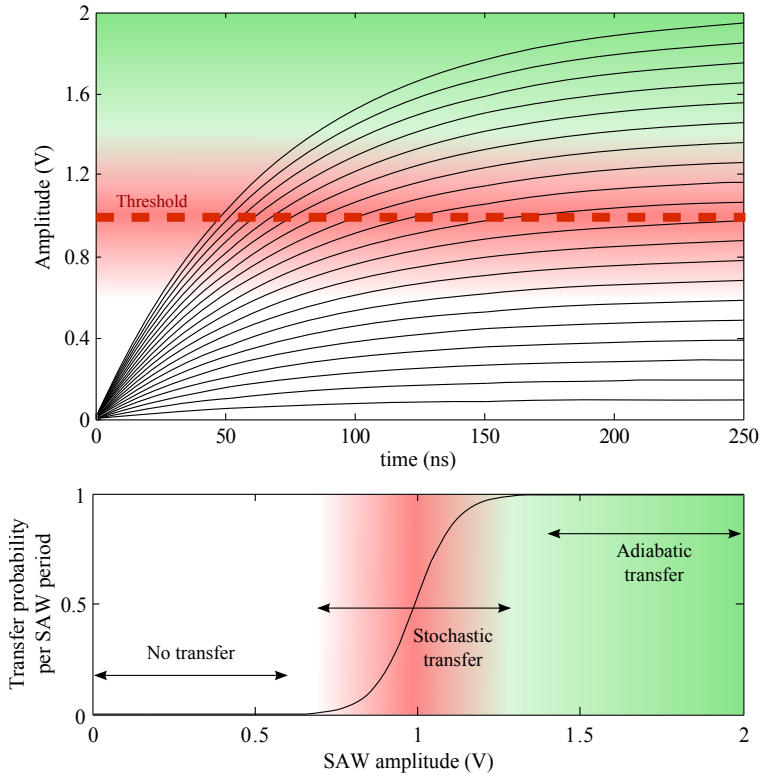

Figure 3.7: (top) Illustration of the SAW envelope rise for different amplitudes applied to the IDT. The IDT rise time is the same for all the curves. The threshold amplitude is pictured as the red dashed line. **(bottom)** Model of the transfer probability per wave minimum as a function of the SAW amplitude. The different transfer mechanisms are attributed to the corresponding probabilities.

periods of SAW can finally be computed as

$$P(n) = 1 - \prod_{i=1}^{n}(1 - p(A(i)) \tag{3.3}$$

where $A(i)$ is the SAW amplitude of the ith period of the wave. This probability can be calculated for varying A_0 and n in order to reconstruct the complete set of data shown on the top left panel of Fig. 3.6. The only fit parameters are the threshold amplitude A_{Th}, the "width" of the threshold δA and the rise time of the IDT τ_{IDT}. The output of the fit procedure is shown on the top right panel of Fig. 3.6.

This model is relatively well fitting the data. It yields to an estimation of the IDT characteristic rise time of $\tau_{IDT} = 63.3\,\text{ns}$. This is consistent with the 2.4 MHz width of the resonance measured on Fig. A.1 which gives a 65 ns characteristic time[1]. This value is

1 Using $\frac{1}{2\pi\tau}$ as bandwidth definition for a first order model.

larger than the 30 ns estimated from the 70 periods of the IDT. This is attributed to the cavity behavior induced by the single-finger geometry of the IDT used (see section 1.6.1).

In summary, this model suggests that the probability to inject the electron to a moving quantum dot is slowly rising from zero to unity during a SAW burst as its amplitude gets larger. This implies that to emit the electron, the system necessarily transits through a stochastic transfer regime. In the next part, we will see that a nanosecond pulsing of the quantum dot potential allows to control the electron injection in a precise moving quantum dot. This enables to access directly the probability $p(A(t))$ to inject the electron in a given SAW minimum.

3.5 Nanosecond electron emission from the source dot

In order to control the exact time of the electron emission, the idea is to engineer a time dependent dot potential during the SAW burst. We have seen that the electron transfer is not possible when the dot potential is too deep and confines too strongly the electron. On the contrary it will be enabled for a shallow dot with its chemical potential sufficiently close to the channel one. By switching for a very short time (limited to ~ 1 ns with the present set-up) between these two positions, the control of the electron emission time should be possible.

Due to the limited amplitude of the nanosecond pulses, the position where the electron is protected from the SAW influence must be found close to the transfer position to be able to switch between these two positions with a nanosecond pulse. For that purpose, a mapping similar to those presented on section 3.3 has been done and is shown on Fig. 3.8. We recall that two regions can be identified, the blue (resp. yellow) one corresponding to the electron remaining on (resp. leaving) the source dot. Ideally, the "protected" position should be as deep as possible into the blue region to have a dot confining strongly the electron whereas the transfer position should be deep into the yellow region. The two positions that have been used for the following experiments are indicated by the point P (protected) and T (transfer) on Fig. 3.8.

The new pulse sequence that is used to perform the nanosecond triggering of the transfer is as follows (see also the lower panel of Fig. 3.8):

- The source quantum dot is coupled to its reservoir in order to load one electron.
- The system is then brought to the intermediate position I (see Fig. 3.3) within a microsecond. Charge readout of the source dot is performed.
- The source dot is then pulsed to the position P for 20 µs. During that time, the SAW burst is applied as well as a 1 ns negative pulse on V_L to reach position T.
- The dot is finally set back to point I, and a new charge measurement is performed in order to learn whether the electron has left the dot or not.

If the electron is transferred, it must be during the nanosecond when the system is in position T. Of course, this nanosecond voltage pulse should have an effect only if it reaches the quantum dot simultaneously with the SAW. In order to tune this synchronization, the time interval Δt_s between the nanosecond pulse triggering and the SAW burst triggering

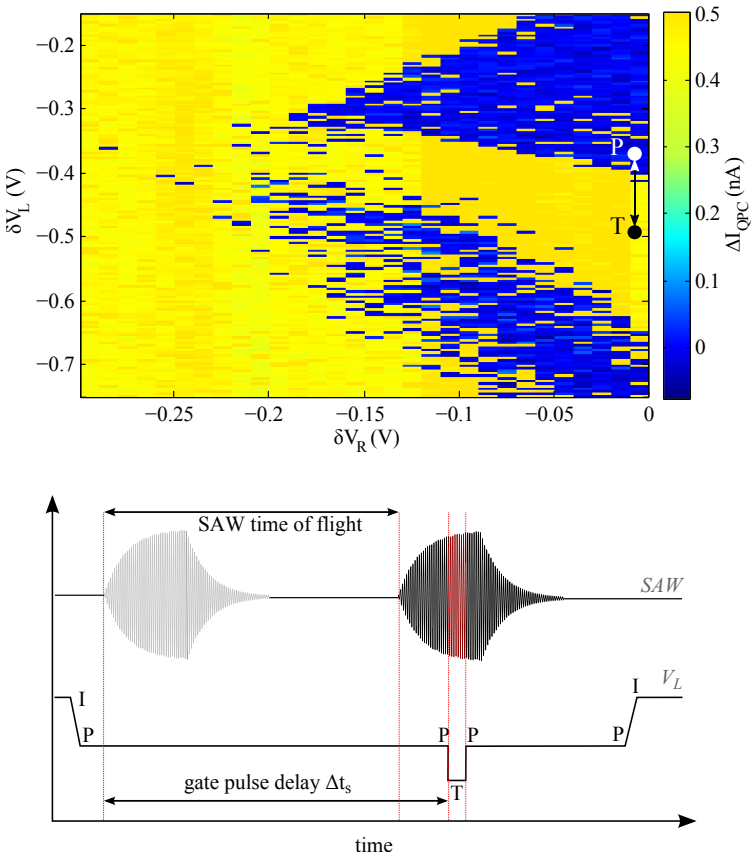

Figure 3.8: (top) Mapping of the transfer efficiency with respect to the gate voltages of the transfer position. One electron is prepared in the intermediate metastable position of the source quantum dot. The system is then pulse for 20 µs in the transfer position and a 15 dBm SAW burst of 70 ns is applied. The charge variation before and after the SAW burst is reported on this diagram. Each data point correspond to a single experiment run. **(bottom)** timing schematics of the experiment. The SAW time of flight is the time required for the SAW to travel from the IDT to the quantum dot. It represents around 2 mm, corresponding roughly to a 700 ns delay given the wave velocity (2800 ms^{-1}). An additional delay of about 100 ns is internal to the RF signal generator. On the same time, the source dot is pulsed to position P for $\sim$ 20 µs. In addition a 1 ns pulse to position T is applied, with a delay Δt_s relative to the SAW burst triggering.

can be varied. Δt_s has to compensate the time for the SAW to propagate from the IDT to the quantum dot (see lower panel of Fig. 3.8). By changing Δt_s, one can then change the part of the SAW burst that is probed. In the end we should recover qualitatively the variation of the transfer probability $p(A(t))$ with time.

The results of this experiment are presented on the top plot of Fig. 3.9. The number of successful electron emissions (over 200 repetitions of the experiment) is shown as a function of Δt_s. The same measurement procedure has been reproduced for different SAW parameters. For too short (resp. too large) values of Δt_s, the nanosecond pulse reaches the dot before (after) the passage of the SAW. The dot is thus in a protected position when the SAW passes and indeed, no electron emission is observed. On the contrary, when the nanosecond pulse and the SAW excite simultaneously the dot system, a peak in the electron emission appears. The value of Δt_s at which this is occurring on the data is consistent with the estimation of the SAW propagation time from the IDT to the system.

We now study in more details the influence of the SAW parameters on these curves. First we consider a change in the SAW duration[1] (we compare the curves with similar 1.50 V amplitude but different duration on the top plot of Fig. 3.9). A longer SAW duration will of course result in a wider observed peak. In addition, it will also enable the SAW amplitude to reach a value closer to its steady state. Therefore, not only the width but also the height of the peaks should be increased when raising the SAW burst duration. This is consistent with the data. The rising parts of the curves obtained with 1.50 V SAW amplitude are perfectly matching. Only the peaks fall, attributed to the end of the SAW burst, is delayed as the SAW burst duration is increased. After that point, the wave amplitude decays back to zero and so does the electron emission probability.

We can now consider a change in the SAW excitation amplitude (A_0 on eq. 3.2). To this aim, we compare the green and orange curves on Fig. 3.9, done with similar SAW burst duration but different amplitudes (respectively 1.78 V and 1.50 V). As expected a larger amplitude results in a higher emission probability. In addition, increasing A_0 implies an earlier crossing of the transfer threshold A_{Th} (see Fig. 3.7) and consequently, the electron emission probability starts rising at shorter delays. This explains the width difference between the two curves. For the 1.78 V SAW amplitude curve, the electron is sent $97 \pm 1.2\%$ of the time within the nanosecond pulse at the moment the SAW amplitude reaches its maximum ($\Delta t_s = 865$ ns). An almost complete on/off of the electron sending is thus achieved. This gives a precision of less than three wave periods for the transfer triggering (and an estimate for the emission probability per wave minimum $p(A)$ between 0.7 and 0.8).

In principle, it should be possible to achieve even better performance either by working with a larger SAW amplitude or by reducing the static potential gradient. The results

1 It can be noted that the SAW duration used here is comparable to the IDT rise time we determined in section 3.4. As a result, the SAW amplitude does not reach a steady state but continuously rises. It explains first why the observed peaks are much narrower compared to the overall SAW burst duration: the amplitude threshold A_{Th} is certainly crossed only in the end of the burst. Only this last part of the burst with an amplitude larger than A_{Th} contributes to the electron transfer and will have a visible effect.

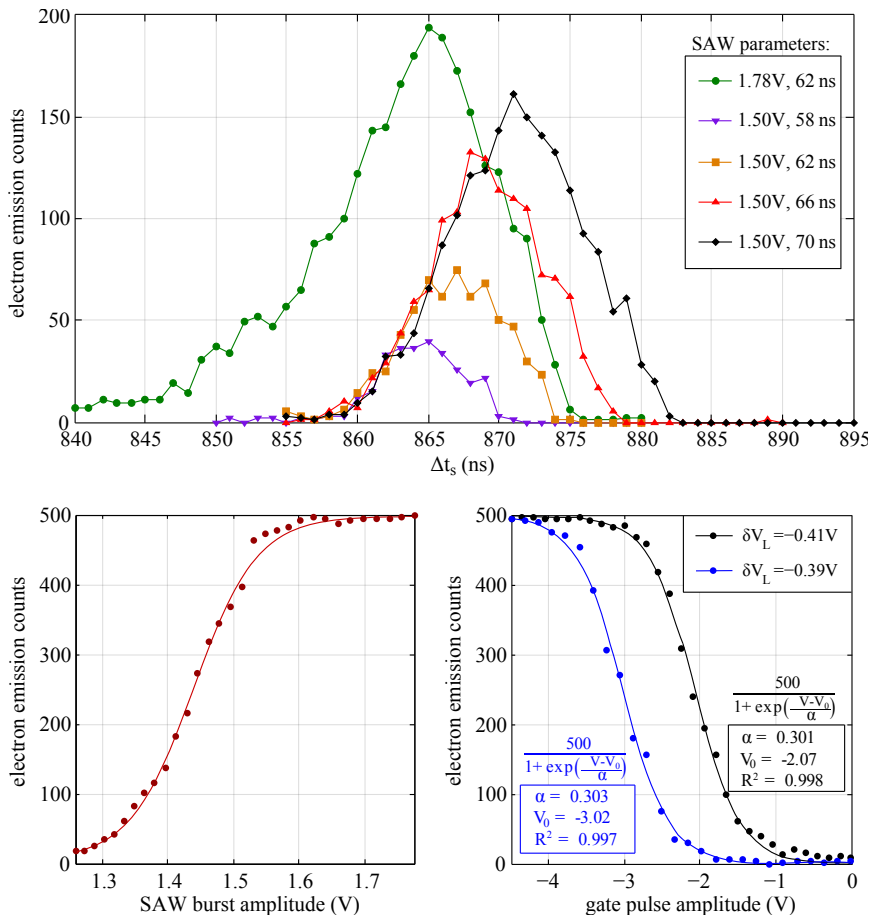

Figure 3.9: (top) Successful electron emission counts as a function of the gate pulse delay for different SAW parameters. A -4.5 V pulse is applied by the AWG with a duration of 1 nanosecond. The experimental sequence is repeated 200 times for each data point. The different SAW parameters used are indicated on the legend. **(bottom left)** Variation of the sending efficiency as a function of the SAW amplitude. The SAW duration was set to 70 ns. The 1 ns gate pulse is applied at $\Delta t_s = 870$ ns. The red line corresponds to a fit of the data with a Fermi-Dirac-like function. **(bottom right)** Variation of the sending efficiency as a function of the nanosecond gate pulse amplitude for two different "starting points" (point P on Fig. 3.8). This was measured for a 1.78 V SAW burst of 70 ns, and with the nanosecond pulse applied at $\Delta t_s = 870$ ns. Data are fitted with Fermi-Dirac functions to estimate precisely the shift in voltage between the curves.

relative to the SAW amplitude variation are shown on the bottom left plot of Fig. 3.9. The SAW duration has been set to 70 ns, the nanosecond pulse is applied at $\Delta t_s = 870$ ns and the SAW amplitude is varied between 1.26 V and 1.78 V. The number of emitted electrons over 500 experiment repetitions is shown as a function of the SAW amplitude. The data can be fitted (see red curve on the graph) with a Fermi-Dirac-like function (eq. 3.3), resulting in a threshold value $A_{Th} = 1.44$ V and $\delta A = 0.048$ V.

The equivalent results relative to the static potential variation are shown as the black curve on bottom right plot of Fig. 3.9. The SAW power and duration have been fixed to 1.78 V and 70 ns, and the nanosecond pulse is applied at $\Delta t_s = 870$ ns. The number of emitted electrons over 500 experiment repetitions is shown as a function of the nanosecond pulse amplitude. Again a clear threshold behavior is observed. If the amplitude of the pulse is close to zero, the quantum dot remains in the protected position and the electron cannot be transferred. As the pulse amplitude is set more negative, the position reached by the dot is closer and closer from its transfer position (point T on Fig. 3.8) and the probability to send the electron increases. The blue curve corresponds to the same measurement reproduced for a slightly different position P (see Fig. 3.8) from which the nanosecond pulse is applied. Since point P has been shifted a little further away from the transfer position (less negative values on V_L), a higher pulse amplitude must be applied as a compensation. This trick allows to deduce the actual amplitude of the signal that reaches the sample: one needs to apply almost 1 V more with the AWG to compensate the 20 mV change of the reference position.

In these last experiments, 100% efficiency of the electron emission has been achieved for the highest SAW and gate pulse amplitude data points. Given the statistics of the measurement, an estimate for the injection efficiency per wave minimum is now around 94%. This is a good indication that we can overcome the stochastic regime shown on Fig. 3.2 and reach the "adiabatic" one where the electron injection is done in a single wave period. Nevertheless in order to definitely prove it, the realization of a gate pulse as short as a single SAW period (0.38 ns) would be required.

3.6 Conclusion

In this chapter, we have studied the interplay of the static potential and the SAW parameters on the electron transfer efficiency. A simple model has been proposed, combining an RC rise time of the SAW burst amplitude and a SAW amplitude threshold above which transfer becomes possible. This model is in a relatively good agreement with the experimental observations. It revealed a rather long timescale associated with the SAW rise time, that could be problematic to achieve fast control of the electron transfer with minimal excitation. It also implies that the system undergoes a transitional regime where the electron emission is stochastic, even for large SAW amplitude used. This induces uncertainties on the electron emission time.

A solution that has been developed consists in compensating this slow variation of the SAW amplitude by fast operations on the static potential. A nanosecond triggering of the electron emission with unity probability has been demonstrated and could be in principle extended down to a single wave period.

Such a fast control of the electron transfer could be used to keep the system in a position where the electron is deeply confined in a quantum dot during most of the passage of SAW. We expect that this should limit the possible influence of the SAW on the electron spin. In addition, it could be very useful in the perspective of coherent spin transfer experiments (where control of the transfer must be achieved faster than T_2^*).

This nanosecond pulsing procedure can also be applied to the reception dot in order to control the time at which the electron is received. By combining it with the source dot triggering, it is possible to verify that the electron time of flight between the dots is consistent with the SAW propagation speed. This point is investigated in appendix B.

CHAPTER 4

Coherent spin manipulations in an isolated double quantum dot

4.1 Introduction

We have seen in chapter 3 that the SAW transfer of an electron requires to bring the source and reception quantum dots in a metastable position, well isolated from their electron reservoirs. With this technique, a high transfer efficiency and a precise control of the electron emission time have been demonstrated. However, no proof has been done that this procedure is not detrimental for the spin degree of freedom of the electron. In particular, the spin coherence must be preserved during the transfer in order to be useful for quantum information processing. As a first step towards this goal, it is of interest to demonstrate that a given spin state can be initialized and manipulated in a way compatible with the transfer procedure.

For that purpose, a thorough study of the metastable configuration used during a transfer sequence has been done. We have demonstrated that in such a position the sample can exhibit a double dot behavior. The charge stability of this metastable double dot has been studied, and is first presented. In particular, it is shown that such a system exhibits an enhanced tunability compared to usual double dots coupled to reservoirs. In a second part, it is then exposed how standard spin readout techniques can be adapted to recover the spin information in this metastable position. We take advantage of the enhanced tunability offered by an isolated double dot system to implement a new scheme for coherent spin manipulation, reproducing the original proposal of Loss and Divincenzo [Los98]. It is shown that this scheme presents a reduced noise sensitivity.

4.2 Observation of a double dot behavior in the metastable position

4.2.1 Potential numerical simulations

To get a better understanding of the potential experienced by the electron in the metastable position, numerical simulations have been performed to model it as a function of the voltage applied on the different gates of the sample. To that purpose, each gate is decomposed in multiple triangles and rectangles thanks to an ear clipping algorithm. The effect on

the 2DEG potential of these elementary pieces can then be calculated following [Dav95]. The interested reader can refer to [Bau14] for further details on the software used. The output of such a computation is shown on the top right plot of Fig. 4.1. The different gate voltages have been chosen to be consistent with the values used during the experiments. In order to describe more precisely the dot potential shape, slices of the potential profile can be done along the white dashed line shown on the plot.

This has been done for two different V_L values, and the corresponding potential profiles are presented on the two lower panels of Fig. 4.1. We recall that during a transfer sequence, a negative pulse is used on V_L in order to bring the dot to a metastable position. This gate defines the dot/reservoir tunnel barrier and has also an influence on the dot chemical potential. Typically, the lower left slice corresponds to the loading position of the quantum dot where the dot is coupled to its reservoir, whereas the right slice corresponds to the metastable position where the dot is well isolated from the reservoir. It can be noted that for both positions we obtain a potential profile characterized by a double well. The left minimum is at the expected quantum dot position whereas the right one sits at the entrance on the 1D channel. The gate V_R defines the potential barrier separating the two minima while V_L controls their relative alignment. In the following, we refer to the left potential minimum as the loading dot and to the right one as the channel dot.

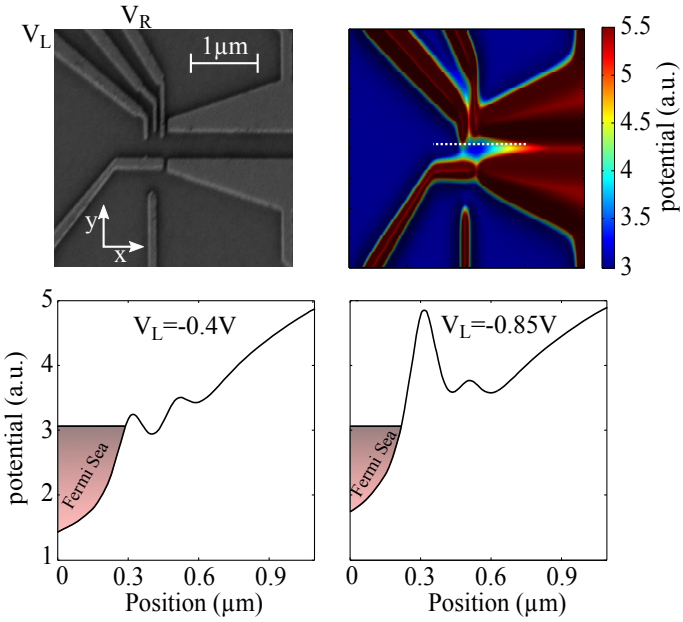

Figure 4.1: Numerical simulations of the electrostatic potential of the device. **(top left)** SEM picture of the part of the sample that is modeled. **(top right)** Numerical simulations of the potential shape with the gates polarized with voltages similar to the experimental ones. Red color stands for a large potential value while blue stands for a low one. **(bottom left)** Slice of the potential along the white dashed line in the top right figure, with a relatively low negative voltage applied on gate V_L. **(bottom right)** Same slice of the potential for a more negative voltage applied on gate V_L. On these two slices, the Fermi level has been arbitrarily added.

4.2.2 Additional patterns in standard stability diagrams

The first experimental signature of this double dot behavior in the metastable position has been observed on charge stability diagrams. We start recalling briefly the main characteristics observed so far on the stability diagrams (see top diagram of Fig. 4.2). On the top part of the diagram (low negative V_L), there is a large coupling between the reservoir and the loading dot, and the electron number it contains can easily vary while V_L is swept. As a result we observe clear charge degeneracy lines. On the bottom part (large negative V_L), the coupling to the reservoir becomes too small and the electron exchange between the loading dot and the reservoir is no longer possible. This is the metastable region. In this position no charge degeneracy line is observed anymore. During a sweep of V_L the charge contained in the dot gets frozen at some point and a given number of electrons are then kept in the dot until the end of the sweep. This diagram has been obtained with the two channel gates polarized with a large negative value ($-0.55\,\mathrm{V}$, which is nearly $80\,\mathrm{mV}$ below the channel gates pinch-off value).

For lower negative values on the channel gates ($-0.505\,\mathrm{V}$ for the bottom diagram of Fig. 4.2), it is possible to see new charge degeneracy lines appearing in the metastable region. The position of these lines can be shifted to more negative V_L values when the voltage on the channel gates is set slightly more negative. This suggests that the corresponding tunneling events are not done towards the reservoir. On the contrary, we assume this is due to electron exchange between the two minima of the double dot that appeared on the numerical simulations. The more negative the channel gates are polarized, the higher the channel dot potential should be and the more negative must be V_L to have the loading and channel dots in a resonant position. Similar patterns in a stability diagram have already been observed in an isolated double dot containing a large electron number [Rus04].

It can be seen on the stability diagram that the number of lines present in the metastable region directly depends on the number of electrons that are brought to this position. On the left part of the diagram, no electron is present in the dot at the beginning of a V_L sweep. Therefore no electron can be trapped to the metastable position and no line is observed. For less negative values on V_R, one electron is brought to the metastable position, and a single charge degeneracy line is observed, delimiting the two possible charge configurations of the double quantum dot. The charge states of the metastable double dot are reported on the diagram as the (i,j) labels, where i (resp. j) stands for the number of electrons stored in the loading (resp. channel) part of the double quantum dot. For two electrons trapped and brought to the metastable region, two different charge degeneracy lines can be seen, delimiting the (2,0), (1,1) and (0,2) charge states. Finally, on the right hand part of the diagram, three electrons are trapped. The (3,0), (2,1) and (1,2) regions can be seen. The (1,2)-(0,3) degeneracy line is missing here, either occurring at a too negative V_L or being too broadened because of a large interdot tunnel coupling. The dependence of the interdot tunnel rate is consistent with the geometrical expectations. For the most negative V_R, the tunnel barrier between the two dots is relatively thick. In this situation, the tunneling time is long compared to the measurement timescale and this leads to the stochastic jumps that

are observed in the one-electron region[1]. On the contrary, the interdot coupling is very strong in the three-electron region (most positive V_R values), resulting in a broadening of the degeneracy lines.

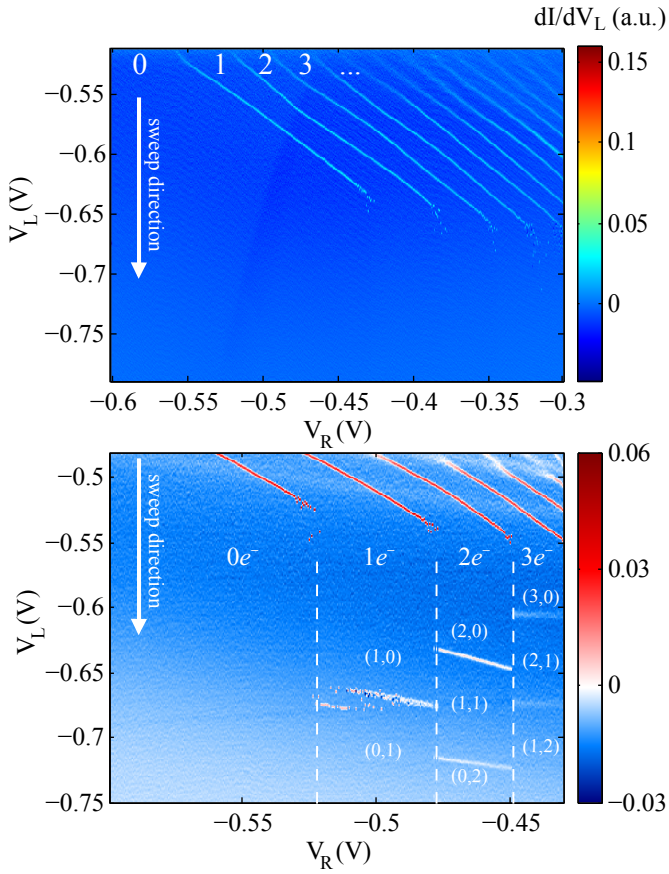

Figure 4.2: (top) Example of the measured stability diagram for a quantum dot coupled to a single lead. Data obtained by sweeping gate V_L towards more negative values, and stepping gate V_R. Acquisition speed is 3 ms per point. Data is numerically smoothed and derived to highlight the changes in the QPC conductance. **(bottom)** Similar stability diagram obtained with the same experimental protocol but for a different tuning of the sample. Mainly, the two channel gates are polarized with less negative values. Signature of double dot is observed on the lower part of the diagram.

4.2.3 Metastability diagrams with fixed number of electrons

In order to allow for further manipulations, it would be interesting to control the number of electrons brought to this metastable position.

The procedure is rather straightforward. The desired number of electrons is prepared in

1 In addition, the charge degeneracy line seems to be shifted to more negative V_L. This is due to tunneling to an excited state of the channel dot. This point is investigated in appendix C.

the loading dot. One must make sure to be in a position where the coupling to the reservoir is not too strong (typically $\ll 1\,\mathrm{MHz}$). In that case, V_L can rapidly be shifted to a large negative value (using a microsecond voltage pulse) in order to bring the system to the metastable configuration without losing any electron. A control of this procedure efficiency is presented on Fig. 4.3. The lower part of the graph (shorter times) corresponds to the electron loading step. The V_L voltage used for the loading position is varied in order to change the number of electrons initialized in the loading dot. Three different QPC current values are observed, corresponding either to zero (yellow), one (light blue) or two (dark blue) electrons loaded into the dot. The horizontal switch at 19.5 ms corresponds to the moment when V_L is pulsed to a large negative voltage to reach the metastable position (here 200 mV more negative). The difference in the QPC signal can still be observed after this pulse. We deduce that the red, orange and green regions correspond respectively to zero, one and two electrons brought to the metastable configuration. There is a perfect correlation between the charge of the dot just before and after the voltage pulse, confirming that the electrons are never lost during this procedure. One can note that on this experiment timescale, the charge is completely frozen once in the metastable position. Similar experiments were done over larger timescales and showed that charge relaxation time can approach a second for negative enough V_L.

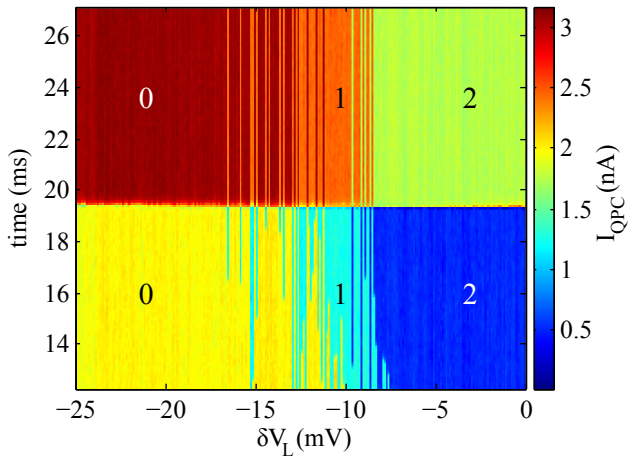

Figure 4.3: Electron pumping to metastable state. The x-axis corresponds to the relative voltage used on V_L for the loading position of the dot (lowest part of the diagram). After $\sim 8\,\mathrm{ms}$, V_L is shifted by 200 mV towards more negative values within 1 µs to reach the metastable position. The cross-talk between V_L and the QPC is numerically corrected on the lowest part of the diagram for a better visibility.

We have just shown that we are able to control the charge initialization of the system in the metastable position. We can use this procedure to characterize the metastable double dot charge stability with a fixed electron number over a wide gate voltage range.

Typical measurements with a constant charge are presented on Fig. 4.4. The top and bottom diagrams correspond respectively to an initialization with a single and two electrons. They are realized as follow:

- First a single or two electrons are initialized in the loading dot.
- Next, V_L is pulsed to a large negative value (up to $V_L = -0.8\,\mathrm{V}$ in the case of Fig. 4.4) to reach the metastable position.
- V_R can then be changed without affecting the electron number of the system, contrary to the case of Fig. 4.2.
- V_L is then swept back towards low negative values, until coupling to the reservoir is restored.

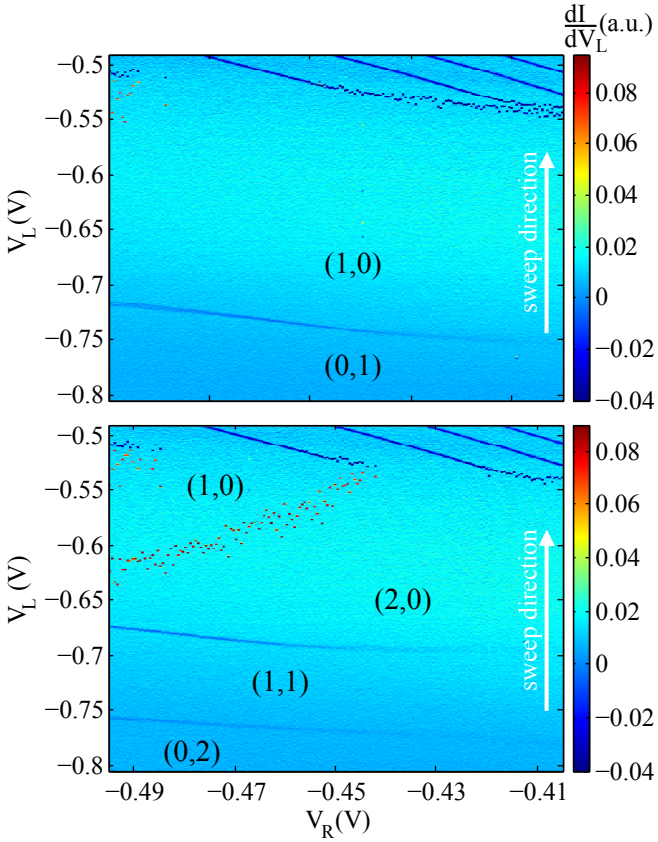

Figure 4.4: Large extent metastability patterns with fixed number of electrons. One **(top)** or two **(bottom)** electrons are pumped to metastable position ($V_R = -0.455\,\mathrm{V}; V_L = -0.8\,\mathrm{V}$) following the method presented on Fig. 4.3. The V_R voltage is then shifted to the value indicated by the x-axis before sweeping V_L from $-0.8\,\mathrm{V}$ to $-0.5\,\mathrm{V}$. The initialization step is reproduced for each sweep. Acquisition speed is 3 ms per point. Data are numerically smoothed and derived.

If we look at the resulting stability diagram obtained with single electron initialization (top diagram of Fig. 4.4), only a single line is observed in the metastable region. It delimits the (1,0) and (0,1) charge states of the double dot. We can note the degeneracy line is almost horizontal, meaning that the double dot detuning is almost independent of V_R.

However, this gate has a strong impact on the interdot tunnel coupling. We can see that the degeneracy line becomes less visible for low negative V_R, revealing an increasing interdot coupling.

The bottom diagram corresponds to the very same measurement with only the charge initialization changed to two electrons. Two charge degeneracy lines can now be seen in the metastable region, delimiting the (2,0), (1,1) and (0,2) configurations. In addition, it can be seen an additional region on the top left part of the diagram. In this position, V_L reaches values for which the dot/reservoir tunnel barrier becomes too thin to prevent the relaxation of an electron to the reservoir. The red points delimiting this region are the signature of an electron tunneling from the dot to the reservoir. It shows the limit over which one can work with two electrons in the metastable state (for a timescale on the order of a few milliseconds).

Since we are working with a fixed number of charges, these stability diagrams characterizing the metastable double dot are much simpler compared to those obtained with standard double dots coupled to reservoirs (see Fig. 4.5). For n electrons in the system, only n parallel degeneracy lines will be observed. More generally, this concept can be applied to larger arrays of quantum dots. The general formula that will quantify the complexity of the stability diagram is given by:

$$N = \binom{N_{dot} + N_{e^-} - 1}{N_{e^-}} \tag{4.1}$$

where N is the maximal number of regions that can be present on the diagram, N_{dot} is the number of dots of the considered array and N_{e^-} is the charge number in the system.

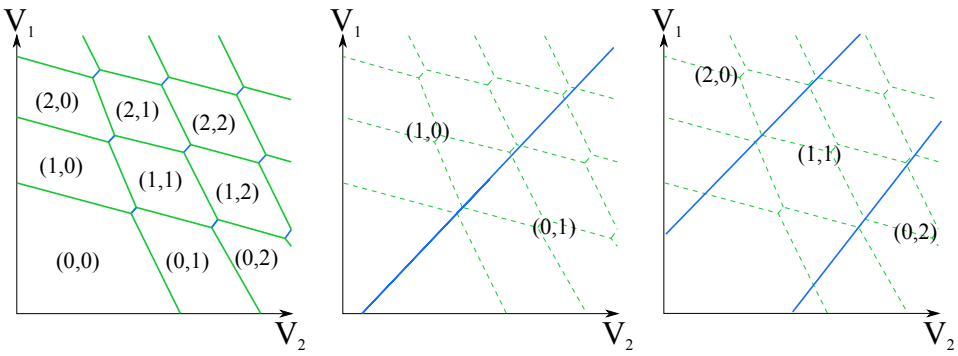

Figure 4.5: (left) Schematic of the stability diagram of standard double dot coupled to electron reservoirs (for intermediate interdot coupling [Wie02]). **(middle)** Only one line remains (solid line) for an isolated double dot initialized with a single electron. The dashed lines serves as comparison with the standard double dot diagram. **(right)** Same schematic as for the middle plot for an isolated double dot initialized with two electrons.

The other striking advantage of the metastable double dot is the facility to tune the two relevant parameters that are the dot detuning and the interdot tunnel coupling at a fixed electron number. With a double dot coupled to electron reservoirs, it is relatively easy to vary the dot detuning but the interdot tunnel coupling can only be varied on a limited

range without varying the total number of electrons in the system. On the contrary, this is no longer a problem in metastable dots since the charge number cannot vary. Moving along a degeneracy line allows to change the tunnel coupling while moving on the perpendicular direction changes the relative detuning of the dots.

4.3 Spin measurement and relaxation in metastable position

So far, it has been shown that a double dot behavior can be observed when bringing electrons to a metastable position. This is of great interest towards the objective of spin information transfer. Indeed, this could provide a very convenient way to manipulate spin states close to the position used for the electron transfer. However one needs first to be able to measure spin properties in such a metastable dot. The point of this section is to present the different methods that can be used to readout electron spin states in such a position. We will concentrate on the case of two-electron spin states.

As a first step, we set-up spin measurement with the dot in a standard position, coupled to the electron reservoir. The first thing we need in order to tune and calibrate the readout procedure is the ability to prepare different spin states. In the case of two-electron spin states, we have seen that four different states are possible: a singlet state (ground state) and three triplets states. When two electrons are loaded into a dot, the probability that a triplet state is formed is given by [Han05]

$$P_T = \frac{3\Gamma_T}{\Gamma_S + 3\Gamma_T} \tag{4.2}$$

where Γ_S and Γ_T are the singlet and triplet tunnel-rates respectively. The factor 3 is due to the triplet degeneracy. We have seen (section 1.2.3) that the coupling to the reservoir of a triplet state is usually stronger than for a singlet. This implies that $\Gamma_T \gg \Gamma_S$ and yields to a triplet probability close to 1 just after loading of the two electrons. In order to prepare a singlet state, one simply has to wait for relaxation of the system (usually a few milliseconds [Han05; Meu06a]) since the ground state is a singlet state. Therefore by studying the triplet to singlet spin relaxation, any singlet/triplet proportion can be prepared and measured, and this constitutes a way to estimate the readout efficiency.

In order to achieve spin readout, we have seen (section 1.2.3) that a precise positioning of the dot chemical potential relative to the Fermi level of the reservoir is required. In order to determine the correct position to use, the following experiment is then performed:

- First two electrons are loaded into the dot (point L_2 on Fig. 4.7). The dot/reservoir tunnel rate in this position is sufficient to ensure the loading of the dot faster than 100 µs.
- It is then waited a time t_{wait} of either 0.1 ms or 20 ms. In the 0.1 ms case, t_{wait} is much smaller compared to the spin relaxation time and there will be a high probability to have a triplet state in the dot. On the contrary in the 20 ms case, t_{wait} is relatively long compared to the relaxation time and there will be a high probability to have a singlet state.
- The system is finally pulsed to different measurement positions around the 1-2

electrons charge degeneracy line. The QPC current is monitored there for a few tens of millisecond.

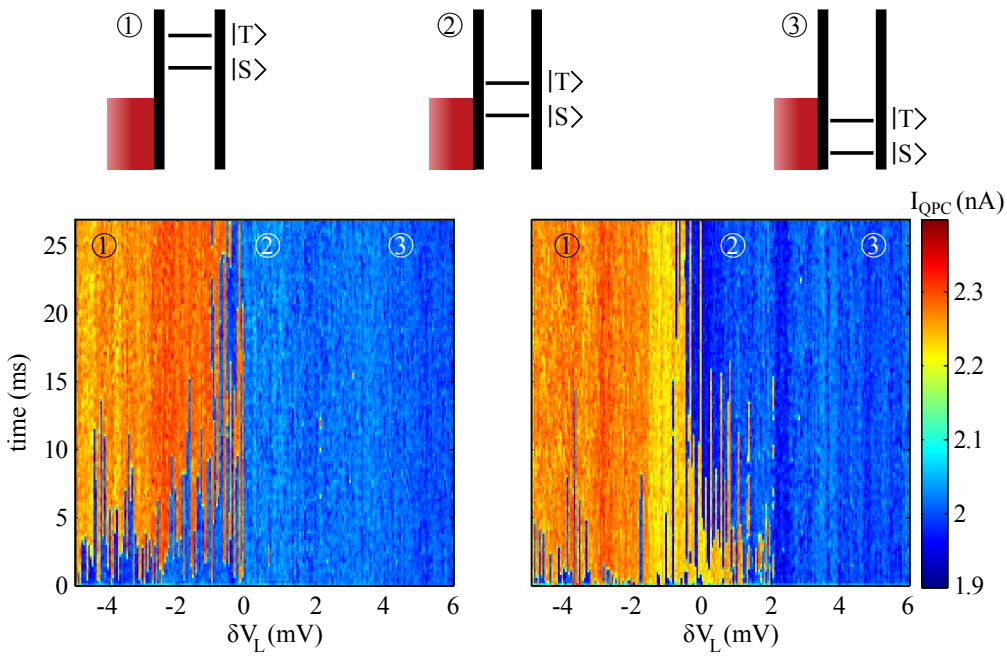

Figure 4.6: (2,0)-(1,0) transition scans for singlet and triplet spin states. **(top)** Schematics of the relative alignment between the dot energy levels and the Fermi energy of the reservoir for different positions on the two bottom plots. **(bottom left)** The system is initialized with two electrons in a singlet state by waiting 15 ms in the loading position (the two electrons are loaded in a time much shorter relative to 100 µs). Each vertical line corresponds to a single-shot measurement. The cross-talk between V_L and the QPC is numerically compensated for clarity. **(bottom right)** Same measurement performed only 100 µs after the loading of the two electrons (initialization in a triplet state).

The result of this experiment is presented on Fig. 4.6. The left graph corresponds to the preparation in a singlet state ($t_{wait} = 20$ ms) and the right graph to a triplet preparation ($t_{wait} = 0.1$ ms). On the x axis is varied the V_L voltage used for the measurement position. The blue (resp. orange) color corresponds to two (resp. one) electrons present in the dot.

For δV_L between 2 mV and 6 mV, both singlet and triplet chemical potentials are below the Fermi level and the two electrons remain in the dot. For δV_L between 0 mV and 2 mV, the singlet chemical potential is still below the Fermi level but the triplet one is above (see Fig. 1.5). An electron tunnels off the dot only in the triplet initialization case (and a new one tunnels into the dot after a short time, forming a singlet state). In this position, energy-selective readout is performed. For $\delta V_L < 0$ mV both the singlet and triplet chemical potentials are above the Fermi level and in any case an electron tunnels off the dot (see Fig. 1.6). A tunnel rate difference is observed between the singlet and triplet cases, allowing for tunnel-rate readout in this position.

For the following experiments we have opted for energy-selective readout, and the system

is thus set to $\delta V_L = 1\,\mathrm{mV}$. This measurement point is indicated as point M on Fig. 4.7. We can now measure the triplet to singlet relaxation as follows:

- Two electrons are loaded into the dot (point L_2 on Fig. 4.7).
- It is then waited a time t_{wait} which is varied between 0.1 ms and 20 ms.
- The system is finally pulsed to point M (see Fig. 4.7) to readout the spin state.

The result of this experiment is shown on the top right plot of Fig. 4.7. The exponential decay depicting the relaxation of the triplet states into the singlet can clearly be seen, and the visibility of the measurement is slightly better than 80 %. The limitation of the visibility can have two different sources. First, the initialization can be imperfect if the tunnel-rate difference between singlet and triplets is not large enough. In that case, there is a non-zero probability to initialize the two electrons in a singlet state and the probability to detect a triplet for short t_{wait} is reduced. The second limitation arises from imperfections of the measurement. Some tunneling events observed during the energy-selective readout can occur too fast compared to the measurement bandwidth ($\sim 1\,\mathrm{kHz}$ in our case) and are not detected. These missed events also lower the signal. Alternately, some thermally-activated tunneling events can be falsely attributed to triplet tunneling. These events result in a residual triplet probability measured even after a long relaxation time.

Now that spin readout has been implemented, the question is to know whether the spin is affected or not when the system is switched between a position coupled to the reservoir and a metastable position. To that purpose, a new experiment is realized:

- Two electrons are loaded into the dot (point L_2 on Fig. 4.7).
- It is waited a time t_{wait} which is varied between 0.1 ms and 20 ms.
- The system is then pulsed to the metastable position and this position is held for 100 µs.
- The system is finally set to the readout position (point M on Fig. 4.7).

If the spin relaxation signal remains unchanged, that would be a good indication that the transition between the coupled and the isolated metastable position is not detrimental for the spin.

Two different metastable positions have been tested. For the first one, labeled A_{20} on the stability diagram of Fig. 4.7, the signal obtained is almost identical compared to the previous case. For the second position however (labeled A_{11} on the figure), an exponential decay can still be seen but the measurement visibility is significantly reduced. This visibility reduction can be explained by hyperfine mixing. When the two electrons are separated, the $|S\rangle$ and $|T_0\rangle$ states are degenerate (the degeneracy with $|T_+\rangle$ and $|T_-\rangle$ is lifted by a 100 mT field in this experiment). Each electron experiences a different effective magnetic field due to the different nuclear environment (see section 1.4.3) that will induce a randomization of the spin phases. As a result, if the spin state was initially in $|S\rangle$ or $|T_0\rangle$, one will obtain after recombination of the two electrons a statistical mixture of these two states. In the end, the measurement will only be sensitive to the $|T_+\rangle$ and $|T_-\rangle$ contributions. If the three triplets states are equally populated at the beginning of the experiment, a complete

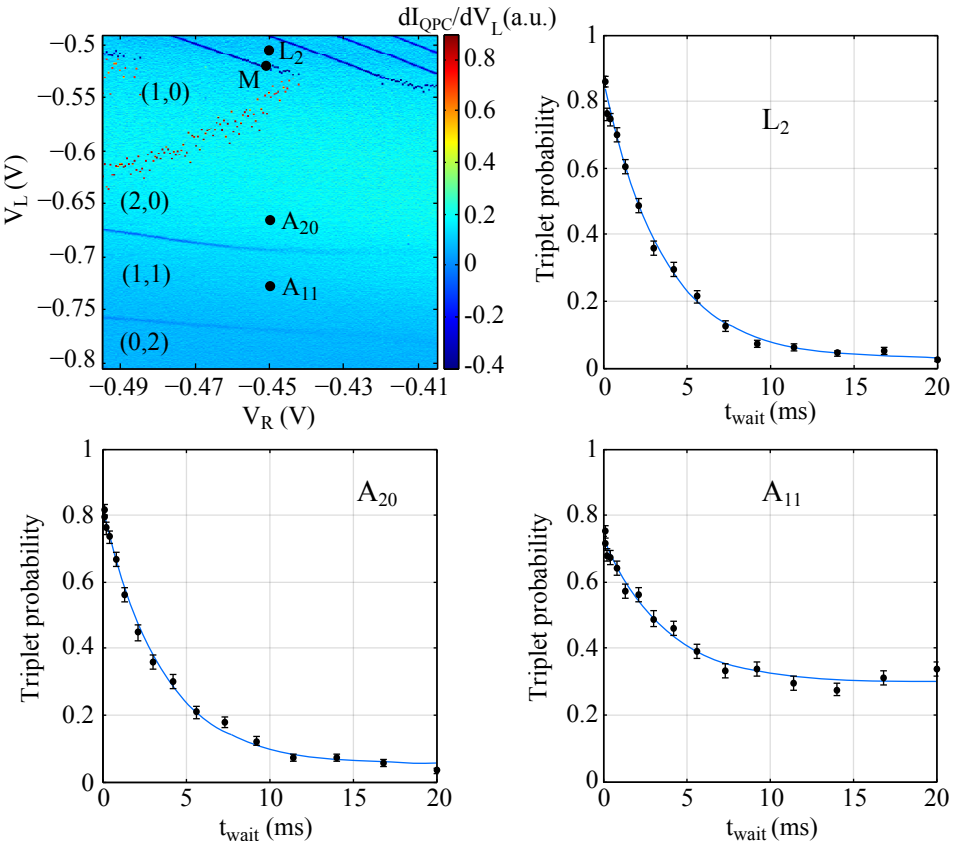

Figure 4.7: Influence of large gate voltage variations on triplet to singlet relaxation measurements. **(top left)** stability diagram of the system. Two electrons are loaded in point L_2. Load time is much shorter compared to 100 µs. The t_{wait} waiting is done in this position. Energy-selective readout is achieved by switching to point M within 1 µs. **(top right)** Triplet to singlet relaxation curve. Each data point is the triplet probability deduced after repetition of 500 single-shot measurements. The system is directly moved from L_2 to point M. The data is fitted with an exponential decay of $82 \pm 3\%$ visibility and 3.55 ± 0.4 ms relaxation time T_1. **(bottom left)** Similar measurement with the system pulsed for 100 µs to point A_{20} before moving to the measurement position. The fit gives a $76 \pm 3\%$ visibility and $T_1 = 3.45 \pm 0.4$ ms. **(bottom right)** Similar measurement with the system moved to point A_{11} for 100 µs before going to the measurement position. The exponential decay obtained has a $38 \pm 4\%$ visibility and 3.6 ± 1 ms for T_1. All the data were obtained under application of a 100 mT magnetic field in the sample plane.

$|S\rangle - |T_0\rangle$ mixing is expected to lead to a two-thirds reduction of the measurement visibility. This is in qualitative agreement with the measurement.

As a conclusion, the ability to readout the spin state of the system is not affected by transitions between the (2,0) metastable position and the position coupled to the reservoir. A reduction of the signal visibility is observed when electrons are separated in the (1,1) charge state, but this is explained by the mixing of the $|S\rangle$ and $|T_0\rangle$ states. Only a distinction between the parallel ($|T_+\rangle$ and $|T_-\rangle$) and antiparallel ($|S\rangle$ and $|T_0\rangle$) spin states can be done in this case. A complementary study on how is affected the spin relaxation process in the (2,0) metastable configuration can be found in appendix D. Eventually, spin state measurement of the metastable system can be achieved simply by re-establishing the coupling to the reservoir and using then any of the standard readout techniques. Another interesting option could be to keep the system in the metastable configuration all along the measurement procedure by implementing a spin blockade readout. This is explored in appendix E.

4.4 Coherent spin manipulations in a metastable double quantum dot

In the previous section it has been shown that the conventional spin measurement techniques are still applicable to readout the electrons spin state in a metastable quantum dot. It has also been demonstrated that single-shot spin measurements are achievable. In addition as far as relaxation is concerned, no unexpected detrimental effect for the spin states has been observed in the metastable position. However, the influence on the spin coherence has not been probed yet.

Coherent spin manipulations in usual double dot systems (coupled to a reservoir) require the ability to rapidly vary the double dot detuning in order to modulate the exchange interaction between the electrons [Pet05]. In the case of the metastable double dot we have seen that both the detuning ε and the interdot tunnel coupling t_c can easily be varied. Therefore, the modulation of the electrons exchange interaction could be achieved by directly changing t_c, as initially proposed by Loss and DiVincenzo [Los98]. We will see that in such a configuration the sensitivity to charge noise is reduced.

4.4.1 Mapping of the spin mixing regions

We have seen in section 4.3 that spin mixing occurred between the $|S_{11}\rangle$ and $|T^0_{11}\rangle$ states because of the hyperfine interaction. In a first experiment, we will try to quantify how fast this phase randomization occurs, following the method developed by Petta *et al.* [Pet05]. The employed procedure is as follows:

- The system is initialized in a (2,0) singlet state. It is prepared by loading two electrons in the dot (point L_2, see top diagram of Fig. 4.8) and waiting long enough to be sure that the system has relaxed to the singlet ground state. The waiting time is 20 ms in our case[1].

1 This is relatively long but could easily be improved by loading the electrons in a position where the dot is more strongly coupled to the reservoirs for instance.

- The V_L voltage is then changed within a microsecond to reach the metastable position, making sure to remain in the (2,0) configuration (point A_{20} on Fig. 4.8).
- From this position, a nanosecond pulse is added (reaching point A_{11} on Fig. 4.8) to separate the two electrons during a controlled time τ_s. The passage between the two positions is done quickly ($< 1\,\text{ns}$) compared to the nuclear mixing time ($\sim h/(g^*\mu_B \Delta B_z) \sim 40\,\text{ns}$), to be certain that a (1,1) singlet is obtained.
- Finally energy-selective spin readout is performed by setting the system back to the the position M on Fig. 4.7).

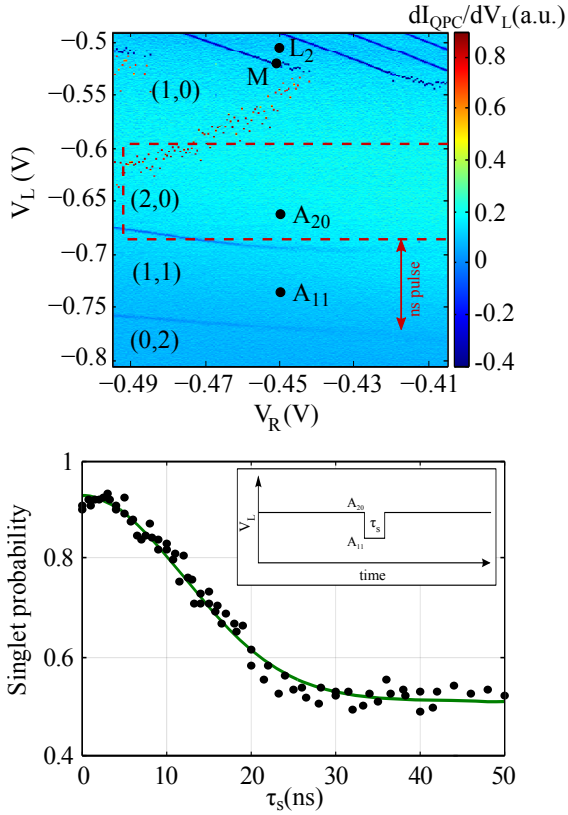

Figure 4.8: (top) Stability diagram of the metastable double dot initialized with two electrons. **(bottom)** Evolution of the singlet probability as a function of the time spent with the two electrons separated (point A_{11} of the stability diagram). The data are fitted with a Gaussian decay, giving a characteristic time $T_2^* = 17\,\text{ns}$. Data obtained under application of a 100 mT magnetic field in the sample plane. (inset) Schematics of the pulse sequence played on gate V_L.

By varying the separation time τ_s, one can then measure how long the electrons can be spatially separated before losing their phase coherence. The probability to measure a singlet as a function of τ_s is shown on the bottom plot of Fig. 4.8. A Gaussian decay is observed. For the shortest times, the singlet probability is close to 1, limited by the measurement fidelity. For longer times, it saturates close to 0.5, meaning that the phase has been lost and one measures either a $|S\rangle$ or a $|T_0\rangle$ state with equal probability. The fit

gives a characteristic time of 17 ns, consistent with previous measurements realized on a double dot coupled to the reservoir [Pet05].

This mixing occurs because the relevant energy in the (1,1) configuration is no longer the exchange energy J but the Zeeman energy relative to the random effective field ΔB_z induced by the hyperfine interaction ($J \ll g^* \mu_B \Delta B_z$). We recall that far in the (1,1) region, the residual exchange energy can be estimated by

$$J \sim \frac{4t_c^2}{U} \tag{4.3}$$

where t_c stands for the interdot tunnel coupling and U is the on-site charging energy. In principle, this could be made arbitrarily large by increasing t_c, so that it finally overcomes the nuclear field gradient ($J \gg g^* \mu_B \Delta B_z$) and prevents any mixing of the separated singlet. For a charging energy on the order of a few meV and $\Delta B_z \sim 0 - 5\,\mathrm{mT}$, it yields to a tunnel coupling that must be large compared to $\sim 1\,\mathrm{GHz}$.

In order to find out if such a regime can be achieved here, a mapping of the singlet-triplet mixing as a function of gate voltages has been realized.

- First, two electrons are injected in the loading dot and initialized in the singlet ground state by waiting longer than the relaxation time.
- Second, the electrons are brought to the metastable position with the use of a microsecond V_L shift, as previously explained. The reached position is varied to explore different positions on the stability diagram, remaining in the (2,0) region (see red dotted rectangle on Fig. 4.8).
- Third, from the reached position, a fast pulse (~ 1 ns rise time) is applied on gate V_L for 50 ns, with an amplitude on the sample estimated to 80 mV. This pulse is used to bring the system in the (1,1) charge configuration and probe the spin mixing (see red arrow on Fig. 4.8).
- Finally, the system is set to the point M (see Fig. 4.9) to perform energy-selective spin readout.

The part of the stability diagram that is explored during the 50 ns pulse has been reproduced at the top diagram of Fig. 4.9. The spin measurement results are presented on the middle panel of Fig. 4.9. Each data point represents the average triplet probability over 200 single-shot readouts.

On the top right corner of this diagram, the system remains in the (2,0) configuration during the 50 ns pulse. As can be expected, no mixing occurs in this case and a singlet state is measured almost every time. On the center of the diagram, the (1,1) charge configuration is reached during the nanosecond pulse. In this case, two different regimes are observed. For the most negative V_R values (left part of the diagram), spin mixing arises during the 50 ns pulse and is characterized by an equal probability of singlet and triplet afterwards. This is consistent with the fact that the interdot tunnel coupling t_c is weak for relatively negative V_R values, resulting in $J \ll g^* \mu_B \Delta B_z$. On the contrary for less negative V_R (right part of the diagram), no mixing is observed anymore (the probability to

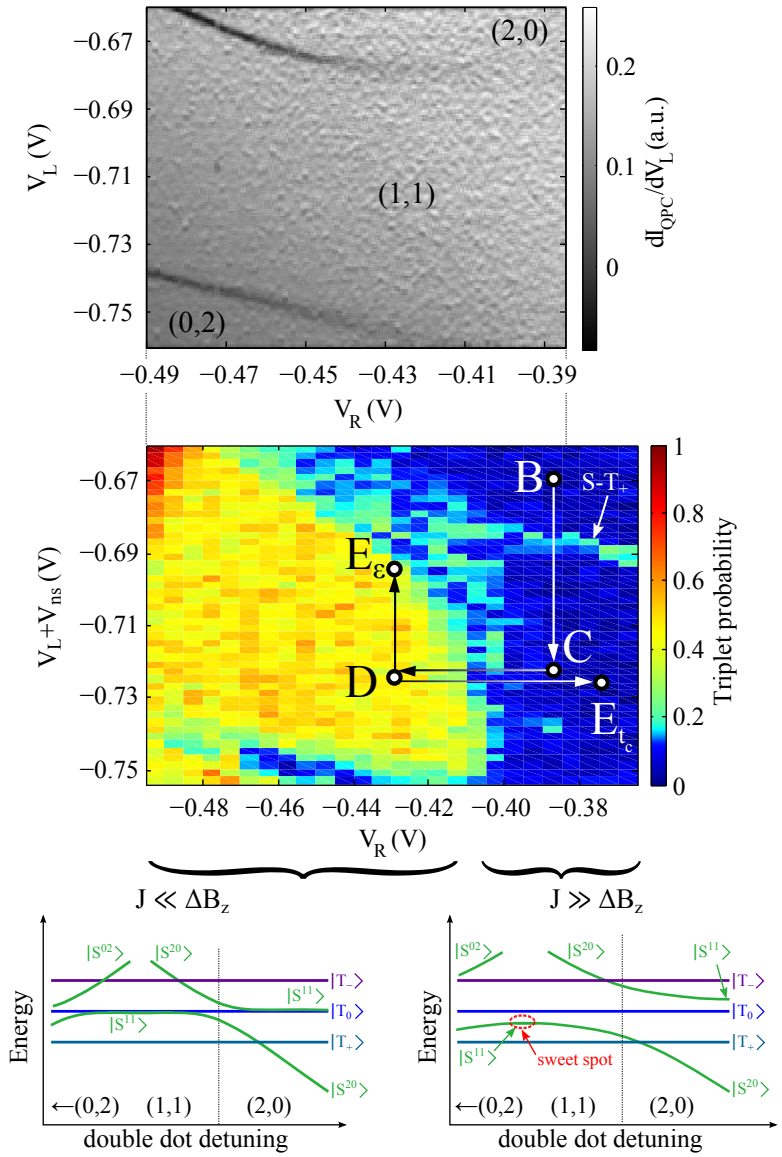

Figure 4.9: **(top)** close-up on the part of the stability diagram that is explored with the 50 ns pulse (see main text). **(middle)** Spin mixing mapping of the system. A singlet state is pumped to a varying position in the (2,0) metastable region with the use of a 1 µs pulse. A 3 V amplitude pulse (on the AWG) is added to project the system for 50 ns into the (1,1) region, before moving back to point M for spin measurement. A matching with the stability diagram (top plot) permits to estimate the effective amplitude of the nanosecond pulse on the sample to $V_{ns} \sim 80$ mV. Data obtained under application of a 100 mT magnetic field along the sample plane. **(bottom)** Schematics of the evolution of the energy levels of a double dot as a function of detuning. On the left plot, tunnel coupling is relatively low, implying degeneracy of the $|T_0\rangle$ and $|S\rangle$ states in the (1,1) region. On the right plot, tunnel coupling is stronger and allows to lift this degeneracy.

detect a singlet after the pulse is almost 1). In this position, t_c is sufficiently large so that $J \gg g^* \mu_B \Delta B_z$. This ensures that $|S^{11}\rangle$ and $|T_0^{11}\rangle$ remain good eigenstates of the system, therefore preventing dephasing of the separated singlet.

In this $J \gg g^* \mu_B \Delta B_z$ region, it is possible to distinguish a line where spin mixing still happens. This line is attributed to the crossing of the $|S\rangle$ and $|T_+\rangle$ states (see inset of Fig. 4.10). Indeed, we have seen that a coupling between the $|S^{11}\rangle$ and $|T_+^{11}\rangle$ states emerges because of the in-plane components of the hyperfine induced magnetic field gradient ($\Delta B_{x,y}$ terms, see section 1.4.3). Due to the relatively small magnitude of this coupling, the resulting $|S\rangle$-$|T_+\rangle$ mixing will be relevant only close to the degeneracy of these two states.

The crossing position depends on both the interdot tunnel coupling and the external magnetic field applied. The lower is the magnetic field, the smaller is the Zeeman splitting E_z between the $|T_+\rangle$ and $|T_0\rangle$ states and the deeper into the (1,1) region will be the $|S\rangle$-$|T_+\rangle$ crossing. In order to confirm our interpretation, the position of this line with respect to the magnetic field has been studied. A slice of the spin mixing mapping (at $V_R = -0.37\,\mathrm{V}$) is reproduced for different magnetic field values. The result of this experiment is presented on the main plot of Fig. 4.10. A clear shift in the crossing position is observed, consistently with our interpretation.

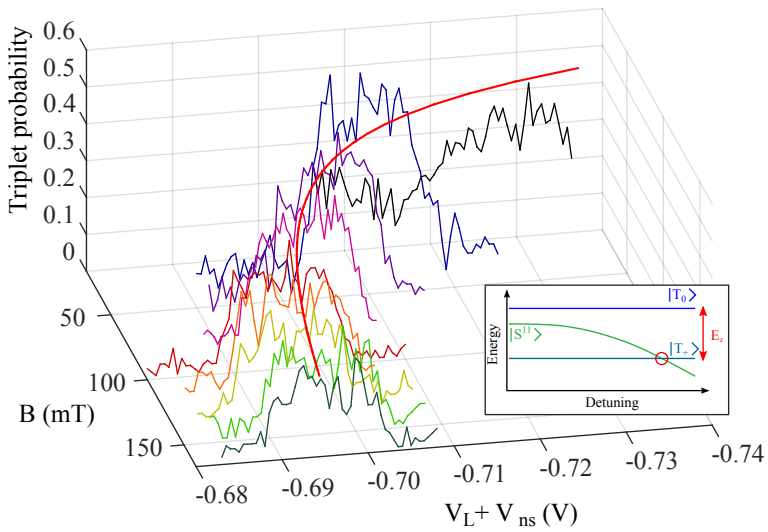

Figure 4.10: (main) Evolution of the $|S\rangle - |T_+\rangle$ crossing with magnetic field. The data has been obtained at $V_R = -0.37\,\mathrm{V}$. Each data point is the average over 100 single-shot measurements. The red line depicts the trend of the observed peaks position with magnetic field. **(inset)** Energy diagram showing the position of the $|S\rangle - |T_+\rangle$ crossing. This position depends on the Zeeman shift E_z of the $|T_+\rangle$ level.

It can be noted that the magnitude of the observed peaks is decaying when the magnetic field is increased. A possible interpretation is as follows. In a general way, the singlet state at the $|S\rangle$-$|T_+\rangle$ crossing can be expressed as a linear combination of $|S^{11}\rangle$ and $|S^{20}\rangle$. The larger is B, the closer to the (2,0) region is occurring the crossing and the smaller will be the $|S^{11}\rangle$ weight on the singlet branch. As a consequence the hyperfine induced coupling

will be smaller (since it couples the $|S^{11}\rangle$ and $|T_+^{11}\rangle$ states).

4.4.2 Coherent oscillations on a sweet spot

In the previous section, we have identified a region of strong interdot tunnel coupling where $J \gg g^*\mu_B \Delta B_z$. What is of particular interest in this configuration is the presence of a specific point where J has a finite value and where $\frac{dJ}{d\varepsilon}$ cancels out. This so-called sweet spot is indicated on the bottom right energy diagram of Fig. 4.9. So far, exchange oscillations in double quantum dots have been studied on a wide range of the detuning parameter ε (see [Dia13]). It has been shown that the observed coherence time (T_2^*) is limited by noise in J and is proportional to $(dJ/d\varepsilon)^{-1}$. In that context, such a sweet spot can be of direct interest to improve the coherence time of the system. In the following, we will adapt the method developed by Petta *et al.* [Pet05] to our system in order to quantify this effect.

- The first step consists in the initialization in the (2,0) singlet state. This is done similarly to the previous experiments by loading two electrons in the dot and waiting (20 ms) for the system to relax in the ground state.
- After this relaxation process, the gate voltages of the dot are shifted within a microsecond to reach the metastable position, stopping just before the $|S\rangle$-$|T_+\rangle$ crossing (up to point B on Fig. 4.9).
- Then the $|S\rangle$-$|T_+\rangle$ degeneracy point must be crossed fast enough to be non-adiabatic relative to the $|S\rangle$-$|T_+\rangle$ coupling but remaining adiabatic relative to the tunnel coupling. This is achieved here by applying a nanosecond pulse on gate V_L to reach the (1,1) region (moving from B to C on the mapping of Fig. 4.9)[1].
- The next step consists in sweeping the system slowly as compared to the nuclear mixing time up to a region where $J \ll g^*\mu_B \Delta B_z$. This allows the adiabatic transformation of the singlet into the $|\uparrow\downarrow\rangle$ state. In our case, in order to reach a region where $J \ll g^*\mu_B \Delta B_z$ (going from point C to D on Fig. 4.9), one has to reduce the tunnel coupling. The voltage on V_R is thus swept to more negative values within 100 ns to 120 ns (see Fig. 4.11).
- Once initialized in the $|\uparrow\downarrow\rangle$ state, the application of a finite exchange J for a time τ_E rotates the spin state around the z-axis of the Bloch sphere (see Fig. 4.11), in the plane containing $|\uparrow\downarrow\rangle$ and $|\downarrow\uparrow\rangle$, by an angle $\phi = J\tau_E/\hbar$. Here, pulsing the exchange J to stronger values can be achieved in principle by two different ways (see Fig. 4.11). The first one, comparable to what is usually done in standard double dots, consists in pulsing the system along the detuning (ε) direction ($\sim V_L$). For the second way, the detuning remains constant and the pulse is applied on the interdot tunnel coupling (t_c) direction ($\sim V_R$). The two methods have been tried and will be discussed in the following.

1 Since this is done in the region where $J \gg g^*\mu_B \Delta B_z$, the tunnel coupling is much larger than ~ 1 GHz, and it is reasonable to consider the gate movement adiabatic with respect to tunnel coupling. On the contrary, an estimate of the $|S\rangle - |T_+\rangle$ coupling is given by and $\langle S^{11}| H_{hf} |T_+^{11}\rangle \sim g^*\mu_B \frac{\Delta B_x - i\Delta B_y}{\sqrt{2}}$, leading to a few tens of MHz coupling. The voltage pulse should therefore be non-adiabatic relative to the $|S\rangle - |T_+\rangle$ coupling.

- Finally, the mirror sequence is applied to bring back the system in the (2,0) region (point B), and the system is then set to the measurement position where the usual single-shot energy-selective readout is performed.

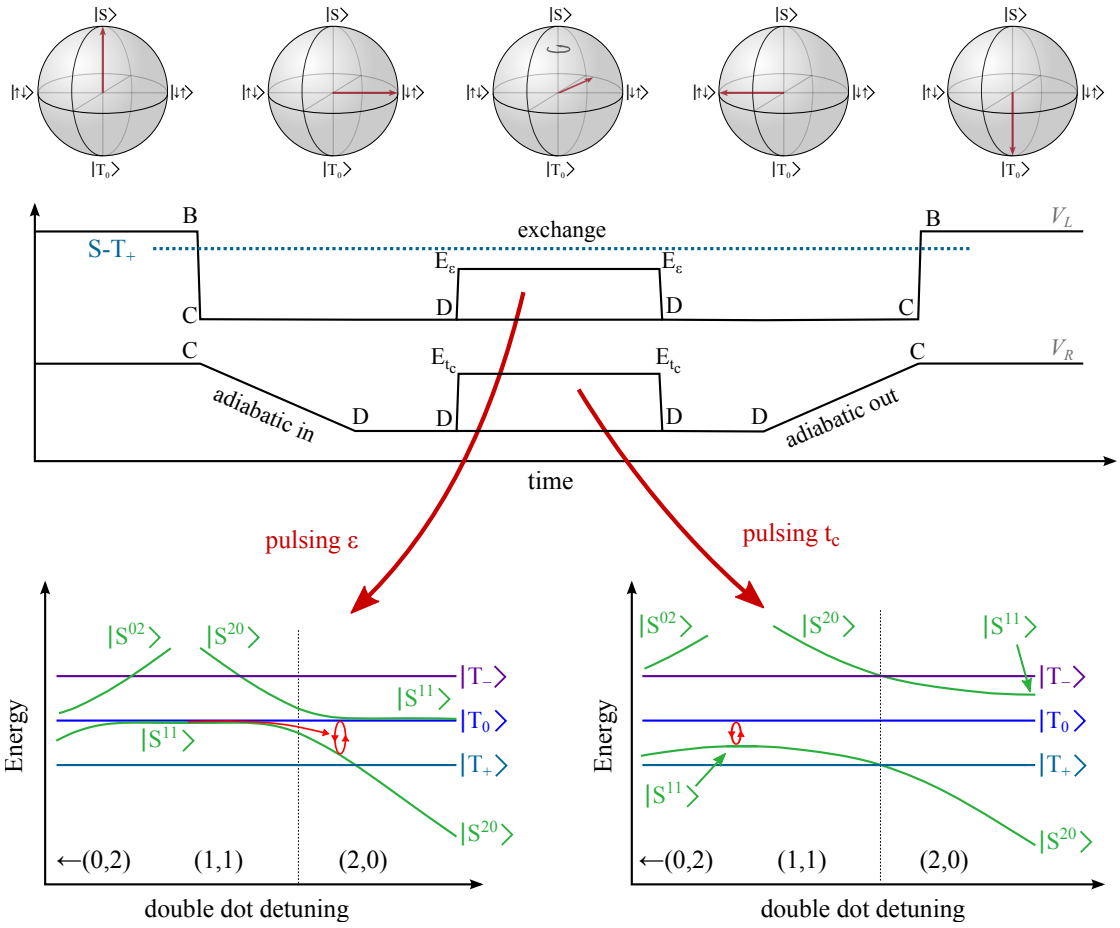

Figure 4.11: Illustration of the two possible exchange pulses. **(top)** Schematics of the voltage sequence used on gates V_L and V_R. The exchange pulse can be applied either on V_L or V_R in order to reach position E_ε or E_{t_c} respectively (see Fig. 4.9). The evolution of the spin state is depicted on a Bloch sphere for the different steps. **(bottom left)** Energy diagram showing the effect of a pulse on V_L. The exchange interaction is increased by moving along the ε direction, and the coherent oscillations are done in a position where $\frac{dJ}{d\varepsilon}$ is large. The system will be highly sensitive to noise fluctuations of ε. **(bottom right)** Energy diagram showing the effect of a pulse on V_R. The exchange interaction is increased by changing the interdot tunnel coupling. It is possible to stay in a position where $\frac{dJ}{d\varepsilon} = 0$, protecting the system against the detuning noise.

The two different methods to apply the exchange pulse are now investigated. First the exchange pulse is applied on V_L, *i.e.* on the detuning ε of the double dot (see top panel of Fig. 4.12). The triplet probability is measured for different τ_E values and Rabi oscillations between singlet and triplet are observed (lower panel of Fig. 4.12). For larger exchange

pulse amplitudes (*i.e.* moving point E_ε to less negative values), the oscillations frequency slightly increases as expected. The associated T_2^* is in each case around 40 ns. However, only a really small number of oscillations are visible. Following [Dia13], we can define the quality of the oscillations (number of coherent oscillations observed) by $Q \equiv JT_2^*/2\pi\hbar$ which is between 1.2 and 1.5 in this case. When trying to achieve larger exchange pulses, the signal was significantly worsened and could not be exploited (curves not shown here).

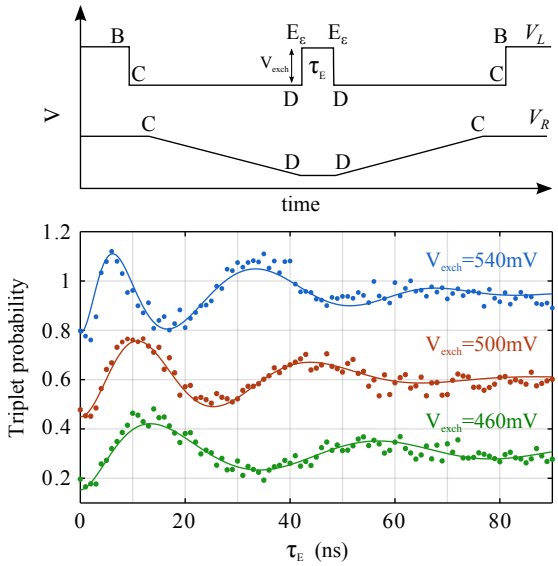

Figure 4.12: Rabi oscillations between $|\uparrow\downarrow\rangle$ and $|\downarrow\uparrow\rangle$ with an exchange pulse along the detuning direction. **(top)** Description of the pulse sequence applied on gates V_L and V_R. Switching between position B and C is done within 1 ns to ensure non-adiabaticity through the $|S\rangle - |T_+\rangle$ crossing. Ramp time τ_A between C and D is 100 ns. **(bottom)** Evolution of the measured triplet probability as a function of the exchange pulse duration τ_E. Each data point is the average over 400 single-shot measurements. Characteristic decay times are close to 40 ns for each curve. Curves are offset for clarity.

As we explained the limitation of the coherence time is attributed to the influence of electrical noise. Small changes in the electrostatic environment can slightly displace the system along the detuning axis. These changes induce fluctuations of the Rabi frequency since J is dependent on ε. The larger $\frac{dJ}{d\varepsilon}$, the larger the J fluctuations (for a constant noise in ε) and so the faster the disappearance of the signal.

We consider now the application of the exchange pulse on V_R, *i.e.* on the interdot tunnel coupling t_c of the double dot. It should allow us to take advantage of the sweet spot in order to cancel the contribution of detuning noise[1]. The result of this experiment is shown on Fig. 4.13.

1 The system is though still sensitive to the V_R voltage noise (tuning the interdot tunnel coupling), since $\frac{dJ}{dt_c} \neq 0$.

Contrary to the previous case, a larger frequency and coherence time can be obtained. Q is linearly increasing from 2 to more than 12 as the exchange pulse amplitude is increased. An almost linear dependence of the Rabi frequency with the exchange pulse amplitude is observed. This suggests that dJ/dV_R is constant in the studied range. Regarding the dephasing time T_2^*, it seems that it is not affected by a change in the exchange pulse amplitude, and remains between 60 and 80 ns in all the experiments. This is consistent with a T_2^* dependence in $(dJ/dV_R)^{-1}$. In principle, it should be possible to keep on increasing the pulse amplitude without observing a degradation of T_2^* as long as the $J(V_R)$ remains linear.

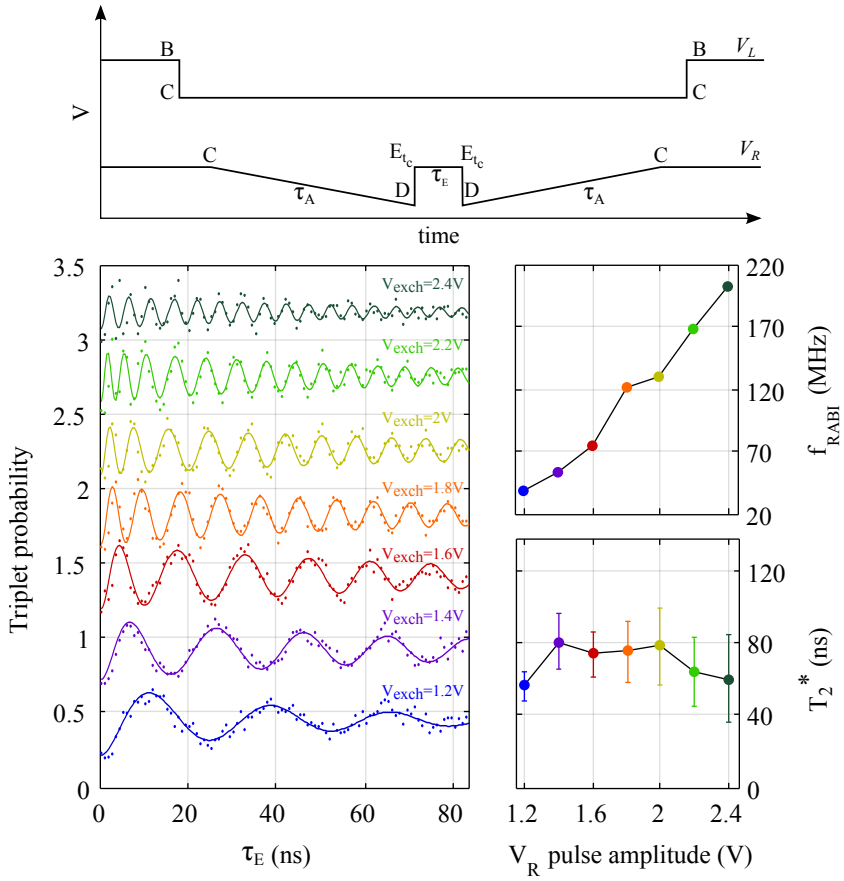

Figure 4.13: Rabi oscillations between $|\uparrow\downarrow\rangle$ and $|\downarrow\uparrow\rangle$ with an exchange pulse along the interdot tunnel coupling direction t_c. **(top)** Description of the pulse sequence applied on gates V_L and V_R. Switching between position B and C is done within 1 ns to ensure non-adiabaticity through the $|S\rangle - |T_+\rangle$ crossing. Ramp time τ_A between position C and D is 125 ns. **(bottom)** Rabi oscillations obtained for different amplitudes of the exchange pulse. Curves are offset for clarity. Each data point is the average over 200 single-shot measurements. The evolution of the Rabi frequency and the characteristic decay time as a function of the exchange pulse amplitude are summarized on the two subplots on the right.

In order to further characterize the influence of this sweet spot on the charge noise sensitivity, an additional experiment has been done. The idea is to perform coherent oscillations in a similar way as the previous experiment but with the system shifted away from the sweet spot. The experimental protocol consists in the following: the exchange pulse is applied on the gate V_R with a constant amplitude of 1.6 V. The resulting Rabi oscillations are recorded for different detuning values. In other words, the exchange pulse sequence is done at different V_L voltages (shifting the position of points C, D, and E_{t_c} along the vertical direction on the mapping of Fig. 4.9). The expected dependence of J with ε is empirically found to be exponential [Dia13; Pet05]. As the position of the exchange point E_{t_c} is progressively shifted toward higher ε values (closer to the (1,1)-(2,0) degeneracy), J (and consequently the oscillation frequency) should exponentially increase. However, this also raises $dJ/d\varepsilon$ and the observed coherence time should fall.

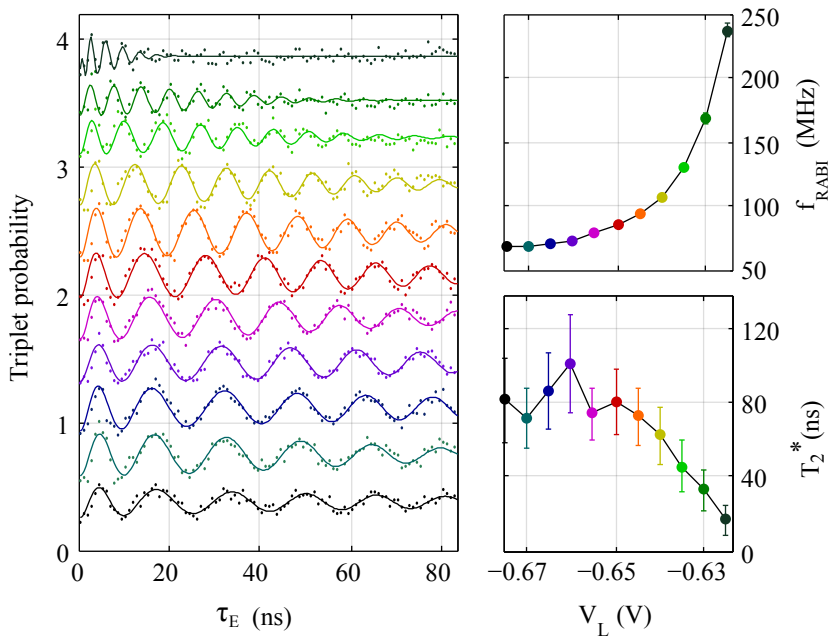

Figure 4.14: Rabi oscillations between $|\uparrow\downarrow\rangle$ and $|\downarrow\uparrow\rangle$ with an exchange pulse along t_c at different ε values. Curves are offset for clarity. The pulse sequence is similar to the one used on Fig. 4.13 (exchange pulse applied on V_R only). The amplitude of the exchange pulse is 1.6 V for each curve. The V_L value from which the pulse sequence is run is varied between the different curves. This allows to move the exchange position E_{t_c} along the detuning axis. Each data point is the average over 200 single-shot measurements. The evolution of the Rabi frequency and the characteristic decay time as a function of the base position V_L value are summarized on the two subplots on the right.

The results of this experiment are presented on Fig. 4.14. As the system is moved away from the sweet spot (less negative V_L values), the oscillation frequency is increasing. The variation of the Rabi frequency with V_L is consistent with the expected exponential dependence of J with detuning. This confirms that the further away from the sweet spot, the larger $\frac{dJ}{d\varepsilon}$. As can be seen on the bottom right panel of the figure, this results in a

significant drop of T_2^* as $\frac{dJ}{d\varepsilon}$ increases.

In summary, it has been shown that coherent spin manipulations can be performed on metastable double dots. This position is directly compatible with a SAW-assisted electron transfer. The impact that might have a SAW burst on spin manipulations and coherence is studied in appendix F. In addition, thanks to the greater tuning possibilities that the system offers, and especially the ability to vary the interdot tunnel coupling independently of the detuning over many orders of magnitude, spin manipulations can be achieved on a sweet spot with respect to detuning noise. This noise source suppression leads to an improvement in dephasing time and in the number of visible coherent oscillations.

CHAPTER 5

Transfer of individual electron spins

5.1 Introduction

In this chapter, we present the first attempts aiming at probing spin conservation during SAW-assisted transfer. As a first step, the objective is only to probe the spin magnetization conservation. For that purpose, two different options have been investigated.

First, the transfer of a two-electron spin state has been considered. The major advantage of working with two-electron spins consists of a much easier spin readout, facilitated by the large energy difference between the singlet and triplet states even at low magnetic field. However, it requires beforehand the adaptation of the transfer procedure in order to work with two electrons instead of one.

The second option that has been explored is the transfer of a single electron spin state. On that case, transfer is already well controlled and straightforward, but spin measurement is more complicated to implement. The application of a large magnetic field is necessary to induce a sufficient energy difference between the spin states and perform energy-selective spin readout (see section 1.2.3).

5.2 Two-electron spin state transfer

We start presenting the results obtained working with two-electron spin states. In the first place, we concentrate on the adaptation of the transfer procedure to the two-electron case. The successive steps of the transfer sequence used are detailed, and the differences relative to the single-electron case are examined. We then show preliminary experiments aiming at calibrating the spin initialization and readout. Finally, the results of the spin transfer experiment are presented and discussed.

5.2.1 Two-electron transfer

The transfer procedure used to ensure two-electron transfer is very similar to the one employed for the single-electron case.

- The first step consists in a reset of the system. The two quantum dots are completely emptied by maintaining them for a sufficient time (a few milliseconds are usually enough) in the zero-electron region of the stability diagrams (see points R and R' on the stability diagrams of Fig. 5.1).

- Two electrons are then loaded into the injection dot (point L_2 on Fig. 5.1). At the same time, the reception dot is set to an intermediate metastable position (point I') making sure that the dot remains empty.
- Next, the injection dot is brought to an intermediate metastable position (point I) within a microsecond. It has been shown in section 4.2.3 (see Fig. 4.3) that it is possible to preserve the initial charge of the dot (zero, one or two electrons) during this pulse. As already explained, the system (injection dot, channel, reception dot) is completely isolated from the electron reservoirs at this step. No electron can be added to it, and no electron can exit on the experiment timescale. This position is held for a few milliseconds to perform a charge measurement on each quantum dot.
- Both dots are then pulsed for a short time (a few microseconds) to the position used for the electron transfer (points T and T'). During this pulse, the SAW burst is applied for a controlled duration τ_{SAW}.
- Finally, once each dot is set back to its intermediate metastable position (point I and I'), the charge states are measured again on both dots and compared to the value before the transfer.

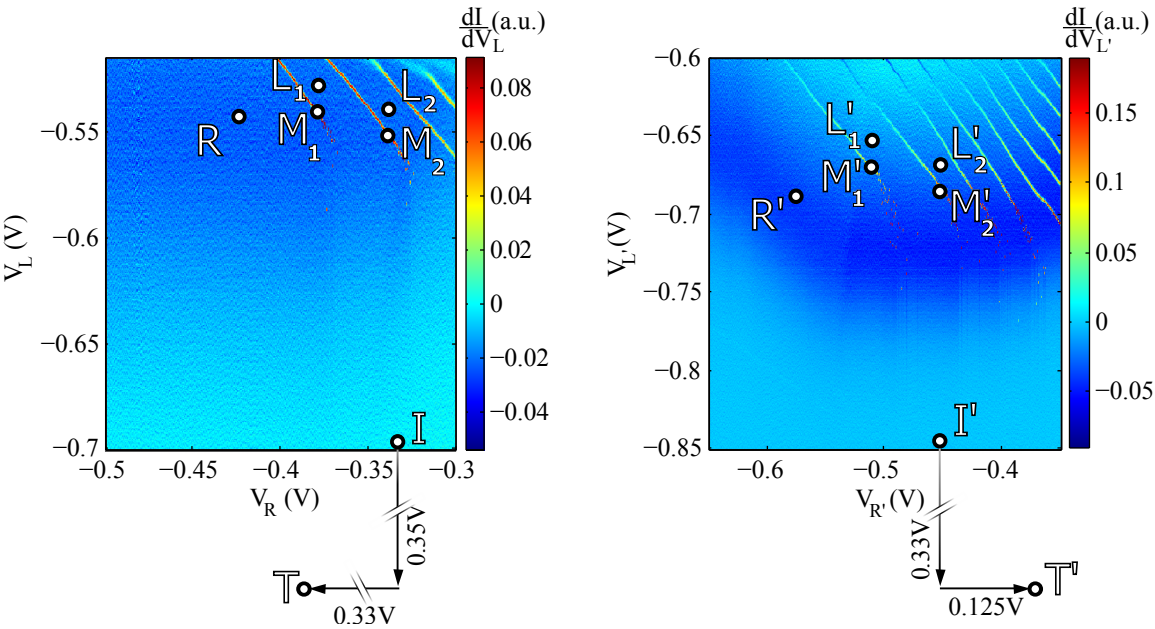

Figure 5.1: Stability diagrams of the injection **(left)** and reception **(right)** quantum dots. Point R indicates the reset position of the source dot. One or two electrons can be loaded in points L_1 and L_2. Spin readout for single and two-electron spin states is performed in points M_1 and M_2 respectively. I refers to the intermediate metastable position used for charge readout before and after the transfer, and T stands for the position used during the transfer. Equivalent positions for the reception dot are indicated on the right diagram.

Examples of the QPC current traces obtained on both dots are presented on Fig. 5.2. The left graph refers to the injection dot and the right one to the reception dot.

The first 10 ms of the measurement are recorded in the intermediate metastable position before the electron transfer. The pulses to the transfer positions as well as the SAW burst are applied at $t = 10$ ms. It results in the large current drops that can be seen on both QPC signals. Finally, the last 10 ms of the measurement are done with the two dots back to the intermediate position.

It can be checked that initially, the injection dot contains two electrons and the reception dot is empty. After the SAW burst, zero, one or the two electrons have left the injection dot. Reciprocally, zero, one or two electrons are recovered in the reception dot.

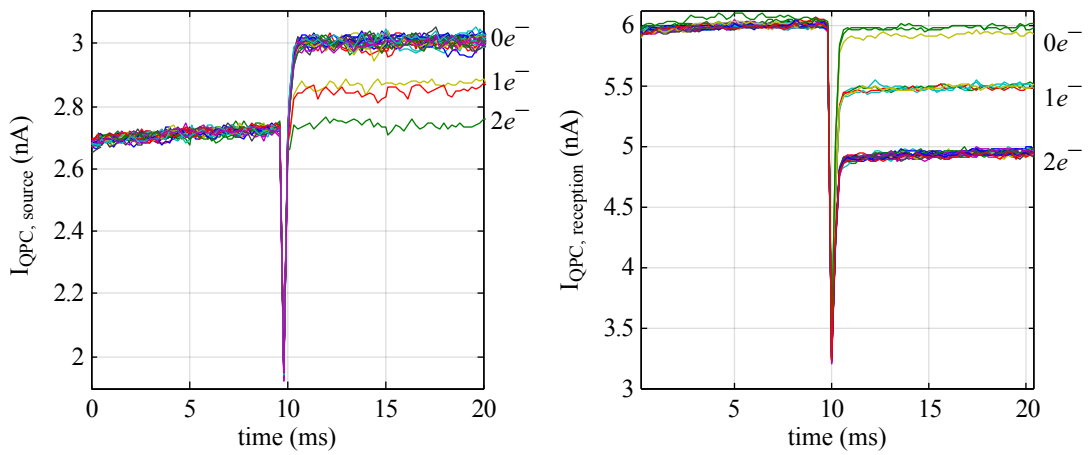

Figure 5.2: Single-shot traces of the QPC current for both dots during two-electron transfer experiments. **(left)** Typical signal obtained for the injection dot. **(right)** Corresponding signal recorded for the reception dot. The SAW burst is applied at $t = 10$ ms. Both dots are set to their intermediate metastable position with two electrons initially prepared on the source dot and zero on the reception dot. The large drop in the current at $t = 10$ ms is due to the microsecond pulse to the transfer position.

In order to quantify the transfer efficiency, we study the correlations between the charge variations of both dots. All the different possible events are labeled $N_{\alpha\beta\gamma\delta}$ where α (resp. β) stands for the number of electrons in the source dot before (resp. after) the transfer and γ (resp. δ) is the equivalent for the reception dot.

By studying the probability of these different types of events as a function of τ_{SAW}, we can obtain some information about the transfer process. The results for the most relevant types of events are summarized on Fig. 5.3.

The probability to send only one electron out of the two ($N_{21\mathrm{XX}}$) is shown as the dotted blue line. It rises rapidly and saturates close to one for short SAW duration (< 150 ns). In most of the cases, this is associated with the arrival of an electron on the reception dot (N_{2101}). The efficiency ($> 96\,\%$) is comparable to the one of the single-electron transfer.

When τ_{SAW} reaches 150 ns, the probability to send a single electron drops and in return, the probability to emit both electrons ($N_{20\mathrm{XX}}$) rises and rapidly reaches 1.

The probability to jointly send and receive the two electrons (N_{2002}) first follows the $N_{20\mathrm{XX}}$ curve, but finally saturates slightly above 80 % before falling back to zero. In return the probability to send both electrons and recover only one of them (N_{2001}) progressively

increases as τ_{SAW} is increased.

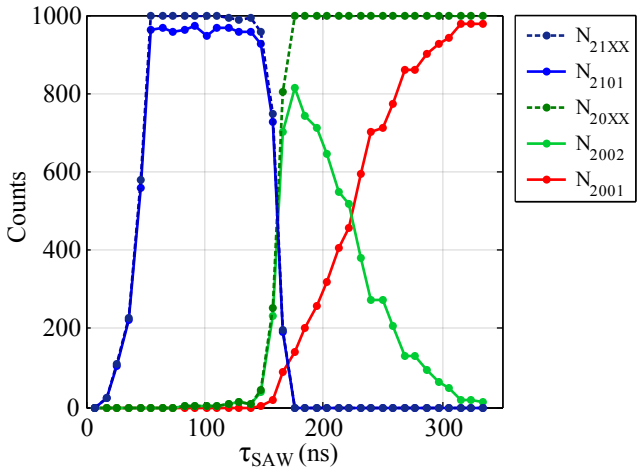

Figure 5.3: Evolution of the transfer events $N_{\alpha\beta\gamma\delta}$ as a function of the SAW duration τ_{SAW}. $N_{\alpha\beta\gamma\delta}$ refers to the counts for the source (reception) dot loaded with α (γ) electrons, ending up with β (δ) electrons after the SAW burst. For each data point, the experiment has been reproduced 1000 times.

This graph is interpreted as follows. When the first electron is transferred, the chemical potential of the system is reduced by the charging energy. Therefore, the remaining electron lies much lower in energy and is thus more difficult to extract. For that reason, there are two different SAW amplitude thresholds corresponding to the extraction of the first and then the second electron. Because of the rather long IDT rise-time, the amplitude of the wave is progressively increasing as the burst duration is extended (see section 3.4). As a result, the SAW amplitude thresholds to transfer the first and then the second electron are successively reached (the first one between 10 ns and 60 ns, and the second between 140 ns and 180 ns). Once the electrons are caught in the reception dot, the SAW excitation can induce the tunneling of an electron to the neighbor reservoir. As a consequence, τ_{SAW} must be precisely set in order to obtain the best efficiency for the two-electron transfer.

In summary, this experiment shows that a rather efficient two-electron transfer is achievable. Nevertheless the two electrons are transferred sequentially in two different moving dots with a separation time on the order of 100 ns between the two transfers.

Such a long separation time can be an issue for the spin of the system. Indeed, for these 100 ns, the two electrons are located in two different dots 4 µm away. This situation is equivalent to the (1,1) charge configuration of a double quantum dot with $J = 0$. We have seen in section 4.4.1 that in such a configuration, the hyperfine interaction induces mixing between $|S\rangle$ and $|T_0\rangle$ within a characteristic time around 17 ns. Therefore, it should no longer be possible to distinguish between these two states after such a transfer. Hopefully, this long separation time should not affect $|T_+\rangle$ or $|T_-\rangle$ (when an external magnetic field is applied to lift the degeneracy between the three triplet states) and consequently a part of the signal should remain after transfer of the electrons.

5.2.2 Calibration of the spin detection

We will now consider the additional tools required to probe the spin conservation during the transfer. The basic principle of the experiment is to prepare a spin state in one quantum dot, transfer the electrons to the other dot and measure whether the spin state has changed or not. It is therefore necessary to be able to prepare a given spin state and measure it.

The initialization scheme is the same as the one presented in section 4.3 for the measurement of two-electron spin relaxation. The tunnel rate to load two electrons in a triplet state is usually much larger than for a singlet state. Therefore, just after the loading of two electrons, there is a high probability for the system to be initialized in one of the triplet states. By waiting a time t_{wait} sufficiently long, the system will relax to the singlet state. It is thus possible by this mean to initialize the injection dot with either a singlet or one of the triplet states (or any mixture of singlet and triplet). This constitutes the initialization step.

For the spin measurement, the quantum dot is coupled to its reservoir in a configuration allowing energy-selective readout, similarly to what has been presented in section 4.3. This measurement techniques enables to differentiate between the system being in the singlet ground state or in one of the excited triplet states.

The measurement of the triplet to singlet relaxation enables to access directly how efficient are both the spin initialization and readout. The successive steps of this experiment are recalled here:

- First, the dot is emptied (point R on Fig. 5.1).
- Two electrons are rapidly loaded ($\sim 1 - 10\,\mu s$) in point L_2.
- A time t_{wait} is waited.
- The system is set to the measurement position (point M) to readout the spin.

This has been done in each dot of the sample. The results of these experiments are presented on Fig. 5.4. The green curve on the left (resp. right) graph is the signal obtained for the injection (resp. reception) dot. The two curves look very similar, with each measurement visibility around 60 % and characteristic times of the spin decay of a few milliseconds.

Because of the similar geometry of each dot and the great similarity between both relaxation signals, it is reasonable to assume that the factors limiting the measurement visibility are the same in each case. Therefore, a similar visibility would be ideally expected for the spin transfer experiment.

Before achieving this spin transfer experiment, an additional calibration measurement can be performed. It consists in checking that the system can be brought to and back from the transfer position without being affected. Indeed, it can be seen on Fig. 5.1 that this implies very large voltage shifts that can significantly affect the shape of the confinement potential. Verifying that this is not affecting the prepared spin state or the readout procedure is therefore a relevant consideration. The sequence of the experiment is the following:

- The dot is emptied (reset to zero electron in point R).
- Two electrons are rapidly loaded ($\sim 1 - 10\,\mu s$) in point L_2.

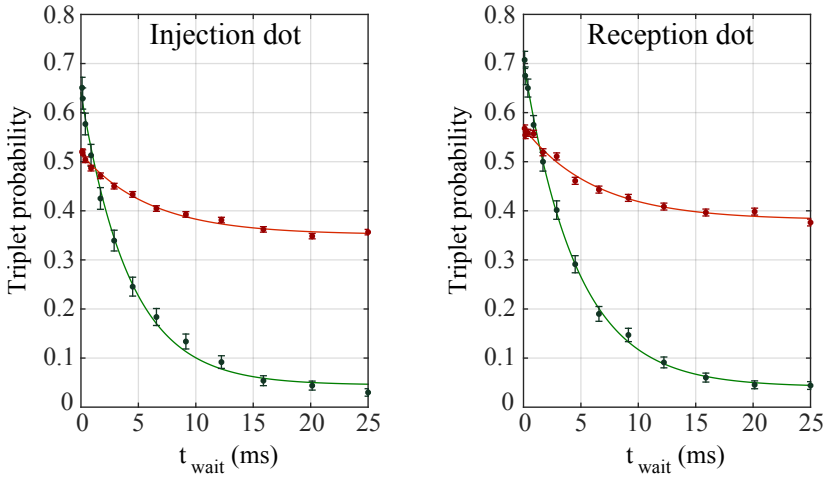

Figure 5.4: Spin relaxation measurements on both injection and reception dots. **(left)** Data corresponding to the injection dot. The green curve is the standard spin relaxation signal. Each data point is the average of 500 single-shot measurements. The data is fitted with an exponential decay with 4.2 ms ± 0.5 ms relaxation time and 59.5 % ± 2.65 % visibility. The red curve is the same measurement with the dot pulsed to its transfer position for 100 µs just before the spin readout. Each data point is the average of 7400 single-shot measurements. It is fitted with an exponential decay of 16.5 % ± 1.1 % contrast and 6 ms ± 1.2 ms relaxation time. **(right)** Equivalent results obtained for the reception dot. The spin relaxation signal (green curve) has 66.2 % ± 1.65 % visibility, with a relaxation time of 4.6 ms ± 0.35 ms. Each data point is the average over 680 repetitions. For the red curve (same measurement with the dot pulsed to its transfer position for 100 µs just before the spin readout), each data point is the average over 4865 repetitions. It is fitted with an exponential decay of 18.8 % ± 1.6 % contrast and 6.2 ms ± 1.6 ms relaxation time.
All these experiments have been done under a 100 mT magnetic field perpendicular to the sample plane (z-direction).

- A time t_{wait} is waited.
- The system is pulsed (∼ 1 µs pulse) to the position used for the electron transfer (point T). This position is hold for 100 µs.
- The dot is finally set to the spin readout position (point M).

This experiment has been done on both dots. The results are shown as the red curves on Fig. 5.4. A large contrast reduction of the spin relaxation curves is observed. This looks similar to the result that has been obtained on Fig. 4.7. The interpretation is therefore that when reaching the transfer position, the two electrons are separated such that hyperfine interaction mixes the $|S\rangle$ and $|T_0\rangle$ spin states.

We now discuss more precisely what should be the impact of this $|S\rangle$-$|T_0\rangle$ mixing on the relaxation curves. We call P_T the probability to detect a triplet state. We assume that

$$P_T = \alpha + v\left(P_{T_0} + P_{T_+} + P_{T_-}\right) \tag{5.1}$$

where P_{T_i} is the probability to have the state $|T_i\rangle$ in the dot, α is the residual background due to thermally activated tunneling and v is the measurement visibility. If we consider the same relaxation time τ for the three triplet states, we can write

$$P_{T_i}(t) = P_{T_i}(0) \exp\left(-\frac{t}{\tau}\right) \tag{5.2}$$

where $P_{T_i}(0)$ is the probability to initially prepare the state $|T_i\rangle$ in the dot. If we do not take into account the $|S\rangle$-$|T_0\rangle$ mixing, this results in

$$P_T(t) = \alpha + v\left(P_{T_0}(0) + P_{T_+}(0) + P_{T_-}(0)\right) \exp\left(-\frac{t}{\tau}\right) \tag{5.3}$$

We then model the spin randomization due to the $|S\rangle$-$|T_0\rangle$ mixing by simply assuming an equal probability for these two states:

$$P_{T_0}^{mix}(t) = P_S^{mix}(t) = \frac{P_{T_0}(t) + P_S(t)}{2} \tag{5.4}$$

where P^{mix} corresponds to the state probability after mixing. We finally end up with

$$P_T^{mix}(t) = \left(\alpha + \frac{v}{2}\right) + v\left(\frac{P_{T_+}(0) + P_{T_-}(0)}{2}\right) \exp\left(-\frac{t}{\tau}\right) \tag{5.5}$$

If we assume that the initial probabilities of the three triplet states are equal, the amplitude of the exponential decay is reduced by a factor 3 between equation 5.3 and 5.5. This is consistent with the order of magnitude of the contrast reduction that is observed in our case.

In summary, we have evaluated through these spin relaxation measurements how well we are able to initialize and measure a two-electron spin state. The contrast of the observed exponential decay is reduced after the large voltage shifts used to bring the system to the transfer position. This is explained by a temporary separation of the electrons allowing the mixing of the $|S\rangle$ and $|T_0\rangle$ states. It does not constitute a major issue since we expect this mixing to occur during the transfer anyway (because of the long separation time between the emission of the first and second electron). The measurement contrast finally expected for the spin transfer experiment is therefore around 19 %.

5.2.3 Spin measurement after transfer

We consider now the complete spin transfer experiment. Spin initialization is ensured by relaxation in the source dot, and the signal is probed in the reception dot after transfer of the electrons. This requires to integrate the initialization and readout steps to the transfer sequence. It is also important to reduce as much as possible the sequence duration between these two steps. For this reason, some control measurements are removed (*e.g.* the charge measurement in position I before the transfer). The detailed steps of the performed experiment are listed in the following:

- The two quantum dots are completely emptied for the reset of the system (point R

and R').

- Two electrons are then loaded into the injection dot (point L_2), while the reception dot is brought to metastable position (point I') making sure it remains empty.
- A time t_{wait} is waited in order to vary the singlet-triplet proportion, and therefore initialize the system in a specific spin state.
- The injection dot is brought to its intermediate metastable position (point I). This step is reduced to only a few microseconds.
- Immediately after, the dots are pulsed (for a few microseconds also) to the transfer position (points T and T') while the SAW burst is applied.
- The two dots are set back to their intermediate metastable positions (point I and I'). This step is reduced to ~ 1 ms. This is sufficient to allow for post-selection of the successful transfer events (see below).
- The reception dot is set to the measurement position (point M') to readout the spin of the transferred electrons.

The transfer statistics as a function of the SAW duration corresponding to this set of data is represented on the left plot of Fig. 5.5. The maximal efficiency for the two-electron transfer is around 80 % for a SAW burst duration close to 70 ns. Since we do not have a perfect efficiency, a post-selection step has to be implemented in order to remove the runs where the two-electron transfer failed. Just after the transfer of the electrons, one waits a short time in position I' (0.5 ms) to measure the charge of the reception dot. Typical QPC current traces are displayed on the right plot of Fig. 5.5. Three different current levels appear, attributed to zero, one or two electrons received in the reception dot. Only the curves passing through the two-electron current level are kept for later statistics (see green curves on the figure). The downside is that ~ 1 ms waiting time allows for a small fraction of spin to relax. This is expected to slightly reduce the measurement contrast, and we expect in the end between 0.85 and 0.9 times the total expected contrast. By taking it into account, one should ideally obtain a signal with contrast around 16.5 % instead of 19 %.

The results of the measurements after transfer are shown on Fig. 5.6. We first concentrate on the left graph. The red curve corresponds to the calibration done with pulsing to the transfer position (no electron transfer here), and is reproduced as a reference. It accounts for the remaining signal after $|S\rangle$-$|T_0\rangle$ mixing in the transfer position. The blue curve corresponds to the spin signal measured after transfer of the two electrons. The data can be fitted with an exponential decay. This characteristic decay time is a few milliseconds long and remains similar to the one obtained for the calibration. However, it can be seen that the contrast of the exponential decay is substantially reduced, lying around 5 % only.

In order to be sure that the observed trend is indeed a spin relaxation signal and not a measurement artifact, a control experiment has been realized. Up to now, the magnetic field was set to 100 mT in order to lift the degeneracy of the three triplet states. We can now reproduce the same experiment with zero magnetic field. In this case, we expect the three triplets to mix with the singlet state when the electrons are separated. In the end, the memory of the initial state should be completely erased. Therefore, no dependence

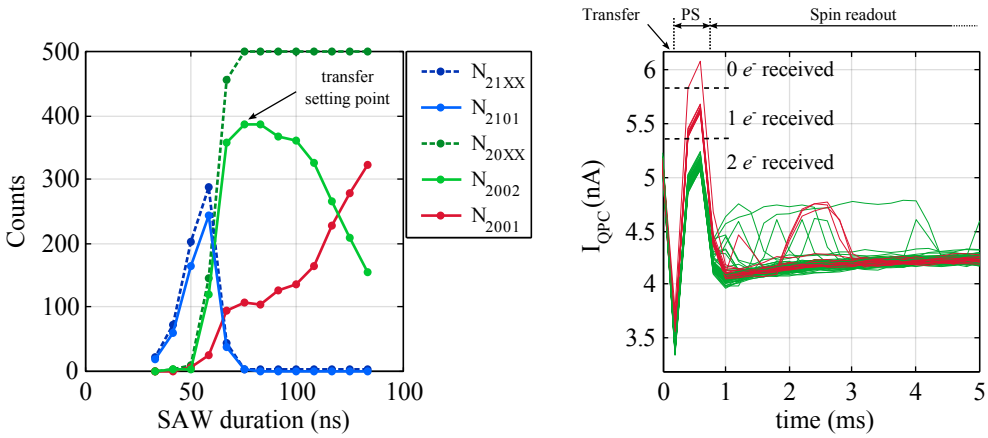

Figure 5.5: (left) Evolution of the transfer events $N_{\alpha\beta\gamma\delta}$ as a function of τ_{SAW} obtained with the same tuning as for the spin transfer experiment of Fig. 5.6. $N_{\alpha\beta\gamma\delta}$ refers to the counts for the source (reception) dot loaded with α (γ) electrons, ending up with β (δ) electrons after the SAW burst. The SAW power used is 18 dBm. The SAW duration has been set around 75 ns that corresponds to a transfer efficiency close to 80 %. **(right)** I_{QPC} traces on the reception dot, with a close-up on the post-selection step used after the electrons transfer. Between $t = 0.5$ ms and 1 ms, the reception dot is in metastable position, preventing any exchange of charge with the reservoir. This allows to read how many electrons have been received. The different current levels and the associated number of charges are indicated on the figure. Only the events where two electrons have been received (green curves) are used afterwards.

with the relaxation time waited should be observed. The result of this experiment is shown as the purple curve on Fig. 5.6. As expected, no clear trend can be seen anymore. This confirms that the residual signal on the 100 mT experiment is spin related. It can therefore be claimed that spin information has been transfer between the two quantum dots. However, we have to explain now why such a contrast reduction is happening.

A first conjecture has been to attribute this effect to spin-orbit interaction during the electron transfer. When an electron travels between the two dots, the spin-orbit interaction will induce an effective magnetic field in the sample plane. At the SAW traveling speed, it has been measured that this field can reach few 10 mT [San13]. Adding this contribution to the static magnetic field might tilt the precession axis of the electron spins during the transport. This could result in the end in a partial rotation away from the z-axis (direction of the external mangetic field applied) for each electron spin during their transport. Assuming similar spin-orbit coupling as in [San13], the upper bound of the angle that can be acquired by a spin over 4 µm is around 25°.

We calculated the influence that such a rotation would have on the measurement contrast. It is considered that each spin experiences a rotation described by

$$R_y(\theta) = \begin{pmatrix} \cos\left(\frac{\theta}{2}\right) & -\sin\left(\frac{\theta}{2}\right) \\ \sin\left(\frac{\theta}{2}\right) & \cos\left(\frac{\theta}{2}\right) \end{pmatrix} \tag{5.6}$$

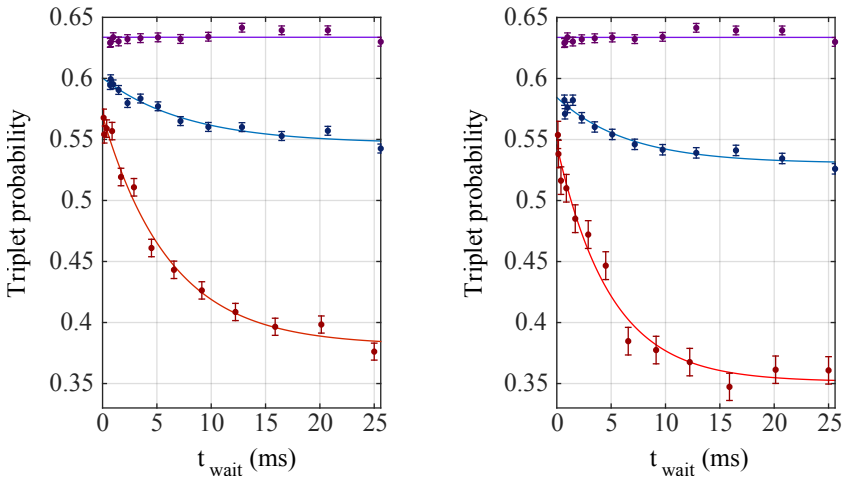

Figure 5.6: Results of the two-electron spin transfer experiment.
(left) 100 mT results. The red curve is the calibration signal previously obtained (with a 100 µs pulse to transfer position inducing $|S\rangle - |T_0\rangle$ mixing), and is used as a reference. It is fitted with an exponential decay of 18.8 % ± 1.6 % contrast and 6.2 ms ± 1.6 ms relaxation time. The signal obtained after electron transfer is plotted in blue. An exponential decay, with 5.4 % ± 1 % contrast and a 7.7 ms ± 4.2 ms relaxation time is found. Each data point is the average over 18620 ± 100 single-shot measurements. The purple curve has been obtained by doing the spin transfer experiment with $B = 0$ mT. This confirms the spin related nature of the observed signal (see main text).
(right) 200 mT results. Calibration of the spin measurement (with a 100 µs pulse to transfer position inducing $|S\rangle - |T_0\rangle$ mixing) has been reproduced with this new value of magnetic field. A 19.4 % ± 2 % contrast and 4.9 ms ± 1.6 ms relaxation time have been obtained. This is comparable to the values found for 100 mT, showing that spin detection has not been affected by the increase of the magnetic field. Each data point is the average over 1920 single-shot measurements. This curve has been offset by −5 % for clarity. The signal obtained after electron transfer is plotted in blue. An exponential decay, with 5.4 % ± 0.9 % contrast and a relaxation time of 6.5 ms ± 3.6 ms is found. Each data point is the average over 13700 ± 100 single-shot measurements. The 0 mT control curve (in purple) is reproduced on this graph for comparison.
The magnetic fields for the different experiments are applied perpendicular to the sample plane. The curves relative to transfer experiments are shifted by 0.6 ms in order to compensate for the duration of the post-selection step.
The electron transfer is ensured by a 75 ns SAW burst of 18 dBm.

For instance, a $|\uparrow\uparrow\rangle$ state will be turned after transfer into

$$\begin{aligned}|\uparrow\uparrow\rangle &\rightarrow \left(\cos\left(\frac{\theta}{2}\right)|\uparrow\rangle + \sin\left(\frac{\theta}{2}\right)|\downarrow\rangle\right) \otimes \left(\cos\left(\frac{\theta}{2}\right)|\uparrow\rangle + \sin\left(\frac{\theta}{2}\right)|\downarrow\rangle\right) \\ &= \cos^2\left(\frac{\theta}{2}\right)|\uparrow\uparrow\rangle + \sin^2\left(\frac{\theta}{2}\right)|\downarrow\downarrow\rangle + \cos\left(\frac{\theta}{2}\right)\sin\left(\frac{\theta}{2}\right)(|\uparrow\downarrow\rangle + |\downarrow\uparrow\rangle)\end{aligned} \tag{5.7}$$

The new spin distribution after this transformation can be calculated by doing a similar operation on all the spin states.

In order to determine the impact it will have on our experiment, the evolution of the relaxation signal is studied. As an initial state, a mixture of the three triplet states with equal probability is assumed. The decay to the singlet state is modeled with a relaxation time similar to the one experimentally measured. Both the mixing between the $|S\rangle$ and $|T_0\rangle$ states and the spin rotations during the transfer are taken into account, and the triplet probability that should be observed experimentally can finally be deduced.

The resulting relaxation signal (triplet probability as a function of t_{wait}) is plotted on Fig. 5.7 for different rotation angles. The greenest and reddest curves correspond respectively to a spin rotation angle θ of 0° and 90°. In order to be in agreement with the experimental result observed on Fig. 5.6, a 60° rotation of each spin during the transport has to be assumed. This is more than twice as much as our upper bound estimation.

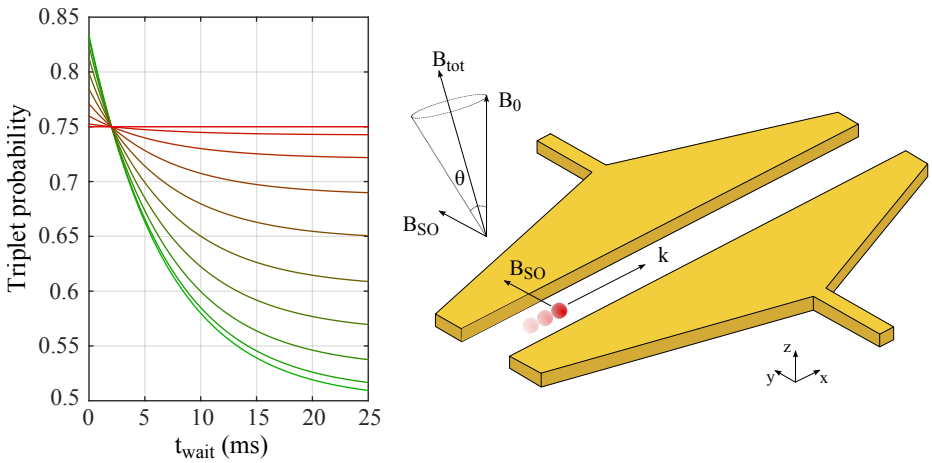

Figure 5.7: Calculation of spin-orbit induced spin rotation during the electrons transfer. **(left)** Calculation of the expected relaxation signal taking into account $|S\rangle - |T_0\rangle$ mixing and spin rotation during the transfer. The rotation angle θ is varied from 0 (green) to 90° (red) between the different curves, with 10° step between each curves.
(right) Schematics of the considered mechanism. Displacement of an electron implies the emergence of an effective magnetic field B_{SO} that will add up to the static field and can induce rotation of the spin away from the z-axis.

In order to confirm experimentally this theory, we changed the external magnetic field B_0. In principle, the impact of the effective spin-orbit field should be reduced for a larger B_0, and thus a better measurement contrast would be expected. The same spin transfer

experiment has therefore been reproduced for $B_0 = 200\,\mathrm{mT}$. At this field value, the measurement contrast should be improved by a factor ~ 2.3 compared to the 100 mT experiment. The result of this experiment is shown on the right panel of Fig. 5.6.

First the calibration curve with pulsing to the transfer position has been reproduced under 200 mT (see red curve). The contrast of this measurement is comparable to the one performed under 100 mT magnetic field, suggesting that the performances of the spin readout has not varied much.

The blue curve corresponds to the signal measured after transfer of the two electrons with $B_0 = 200\,\mathrm{mT}$. Once again, the data can be fitted using an exponential decay that has similar characteristic time as the calibration curve. A contrast reduction can still be observed. The contrast of the remaining signal is around 5 % similarly to the 100 mT experiment. As a consequence, a spin-orbit mediated spin rotation during the transfer seems unlikely to be the actual origin of the contrast reduction.

A second mechanism that we considered as a potential source for spin randomization is illustrated on the top diagram of Fig. 5.8. We have seen that when reaching the transfer position, the electrons are separated and hyperfine mixing occurs between the states $|S\rangle$ and $|T_0\rangle$. This suggests that a double dot behavior is present, similarly to what we saw in chapter 4. It is therefore reasonable to consider a double dot energy diagram to describe our system. As can be seen on Fig. F.2, the influence of the SAW on the system will induce a modulation of the double dot detuning that can result in successive passages through energy level crossings (see top diagram of Fig. 5.8). With the SAW duration used for the transfer experiment, the total number of passages through these crossings could be as high as 400.

As a first approximation, we restrict the study to only a single $|S\rangle$-$|T_+\rangle$ level crossing. It is known from the Landau-Zener theory [Lan32; Zen32] that the final state after passage through such a crossing will depend on the rate at which it is passed. In our case, the probability to preserve the initial spin is given by:

$$p_{LZ} = \exp\left(-2\pi \frac{|\Omega_{ST_+}|^2}{\hbar \frac{dE}{dt}}\right) \tag{5.8}$$

where Ω_{ST_+} is the coupling between the two spin states and $\frac{d\varepsilon}{dt}$ is the slew rate across the avoided crossing. For a 1 meV SAW modulation within a typical time around 0.1 ns, we have $\frac{dE}{dt} \sim 10^7\,\mathrm{eV\,s^{-1}}$. In addition, the coupling between the two states is around $\Omega_{ST_+} \sim t_c \frac{l_{dot}}{l_{SO}} \sim 400\,\mathrm{neV}$ for a 1 GHz interdot tunnel coupling. With these parameters, one obtains an estimate of $p_{LZ} = 0.9998$.

The multiple SAW-induced passages through this crossing is a problem very similar to Landau-Zener-Stückelberg interferometry [Pet10; Rib10; She10; Stu32]. In our case however, we assume that coherent effects will be wiped out because of the large number of passages through the crossing and the long timescale involved ($\sim 100\,\mathrm{ns} \gg \mathrm{T}_2^*$). As a consequence, a classical treatment of the problem should be sufficient. We consider a state initially prepared in $|S\rangle$. For each passage through the $|S\rangle$-$|T_+\rangle$ crossing, there is a probability p_{LZ} to remain on the same spin state (and a probability $1 - p_{LZ}$ to change).

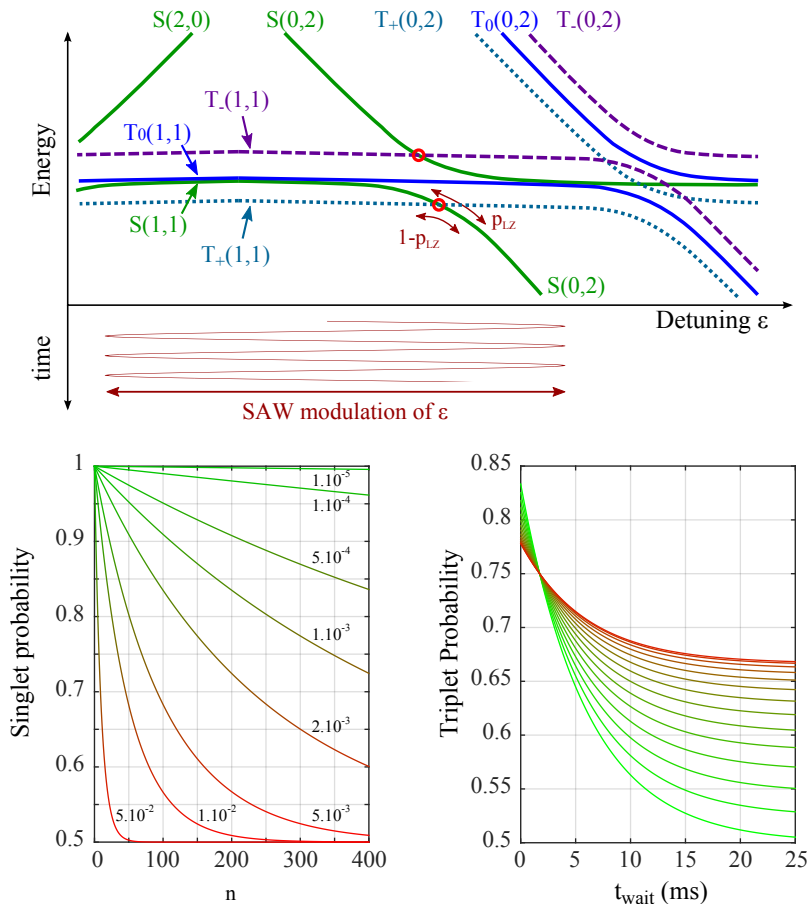

Figure 5.8: Impact of imperfect passages through the $|S\rangle$-$|T_+\rangle$ crossing on measurement contrast. **(top)** Energy diagram of a double dot occupied with two electrons. **(bottom left)** Evolution of the singlet probability (for a state initially in $|S\rangle$) as a function of the number of passages through a Landau-Zener crossing for different values of $(1 - p_{LZ})$. **(bottom right)** Calculation of the expected relaxation signal for different magnitudes of the $|S\rangle$-$|T_+\rangle$ mixing. The greenest curve corresponds to no $|S\rangle$-$|T_+\rangle$ mixing whereas the reddest curve corresponds to a complete $|S\rangle$-$|T_+\rangle$ mixing. A complete $|S\rangle$-$|T_0\rangle$ mixing is assumed for all curves.

After n passages, the probability to retrieve a singlet can be written as:

$$P_S(n) = \frac{1}{2}\left(2p_{LZ} - 1\right)^n + \frac{1}{2} \tag{5.9}$$

The evolution of $P_S(n)$ as a function of n is plotted on the bottom left plot of Fig. 5.8 for different values of p_{LZ} (the values indicated on the graph correspond to $1 - p_{LZ}$). The singlet probability is exponentially decreasing until saturating to 0.5 for large values of n, revealing a complete randomization of the spin states. The smaller is $1 - p_{LZ}$, the longer survives the memory of the initial spin state. It can be seen that for values of $1 - p_{LZ}$ above 10^{-4} (which is the case with our estimation of p_{LZ}), there is a non-negligible mixing

of the $|S\rangle$ and $|T_+\rangle$ states.

To illustrate the impact of such a mechanism, we show on the bottom right plot of Fig. 5.8 the expected relaxation signals for the transfer experiment with varying magnitude of the $|S\rangle$-$|T_+\rangle$ spin mixing. The greenest curve takes into account only the $|S\rangle$-$|T_0\rangle$ mixing contribution ($1-p_{LZ}=0$) while the reddest curve corresponds to a complete randomization of the $|S\rangle$, $|T_0\rangle$ and $|T_+\rangle$ states. In that case, the remaining signal corresponds to the $|T_-\rangle$ state contribution.

This simple model where only the impact of multiple passages through the $|S\rangle$-$|T_+\rangle$ crossing is considered allows to capture the essence of the mechanism that we think is responsible for the contrast reduction observed in our experiment. To be more precise, a similar treatment should be done for all the different Landau-Zener crossings that could be encountered, like for instance the one between the $|T_-\rangle$ state and the upper branch of the $|S\rangle$ state for instance.

In summary, we have seen that spin information stored on two-electron spin states can be transferred between distant quantum dots using SAW-assisted electron transport. A fraction of the information is nevertheless lost during this procedure. A model considering spin-orbit mediated spin rotation during the motion of the electrons seems not consistent with our observations. We speculate that another model where multiple passages through level crossings of the metastable double dot can lead to spin randomization. These passages can be mediated by the perturbation of the SAW burst when the electrons are confined in the source or reception quantum dots. If this interpretation is correct, it would mean that the loss of spin information is not happening during the transfer itself but just before or after it.

5.3 Single electron spin transfer

We have seen in the previous part that at least a fraction of spin information stored on a two-electron state can be preserved after a SAW-assisted transfer. Contrary to the two-electron case, working with a single electron should greatly simplify the problem as far as spin states are concerned. For instance, the $|S\rangle$-$|T_0\rangle$ mixing induced by hyperfine interaction occuring both during the transfer and in the dots should no longer be an issue. However, the measurement of a single electron spin is more challenging.

In this section, it is first presented the developments that have been done to perform single-electron spin readout. The single-electron spin transfer experiment is then presented and the results are discussed.

5.3.1 Adaptation of the spin readout technique to single-electron states

The realization of a spin transfer experiment requires the development of both spin initialization and readout steps that have to be combined to the electron transfer sequence. Compared to the two-electron spin case, these two steps are more challenging when working with a single electron spin.

Spin initialization

We first discuss the single electron spin initialization. In the two-electron case, highly efficient preparation in the excited spin state was obtained thanks to a stronger tunnel

coupling to the reservoir relative to the ground spin state. In the single electron case, the ground and excited spin states occupy the same orbital, and have in principle the same tunnel coupling to the reservoir[1]. As a result, it is not possible to load more (excited) spin-down than (ground) spin-up electrons, and we are not able to initialize properly the excited spin state. Just after the electron loading, we should therefore have an equal proportion of up and down spins. Nevertheless, initialization in the ground spin state is still possible. The simplest scheme, similarly to the two-electron case, consists in waiting for the spin relaxation.

In summary, we are able to initialize either an equal mixture of up and down spins or a pure spin-up. The observation of the spin-down to spin-up relaxation is still possible. However the signal will be intrinsically reduced by a factor of two relative to the ideal case because of this imperfect initialization.

Magnetic field influence

We will now focus on the second requirement, which is single electron spin measurement. The technique used is energy-selective readout, similarly to the two-electron case. This type of measurement requires to lift the degeneracy of the spin states. This is done by the application of a large magnetic field. It is applied in the sample plane in order to avoid the quantum Hall regime and not to affect the quantum dot orbital states.

The larger the magnetic field, the larger the splitting and the easier should be the energy-selective spin readout. This is the reason why the very first measurements of a single spin relaxation were done at very high magnetic field, between 7 T and 11 T (see [Han03] for transport measurement and [Elz04] for single-shot readout). Such fields allow to reach a few 100 µeV, and have an equivalent energy splitting as for two-electrons spin states at zero field. However, the relaxation times found for these magnetic fields are only of a few hundreds of microseconds and might be too fast for the experiment we plan[2] and our measurement bandwidth. However, it has been shown [Gol04] that the relaxation rate is varying as B^5. Therefore at a lower field, the relaxation time will be more compatible with our requirements. Such relaxation measurements at low magnetic fields have been achieved by Amasha *et al.* [Ama08b] and are consistent with this prediction.

There is thus a trade-off between large energy splitting and slow relaxation time. As a compromise, a 3 T magnetic field has been chosen, for which a relaxation time around 10 ms is expected [Ama08b].

Temperature influence

The resulting Zeeman splitting[3] for this field value is about 75 µeV. This is somewhat smaller than the $|S\rangle$-$|T\rangle$ splitting in the two-electron case. As a result, the influence of

1 In fact, spin-dependent tunnel coupling has already been observed [Ama08c; Hou13; Yam14], usually at very high magnetic field. However in these experiments, the tunnel coupling to the ground spin state is stronger and cannot be used to initialize an excited spin state.

2 The transfer sequence duration is limited around 100 µs, and the post-selection step is around 1 ms.

3 The value is calculated using the g-factor of bulk GaAs ($g = -0.44$). In quantum dots systems, smaller g-factors are usually observed [Bev05; Han03]. This value is thus an upper bound to the actual Zeeman splitting.

the electronic temperature of the lead becomes much more critical in this case. In an optimal configuration (see left sketch of Fig. 5.9), the excited spin state is well above the Fermi energy. All the states of the reservoir at the corresponding energy are empty. On the contrary, the ground state is below the Fermi sea with all the reservoir states at the corresponding energy being occupied. Therefore, an electron on the ground state cannot tunnel off the dot while this is possible for an electron on the excited state.

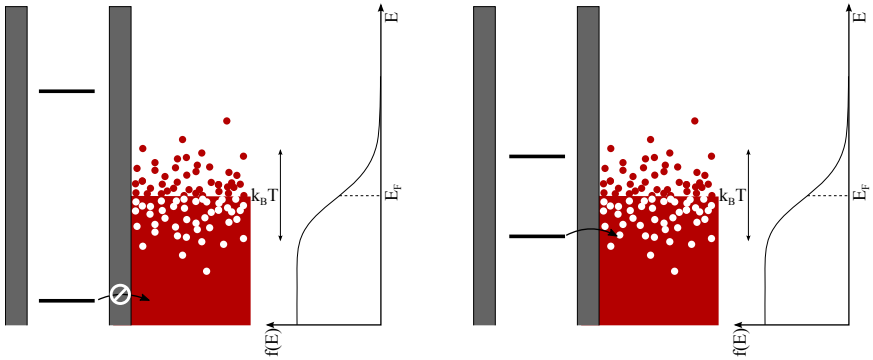

Figure 5.9: (left) Ideal measurement configuration with $\Delta E \gg k_B T$. Tunneling off the dot is allowed for excited state only. **(right)** Configuration with $\Delta E \sim k_B T$. Tunneling off the dot is allowed for both excited and ground state.

When the temperature is no longer negligible compared to the energy splitting of the dot levels (right sketch of Fig. 5.9), there will exist some available states in the lead resonant with the ground state of the dot. This enables an electron in the ground state to tunnel off of the dot. Such events will be wrongly interpreted as an excited spin state signature and will alter the measurement.

Tunnel rates study

In order to deal with this side effect, the idea is to investigate about the different tunnel rates involved, similarly to the work of Amasha *et al.* [Ama08a; Ama08b]. Indeed, as can be seen on the right sketch of Fig. 5.9, the number of resonant available states in the reservoir is not the same for each spin state. This difference can be seen on the tunnel-off rate, which is given by

$$\Gamma_{off} = \Gamma(1 - f(E)) \tag{5.10}$$

where Γ is the bare tunneling rate through the barrier and $(1 - f(E))$ is the density of empty states in the reservoir. Basically, a tunneling event associated with an excited spin state should happen in average sooner than for a ground state. In the following, we present a study aiming at checking whether we are able to make a distinction between these two types of tunneling and therefore distinguish the different spin states.

The experiment that is realized follows the standard procedure for spin relaxation measurement:

- The quantum dot is emptied (point R').
- One electron is loaded into the dot (point L_1').

- A time t_{wait} of either 0.5 ms or 250 ms is then waited (remaining in L_1').
- The dot is finally brought to the spin readout position (point M_1').

Examples of typical QPC current traces observed at the readout position are shown on Fig. 5.10. We define the dwell time t_{dwell} as the time it takes before the electron contained in the quantum dot tunnels off. For each current trace, an arrow indicates the deduced dwell time. It can be noted that multiple events are often present. These are attributed to thermally activated tunneling-off of the ground spin state and it illustrates how measurement is affected by the temperature.

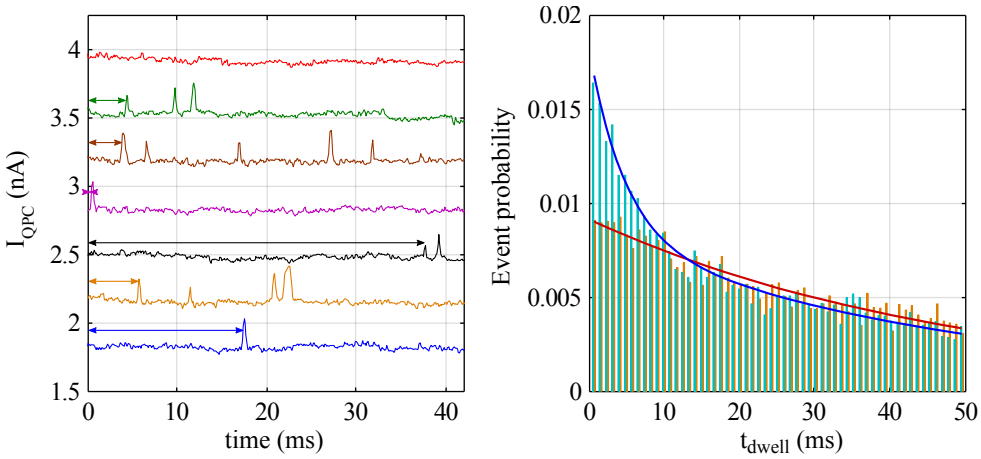

Figure 5.10: Measurement of the tunneling rates for ground and excited spin states. **(left)** Example of typical QPC current traces obtained with the dot in the spin readout position. The dwell time of an electron can be determined (indicated by the arrows). **(right)** Event probability as a function of the dwell time. Red data has been obtained after $t_{wait} = 250$ ms. The fit model is $A\exp(-t/\tau)$, and results in $A = 9.13 \times 10^{-3}$ and $\tau = 48$ ms. Blue data has been obtained after $t_{wait} = 0.5$ ms. The fit model is $A\exp(-t/48\,\text{ms}) + B\exp(-t/\tau)$, and results in $A = 8.31 \times 10^{-3}$, $B = 9.98 \times 10^{-3}$ and $\tau = 4.74$ ms.

The time axis is then divided into different time bins, and the probability to find t_{dwell} within a given time bin is computed. This experiment has been done for two different waiting times ($t_{wait} = 0.5$ ms and $t_{wait} = 250$ ms). The results obtained are displayed on the right plot of Fig. 5.10.

We first concentrate on the $t_{wait} = 250$ ms data (plotted in red). We expect this time to be long compared to the characteristic spin relaxation time. In that case, a ground spin state should occupy the dot, and only thermally activated tunneling events of the ground state should be probed. We can extract from this measurement the characteristic time of the ground state tunneling-off. The data is fitted with a decaying exponential of 48 ms characteristic time (see red continuous line).

We switch now to the $t_{wait} = 0.5$ ms data (plotted in blue). In this case, we should be sensitive to both ground and excited state contributions. Therefore, two different tunnel rates should be observed. Compared to the $t_{wait} = 250$ ms case, it can clearly be seen that there is an excess of events detected for the shortest dwell times, suggesting an additional

contribution with a shorter tunnel rate. To be more quantitative, the data is fitted with a sum of two decaying exponential functions, one associated with the tunneling of the ground state, the other with the tunneling of the excited state. One of the decay time is fixed to the 48 ms previously found. The other one, as well as the weight of each exponential are fit parameters. The result of the fit corresponds to the blue curve. A 4.7 ms characteristic time is found for the excited state tunneling.

The observation of these two different tunnel rates proves that we are indeed able to probe the spin of a single electron. All the signal indicating the presence of an excited spin state is acquired during the first ~ 10 ms after the beginning of the measurement. If the measurement window Δt_{dwell} is chosen too short, one will recover only a fraction of this signal. From this point of view, it is preferable to have a large measurement window. However, the longer Δt_{dwell}, the more parasitic tunneling-off events from the ground state are taken into account, lowering the global contrast. Since the two mechanisms have different timescales, the best trade-off for the measurement duration should be at an intermediate timescale. This can be studied in more details in order to find out the optimal value for Δt_{dwell}.

The same experiment has been done once again with values of t_{wait} varying now between 0.1 ms and 50 ms. The QPC current is recorded for 50 ms after reaching the measurement position. The data treatment is done for different values of Δt_{dwell}. For each value, the probability to detect an event within the measurement window as a function of t_{wait} is computed. The resulting data are fitted with an exponential decay function in order to extract the amplitude of the decay signal (referred to as the "measurement contrast") and its characteristic time.

The top two graphs of Fig. 5.11 show examples of the obtained relaxation curve. The left one corresponds to $\Delta t_{dwell} = 50$ ms and the right one to $\Delta t_{dwell} = 12$ ms (using strictly the same set of data). Similar decay times are found in both cases (11.5 ms for the left and 16.5 ms for the right plot). However, the measurement contrast for $\Delta t_{dwell} = 12$ ms (10.6 %) is more than twice as high as for $\Delta t_{dwell} = 50$ ms (4.6 %).

On the lower two graphs are represented the measurement contrast (left) and the relaxation time (right) evolution as a function of Δt_{dwell}. Regarding the evolution of the contrast, it can be seen that it first rises as the measurement window is enlarged, then reaches a maximum and finally decreases. This is consistent with our expectations. The optimal point can precisely be determined at $\Delta t_{dwell} = 12$ ms. On the contrary, there should not be a large dependence of the relaxation time with Δt_{dwell}. It can be seen on the graph that T_1 undergoes some fluctuations that remain within the errorbars of the measurement. No particular dependence with the measurement window is observed.

In summary, it has been shown that we are able to perform measurements of single electron spin relaxation. Despite the problem of spin initialization and the relatively low energy splitting of the spin states, a decent measurement contrast can be obtained. This is sufficient to start working on single electron spin transfer.

5.3.2 Spin measurement after transfer

First, similarly to the two-electron case, a calibration measurement has been done. The objective is to be sure that all the steps used for the transfer procedure are not affecting

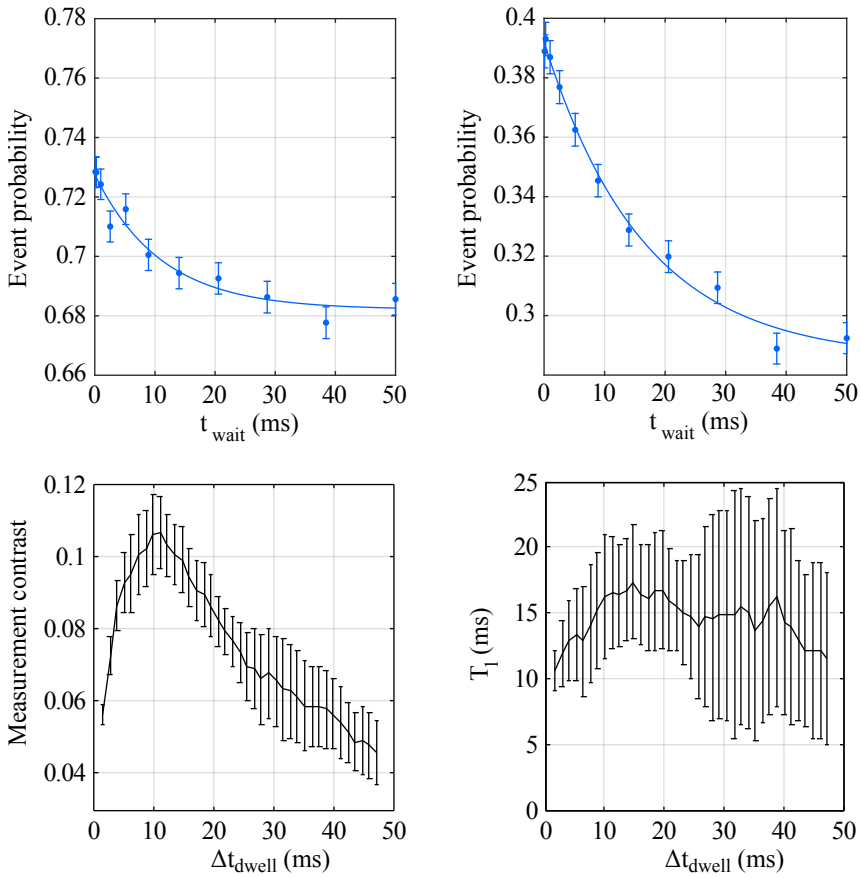

Figure 5.11: Influence of the measurement window on the signal contrast. **(top left)** Data obtained using the complete measurement window (50 ms). Signal contrast is 4.6 % ± 0.88 % and T_1 = 11.53 ms ± 6.6 ms. **(top right)** Data obtained using the optimal measurement window (12 ms). Signal contrast is 10.6 % ± 1 % and T_1 = 16.5 ms ± 4.3 ms. **(bottom left)** Evolution of the measurement contrast as a function of the size of the measurement window Δt_{dwell}. **(bottom right)** Evolution of the relaxation time T_1 as a function of the size of the measurement window Δt_{dwell}. For these two bottom graphs, each point is obtained by fitting the data with a decaying exponential. Error bars corresponds to the 95 % confidence bound of the fitting parameters.

the measurement efficiency. To that purpose, the following experiment is realized:

- The two quantum dots are completely emptied to reset the system.
- The reception dot is set to its intermediate metastable position.
- One electron is loaded on the injection dot (point L_1'). This position is held for 0.1 ms. A statistical mixture of $|\uparrow\rangle$ and $|\downarrow\rangle$ is therefore expected after this step.
- The injection dot is then brought to its intermediate metastable position.
- A few microseconds after, the dots are pulsed (for a few microseconds also) to their transfer positions while a SAW burst is applied.
- The two dots are set back to their intermediate metastable positions. A ~ 1 ms waiting step is done in order to check whether the transfer was successful or not. In addition, one waits a time t_{wait} varied between 0.1 ms and 50 ms.
- The reception dot is finally set to the measurement position to readout the spin of the transferred electron.

This calibration experiment has the advantage to contain all the steps that will be used for the spin transport experiment. The only change is that the waiting step used to vary the prepared spin state is performed in the reception dot after the electron transfer. The post-selection step is adding ~ 1 ms to this waiting time, which should slightly reduce the measurement contrast (by a factor 0.92).

The resulting relaxation signal is shown as the red curve on Fig. 5.12. A contrast around 8 % is obtained with a relaxation time of 13.6 ms. This is comparable with the previous spin measurement presented (see Fig. 5.11). It can be concluded that the large gate movements and the post-selection step have no significant impact on the spin nor on the readout efficiency.

We can now perform the spin transfer experiment, using the same sequence as previously, but the waiting step (aiming at changing the prepared spin state) is now performed on the source dot, before the electron transfer:

- The two quantum dots are completely emptied (reset of the system).
- The reception dot is set to its intermediate metastable position.
- One electron is loaded on the injection dot.
- The injection dot is brought to its intermediate metastable position.
- A time t_{wait} is waited in order to vary the proportion of up and down spins prepared.
- A few microseconds after, both dots are pulsed (for again a few microseconds) to their transfer positions while the SAW burst is applied.
- The two dots are set back to their intermediate metastable positions for ~ 1 ms, to allow for post-selection of the successful transfers.
- The reception dot is set to the measurement position to readout the spin of the transferred electron.

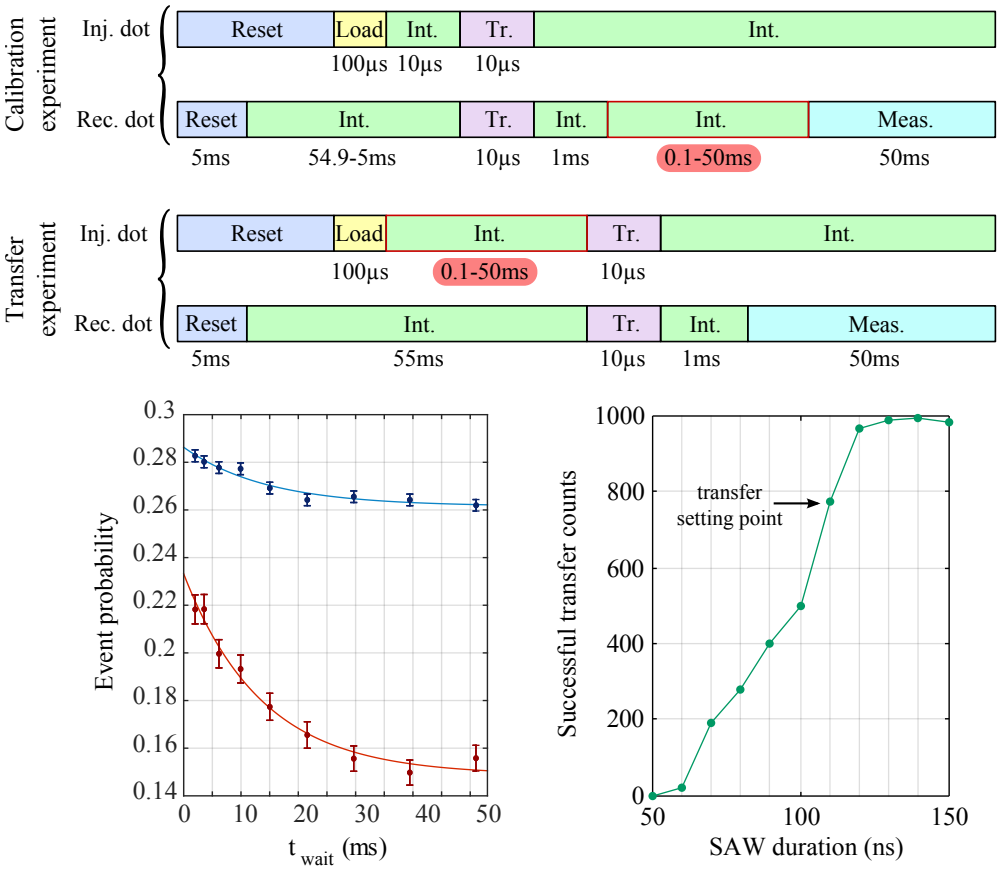

Figure 5.12: Result of the single electron transfer experiment. **(top)** Description of the sequence used for the calibration and transfer measurements. Steps where the spin initialization is performed are highlighted in red. **(bottom left)** The red curve corresponds to the calibration measurement done with the electron transfer on and with the waiting step aimed at varying the spin state performed after the electron transfer, in the reception dot. The measurement contrast is $8.5\,\% \pm 0.8\,\%$, with a T_1 time of $13.6\,\text{ms} \pm 4.1\,\text{ms}$. The blue curve corresponds to the signal obtained with the electron transfer on and with the waiting step aimed at varying the spin state performed in the source dot before the electron transfer. The measurement contrast is $2.5\,\% \pm 0.5\,\%$ with a T_1 time of $14.5\,\text{ms} \pm 10\,\text{ms}$. Both curves are shifted by 1 ms to compensate for the time of the post-selection step. **(bottom right)** Evolution of the successful transfer counts as a function of the SAW burst duration (1000 repetitions for each data point). A SAW burst of 110 ns and 28 dBm was used for the transfer.

In order to work with a SAW duration as short as possible, the system was set to a position with non-perfect transfer efficiency (see bottom right plot of Fig.5.12). This is why a post-selection step was employed here also.

The result of this experiment is shown as the blue curve on Fig. 5.12. The data can be fitted by an exponential decay. It gives 2.5 % measurement contrast (corresponding to nearly 30 % of the calibration measurement contrast) and a relaxation time of 14.5 ms. Similarly to the two-electron spin experiments, a significant reduction of the measurement contrast is observed after transfer.

Since a very large magnetic field was applied (relative to the spin-orbit effective field), we can now clearly claim that this is not due to spin-orbit interaction during the transfer. However, there is still a possibility to have spin mixing caused by multiple passages through level anti-crossings, similarly to what has been discussed for the two-electron case. This point will be detailed in the following part.

5.3.3 SAW impact on the electron spin

The energy diagram of a double quantum dot occupied with a single electron as a function of detuning is represented on the bottom left panel of Fig. 5.13. By changing the detuning value, the occupation of the left or right part of the double dot can be made energetically more favorable. The degeneracy between spin-up and spin-down states is lifted by the application of the 3 T in-plane magnetic field. Using the GaAs bulk value for the g factor ($g = -0.44$), the Zeeman splitting is estimated around 18.5 GHz. Assuming that the interdot tunnel coupling is smaller than this value, it results in two crossings between up and down branches (highlighted by the red circles on the diagram). Similarly to the two-electron case, multiple passages through these crossing points could be a reason for the measurement contrast reduction.

The following experiment has then been done to try to observe this SAW-mediated spin randomization when the electron remains in the reception dot (see also top part of Fig. 5.13):

- One electron is loaded in the source dot and transferred to the reception dot, similarly as for the previous calibration measurement.
- A time t_{wait} is waited, either 0.1 ms or 50 ms, in order to end up with either a mixture of ground and excited states or a pure ground state.
- The reception dot is then pulsed (for a few microseconds) to the transfer position, and a SAW burst of varying duration is applied.
- The reception dot is set back to its intermediate metastable position for ~ 1.5 ms in order to post-select the runs when the electron remained in the reception dot.
- The reception dot is finally set to the measurement position to readout the spin of the electron.

This experiment should allow to probe the effect of the SAW irradiation on a single electron spin confined in a static dot. The result is shown on the bottom right plot of Fig. 5.13. The measured spin signal is plotted as a function of the SAW burst duration for the two different spin initializations ($t_{wait} = 0.1$ ms in light blue and $t_{wait} = 50$ ms in green).

The difference between the two curves should correspond to the contrast that would be obtained for a spin relaxation measurement.

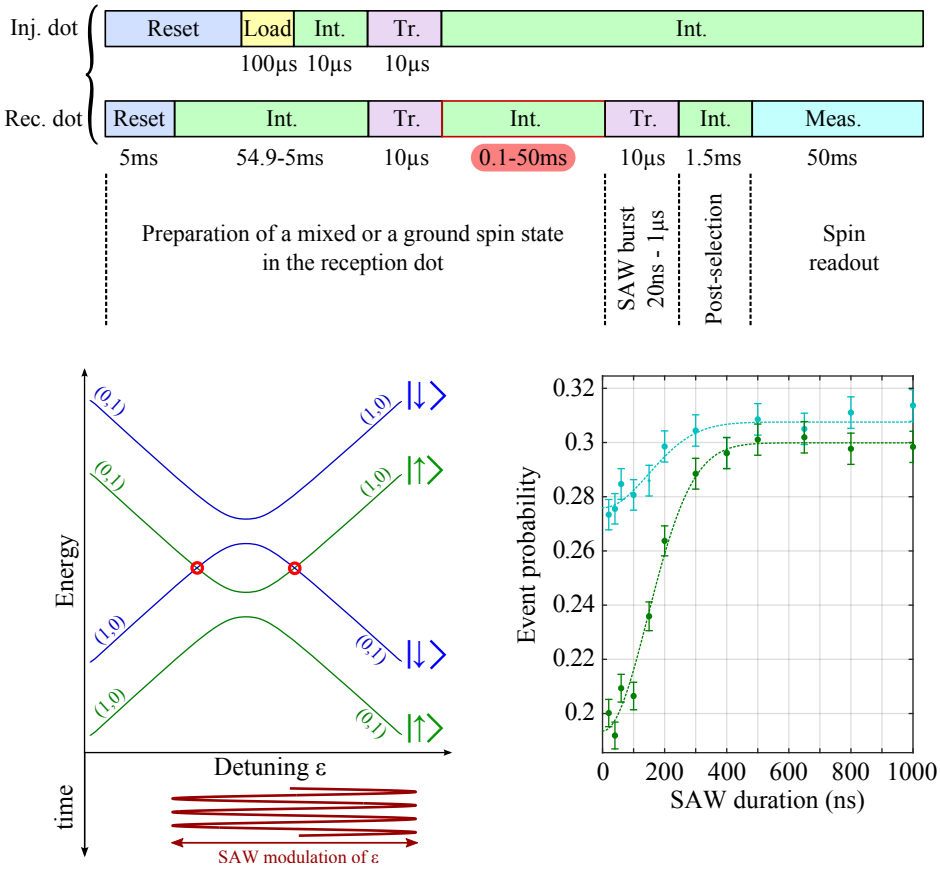

Figure 5.13: Influence of SAWs on spin measurement contrast. **(top)** Description of the sequence used for the measurements. The step where the spin initialization is performed is highlighted in red. **(bottom left)** Energy diagram of a double quantum dot occupied with a single electron as a function of detuning. Crossings between different spin states occur when the Zeeman splitting is larger than the interdot tunnel coupling. **(bottom right)** Evolution of the excited spin state probability as a function of the SAW burst duration. The reception dot is prepared with one electron and brought to its transfer position while the SAW burst is applied. The spin initialization is performed in the reception dot just before the application of the SAW burst. The blue (resp. green) curve has been obtained for $t_{wait} = 0.1$ ms (resp. $t_{wait} = 50$ ms). The power used for the generation of the SAW burst is 28 dBm.

For the shortest SAW burst values, we can see that the difference between the two curves is around 8 %, consistently with the contrast of the calibration measurement of Fig. 5.12. Then as the SAW duration is increased, the probability to detect an event is rising for both curves and they end up approximately at the same value, meaning that no spin signal remains.

We assume that this final value corresponds to a complete spin randomization, *i.e.* an equal probability of $|\uparrow\rangle$ and $|\downarrow\rangle$ in the dot. The fact that the $t_{wait} = 0.1$ ms curve is not

completely flat could be explained by several reasons. First, a fraction of spin-down may have the time to relax before we perform the spin readout, especially during the post-selection step that lasts around 1.5 ms. In addition, there might also be a small contribution due to a slightly higher tunnel-rate for spin-up compared to spin-down electrons, similarly to what has been reported in [Yam14]. In that case, the probability to have a spin-up just after the electron loading should be a little larger than for a spin-down. More precise investigation would be required to quantitatively estimate this tunnel rate difference in our system.

This measurement proves that the SAW has an impact on a spin confined in the reception dot at the transfer position. After a too long irradiation, the initial spin state seems completely randomized. However, the measurement contrast is only reduced from $\sim 8\,\%$ to $\sim 6\,\%$ for a 110 ns SAW burst (similar to the one used in the transfer experiment). Therefore, it explains only partially the contrast reduction observed after transfer (only 2 % measurement contrast remaining). The additional signal loss might be due to a stronger effect of this mechanism for an electron spin confined in the source dot.

5.4 Conclusion

In this chapter, we have demonstrated that spin information can be transferred between distant quantum dots using individual electrons. This has been achieved using either single or two-electron spin states. In both cases, the fidelity of the spin transfer is close to 30%. We believe that this is limited by depolarization occurring before and after the transfer when the electrons are confined in the static dots. The parasitic double dot behavior, that is present on both sides of the sample, allows for multiple passages through spin level crossings that we think induces spin mixing (see appendix F). This interpretation is strengthened by the observation of SAW-induced spin randomization in the case of a single electron confined in the reception dot. Different approaches have been imagined to prevent this effect. A new sample geometry with double dots orthogonal to the propagation direction of the SAW could be used. The dots potential could also be controlled on a nanosecond timescale to bring the system to the transfer configuration only for the minimum required time.

Conclusion and perspectives

The aim of my PhD was to explore the feasibility of transferring spin information between distant quantum dots by displacing individual electrons. Single electrons can indeed be transported from a dot to another using dynamical quantum dots induced by surface acoustic waves. If such a transfer is shown to preserve the electron spin coherence, it could facilitate the scaling of spin-based quantum computing by providing a way to achieve long distance entanglement.

In the presented work, the spin magnetization preservation during the electron transfer has been demonstrated (see chapter 5). It has been observed by implementing a "non-local measurement" of spin relaxation. To that purpose, an initial spin state is prepared, and can be changed using spin relaxation. The electron spin is transferred to a second quantum dot where spin readout is performed. We interpret the spin relaxation signal that is measured after the transfer as a proof of spin information transport.

This experiment has been achieved using either single-electron or two-electron spin states. In each case, the magnitude of the spin relaxation signal after transfer is lower than what is expected from the calibration measurements. We attribute this contrast reduction to a partial information loss occurring before and after the actual electron spin transfer. Indeed, a parasitic double dot behavior has been revealed in both the source and reception dots when they are tuned to their respective transfer positions. The SAW passage across these double dots results in a periodic modulation of their detuning parameters that we think induces mixing between the different spin states. By getting rid of these parasitic dots, a better spin magnetization transfer should be achievable.

The final objective does not only consist in transferring spin magnetization but also to preserve its quantum phase. This requires further developments. In particular, it will be needed to control the electron spin transfer on a faster timescale than the spin coherence time ($\sim 10\,\mathrm{ns}$). In that context, we investigated the injection process from a static to a dynamical quantum dot (see chapter 3).

It has been found that the shape of the static potential has a crucial effect on the electron transfer efficiency. As a result, the electron contained in the source quantum dot is protected from the SAW influence for a given tuning, while its transfer is enabled for a slightly different one. A nanosecond voltage pulse can thus be used to switch between these two positions and control with unity probability the time at which the electron is emitted.

Combining this triggered electron emission with the two electron transfer experiment presented in chapter 5, we can envision a first experiment to probe the spin coherence

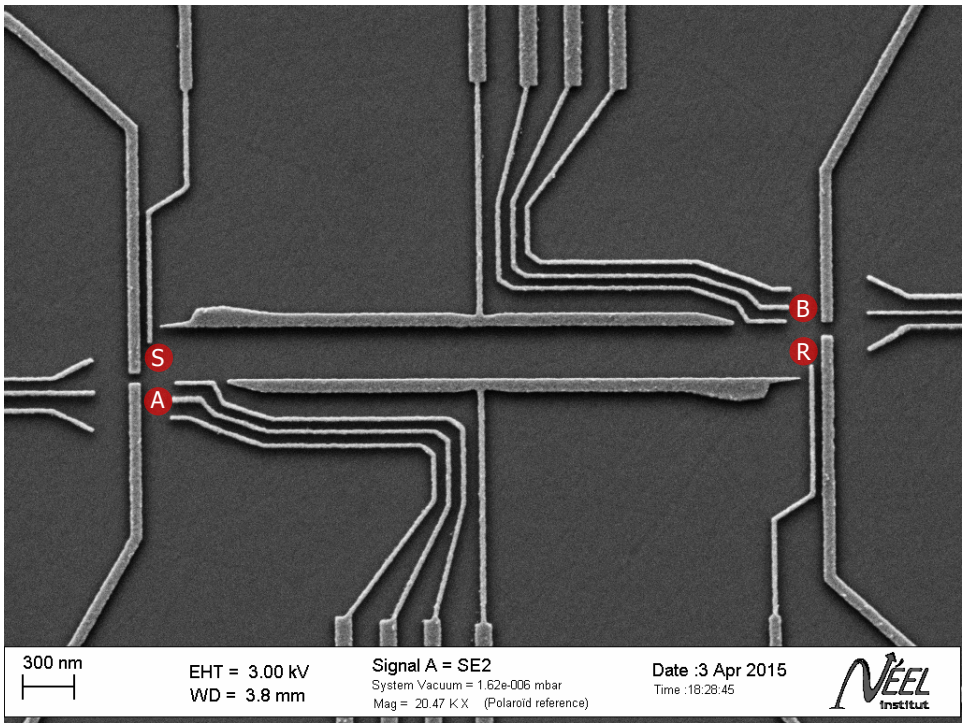

Figure 5.14: SEM picture of a new sample under development. Double quantum dots are present on each side of the sample to allow for coherent spin manipulation of two-electron spin states. They are aligned orthogonal to the channel to prevent any deleterious effect from the SAW modulation.

preservation during the transfer. Basically, it would consist in a "non-local measurement" of the separated singlet dephasing. Two electrons in a singlet state could be prepared in the source quantum dot. They would then be transferred to the reception dot, with a controlled time τ_S between the emission of each of them from the source dot[1]. The spin state that is obtained in the reception dot should depend on the time τ_S during which the two electrons have been separated. For a separation time shorter than the dephasing time, a singlet should be recovered whereas for long separation times, spin mixing should occur. Such an observation would constitute a first proof of coherent spin transfer.

In order to go one step further probing coherent spin transfer, double dots have to be engineered on the source and reception sides. It should then be possible to prepare a coherent superposition of two-electron spin states on the source double dot, transfer it and measure it on the reception double dot, performing in some sens a "non-local measurement" of Rabi oscillations. In chapter 4, the first steps towards the realization of this experiment

1 The relevant timescale for the capture of an electron in a moving quantum dot is expected to be a fraction of the SAW period ($T_{SAW} = 380\,\text{ps}$). This is very short compared to the hyperfine effective magnetic field that is typically up to 5 mT, giving a timescale around 30 ns. This ensures that the electron separation and recombination are done in a non-adiabatic way.

have been achieved with the preparation and measurement of coherent spin states in a position compatible with the SAW-assisted transfer. It has been performed by taking advantage of the parasitic double dot behavior that emerges when tuning the dots to their metastable positions. We have seen that working with such isolated double dots results in a striking simplification of the device tuning, and provides an extended control over the system. First, this should greatly facilitate the work with many-dots systems, and so opens an interesting perspective towards the realization of larger arrays of coherently coupled quantum dots. Second, it enables spin manipulations on a sweet spot with respect to detuning noise. This was achieved by modulating the tunnel barrier between the neighbor dots, similarly to the original proposal of Loss and Divincenzo [Los98]. Such isolated dots are thus an efficient way to improve the coherence of the system and simplify its manipulation.

Nevertheless, it does not seem possible to go further towards the realization of the non-local Rabi oscillations measurement with the current sample. Indeed, we have seen that a double dot orientated along the SAW propagation direction is detrimental since spin mixing can easily be induced. A sample is in preparation, taking advantage of a new design (see Fig. 5.14). The parasitic dots should be suppressed and double dots are engineered instead, orthogonal to the SAW propagation direction.

If coherent SAW-assisted transfer is demonstrated, such a sample could then be used to perform the entanglement of two distant electron spins. A proposal for such an experiment is described below. Two electrons are prepared in a singlet state and are stored in the dot S (see Fig. 5.14). In addition, one electron is loaded in the dot A, and another in dot B. We assume for simplicity that these two electrons are in a $|\uparrow\rangle$ state, but the same operation can be done with any arbitrary spin state. The complete system is then written as:

$$|\uparrow_A\rangle \otimes |S\rangle_S \otimes |\uparrow_B\rangle = |\uparrow_A\rangle \otimes \frac{1}{\sqrt{2}} \left(|\uparrow\downarrow\rangle_S - |\downarrow\uparrow\rangle_S\right) \otimes |\uparrow_B\rangle \tag{5.11}$$

where the subscripts indicate the location of the particles. One electron of the singlet pair is then transferred to the dot R. We can rewrite the system as:

$$|\uparrow_A\rangle \otimes \frac{1}{\sqrt{2}} \left(|\uparrow_S\downarrow_R\rangle - |\downarrow_S\uparrow_R\rangle\right) \otimes |\uparrow_B\rangle = \frac{1}{\sqrt{2}} \left(|\uparrow_A\uparrow_S\downarrow_R\uparrow_B\rangle - |\uparrow_A\downarrow_S\uparrow_R\uparrow_B\rangle\right) \tag{5.12}$$

It is now possible to perform a SWAP operation on each double quantum dot of the sample (A and S on one side, and R and B on the other side). We recall that this operation exchanges the spins of two electrons. It is finally obtained:

$$\frac{1}{\sqrt{2}} \left(|\uparrow_A\uparrow_S\uparrow_R\downarrow_B\rangle - |\downarrow_A\uparrow_S\uparrow_R\uparrow_B\rangle\right) = \frac{1}{\sqrt{2}} \left(|\uparrow_A\downarrow_B\rangle - |\downarrow_A\uparrow_B\rangle\right) \otimes |\uparrow_S\uparrow_R\rangle \tag{5.13}$$

It can be seen that the entanglement originally between the particles in S and R has been induced between the spins in A and B. Very similar experiments, using a separated singlet pair, could then be done to achieve a quantum teleportation scheme [Bou97].

All these perspectives are just a part of the possible developments to come, but already promise very exciting research over the coming years.

Bibliography

[Ama08a] S. Amasha: 'Electron Tunneling and Spin Relaxation in a Lateral Quantum Dot', PhD thesis, Massachusetts Institute of Technology, 2008 (see p. 104).

[Ama08b] S. Amasha, K. MacLean, I. P. Radu, D. M. Zumbühl, M. A. Kastner, M. P. Hanson, and A. C. Gossard: 'Electrical Control of Spin Relaxation in a Quantum Dot', *Phys. Rev. Lett.* **100** (2008), 046803, DOI: 10.1103/PhysRevLett.100.046803 (see pp. 25, 103, 104).

[Ama08c] S. Amasha, K. MacLean, I. P. Radu, D. M. Zumbühl, M. A. Kastner, M. P. Hanson, and A. C. Gossard: 'Spin-dependent tunneling of single electrons into an empty quantum dot', *Phys. Rev. B* **78** (2008), 041306, DOI: 10.1103/PhysRevB.78.041306 (see pp. 16, 103).

[Ang07] S. J. Angus, A. J. Ferguson, A. S. Dzurak, and R. G. Clark: 'Gate-Defined Quantum Dots in Intrinsic Silicon', *Nano Letters* **7** (2007), 2051–2055, DOI: 10.1021/nl070949k (see pp. 3, 167).

[Ash76] N.W. Ashcroft and N.D. Mermin: *Solid State Physics*, Saunders College, 1976 (see p. 14).

[Ast07] M. R. Astley, M. Kataoka, C. J. B. Ford, C. H. W. Barnes, D. Anderson, G. A. C. Jones, I. Farrer, D. A. Ritchie, and M. Pepper: 'Energy-Dependent Tunneling from Few-Electron Dynamic Quantum Dots', *Phys. Rev. Lett.* **99** (2007), 156802, DOI: 10.1103/PhysRevLett.99.156802 (see p. 36).

[BG13] N. Bar-Gill, L. M. Pham, A. Jarmola, D. Budker, and R. L. Walsworth: 'Solid-state electronic spin coherence time appapproach one second', *Nature Communications* **4** (2013), DOI: 10.1038/ncomms2771 (see pp. 3, 167).

[Bar95] A. Barenco, C. H. Bennett, R. Cleve, D. P. DiVincenzo, N. Margolus, P. Shor, T. Sleator, J. A. Smolin, and H. Weinfurter: 'Elementary gates for quantum computation', *Phys. Rev. A* **52** (1995), 3457–3467, DOI: 10.1103/PhysRevA.52.3457 (see pp. 2, 166).

[Bar00] C. H. W. Barnes, J. M. Shilton, and A. M. Robinson: 'Quantum computation using electrons trapped by surface acoustic waves', *Phys. Rev. B* **62** (2000), 8410–8419, DOI: 10.1103/PhysRevB.62.8410 (see p. 36).

[Bar09] C. Barthel, D. J. Reilly, C. M. Marcus, M. P. Hanson, and A. C. Gossard: 'Rapid Single-Shot Measurement of a Singlet-Triplet Qubit', *Phys. Rev. Lett.* **103** (2009), 160503, DOI: 10.1103/PhysRevLett.103.160503 (see pp. 21, 26, 157).

[Bau14] T. Bautze: 'Towards quantum optics experiments with single flying electrons in a solid state system', PhD thesis, Université de Grenoble, 2014 (see pp. 33, 68).

[Ber13] J. W. G. van den Berg, S. Nadj-Perge, V. S. Pribiag, S. R. Plissard, E. P. A. M. Bakkers, S. M. Frolov, and L. P. Kouwenhoven: 'Fast Spin-Orbit Qubit in an Indium Antimonide Nanowire', *Phys. Rev. Lett.* **110** (2013), 066806, DOI: 10.1103/PhysRevLett.110.066806 (see p. 29).

[Bev02] A. Beveratos, R. Brouri, T. Gacoin, A. Villing, J.-P. Poizat, and P. Grangier: 'Single Photon Quantum Cryptography', *Phys. Rev. Lett.* **89** (2002), 187901, DOI: 10.1103/PhysRevLett.89.187901 (see p. 35).

[Bev05] L. H. Willems van Beveren, R. Hanson, I. T. Vink, F. H. L. Koppens, L. P. Kouwenhoven, and L. M. K. Vandersypen: 'Spin filling of a quantum dot derived from excited-state spectroscopy', *New Journal of Physics* **7** (2005), 182, DOI: 10.1088/1367-2630/7/1/182 (see p. 103).

[Bjo04] M. T. Bjork, C. Thelander, A. E. Hansen, L. E. Jensen, M. W. Larsson, L. R. Wallenberg, and L. Samuelson: 'Few-Electron Quantum Dots in Nanowires', *Nano Letters* **4** (2004), 1621–1625, DOI: 10.1021/nl049230s (see p. 5).

[Blu11] H. Bluhm, S. Foletti, I. Neder, M. Rudner, D. Mahalu, V. Umansky, and A. Yacoby: 'Dephasing time of GaAs electron-spin qubits coupled to a nuclear bath exceeding 200 µs', *Nature Physics* **7** (2011), 109, DOI: 10.1038/nphys1856 (see p. 28).

[Blu10] H. Bluhm, S. Foletti, D. Mahalu, V. Umansky, and A. Yacoby: 'Enhancing the Coherence of a Spin Qubit by Operating it as a Feedback Loop That Controls its Nuclear Spin Bath', *Phys. Rev. Lett.* **105** (2010), 216803, DOI: 10.1103/PhysRevLett.105.216803 (see p. 28).

[Blu07] M. D. Blumenthal, B. Kaestner, L. Li, S. Giblin, T. J. B. M. Janssen, M. Pepper, D. Anderson, G. Jones, and D. A. Ritchie: 'Gigahertz quantized charge pumping', *Nature Physics* **3** (2007), 343–347, DOI: 10.1038/nphys582 (see p. 35).

[Bor06] M. Borhani, V. N. Golovach, and D. Loss: 'Spin decay in a quantum dot coupled to a quantum point contact', *Phys. Rev. B* **73** (2006), 155311, DOI: 10.1103/PhysRevB.73.155311 (see p. 25).

[Bou97] D. Bouwmeester, J.-W. Pan, K. Mattle, M. Eibl, H. Weinfurter, and A. Zeilinger: 'Experimental quantum teleportation', *Nature* **390** (1997), 575–579, DOI: 10.1038/37539 (see pp. 115, 176).

[Bra13] F. R. Braakman, P. Barthelemy, C. Reichl, W. Wegscheider, and L. M. K. Vandersypen: 'Long-distance coherent coupling in a quantum dot array', *Nature nanotechnology* **8** (2013), 432–437, DOI: 10.1038/nnano.2013.67 (see pp. 3, 167).

[Bra12] A. Brataas, A. D. Kent, and H. Ohno: 'Current-induced torques in magnetic materials', *Nature Materials* **11** (2012), 372–381, DOI: 10.1038/nmat3311 (see pp. 4, 168).

[Bra05] P.-F. Braun, X. Marie, L. Lombez, B. Urbaszek, T. Amand, P. Renucci, V. K. Kalevich, K. V. Kavokin, O. Krebs, P. Voisin, and Y. Masumoto: 'Direct Observation of the Electron Spin Relaxation Induced by Nuclei in Quantum Dots', *Phys. Rev. Lett.* **94** (2005), 116601, DOI: 10.1103/PhysRevLett.94.116601 (see p. 26).

[Bra98] S. B. Bravyi and A. Yu. Kitaev: 'Quantum codes on a lattice with boundary', *arXiv:quant-ph/9811052* (1998) (see pp. 2, 166).

[Bri72] T. W. Bristol, W. Jones, P. B. Snow, and W. R. Smith: 'Application of Double Electrodes in SAW Device Design', *IEEE International Ultrasonics Symposium* (1972), 377–380, DOI: 10.1109/ULTSYM.1972.196097 (see p. 34).

[Bur99] G. Burkard, D. Loss, and D. P. DiVincenzo: 'Coupled quantum dots as quantum gates', *Phys. Rev. B* **59** (1999), 2070–2078, DOI: 10.1103/PhysRevB.59.2070 (see p. 19).

[Bur06] G. Burkard and A. Imamoglu: 'Ultra-long-distance interaction between spin qubits', *Phys. Rev. B* **74** (2006), 041307, DOI: 10.1103/PhysRevB.74.041307 (see pp. 3, 168).

[Byc84] Yu. A. Bychkov and E. I. Rashba: 'Properties of a 2D electron gas with lifted spectral degeneracy', *JETP lett* **39** (1984), 78 (see p. 24).

[Chi04] L. Childress, A. S. Sørensen, and M. D. Lukin: 'Mesoscopic cavity quantum electrodynamics with quantum dots', *Phys. Rev. A* **69** (2004), 042302, DOI: 10.1103/PhysRevA.69.042302 (see pp. 3, 168).

[Cio00] M. Ciorga, A. S. Sachrajda, P. Hawrylak, C. Gould, P. Zawadzki, S. Jullian, Y. Feng, and Z. Wasilewski: 'Addition spectrum of a lateral dot from Coulomb and spin-blockade spectroscopy', *Phys. Rev. B* **61** (2000), R16315–R16318, DOI: 10.1103/PhysRevB.61.R16315 (see p. 17).

[Cio02] M. Ciorga, M. Pioro-Ladriere, P. Zawadzki, P. Hawrylak, and A. S. Sachrajda: 'Tunable negative differential resistance controlled by spin blockade in single-electron transistors', *Applied Physics Letters* **80** (2002), 2177–2179, DOI: 10.1063/1.1459489 (see p. 17).

[Cir95] J. I. Cirac and P. Zoller: 'Quantum Computations with Cold Trapped Ions', *Phys. Rev. Lett.* **74** (1995), 4091–4094, DOI: 10.1103/PhysRevLett.74.4091 (see pp. 2, 167).

[CT77] C. Cohen-Tannoudji, B. Diu, and F. Laloë: *Quantum Mechanics*, John Wiley, New York, 1977 (see p. 18).

[Coo00] J. Cooper, C. G. Smith, D. A. Ritchie, E. H. Linfield, Y. Jin, and H. Launois: 'Direct observation of single-electron decay from an artificial nucleus', *Physica E: Low-dimensional Systems and Nanostructures* **6** (2000), 457 –460, DOI: 10.1016/S1386-9477(99)00208-8 (see p. 13).

[Cun99] J. Cunningham, V. I. Talyanskii, J. M. Shilton, M. Pepper, M. Y. Simmons, and D. A. Ritchie: 'Single-electron acoustic charge transport by two counter-propagating surface acoustic wave beams', *Phys. Rev. B* **60** (1999), 4850–4855, DOI: 10.1103/PhysRevB.60.4850 (see p. 35).

[Cun00] J. Cunningham, V. I. Talyanskii, J. M. Shilton, M. Pepper, A. Kristensen, and P. E. Lindelof: 'Single-electron acoustic charge transport on shallow-etched channels in a perpendicular magnetic field', *Phys. Rev. B* **62** (2000), 1564–1567, DOI: 10.1103/PhysRevB.62.1564 (see p. 35).

[Dan13] J. Danon: 'Spin-flip phonon-mediated charge relaxation in double quantum dots', *Phys. Rev. B* **88** (2013), 075306, DOI: 10.1103/PhysRevB.88.075306 (see p. 155).

[Dav95] J. H. Davies, I. A. Larkin, and E. V. Sukhorukov: 'Modeling the patterned two-dimensional electron gas: Electrostatics', *Journal of Applied Physics* **77** (1995), 4504–4512, DOI: 10.1063/1.359446 (see p. 68).

[Dav98] John H. Davies: *The physics of low-dimensional semiconductors: an introduction*, Cambridge university press, 1998 (see p. 6).

[DV72] A. J. De Vries, R. L. Miller, and T. S. Wojcik: 'Reflection of a Surface Wave from Three Types of ID Transducers', *IEEE International Ultrasonics Symposium* (1972), 353–358, DOI: 10.1109/ULTSYM.1972.196099 (see p. 34).

[Deb05] S. Debald and C. Emary: 'Spin-Orbit-Driven Coherent Oscillations in a Few-Electron Quantum Dot', *Phys. Rev. Lett.* **94** (2005), 226803, DOI: 10.1103/PhysRevLett.94.226803 (see p. 25).

[Dek99] C. Dekker: 'Carbon nanotubes as molecular quantum wires', *Physics today* **52** (1999), 22–30 (see p. 5).

[Del11] M. Delbecq, V. Schmitt, F. Parmentier, N. Roch, J. Viennot, G. Fève, B. Huard, C. Mora, A. Cottet, and T. Kontos: 'Coupling a Quantum Dot, Fermionic Leads, and a Microwave Cavity on a Chip', *Phys. Rev. Lett.* **107** (2011), 256804, DOI: 10.1103/PhysRevLett.107.256804 (see pp. 4, 168).

[Del14] M. R. Delbecq, T. Nakajima, T. Otsuka, S. Amaha, J. D. Watson, M. J. Manfra, and S. Tarucha: 'Full control of quadruple quantum dot circuit charge states in the single electron regime', *Applied Physics Letters* **104**, 183111 (2014), DOI: 10.1063/1.4875909 (see pp. 3, 167).

[Den02] E. Dennis, A. Kitaev, A. Landahl, and J. Preskill: 'Topological quantum memory', *Journal of Mathematical Physics* **43** (2002), 4452–4505, DOI: http://dx.doi.org/10.1063/1.1499754 (see pp. 2, 166).

[Dia13] O. E. Dial, M. D. Shulman, S. P. Harvey, H. Bluhm, V. Umansky, and A. Yacoby: 'Charge Noise Spectroscopy Using Coherent Exchange Oscillations in a Singlet-Triplet Qubit', *Phys. Rev. Lett.* **110** (2013), 146804, DOI: 10.1103/PhysRevLett.110.146804 (see pp. 83, 85, 87).

[DiV00] D. P. DiVincenzo: 'The Physical Implementation of Quantum Computation', *Fortschritte der Physik* **48** (2000), 771–783 (see pp. 1, 166).

[Dre55] G. Dresselhaus: 'Spin-Orbit Coupling Effects in Zinc Blende Structures', *Phys. Rev.* **100** (1955), 580–586, DOI: 10.1103/PhysRev.100.580 (see p. 24).

[Dut05] M. V. G. Dutt, J. Cheng, B. Li, X. Xu, X. Li, P. R. Berman, D. G. Steel, A. S. Bracker, D. Gammon, S. E. Economou, R.-B. Liu, and L. J. Sham: 'Stimulated and Spontaneous Optical Generation of Electron Spin Coherence in Charged GaAs Quantum Dots', *Phys. Rev. Lett.* **94** (2005), 227403, DOI: 10.1103/PhysRevLett.94.227403 (see p. 26).

[Dya72] M. I. Dyakonov and V. I. Perel: 'Spin relaxation of conduction electrons in noncentrosymmetric semiconductors', *Soviet Physics Solid State* **13** (1972), 3023–3026 (see pp. 4, 168).

[Elz03] J. M. Elzerman, R. Hanson, J. S. Greidanus, L. H. Willems van Beveren, S. De Franceschi, L. M. K. Vandersypen, S. Tarucha, and L. P. Kouwenhoven: 'Few-electron quantum dot circuit with integrated charge read out', *Phys. Rev. B* **67** (2003), 161308, DOI: 10.1103/PhysRevB.67.161308 (see p. 11).

[Elz04] J. M. Elzerman, R. Hanson, L. H. Willems van Beveren, B. Witkamp, L. M. K. Vandersypen, and L. P. Kouwenhoven: 'Single-shot read-out of an individual electron spin in a quantum dot', *Nature* **430** (2004), 431, DOI: 10.1038/nature02693 (see pp. 15, 25, 103).

[Eng04] H.-A. Engel, V. N. Golovach, D. Loss, L. M. K. Vandersypen, J. M. Elzerman, R. Hanson, and L. P. Kouwenhoven: 'Measurement Efficiency and n-Shot Readout of Spin Qubits', *Phys. Rev. Lett.* **93** (2004), 106804, DOI: 10.1103/PhysRevLett.93.106804 (see p. 20).

[Fey82] R. P. Feynman: 'Simulating physics with computers', English, *International Journal of Theoretical Physics* **21** (1982), 467–488, DOI: 10.1007/BF02650179 (see pp. 1, 165).

[Fie93] M. Field, C. G. Smith, M. Pepper, D. A. Ritchie, J. E. F. Frost, G. A. C. Jones, and D. G. Hasko: 'Measurements of Coulomb blockade with a noninvasive voltage probe', *Phys. Rev. Lett.* **70** (1993), 1311–1314, DOI: 10.1103/PhysRevLett.70.1311 (see p. 10).

[Fle03] N. E. Fletcher, J. Ebbecke, T. J. B. M. Janssen, F. J. Ahlers, M. Pepper, H. E. Beere, and D. A. Ritchie: 'Quantized acoustoelectric current transport through a static quantum dot using a surface acoustic wave', *Phys. Rev. B* **68** (2003), 245310, DOI: 10.1103/PhysRevB.68.245310 (see p. 35).

[Fli06] C. Flindt, A. S. Sørensen, and K. Flensberg: 'Spin-Orbit Mediated Control of Spin Qubits', *Phys. Rev. Lett.* **97** (2006), 240501, DOI: 10.1103/PhysRevLett.97.240501 (see p. 25).

[Fod00] C. L. Foden, V. I. Talyanskii, G. J. Milburn, M. L. Leadbeater, and M. Pepper: 'High-frequency acousto-electric single-photon source', *Phys. Rev. A* **62** (2000), 011803, DOI: 10.1103/PhysRevA.62.011803 (see p. 35).

[Fol09] S. Foletti, H. Bluhm, D. Mahalu, V. Umansky, and A. Yacoby: 'Universal quantum control of two-electron spin quantum bits using dynamic nuclear polarization', *Nature Physics* **5** (2009), 903–908, DOI: 10.1038/nphys1424 (see pp. 3, 22, 167).

[Fow12] A. Fowler, M. Mariantoni, J. Martinis, and A. Cleland: 'Surface codes: Towards practical large-scale quantum computation', *Phys. Rev. A* **86** (2012), 032324, DOI: 10.1103/PhysRevA.86.032324 (see pp. 2, 166).

[Fre12] T. Frey, P. Leek, M. Beck, A. Blais, T. Ihn, K. Ensslin, and A. Wallraff: 'Dipole Coupling of a Double Quantum Dot to a Microwave Resonator', *Phys. Rev. Lett.* **108** (2012), 046807, DOI: 10.1103/PhysRevLett.108.046807 (see pp. 4, 168).

[Fue12] M. Fuechsle, J. A. Miwa, S. Mahapatra, H. Ryu, S. Lee, O. Warschkow, L. C. L. Hollenberg, G. Klimeck, and M. Y. Simmons: 'A single-atom transistor', *Nature Nanotechnology* **7** (2012), 242–246, DOI: 10.1038/nnano.2012.21 (see pp. 1, 165).

[Fur04] S. Furuta, C. H. W. Barnes, and C. J. L. Doran: 'Single-qubit gates and measurements in the surface acoustic wave quantum computer', *Phys. Rev. B* **70** (2004), 205320, DOI: 10.1103/PhysRevB.70.205320 (see p. 36).

[Geo14] I. M. Georgescu, S. Ashhab, and Franco Nori: 'Quantum simulation', *Rev. Mod. Phys.* **86** (2014), 153–185, DOI: 10.1103/RevModPhys.86.153 (see pp. 1, 165).

[Ger97] N. A. Gershenfeld and I. L. Chuang: 'Bulk Spin-Resonance Quantum Computation', *Science* **275** (1997), 350–356, DOI: 10.1126/science.275.5298.350 (see pp. 3, 167).

[Gol06] V. N. Golovach, M. Borhani, and D. Loss: 'Electric-dipole-induced spin resonance in quantum dots', *Phys. Rev. B* **74** (2006), 165319, DOI: 10.1103/PhysRevB.74.165319 (see p. 29).

[Gol04] V. N. Golovach, A. Khaetskii, and D. Loss: 'Phonon-Induced Decay of the Electron Spin in Quantum Dots', *Phys. Rev. Lett.* **93** (2004), 016601, DOI: 10.1103/PhysRevLett.93.016601 (see pp. 25, 103).

[Gol08] V. N. Golovach, A. Khaetskii, and D. Loss: 'Spin relaxation at the singlet-triplet crossing in a quantum dot', *Phys. Rev. B* **77** (2008), 045328, DOI: 10.1103/PhysRevB.77.045328 (see pp. 24, 25).

[Gro96] L. K. Grover: 'A Fast Quantum Mechanical Algorithm for Database Search', *Proceedings of the Twenty-eighth Annual ACM Symposium on Theory of Computing*, 1996, 212–219, DOI: 10.1145/237814.237866 (see pp. 1, 165).

[Gue99] S. Gueron, M. M. Deshmukh, E. B. Myers, and D. C. Ralph: 'Tunneling via Individual Electronic States in Ferromagnetic Nanoparticles', *Phys. Rev. Lett.* **83** (1999), 4148–4151, DOI: 10.1103/PhysRevLett.83.4148 (see p. 5).

[Gum04] G. Gumbs and Y. Abranyos: 'Quantum entanglement for acoustic spintronics', *Phys. Rev. A* **70** (2004), 050302, DOI: 10.1103/PhysRevA.70.050302 (see p. 36).

[Haf08] H. Haffner, C. F. Roos, and R. Blatt: 'Quantum computing with trapped ions', *Physics Reports* **469** (2008), 155–203, DOI: 10.1016/j.physrep.2008.09.003 (see pp. 2, 167).

[Hah50] E. L. Hahn: 'Spin Echoes', *Phys. Rev.* **80** (1950), 580–594, DOI: 10.1103/PhysRev.80.580 (see p. 23).

[Han05] R. Hanson, L. H. Willems van Beveren, I. T. Vink, J. M. Elzerman, W. J. M. Naber, F. H. L. Koppens, L. P. Kouwenhoven, and L. M. K. Vandersypen: 'Single-Shot Readout of Electron Spin States in a Quantum Dot Using Spin-Dependent Tunnel Rates', *Phys. Rev. Lett.* **94** (2005), 196802, DOI: 10.1103/PhysRevLett.94.196802 (see pp. 15, 74).

[Han07a] R. Hanson, L. P. Kouwenhoven, J. R. Petta, S. Tarucha, and L. M. K. Vandersypen: 'Spins in few-electron quantum dots', *Rev. Mod. Phys.* **79** (2007), 1455, DOI: 10.1103/RevModPhys.79.1455 (see pp. 8, 25).

[Han07b] R. Hanson and G. Burkard: 'Universal Set of Quantum Gates for Double-Dot Spin Qubits with Fixed Interdot Coupling', *Phys. Rev. Lett.* **98** (2007), 050502, DOI: 10.1103/PhysRevLett.98.050502 (see pp. 3, 167).

[Han03] R. Hanson, B. Witkamp, L. M. K. Vandersypen, L. H. Willems van Beveren, J. M. Elzerman, and L. P. Kouwenhoven: 'Zeeman Energy and Spin Relaxation in a One-Electron Quantum Dot', *Phys. Rev. Lett.* **91** (2003), 196802, DOI: 10.1103/PhysRevLett.91.196802 (see p. 103).

[Her12] S. Hermelin: 'Transport d'un électron unique dans des nanostructures', PhD thesis, Université de Grenoble, 2012 (see p. 137).

[Her11] S. Hermelin, S. Takada, M. Yamamoto, S. Tarucha, A. D. Wieck, L. Saminadayar, C. Bäuerle, and T. Meunier: 'Electrons surfing on a sound wave as a platform for quantum optics with flying electrons', *Nature* **477** (2011), 435–438, DOI: 10.1038/nature10416 (see pp. 4, 37, 49, 168, 170).

[Hou13] M. G. House, M. Xiao, G. Guo, H. Li, G. Cao, M. M. Rosenthal, and H. Jiang: 'Detection and Measurement of Spin-Dependent Dynamics in Random Telegraph Signals', *Phys. Rev. Lett.* **111** (2013), 126803, DOI: 10.1103/PhysRevLett.111.126803 (see pp. 16, 103).

[Hu00] X. Hu and S. Das Sarma: 'Hilbert-space structure of a solid-state quantum computer: Two-electron states of a double-quantum-dot artificial molecule', *Phys. Rev. A* **61** (2000), 062301, DOI: 10.1103/PhysRevA.61.062301 (see p. 19).

[Jef14] E. Jeffrey et al.: 'Fast Accurate State Measurement with Superconducting Qubits', *Phys. Rev. Lett.* **112** (2014), 190504, DOI: 10.1103/PhysRevLett.112.190504 (see pp. 2, 167).

[Jel04] F. Jelezko, T. Gaebel, I. Popa, M. Domhan, A. Gruber, and J. Wrachtrup: 'Observation of Coherent Oscillation of a Single Nuclear Spin and Realization of a Two-Qubit Conditional Quantum Gate', *Phys. Rev. Lett.* **93** (2004), 130501, DOI: 10.1103/PhysRevLett.93.130501 (see pp. 3, 167).

[Joh05a] A. C. Johnson, C. M. Marcus, M. P. Hanson, and A. C. Gossard: 'Charge sensing of excited states in an isolated double quantum dot', *Phys. Rev. B* **71** (2005), 115333, DOI: 10.1103/PhysRevB.71.115333 (see p. 149).

[Joh05b] A. C. Johnson, J. R. Petta, C. M. Marcus, M. P. Hanson, and A. C. Gossard: 'Singlet-triplet spin blockade and charge sensing in a few-electron double quantum dot', *Phys. Rev. B* **72** (2005), 165308, DOI: 10.1103/PhysRevB.72.165308 (see p. 20).

[Joh05c] A. C. Johnson, J. R. Petta, J. M. Taylor, A. Yacoby, M. D. Lukin, C. M. Marcus, M. P. Hanson, and A. C. Gossard: 'Triplet-singlet spin relaxation via nuclei in a double quantum dot', *Nature* **435** (2005), 925–928, DOI: 10.1038/nature03815 (see p. 26).

[Jon11] J. A. Jones: 'Quantum computing with NMR', *Progress in nuclear magnetic resonance spectroscopy* **59** (2011), 91–120, DOI: 10.1016/j.pnmrs.2010.11.001 (see pp. 3, 167).

[Jou06] O. N. Jouravlev and Yu. V. Nazarov: 'Electron Transport in a Double Quantum Dot Governed by a Nuclear Magnetic Field', *Phys. Rev. Lett.* **96** (2006), 176804, DOI: 10.1103/PhysRevLett.96.176804 (see p. 28).

[Jun04] S. W. Jung, T. Fujisawa, Y. Hirayama, and Y. H. Jeong: 'Background charge fluctuation in a GaAs quantum dot device', *Applied Physics Letters* **85** (2004), 768–770, DOI: 10.1063/1.1777802 (see pp. 16, 25).

[Kat09] M. Kataoka, M. R. Astley, A. L. Thorn, D. K. L. Oi, C. H. W. Barnes, C. J. B. Ford, D. Anderson, G. A. C. Jones, I. Farrer, D. A. Ritchie, and M. Pepper: 'Coherent Time Evolution of a Single-Electron Wave Function', *Phys. Rev. Lett.* **102** (2009), 156801, DOI: 10.1103/PhysRevLett.102.156801 (see p. 36).

[Kat06] M. Kataoka, C. H. W. Barnes, H. E. Beere, D. A. Ritchie, and M. Pepper: 'Experimental investigation of the surface acoustic wave electron capture mechanism', *Phys. Rev. B* **74** (2006), 085302, DOI: 10.1103/PhysRevB.74.085302 (see p. 49).

[Kat07] M. Kataoka, R. J. Schneble, A. L. Thorn, C. H. W. Barnes, C. J. B. Ford, D. Anderson, G. A. C. Jones, I. Farrer, D. A. Ritchie, and M. Pepper: 'Single-Electron Population and Depopulation of an Isolated Quantum Dot Using a Surface-Acoustic-Wave Pulse', *Phys. Rev. Lett.* **98** (2007), 046801, DOI: 10.1103/PhysRevLett.98.046801 (see pp. 37, 49).

[Kat03] Y. Kato, R. C. Myers, D. C. Driscoll, A. C. Gossard, J. Levy, and D. D. Awschalom: 'Gigahertz Electron Spin Manipulation Using Voltage-Controlled g-Tensor Modulation', *Science* **299** (2003), 1201–1204, DOI: 10.1126/science.1080880 (see p. 30).

[Ken02] T.A. Kennedy, F.T. Charnock, J.S. Colton, J.E. Butler, R.C. Linares, and P.J. Doering: 'Single-Qubit Operations with the Nitrogen-Vacancy Center in Diamond', *physica status solidi (b)* **233** (2002), 416–426 (see pp. 3, 167).

[Kha01] A. V. Khaetskii and Yu. V. Nazarov: 'Spin-flip transitions between Zeeman sublevels in semiconductor quantum dots', *Phys. Rev. B* **64** (2001), 125316, DOI: 10.1103/PhysRevB.64.125316 (see p. 25).

[Kha00] A. V. Khaetskii and Yu. V. Nazarov: 'Spin relaxation in semiconductor quantum dots', *Phys. Rev. B* **61** (2000), 12639–12642, DOI: 10.1103/PhysRevB.61.12639 (see pp. 24, 25).

[Kle96] D. L. Klein, P. L. McEuen, J. E. Bowen Katari, R. Roth, and A. P. Alivisatos: 'An approach to electrical studies of single nanocrystals', *Applied Physics Letters* **68** (1996), 2574–2576, DOI: 10.1063/1.116188 (see p. 5).

[Kni01] E. Knill, R. Laflamme, and G. J. Milburn: 'A scheme for efficient quantum computation with linear optics', *Nature* **409** (2001), 46–52, DOI: 10.1038/35051009 (see p. 35).

[Koc07] J. Koch, T. M. Yu, J. Gambetta, A. A. Houck, D. I. Schuster, J. Majer, A. Blais, M. H. Devoret, S. M. Girvin, and R. J. Schoelkopf: 'Charge-insensitive qubit design derived from the Cooper pair box', *Phys. Rev. A* **76** (2007), 042319, DOI: 10.1103/PhysRevA.76.042319 (see pp. 2, 167).

[Kop05] F. H. L. Koppens, J. A. Folk, J. M. Elzerman, R. Hanson, L. H. Willems van Beveren, I. T. Vink, H. P. Tranitz, W. Wegscheider, L. P. Kouwenhoven, and L. M. K. Vandersypen: 'Control and Detection of Singlet-Triplet Mixing in a Random Nuclear Field', *Science* **309** (2005), 1346–1350, DOI: 10.1126/science.1113719 (see p. 26).

[Kop06] F. H. L. Koppens, C. Buizert, K-J. Tielrooij, I. T. Vink, K. C. Nowack, T. Meunier, L. P. Kouwenhoven, and L. M. K. Vandersypen: 'Driven coherent oscillations of a single electron spin in a quantum dot', *Nature* **442** (2006), 766–771, DOI: 10.1038/nature05065 (see pp. 3, 29, 167).

[Kou97] L. P. Kouwenhoven, C. M. Marcus, P. L. McEuen, S. Tarucha, R. M. Westervelt, and N. S. Wingreen: 'Electron Transport in Quantum Dots', English, *Mesoscopic Electron Transport*, vol. 345, 1997, 105–214, DOI: 10.1007/978-94-015-8839-3_4 (see pp. 5, 9, 149, 169).

[Kou01] L. P. Kouwenhoven, D. G. Austing, and S. Tarucha: 'Few-electron quantum dots', *Reports on Progress in Physics* **64** (2001), 701–736, DOI: 10.1088/0034-4885/64/6/201 (see pp. 5, 8, 10).

[Lai10] E. A. Laird, J. M. Taylor, D. P. DiVincenzo, C. M. Marcus, M. P. Hanson, and A. C. Gossard: 'Coherent spin manipulation in an exchange-only qubit', *Phys. Rev. B* **82** (2010), 075403, DOI: 10.1103/PhysRevB.82.075403 (see pp. 3, 167).

[Lai07] E. A. Laird, C. Barthel, E. I. Rashba, C. M. Marcus, M. P. Hanson, and A. C. Gossard: 'Hyperfine-Mediated Gate-Driven Electron Spin Resonance', *Phys. Rev. Lett.* **99** (2007), 246601, DOI: 10.1103/PhysRevLett.99.246601 (see p. 30).

[Lan32] L. D. Landau: 'On the theory of transfer of energy at collisions II', *Phys. Z. Sowjetunion* **2** (1932), 46–51 (see pp. 31, 100).

[Lev03] L. S. Levitov and E. I. Rashba: 'Dynamical spin-electric coupling in a quantum dot', *Phys. Rev. B* **67** (2003), 115324, DOI: 10.1103/PhysRevB.67.115324 (see p. 25).

[Lim03] M. M. de Lima, F. Alsina, W. Seidel, and P. V. Santos: 'Focusing of surface-acoustic-wave fields on (100) GaAs surfaces', *Journal of Applied Physics* **94** (2003), 7848–7855, DOI: 10.1063/1.1625419 (see p. 35).

[Llo96] S. Lloyd: 'Universal Quantum Simulators', *Science* **273** (1996), 1073–1078, DOI: 10.1126/science.273.5278.1073 (see pp. 1, 165).

[Los98] D. Loss and D. P. DiVincenzo: 'Quantum computation with quantum dots', *Phys. Rev. A* **57** (1998), 120–126, DOI: 10.1103/PhysRevA.57.120 (see pp. 3, 19, 67, 78, 115, 167, 175).

[Lou74] Olli V Lounasmaa, OV Louasmaa, and OV Lounasmaa: *Experimental principles and methods below 1 K*, vol. 8, Academic Press London, 1974 (see p. 39).

[Maj07] J. Majer, J. M. Chow, J. M. Gambetta, J. Koch, B. R. Johnson, J. A. Schreier, L. Frunzio, D. I. Schuster, A. A. Houck, A. Wallraff, A. Blais, M. H. Devoret, S. M. Girvin, and R. J. Schoelkopf: 'Coupling superconducting qubits via a cavity bus', *Nature* **449** (2007), 443–447, DOI: 10.1038/nature06184 (see pp. 4, 168).

[Mar05] F. Marquardt and V. A. Abalmassov: 'Spin relaxation in a quantum dot due to Nyquist noise', *Phys. Rev. B* **71** (2005), 165325, DOI: 10.1103/PhysRevB.71.165325 (see p. 25).

[McE00] P. L. McEuen: 'Single-wall carbon nanotubes', *Physics World* **13** (2000), 31–36 (see p. 5).

[McN11] R. P. G. McNeil, M. Kataoka, C. J. B. Ford, C. H. W. Barnes, D. Anderson, G. A. C. Jones, I. Farrer, and D. A. Ritchie: 'On-demand single-electron transfer between distant quantum dots', *Nature* **477** (2011), 439–442, DOI: 10.1038/nature10444 (see pp. 4, 37, 49, 168, 170).

[Med13] J Medford, J. Beil, J. M. Taylor, S. D. Bartlett, A. C. Doherty, E. I. Rashba, D. P. DiVincenzo, H. Lu, A. C. Gossard, and C. M. Marcus: 'Self-consistent measurement and state tomography of an exchange-only spin qubit', *Nature nanotechnology* **8** (2013), 654–659, DOI: 10.1038/nnano.2013.168 (see pp. 3, 167).

[Meh14] S. Mehl, H. Bluhm, and D. P. DiVincenzo: 'Two-qubit couplings of singlet-triplet qubits mediated by one quantum state', *Phys. Rev. B* **90** (2014), 045404, DOI: 10.1103/PhysRevB.90.045404 (see pp. 3, 167).

[Mer02] I. A. Merkulov, Al. L. Efros, and M. Rosen: 'Electron spin relaxation by nuclei in semiconductor quantum dots', *Phys. Rev. B* **65** (2002), 205309, DOI: 10.1103/PhysRevB.65.205309 (see p. 27).

[Meu07] T. Meunier, I. T. Vink, L. H. Willems van Beveren, K-J. Tielrooij, R. Hanson, F. H. L. Koppens, H. P. Tranitz, W. Wegscheider, L. P. Kouwenhoven, and L. M. K. Vandersypen: 'Experimental Signature of Phonon-Mediated Spin Relaxation in a Two-Electron Quantum Dot', *Phys. Rev. Lett.* **98** (2007), 126601, DOI: 10.1103/PhysRevLett.98.126601 (see p. 23).

[Meu06a] T. Meunier, K.-J. Tielrooij, I. T. Vink, F. H. L. Koppens, H. P. Tranitz, W. Wegscheider, L. P. Kouwenhoven, and L. M. K. Vandersypen: 'High fidelity measurement of singlet–triplet state in a quantum dot', *physica status solidi (b)* **243** (2006), 3855–3858, DOI: 10.1002/pssb.200671503 (see pp. 15, 74).

[Meu06b] T. Meunier, I. T. Vink, L. H. Willems van Beveren, F. H. L. Koppens, H. P. Tranitz, W. Wegscheider, L. P. Kouwenhoven, and L. M. K. Vandersypen: 'Nondestructive measurement of electron spins in a quantum dot', *Phys. Rev. B* **74** (2006), 195303, DOI: 10.1103/PhysRevB.74.195303 (see p. 17).

[Mor10] D. Morgan: *Surface acoustic wave filters: With applications to electronic communications and signal processing*, Academic Press, 2010 (see pp. 33, 34).

[NP10] S. Nadj-Perge, S. M. Frolov, E. P. A. M. Bakkers, and L. P. Kouwenhoven: 'Spin-orbit qubit in a semiconductor nanowire', *Nature* **468** (2010), 1084–1087, DOI: 10.1038/nature09682 (see p. 29).

[Nak99] Y. Nakamura, Yu. A. Pashkin, and J. S. Tsai: 'Coherent control of macroscopic quantum states in a single-Cooper-pair box', *Nature* **398** (1999), 786–788, DOI: 10.1038/19718 (see pp. 2, 167).

[Nie10] M. A. Nielsen and I. L. Chuang: *Quantum computation and quantum information*, Cambridge university press, 2010 (see p. 22).

[Now07] K. C. Nowack, F. H. L. Koppens, Yu. V. Nazarov, and L. M. K. Vandersypen: 'Coherent Control of a Single Electron Spin with Electric Fields', *Science* **318** (2007), 1430–1433, DOI: 10.1126/science.1148092 (see pp. 22, 29).

[Oka10] Katsunari Okamoto: *Fundamentals of optical waveguides*, Academic press, 2010 (see p. 34).

[Ono02] K. Ono, D. G. Austing, Y. Tokura, and S. Tarucha: 'Current Rectification by Pauli Exclusion in a Weakly Coupled Double Quantum Dot System', *Science* **297** (2002), 1313–1317, DOI: 10.1126/science.1070958 (see p. 20).

[Pag77] D. Paget, G. Lampel, B. Sapoval, and V. I. Safarov: 'Low field electron-nuclear spin coupling in gallium arsenide under optical pumping conditions', *Phys. Rev. B* **15** (1977), 5780–5796, DOI: 10.1103/PhysRevB.15.5780 (see p. 26).

[Par02] J. Park, A. N. Pasupathy, J. I. Goldsmith, C. Chang, Y. Yaish, J. R. Petta, M. Rinkoski, J. P. Sethna, H. D. Abruña, P. L. McEuen, and D. C. Ralph: 'Coulomb blockade and the Kondo effect in single-atom transistors', *Nature* **417** (2002), 722–725, DOI: 10.1038/nature00791 (see p. 5).

[Par55] R. H. Parmenter: 'Symmetry Properties of the Energy Bands of the Zinc Blende Structure', *Phys. Rev.* **100** (1955), 573–579, DOI: 10.1103/PhysRev.100.573 (see p. 24).

[Pet12] K. D. Petersson, L. W. McFaul, M. D. Schroer, M. Jung, J. M. Taylor, A. A. Houck, and J. R. Petta: 'Circuit quantum electrodynamics with a spin qubit', *Nature* **490** (2012), 380–383, DOI: 10.1038/nature11559 (see pp. 4, 168).

[Pet10] J. R. Petta, H. Lu, and A. C. Gossard: 'A coherent beam splitter for electronic spin states', *Science* **327** (2010), 669, DOI: 10.1126/science.1183628 (see p. 100).

[Pet05] J. R. Petta, A. C. Johnson, J. M. Taylor, E. A. Laird, A. Yacoby, M. D. Lukin, C. M. Marcus, M. P. Hanson, and A. C. Gossard: 'Coherent Manipulation of Coupled Electron Spins in Semiconductor Quantum Dots', *Science* **309** (2005), 2180–2184, DOI: 10.1126/science.1116955 (see pp. 3, 30, 78, 80, 83, 87, 155, 167).

[Pet01] J. R. Petta and D. C. Ralph: 'Studies of Spin-Orbit Scattering in Noble-Metal Nanoparticles Using Energy-Level Tunneling Spectroscopy', *Phys. Rev. Lett.* **87** (2001), 266801, DOI: 10.1103/PhysRevLett.87.266801 (see p. 5).

[PL08] M. Pioro-Ladrière, T. Obata, Y. Tokura, Y.-S. Shin, T. Kubo, K. Yoshida, T. Taniyama, and S. Tarucha: 'Electrically driven single-electron spin resonance in a slanting Zeeman field', *Nat Phys* **4** (2008), 776–779, DOI: 10.1038/nphys1053 (see pp. 3, 29, 167).

[Pob07] F. Pobell: *Matter and methods at low temperatures*, vol. 2, Springer, 2007 (see p. 39).

[Poo96] C. P. Poole: *Electron spin resonance: a comprehensive treatise on experimental techniques*, Courier Dover Publications, 1996 (see p. 28).

[Pra12] J. R. Prance, Z. Shi, C. B. Simmons, D. E. Savage, M. G. Lagally, L. R. Schreiber, L. M. K. Vandersypen, M. Friesen, R. Joynt, S. N. Coppersmith, and M. A. Eriksson: 'Single-Shot Measurement of Triplet-Singlet Relaxation in a Si/SiGe Double Quantum Dot', *Phys. Rev. Lett.* **108** (2012), 046808, DOI: 10.1103/PhysRevLett.108.046808 (see p. 21).

[Ral95] D. C. Ralph, C. T. Black, and M. Tinkham: 'Spectroscopic Measurements of Discrete Electronic States in Single Metal Particles', *Phys. Rev. Lett.* **74** (1995), 3241–3244, DOI: 10.1103/PhysRevLett.74.3241 (see p. 5).

[Ras60] E. I. Rashba: 'Properties of semiconductors with an extremum loop. 1. Cyclotron and combinational resonance in a magnetic field perpendicular to the plane of the loop', *Soviet Physics-Solid State* **2** (1960), 1109–1122 (see p. 24).

[Ray85] Lord Rayleigh: 'On Waves Propagated along the Plane Surface of an Elastic Solid', *Proceedings of the London Mathematical Society* **s1-17** (1885), 4–11, DOI: 10.1112/plms/s1-17.1.4 (see p. 33).

[Rei08] D. J. Reilly, J. M. Taylor, J. R. Petta, C. M. Marcus, M. P. Hanson, and A. C. Gossard: 'Supressing spin qubit dephasing by nuclear state preparation', *Science* **321** (2008), 817, DOI: 10.1126/science.1159221 (see p. 26).

[Rib10] H. Ribeiro, J. R. Petta, and G. Burkard: 'Harnessing the GaAs nuclear spin bath for quantum control', *Phys. Rev. B* **82** (2010), 115445, DOI: 10.1103/PhysRevB.82.115445 (see p. 100).

[Roo99] C. Roos, T. Zeiger, H. Rohde, H. C. Nägerl, J. Eschner, D. Leibfried, F. Schmidt-Kaler, and R. Blatt: 'Quantum State Engineering on an Optical Transition and Decoherence in a Paul Trap', *Phys. Rev. Lett.* **83** (1999), 4713–4716, DOI: 10.1103/PhysRevLett.83.4713 (see pp. 2, 167).

[Ros14] A. Rossi, T. Tanttu, K. Y. Tan, I. Iisakka, R. Zhao, K. W. Chan, G. C. Tettamanzi, S. Rogge, A. S. Dzurak, and M. Möttönen: 'An Accurate Single-Electron Pump Based on a Highly Tunable Silicon Quantum Dot', *Nano Letters* **14** (2014), 3405–3411, DOI: 10.1021/nl500927q (see p. 35).

[Rug04] D. Rugar, R. Budakian, H. J. Mamin, and B. W. Chui: 'Single spin detection by magnetic resonance force microscopy', *Nature* **430** (2004), 329–332, DOI: 10.1038/nature02658 (see p. 14).

[Rus04] A. W. Rushforth, C. G. Smith, M. D. Godfrey, H. E. Beere, D. A. Ritchie, and M. Pepper: 'Noninvasive detection of the evolution of the charge states of a double dot system', *Phys. Rev. B* **69** (2004), 113309, DOI: 10.1103/PhysRevB.69.113309 (see p. 69).

[San13] H. Sanada, Y. Kunihashi, H. Gotoh, K. Onomitsu, M. Kohda, J. Nitta, P. V. Santos, and T. Sogawa: 'Manipulation of mobile spin coherence using magnetic-field-free electron spin resonance', *Nature Physics* **9** (2013), 280–283, DOI: 10.1038/nphys2573 (see p. 97).

[San14] R. Sanchez, G. Granger, L. Gaudreau, A. Kam, M. Pioro-Ladrière, S. A. Studenikin, P. Zawadzki, A. S. Sachrajda, and G. Platero: 'Long-Range Spin Transfer in Triple Quantum Dots', *Phys. Rev. Lett.* **112** (2014), 176803, DOI: 10.1103/PhysRevLett.112.176803 (see pp. 3, 167).

[Sch04] R. Schleser, E. Ruh, T. Ihn, K. Ensslin, D. C. Driscoll, and A. C. Gossard: 'Time-resolved detection of individual electrons in a quantum dot', *Applied Physics Letters* **85** (2004), 2005–2007, DOI: 10.1063/1.1784875 (see p. 42).

[She10] S. N. Shevchenko, S. Ashhab, and F. Nori: 'Landau-Zener-Stückelberg interferometry', *Physics Reports* **492** (2010), 1–30, DOI: 10.1016/j.physrep.2010.03.002 (see p. 100).

[Shi96a] J. M. Shilton, V. I. Talyanskii, M. Pepper, D. A. Ritchie, J. E. F. Frost, C. J. B. Ford, C. G. Smith, and G. A. C. Jones: 'High-frequency single-electron transport in a quasi-one-dimensional GaAs channel induced by surface acoustic waves', *Journal of Physics: Condensed Matter* **8** (1996), L531, DOI: 10.1088/0953-8984/8/38/001 (see pp. 35, 36).

[Shi96b] J. M. Shilton, D. R. Mace, V. I. Talyanskii, Y. Galperin, C. B. Simmons, M. Pepper, and D. A. Ritchie: 'On the acoustoelectric current in a one-dimensional channel', *Journal of Physics: Condensed Matter* **8** (1996), L337, DOI: 10.1088/0953-8984/8/24/001 (see p. 35).

[Sho94] P. W. Shor: 'Algorithms for Quantum Computation: Discrete Logarithms and Factoring', *Proceedings of the 35th Annual Symposium on Foundations of Computer Science*, 1994, 124–134, DOI: 10.1109/SFCS.1994.365700 (see pp. 1, 165).

[Sho95] P. W. Shor: 'Scheme for reducing decoherence in quantum computer memory', *Phys. Rev. A* **52** (1995), R2493–R2496, DOI: 10.1103/PhysRevA.52.R2493 (see pp. 2, 166).

[Sil07] M. A. Sillanpää, J. I. Park, and R. W. Simmonds: 'Coherent quantum state storage and transfer between two phase qubits via a resonant cavity', *Nature* **449** (2007), 438–442, DOI: 10.1038/nature06124 (see pp. 4, 168).

[Spr02] D. Sprinzak, Y. Ji, M. Heiblum, D. Mahalu, and H. Shtrikman: 'Charge Distribution in a Kondo-Correlated Quantum Dot', *Phys. Rev. Lett.* **88** (2002), 176805, DOI: 10.1103/PhysRevLett.88.176805 (see p. 11).

[Ste96] A. M. Steane: 'Error Correcting Codes in Quantum Theory', *Phys. Rev. Lett.* **77** (1996), 793–797, DOI: 10.1103/PhysRevLett.77.793 (see pp. 2, 166).

[Sto05] J. A. H. Stotz, R. Hey, P. V. Santos, and K. H. Ploog: 'Coherent spin transport through dynamic quantum dots', *Nature Materials* **4** (2005), 585–588, DOI: 10.1038/nmat1430 (see pp. 4, 36, 168).

[Sto08] J. A. H. Stotz, R. Hey, P. V. Santos, and K. H. Ploog: 'Enhanced spin coherence via mesoscopic confinement during acoustically induced transport', *New Journal of Physics* **10** (2008), 093013 (see pp. 4, 37, 168).

[Stu32] E. C. G. Stueckelberg: 'Theorie der unelastischen Stosse zwischen Atomen', *Helvetica Physica Acta* **5** (1932), 369–422 (see p. 100).

[Tay05] J. M. Taylor, H.-A. Engel, W. Dür, A. Yacoby, C. M. Marcus, P. Zoller, and M. D. Lukin: 'Fault-tolerant architecture for quantum computation using electrically controlled semiconductor spins', *Nature Physics* **1** (2005), 177–183, DOI: 10.1038/nphys174 (see pp. 3, 167).

[Tay07] J. M. Taylor, J. R. Petta, A. C. Johnson, A. Yacoby, C. M. Marcus, and M. D. Lukin: 'Relaxation, dephasing, and quantum control of electron spins in double quantum dots', *Phys. Rev. B* **76** (2007), 035315, DOI: 10.1103/PhysRevB.76.035315 (see pp. 26, 28).

[Tha12] R. Thalineau, S. Hermelin, A. D. Wieck, C. Bäuerle, L. Saminadayar, and T. Meunier: 'A few-electron quadruple quantum dot in a closed loop', *Applied Physics Letters* **101**, 103102 (2012), DOI: 10.1063/1.4749811 (see pp. 3, 167).

[Tok06] Y. Tokura, W. G. van der Wiel, T. Obata, and S. Tarucha: 'Coherent Single Electron Spin Control in a Slanting Zeeman Field', *Phys. Rev. Lett.* **96** (2006), 047202, DOI: 10.1103/PhysRevLett.96.047202 (see p. 29).

[Tri08] M. Trif, V. N. Golovach, and D. Loss: 'Spin dynamics in InAs nanowire quantum dots coupled to a transmission line', *Phys. Rev. B* **77** (2008), 045434, DOI: 10.1103/PhysRevB.77.045434 (see pp. 3, 168).

[Tri13] L. Trifunovic, F. L. Pedrocchi, and D. Loss: 'Long-Distance Entanglement of Spin Qubits via Ferromagnet', *Phys. Rev. X* **3** (2013), 041023, DOI: 10.1103/PhysRevX.3.041023 (see pp. 4, 168).

[Tri12] L. Trifunovic, O. Dial, M. Trif, J. R. Wootton, R. Abebe, A. Yacoby, and D. Loss: 'Long-Distance Spin-Spin Coupling via Floating Gates', *Phys. Rev. X* **2** (2012), 011006, DOI: 10.1103/PhysRevX.2.011006 (see pp. 4, 168).

[Tyr12] A. M. Tyryshkin, S. Tojo, J. J. L. Morton, H. Riemann, N. V. Abrosimov, P. Becker, H.-J. Pohl, T. Schenkel, L. W. Thewalt, K. M. Itoh, and S. A. Lyon: 'Electron spin coherence exceeding seconds in high-purity silicon', *Nature Materials* **11** (2012), 143–147, DOI: 10.1038/nmat3182 (see pp. 3, 167).

[VH92] H. Van Houten, C.W.J. Beenakker, and A.A.M. Staring: 'Coulomb-Blockade Oscillations in Semiconductor Nanostructures', English, *Single Charge Tunneling*, vol. 294, 1992, 167–216, DOI: 10.1007/978-1-4757-2166-9_5 (see pp. 9, 169).

[Vel14] M. Veldhorst, J. C. C. Hwang, C. H. Yang, A. W. Leenstra, B. de Ronde, J. P. Dehollain, J. T. Muhonen, F. E. Hudson, K. M. Itoh, A. Morello, and A. S. Dzurak: 'An addressable quantum dot qubit with fault-tolerant control-fidelity', *Nature Nanotechnology* (2014), DOI: 10.1038/nnano.2014.216 (see pp. 3, 167).

[VD01] J. Von Delft and D. C. Ralph: 'Spectroscopy of discrete energy levels in ultrasmall metallic grains', *Physics Reports* **345** (2001), 61–173 (see p. 5).

[Wan11] X. Wang, S. Yang, and S. Das Sarma: 'Quantum theory of the charge-stability diagram of semiconductor double-quantum-dot systems', *Phys. Rev. B* **84** (2011), 115301, DOI: 10.1103/PhysRevB.84.115301 (see pp. 9, 169).

[Wee88] B. J. van Wees, H. van Houten, C. W. J. Beenakker, J. G. Williamson, L. P. Kouwenhoven, D. van der Marel, and C. T. Foxon: 'Quantized conductance of point contacts in a two-dimensional electron gas', *Phys. Rev. Lett.* **60** (1988), 848–850, DOI: 10.1103/PhysRevLett.60.848 (see p. 10).

[Wei57] G. Weinreich and H. G. White: 'Observation of the Acoustoelectric Effect', *Phys. Rev.* **106** (1957), 1104–1106, DOI: 10.1103/PhysRev.106.1104 (see p. 35).

[Wha88] D. A. Wharam, T. J. Thornton, R. Newbury, M. Pepper, H. Ahmed, J. E. F. Frost, D. G. Hasko, D. C. Peacock, D. A. Ritchie, and G. A. C. Jones: 'One-dimensional transport and the quantisation of the ballistic resistance', *Journal of Physics C: Solid State Physics* **21** (1988), L209, DOI: 10.1088/0022-3719/21/8/002 (see p. 10).

[Wie02] W. G. van der Wiel, S. De Franceschi, J. M. Elzerman, T. Fujisawa, S. Tarucha, and L. P. Kouwenhoven: 'Electron transport through double quantum dots', *Rev. Mod. Phys.* **75** (2002), 1–22, DOI: 10.1103/RevModPhys.75.1 (see pp. 8, 10, 18, 73, 149).

[Woo02] L. M. Woods, T. L. Reinecke, and Y. Lyanda-Geller: 'Spin relaxation in quantum dots', *Phys. Rev. B* **66** (2002), 161318, DOI: 10.1103/PhysRevB.66.161318 (see p. 25).

[Yam14] M. Yamagishi, N. Watase, M. Hashisaka, K. Muraki, and T. Fujisawa: 'Spin-dependent tunneling rates for electrostatically defined GaAs quantum dots', *Phys. Rev. B* **90** (2014), 035306, DOI: 10.1103/PhysRevB.90.035306 (see pp. 16, 103, 112).

[Zen32] C. Zener: 'Non-Adiabatic Crossing of Energy Levels', *Proc. R. Soc. Lond. A* **137** (1932), 696–702, DOI: 10.1098/rspa.1932.0165 (see pp. 31, 100).

[Zim03] N. M. Zimmerman and M. W. Keller: 'Electrical metrology with single electrons', *Measurement Science and Technology* **14** (2003), 1237, DOI: 10.1088/0957-0233/14/8/307 (see p. 35).

[Zor95] A. B. Zorin: 'The thermocoax cable as the microwave frequency filter for single electron circuits', *Review of Scientific Instruments* **66** (1995), 4296–4300, DOI: 10.1063/1.1145385 (see p. 40).

[Zum02] D. M. Zumbühl, J. B. Miller, C. M. Marcus, K. Campman, and A. C. Gossard: 'Spin-Orbit Coupling, Antilocalization, and Parallel Magnetic Fields in Quantum Dots', *Phys. Rev. Lett.* **89** (2002), 276803, DOI: 10.1103/PhysRevLett.89.276803 (see p. 24).

List of Figures

1.1 Heterostructure layers and band structure schematics 6
1.2 Schematics of the 2DEG depletion to form a quantum dot 8
1.3 Scheme of the quantum dot description used in the CI model 10
1.4 Typical QPC signal and charge stability diagram 12
1.5 Principle of energy-selective readout 16
1.6 Principle of tunnel-rate selective readout 17
1.7 Double quantum dot potential shape as a function of detuning 18
1.8 Energy diagram of the different spin states in a double quantum dot 20
1.9 Principle of Spin Blockade readout 21
1.10 Quantum state representation on a Bloch sphere 22
1.11 Influence of hyperfine interaction 27
1.12 Measurement scheme used to probe single-spin manipulation 29
1.13 Passage through an avoided crossing - Landau-Zener probability 30
1.14 Spin exchange experiment 32
1.15 Description of a surface acoustic wave 33
1.16 Basic geometries of Inter-Digital Transducers 34
1.17 Formation of moving quantum dots 36
1.18 Transfer of a single electron between distant quantum dots 38

2.1 Dilution refrigerator principle 41
2.2 Electron temperature estimation from time-averaged dot population 42
2.3 Description of the bias tees used 44
2.4 Description of the earliest SAW burst generation setup 44
2.5 Limitations of the earliest SAW burst generation setup 45
2.6 Description and characteristics of the new SAW burst generation setup . . . 46

3.1 Illustration of the different SAW-induced mechanisms involved 50
3.2 Illustration of different transfer regimes 51
3.3 Stability diagram and pulse sequence used on the source dot 53
3.4 Mappings of the electron emission with source dot potential 54
3.5 Correlations of the source and reception dots µs pulse mappings 55
3.6 Influence of the SAW parameters on the transfer statistics 57
3.7 Illustration of amplitude threshold and rise time model 59

3.8 Description of the sequence used for the source dot ns triggering 61
3.9 Nanosecond pulse effect for different SAW parameters 63

4.1 Numerical simulations of the electrostatic potential of the device 68
4.2 Stability diagrams and observation of metastable double dot patterns 70
4.3 Electron pumping to the metastable state 71
4.4 Large extent metastability patterns with fixed number of electrons 72
4.5 Standard and isolated double dot stability diagrams comparison 73
4.6 (2,0)-(1,0) transition scans for singlet and triplet spin states 75
4.7 Spin relaxation measurements with pulses to the metastable configuration . 77
4.8 Spin mixing of the separated singlet 79
4.9 Separated singlet spin mixing mapping 81
4.10 Evolution of the $|S\rangle - |T_+\rangle$ crossing with magnetic field 82
4.11 Illustration of the two possible exchange pulses 84
4.12 Rabi oscillations with an exchange pulse in detuning 85
4.13 Rabi oscillation with an exchange pulse in interdot tunnel coupling 86
4.14 Evolution of Rabi oscillations with exchange pulse in t_c at different ε values 87

5.1 Source and reception quantum dot stability diagrams 90
5.2 I_{QPC} traces of both dots during two-electron transfer experiments 91
5.3 Evolution of transfer statistics with the SAW duration 92
5.4 Spin measurement calibration on injection and reception dots 94
5.5 Post-selection step used after the electrons transfer 97
5.6 Two-electron spin transfer signal 98
5.7 Estimation of spin-orbit induced spin rotation during the transfer 99
5.8 Impact of imperfect passages through the $|S\rangle$-$|T_+\rangle$ crossing 101
5.9 Influence of spin level splitting and temperature on readout efficiency 104
5.10 Measurement of the tunneling rates for ground and excited spin states . . . 105
5.11 Influence of the measurement window on the signal contrast 107
5.12 Result of the single-electron spin transfer experiment 109
5.13 Influence of SAWs on spin measurement contrast 111
5.14 New sample in preparation for future experiments on spin coherence 114

A.1 IDT spectroscopy via transfer efficiency 138

B.1 Sequence used on the reception dot to recover the transferred electron . . . 140
B.2 Calibration of the nanosecond triggering on the reception dot 142
B.3 Transfer efficiency vs. source dot gate pulse delay 144
B.4 Time of flight experiment - data interpretation 145
B.5 Time of flight experiment - changing emission delay 146

C.1 Double dot spectroscopy via interdot tunneling to excited states 150

D.1 Triplet to singlet relaxation in the metastable position 154

E.1 Position used for spin blockade measurement 156
E.2 Observation of quantum jumps in metastable spin blockade configuration . 158

F.1 Impact of SAWs on spin coherence 160
F.2 SAW influence on double dot parameters and induced transition crossing . . 162
F.3 SAW induced spin exchange 163

APPENDIX A

Frequency dependence of the transfer efficiency

In order to generate a SAW, the IDT must be driven at its resonant frequency. It is usually determined by reflection measurements (see [Her12]) or by SAW-assisted transport experiments. However, it can also be done by looking at the dependence of the transfer efficiency with the IDT excitation frequency. The results obtained with this approach are presented in this appendix.

On the top left plot of Fig. A.1 the number of successful transfer (electron emitted from the source dot and recovered in the reception dot) is recorded as a function of the frequency of the signal applied on the IDT. It reveals several resonant frequencies, each being more or less significant. The existence of more than one resonant frequency was not expected. It might be due to cavity effect that can be encountered with single finger IDTs (see section 1.6.1). Considering the IDT width of $L = 70\,\mu\text{m}$ and the SAW velocity around $c = 2800\,\text{m}\,\text{s}^{-1}$, the spectral range between two modes of the cavity can be estimated by $\Delta\nu = \frac{c}{2L} = 20\,\text{MHz}$. This looks consistent with the separation between the two major peaks observed on the data.

As the transfer efficiency is saturating close to 1 for two peaks it is not possible to know which resonance is the best to achieve the electron transfer. In order to compare their relative magnitude, the SAW burst duration is reduced to lower the electron transfer efficiency. This new measurement is presented on the bottom left plot of Fig. A.1. It is now clear that the best position corresponds to the peak at $f_{RF} = 2.632\,\text{GHz}$. It can be noted that the sensitivity to smaller amplitude signals has been lost as a counterpart. A finer scan of the left resonance (right plot of Fig. A.1) allows to determine the optimal frequency at 2.6322 GHz. In principle, this resonance should have a Lorentzian shape. However, this poorly fits to the data in our case (see red line). We conjecture that the base of the resonance does not appear in this curve. Indeed away from the resonance, the amplitude reached by the generated SAW gets smaller, it will not be sufficient at some point to ensure the electron transfer and appear in the data. This effect can be taken into account by adding a constant parameter to the fit model in order to assume that only the top of the resonance is seen here. This is in better agreement with the data. The $-3\,\text{dB}$ bandwidth of the resonance is found to be 2.4 MHz. This result is consistent with the IDT rise time determined in section 3.4.

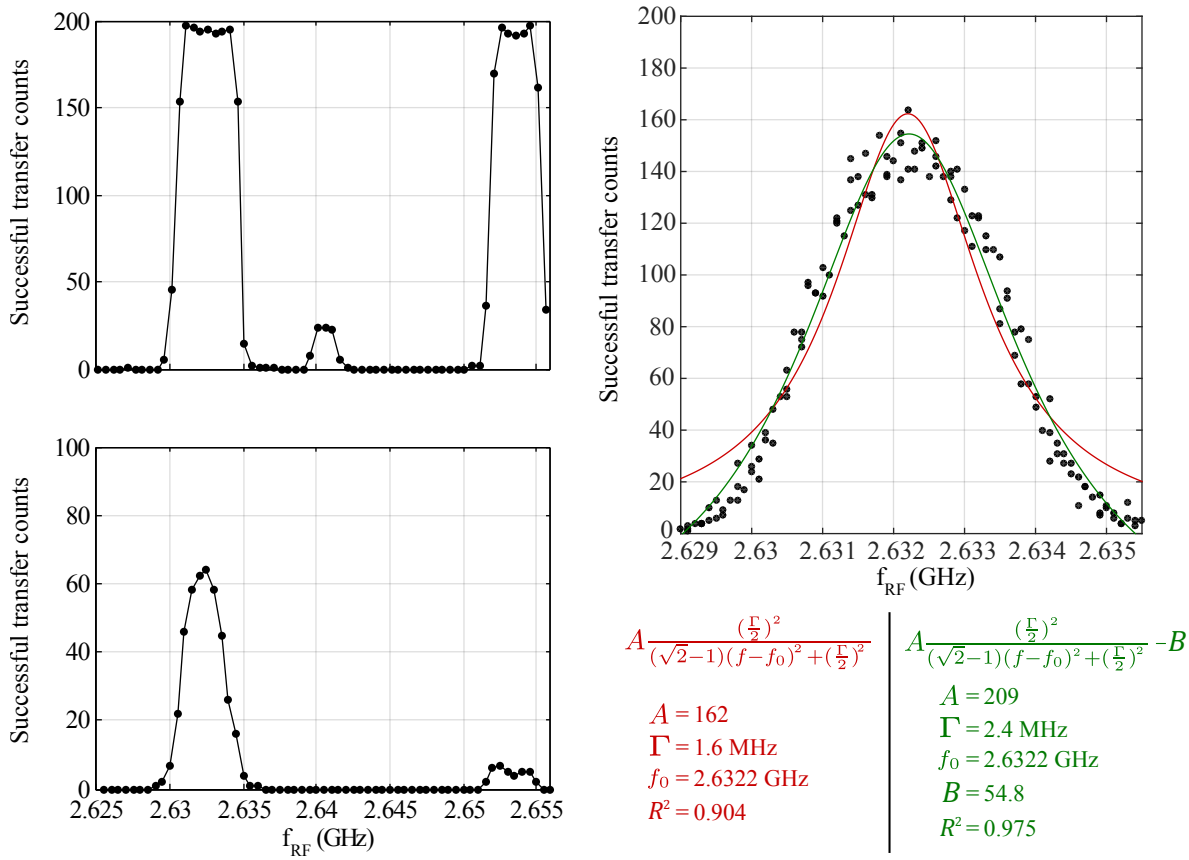

Figure A.1: (top left) Number of successful electron transfers as a function of the RF frequency applied on the IDT (25 dBm applied for 170 ns). Experiments are repeated 200 times for each data point. **(bottom left)** Same scan using a 25 dBm burst of only 140 ns in order to reduce the transfer efficiency and avoid the signal saturation. Experiments are repeated 100 times for each data point. **(right)** Close up scan on the largest IDT resonance (200 repetitions per point). Data are fitted with two Lorentzian models. The models, fit parameters and coefficients of determination are listed below the plot.

APPENDIX B

Extending nanosecond triggering to the reception dot and time of flight measurements

Nanosecond pulsing on the reception dot

The work presented here consists in adapting to the reception dot the triggering developments that have been achieved on the source dot (see section 3.5). The interest is a proof of principle for time of flight experiments. In our case it should enable to check the time spent by the electron within the 1D channel. Up to now it has been shown that under proper conditions, less than 1 ns is required to initiate the electron emission from the source dot, but there is no proof that the transfer is straightforward after that (electron traveling in the same moving dot from one side to another). For instance, irregularities in the channel potential might hinder the transfer to the reception dot and therefore might increase the electron traveling time (for instance need of several SAW periods to pass across impurities in the channel).

In order to allow triggering on each side of the sample, another run of experiments has been done with both source and reception dots equipped with bias tees. We will first focus on the reception dot. As a start we explain in details the gate voltage sequence that is used on the reception dot without nanosecond pulsing. This is very similar to what is done on the injection side:

- First the reception quantum dot is completely emptied (point L'_0 on the stability diagram of Fig. B.1).
- It is then rapidly (microsecond timescale) brought to an intermediate metastable position (point I'). Charge measurement is performed at this point.
- A 20 µs negative pulse is finally used on $V_{L'}$ to bring the dot to point T'. This voltage pulse aims at engineering a large tunnel barrier with a slope as steep as possible between the reception dot and its reservoir, in order to stop the transferred electron in the reception dot.
- Once back in position I', the charge is monitored again in order to check whether the electron has been received or not.

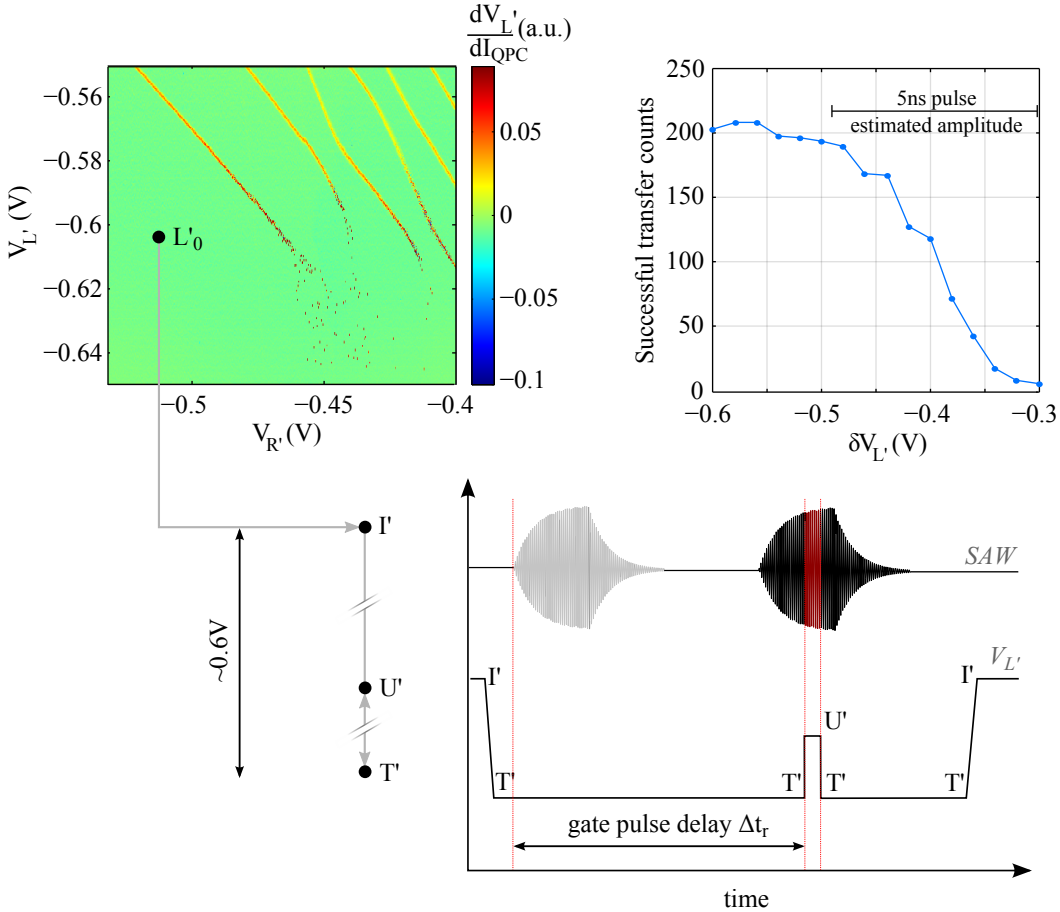

Figure B.1: Sequence used on the reception dot in order to recover the transferred electron. **(top left)** Stability diagram of the reception dot. The different positions used during a transfer sequence are indicated. **(top right)** Evolution of the successful transfer counts (out of 250 repetitions) as a function of the relative voltage applied on the reception gate $V_{L'}$ (position I' used as reference). The experiment is done with a SAW burst of 28 dBm and 170 ns. **(bottom)** Timing schematics of the nanosecond pulsing experiment. The reception dot is pulsed to position T' for $\sim 20\,\mu$s. In addition a 5 ns pulse to position U' is applied, with a delay Δt_r with respect to the SAW burst triggering.

To characterize the reception efficiency, a transfer experiment has been done for different positions of the point T' ($\delta V_{L'}$ corresponds to the relative shift with respect to point I'). The standard procedure has been used to prepare an electron in transfer position on the source quantum dot (no nanosecond pulse applied). The result is shown on the top right plot of Fig. B.1. The number of successful transfer (*i.e.* electron emitted from the source dot and recovered in the reception dot) is plotted as a function of $\delta V_{L'}$. The transfer efficiency increases as the position of T' is made more negative. This is interpreted as follows: if the $\delta V_{L'}$ coordinate of T' is large enough, the tunnel barrier that is induced becomes too thick and steep to be crossed and the electron ends up blocked in the reception dot. Without this pulse, the electron will not be stopped in the reception dot but will end up in the reservoir (and therefore will not be detected).

We now consider the engineering of some triggering on the reception dot. We have seen that a change on the $V_{L'}$ voltage has an impact on the reception efficiency. Similarly to the injection case, it should be possible to vary this parameter at a nanosecond timescale during the passage of the SAW. The pulse sequence used on the reception dot is then as follows (see also bottom right of Fig. B.1):

- The reception quantum dot is emptied (point L_0' on Fig. B.1 stability diagram).
- It is brought (microsecond timescale) to the intermediate metastable position (point I'). Charge measurement is performed at this point.
- The dot is then pulsed to the position T' for 20 µs. During that time, the SAW burst is applied as well as a 5 ns positive pulse[1] on V_L' to reach position U'.
- The dot is finally set back to point I', and a new charge measurement is performed in order to learn whether the electron has been received or not.

Point T' is used as a base position while the SAW burst is applied. The coordinate used for this point in the following is $\delta V_{L'} = -0.48\,\mathrm{V}$. In this position the electron is stopped in the reception dot. On top of it, the nanosecond pulse to position U' temporarily reduces the dot/reservoir potential barrier and disables the capacity to retain the electron under SAW irradiation. The estimated amplitude of the nanosecond pulse gives a coordinate of $\delta V_{L'} = -0.3\,\mathrm{V}$ for this point (see top right plot of Fig. B.1). Similarly to the injection case, the coincidence of the gate voltage pulse and the SAW excitation arrival to the dot can be adjusted through the delay parameter Δt_r (see bottom right schematics of Fig. B.1).

There are two main differences compared to the case of the injection triggering. First, the effect of the nanosecond pulse should be seen as a reduction of the transfer efficiency since it will prevent the good reception of the electron. Therefore, we should not observe a peak but a dip in the transfer efficiency. Second, this procedure does not give access to the probability for an electron to arrive during the nanosecond pulse, but rather to the probability that it arrived before that time. This is in some sense equivalent to a cumulative probability. In principle, it should be possible to recover the arrival time probability through the signal derivative.

1 The nanosecond pulse is elongated to 5 ns instead of 1 ns in order to achieve better signal visibility.

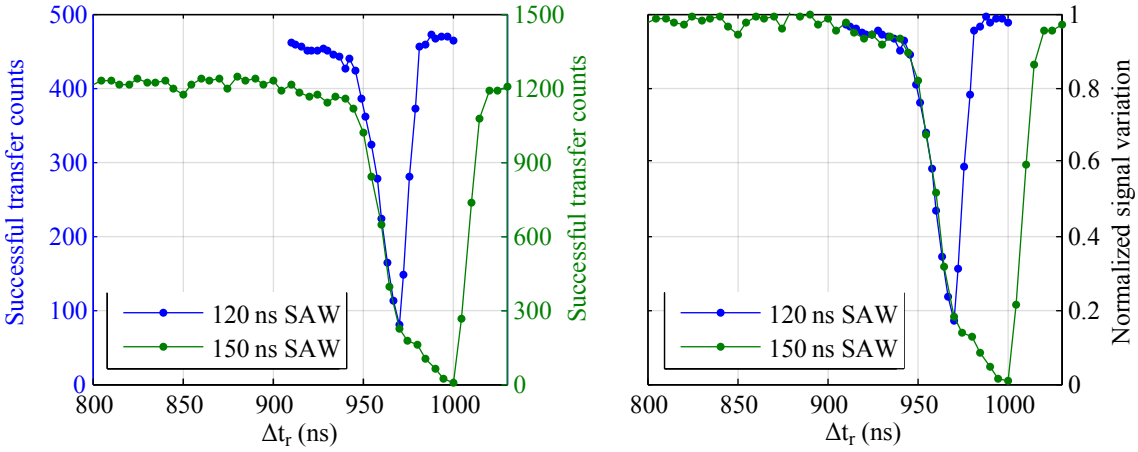

Figure B.2: Calibration of the nanosecond triggering on the reception dot. The source dot is maintained in position T during the transfer (no nanosecond pulse is used on the source dot). On the reception dot, a 5 ns positive pulse is applied on gate $V_{L'}$ in order to set the dot for a short time in the unprotected position U'. **(left)** Raw signal obtained for different SAW duration. SAW power is 28 dBm on the RF source. The signal background for the 120 ns SAW burst data (blue curve) corresponds to the usual transfer efficiency around 95%. For the 150 ns SAW burst data (green curve), the background transfer efficiency drops around 80%. This is due to the fact that the probability to preserve an electron in the reception dot is lowered for longer SAW duration. Indeed a longer SAW burst reaches a higher amplitude and offers more attempts for the electron to leave the reception dot. **(right)** Same data with removed background and rescaled signal for better comparison of the curves.

In order to calibrate the effect of this procedure, the transfer efficiency dependence as a function of Δt_r has been measured. The source dot is maintained at position T during the whole passage of the SAW (no electron emission triggering is implemented). The electron emission efficiency achieved is close to unity. The results of this experiment are shown on the left plot of Fig. B.2. The transfer efficiency is plotted as a function of Δt_r. It has been done for two different SAW duration values, respectively 120 ns and 150 ns.

For $\Delta t_r \leq 940$ ns, the transfer efficiency remains at a background value around 95 % (resp. 80 %). A large decrease of the transfer efficiency is then observed until $\Delta t_r = 970$ ns (resp. $\Delta t_r = 1000$ ns) and finally reaches back its initial background value. The interpretation is as follows. For $\Delta t_r \leq 940$ ns, the nanosecond voltage pulse to position U' is applied before the arrival of the electron. The reception dot remains therefore in position T' during all the passage of the SAW burst, ensuring a high probability to catch the transferred electron. A high transfer efficiency is thus measured. When the reception dot pulse to U' and the SAW excitation coincides, the transferred electron can be removed, resulting in the observed drop of the transfer efficiency. Finally for too large values of Δt_r, the nanosecond voltage pulse is applied after the passage of the SAW burst and has no effect again. This confirms that the nanosecond pulse has to coincide with the SAW excitation in order to empty the reception dot (via SAW-assisted tunneling of the electron through the dot/reservoir barrier). It is worth noting that the successful transfer probability is indeed similar for the

shortest and largest values of Δt_r.

We can now look at the influence of the SAW duration on the signal. Two different SAW bursts have been used with duration of either 120 ns or 150 ns. In order to be able to better compare the two experiments, the background difference is suppressed and the curves are renormalized (see right plot of Fig. B.2). It can be seen that the falling edges of both curves coincide perfectly. Consistently with our interpretation, the return to the background value is postponed by 30 ns when the SAW duration is increased by this amount.

In summary, this first experiment proves that the reception dot can be emptied at a specific time during the SAW burst thanks to the application of a nanosecond pulse. If the electron is already present in the dot, the SAW modulation of the potential will allow it to tunnel off the dot and relax to the reservoir. This tends to lower the transfer efficiency. On the contrary if the pulse is applied before the electron arrives, it will have no effect and the transferred electron remains blocked in the reception dot. In that case the transfer efficiency stays high.

Measurement of the electron transfer time

The objective is now to implement nanosecond pulsing on the source dot and combine it to the nanosecond pulsing of the reception dot. Indeed, we have demonstrated that the source dot pulsing procedure enables to trigger the electron emission time. Reciprocally, the reception dot pulsing procedure provides information about its arrival time. Using both procedures simultaneously should permit to estimate the electron time of flight. The sequence used for the experiment is as follows:

- The source quantum dot is coupled to its reservoir in order to load one electron. On the same time the reception quantum dot is emptied.
- Both dots are brought to their intermediate metastable positions in a microsecond timescale (point I and I'). Charge measurements are performed at this point.
- The source dot is then pulsed to the position P for 20 µs. In parallel, the reception dot is pulsed to the position T'. During that time, the SAW burst is applied as well as a 3 ns negative pulse on V_L (to reach position T, see Fig. B.3) and a 5 ns positive pulse on V_L' (to reach position U', similarly to the experiment of Fig. B.2).
- The dots are finally set back to point I and I', and new charge measurements are performed in order to learn about the transfer outcome.

The result of this experiment is shown on the top left plot of Fig. B.4 (blue curve). The 3 ns pulse on the source dot is applied at $\Delta t_s = 963$ ns. The 5 ns pulse on the reception dot is applied with varying Δt_r. The successful transfer number (out of 1000 repetitions) is represented as a function of Δt_r. The background value is around 60 % transfer efficiency, which is consistent with the transfer efficiency measured at $\Delta t_s = 963$ ns on Fig. B.3.

As we have seen on Fig. B.3, the electron emission triggering is not perfect and it remains a probability that the electron leaves the source dot at a non-controlled time (*i.e.* while the dot is in the protected position P). The influence of these events on the data can be deduced by doing the same measurement but removing the nanosecond pulse on

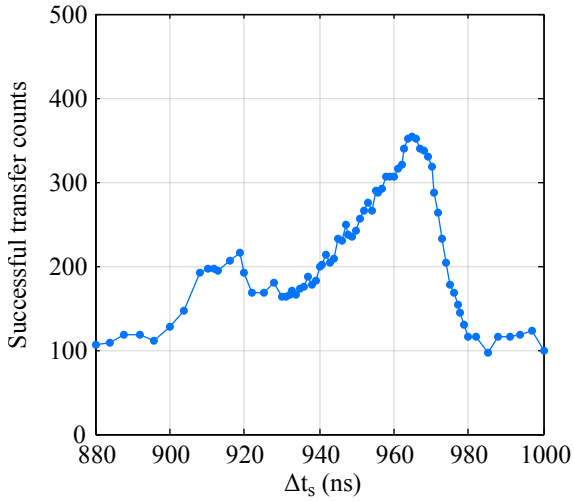

Figure B.3: Evolution of the transfer efficiency as a function of the nanosecond pulse delay Δt_s. The triggering of the source dot has been implemented similarly to what has been presented in section 3.5. However during this experiment the voltage difference between the protected and transfer position was larger than the achievable amplitude of the nanosecond pulse. As a result a perfect on/off of the electron emission was not possible and a trade-off had to be done. A 3 ns pulse applied on V_L (instead of 1 ns) in order to achieve better signal visibility. A transfer efficiency of more than 70% is achieved when working around $\Delta t_s = 965$ ns. However, the curve background is not zero but 20% (see shortest and largest values of Δt_s). It reveals that a finite probability remains for an electron to be emitted at another time that during the nanosecond pulse. This is due to an imperfect "protected" position. In the end one can only claim a lower bound of 50% for the probability to send the electron during the 3 ns pulse. A 28 dBm SAW burst of 120 ns is used.

the source dot (*i.e.* maintaining it in position P during the whole passage of the SAW burst). Only non-triggered events will therefore be detected. The result of this experiment corresponds to the black curve on the top left plot of Fig. B.4. Subtracting this signal to the previous curve will allow to keep only the triggered events contribution.

The remaining contribution of the triggered events is shown on the top right plot of Fig. B.4. The background signal is removed and the signal amplitude is normalized. It is interpreted as follows. At the very beginning of the curve (point A), the nanosecond pulse on the reception dot is applied before the electron emission and has thus no effect (see timing schematics on the bottom of Fig. B.4). One has to wait for this pulse to overlap with the time window during which the electron arrives to the reception dot (see point B) in order to start having electrons lost to the reservoir. For larger delays, it is more and more likely that the electron gets cleared out, until saturating when the reception pulse is applied after all the electrons arrived (point D). The count of electrons that remained in the dot is then constant up to the moment when the SAW amplitude starts decaying (point E). Indeed we have seen that the impact of the reception pulse is suppressed if the SAW amplitude becomes too small. This is why the signal is finally back to its initial value for large Δt_r (point F).

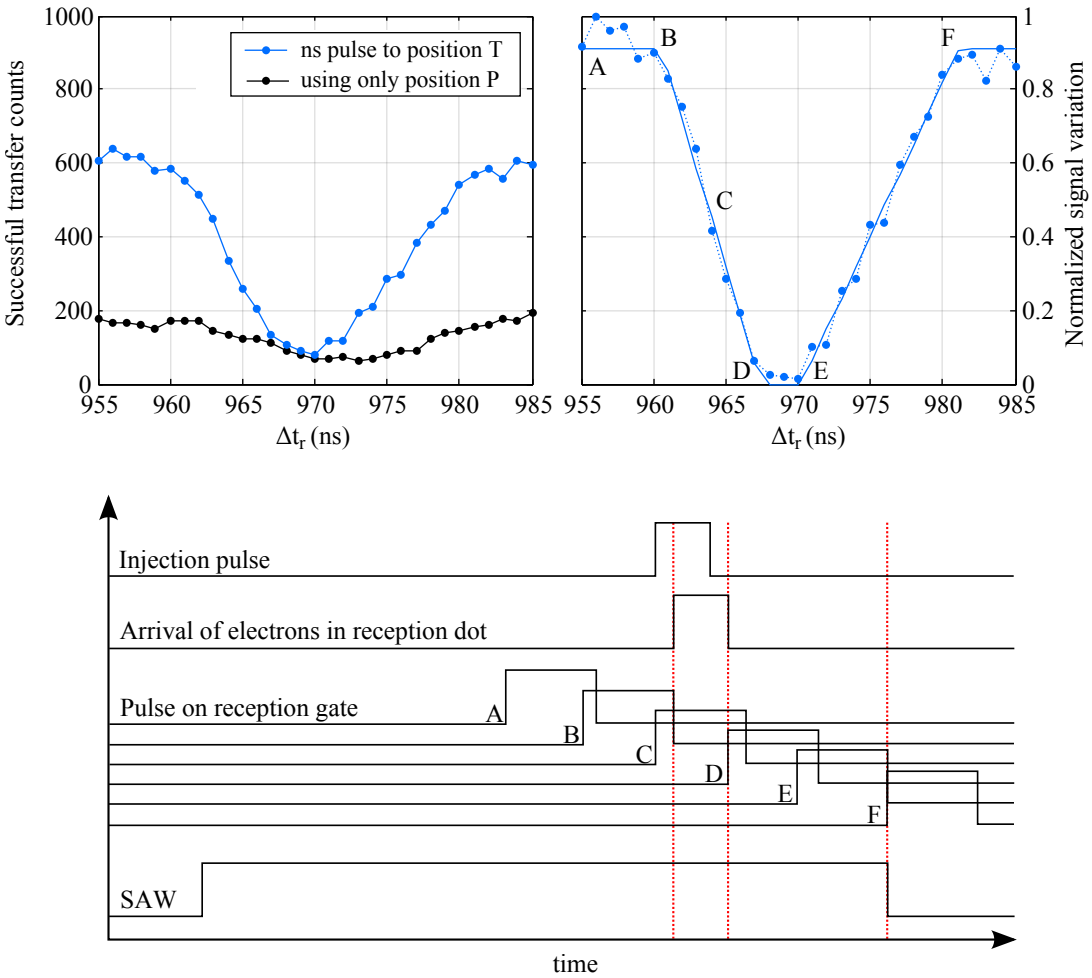

Figure B.4: Experimental transfer results with triggering on both quantum dots. **(top left)** Successful transfer counts as a function of the reception dot nanosecond pulse (T'-U') delay (Δt_r). The duration of this nanosecond pulse is 5 ns. For the blue curve, a 3 ns pulse (P-T) is used to trigger the electron emission time. For the black curve, the source dot remains in the protected position P (no nanosecond pulse is applied). The SAW amplitude and duration are 28 dBm and 120 ns on both curves. **(top right)** Difference between the two curves of the top left graph. This allows to select only the contribution of triggered emissions. The remaining signal is normalized. **(bottom)** timing schematics of the experiment. The different reception gate pulse delays drawn are labeled on the top right figure.

In order to determine the electron time of flight, we can look at the Δt_r value of specific points we have defined. We call τ_{flight} the electron travel time between the quantum dots, τ_s the source pulse duration and τ_r the reception pulse duration. Using the basic model shown on Fig. B.4, we should have:

$$\Delta t_r(B) = \Delta t_s + \tau_{flight} - \tau_r \tag{B.1a}$$

$$\Delta t_r(D) = \Delta t_s + \tau_s + \tau_{flight} \tag{B.1b}$$

In our case, the experiment parameters are $\Delta t_s = 963\,\text{ns}$, $\tau_s = 3\,\text{ns}$ and $\tau_r = 5\,\text{ns}$, and we measure $\Delta t_r(B) \approx 960\,\text{ns}$ and $\Delta t_r(D) \approx 968\,\text{ns}$. It results in $\tau_{flight} \approx 2\,\text{ns}$.

Similar curves have been measured for different values of the Δt_s (see Fig. B.5). It can be seen that a change in the electron emission time results in a shift of the same value of the falling part of the signal (BD segment). This is consistent with our interpretation.

Each curve of the dataset has been fitted using an elementary model. It is assumed that the electron have zero probability to leave the source dot in position P, and a constant probability per unit of time p_e to be emitted during the 3 ns pulse to position T. This results in a step-like occupancy probability of the reception dot, with a linear rise of 3 ns starting at $\Delta t_s + \tau_{flight}$. Since we consider normalized signals, p_e is set to $\frac{1}{3}\,\text{ns}^{-1}$. On the reception side, it is considered a constant probability p_r per unit of time to remove an electron initially present in the dot when it is set to position U' (*i.e.* between Δt_r

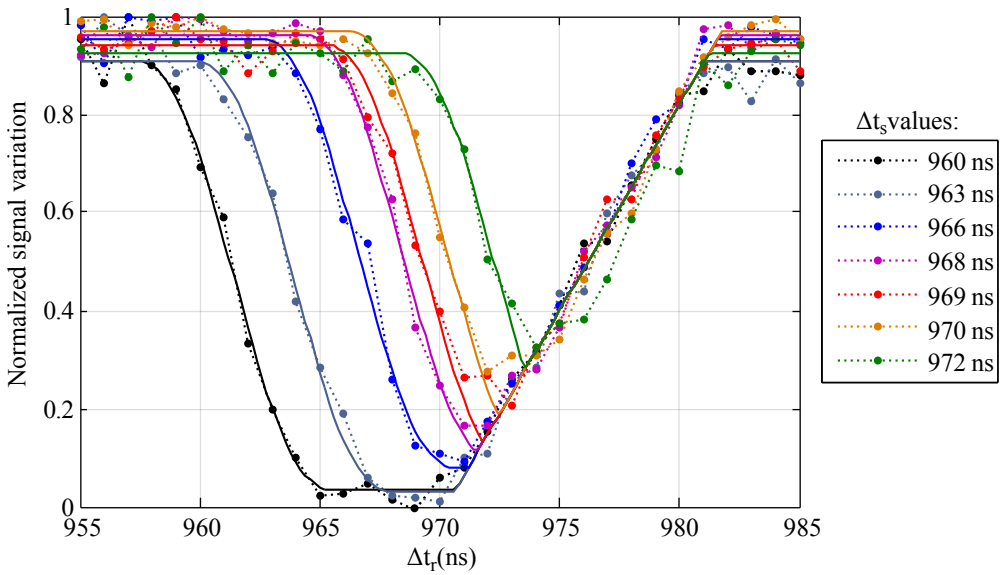

Figure B.5: Transfer efficiency signal as a function of Δt_r for different electron emission triggering time (Δt_s). Similar data post-treatment as for the top right plot of Fig. B.4 has been done for all the curves. Dashed lines corresponds to the data and continuous lines are fits computed with the toy model described in the main text. The SAW parameters are 28 dBm for 120 ns.

and $\Delta t_r + 5\,\mathrm{ns}$). p_r is assumed to be zero otherwise. The fit procedure consists in the convolution of the reception dot occupancy and p_r in order to interpolated the falling part of the signals. The fit parameters are the background value of the signal, the value of p_r during the reception pulse and the electron time of flight τ_{flight}. The decay of the SAW burst amplitude at large Δt_r (*i.e.* the "EF" part of the data) is not modeled here and is manually adjusted afterward.

The τ_{flight} values extracted from the fits of the different curves are ranging between 1.2 ns and 2.4 ns, with an average value of 1.6 ns. Given the distance separating the two quantum dots (around 4.1 µm) and the SAW velocity equals ($2800\,\mathrm{m\,s^{-1}}$), it results in an expected time of flight of 1.5 ns, consistent with the output of the fit.

APPENDIX C

Probing the excited states of the metastable double quantum dot

In order to further characterize the metastable double dot system, it could be interesting to reveal the excited charge states on both parts of the double dot. To that purpose, a usual technique for quantum dots consists in transport measurement across the system. When changing the relative alignment of the different chemical potentials, the conductance of the system varies and can be measured [Kou97; Wie02]. In the case of an isolated quantum dot, transport measurement through the system is not possible. The equivalent of transport in our case is the transfer of a single charge from one minimum of potential to the other. If one is able to access the typical time of this single charge transfer, it is possible to deduce an equivalent of the conductance of the system. The method presented here is equivalent to the pulse-sense method proposed in [Joh05a], but with much smaller interdot coupling that allows for a real-time detection of the tunneling events.

The procedure is as follows:

- First, the charging dot is coupled to the reservoir and loaded with two electrons. It is waited 15 ms in this position.
- Next, the system is brought within a microsecond to the metastable position in the (1,1) (resp. (2,0)) configuration. 200 µs are waited in this position.
- The system is then set in a microsecond close to the (2,0)-(1,1) degeneracy line. This is done for varying V_L in order to scan across the degeneracy line. Tunneling of an electron between the two parts of the double dot will be induced when reaching the (2,0) (resp. (1,1)) region. The interdot tunnel coupling is chosen to be comparable to our measurement bandwidth (kHz). The QPC signal is monitored for 20 ms.

The results of such an experiment are presented on Fig. C.1. On the x-axis is indicated the V_L voltage shift relative to the charge degeneracy line (labeled δV_L), the y-axis corresponds to the time elapsed after setting the system to this position, and the color refers to the current monitored by the QPC. Each vertical line is the average of 200 single-shot measurements.

On the left graph, the system is initialized in the (1,1) metastable region before being pulsed close to the degeneracy line. For the most negative values of δV_L, the ground state

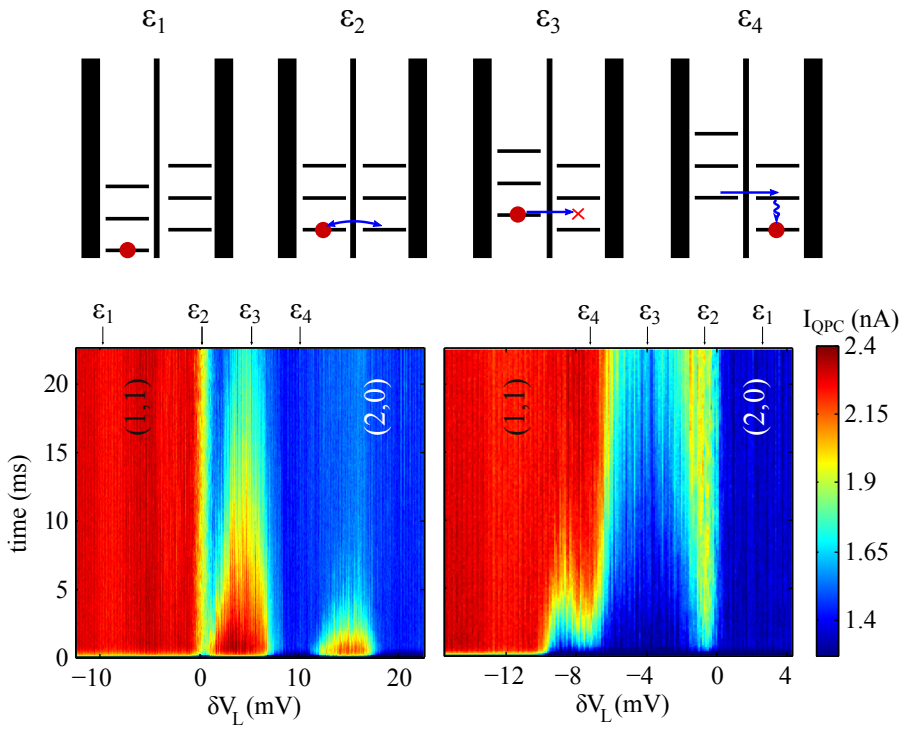

Figure C.1: Double dot spectroscopy through interdot tunneling to excited states. **(top)** Schematics of the relative alignment of the two minima of the double dot in different positions on the two lower plots. **(bottom left)** Each vertical line corresponds to the average of 200 single-shot measurements. For each measurement, the system is initialized in the (1,1) charge configuration. It is then pulsed to a small interdot coupling position within 1 µs close to the (1,1)-(2,0) degeneracy. Different values of V_L are tried around the degeneracy point, corresponding to $\delta V_L = 0$ mV. The energy levels configuration of the double dot is depicted on the upper schematics for different V_L values. **(bottom right)** Same scan with the system initialized in the (2,0) charge configuration before the measurement.

is still (1,1) after the pulse (see detuning value ε_1 on the top sketch). No tunneling can happen. At $\delta V_L = 0$, the (1,1) and (2,0) ground states are resonant (case ε_2). It is therefore possible for an electron to alternately tunnel between both parts of the double dot and a QPC current corresponding to the mean of the (1,1) and (2,0) values is measured. For slightly positive values of δV_L, it becomes energetically favorable for the system to be in a (2,0) configuration. However no state is available at the corresponding energy (case ε_3). Inelastic tunneling is thus required to reach a (2,0) state and will result in long tunneling times. Around $\delta V_L = 10$ mV, the (1,1) ground state is resonant with the first (2,0) excited state (case ε_4). Resonant tunneling happens on a much faster timescale and cannot be seen on this measurement. After tunneling, the system relaxes to the (2,0) ground state and the charge is blocked. For even more positive values of δV_L, one can see another alternation between resonant and off-resonant situations. It can be noted that inelastic tunneling

becomes faster and faster as δV_L is increased, which prevents us from probing the higher excited states. The reason might be that the overlap between the reservoir and the dot orbital becomes larger when dealing with higher excited states, inducing a stronger tunnel rate. A similar reasoning can be done to explain the right graph by simply reversing the initial and final charge configurations. The equivalent position ε_1 to ε_4 are reported on the graph.

On the left graph, tunneling occurs from right to left and allows to probe the left dot excited states while on the left graph, tunneling is from left to right and enables the spectroscopy of the right dot. Taking into account the lever arm of the gate V_L, the energy of the first excited states for each part of the double dot can be estimated around $400 - 500\,\mu\text{eV}$. Since we find comparable energies for both parts of the system, it can be concluded that the size of the channel dot is comparable to the one of the loading dot.

APPENDIX D

Observation of long relaxation times in metastable position

In the experiments presented in section 4.3, only a very short time is spent in the isolated metastable position. The relaxation process was occurring in the position L_2, *i.e.* coupled to the electron reservoir. It could be interesting to check how is affected the spin relaxation process when the system is in the metastable position. To that purpose, we have performed a very similar experiment as in section 4.3 but with the relaxation process occurring in the metastable position. The successive steps of the experiment are as follows:

- Two electrons are loaded into the dot (point L_2 on Fig. 4.7).
- After 100 µs (to ensure that the two electrons are loaded) the system is pulsed to a metastable position, remaining in the (2,0) region. Therefore, a triplet state is prepared in the metastable position.
- It is then waited a time t_{wait}, still in the metastable position.
- The system is finally set to the readout position (point M on Fig. 4.7).

The data are shown on Fig. D.1. The dark blue curve corresponds to the relaxation in point L_2. For the other curves, the waiting step is done in the metastable position. The V_L shift relative to point L_2 (labeled δV_L) is given in the legend for each curve. The more metastable is the waiting position, the longer is the relaxation time. The evolution of T_1 as a function of the relative gate voltage is shown on the right plot. An increase of almost two orders of magnitude is observed. On a different cool-down, no significant reduction of the triplet probability was observed after 500 ms, suggesting a decay on the order of the second or more. There is no clear understanding of this phenomenon for the moment. It might be related to a variation of the shape of the loading dot when varying V_L.

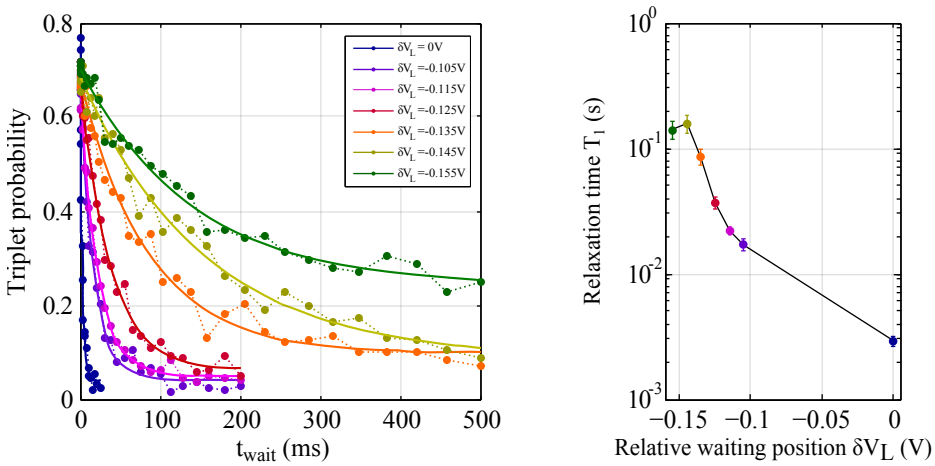

Figure D.1: (left) Triplet to singlet relaxation in the metastable position. Two electrons are loaded in point L_2. This position is held for 100 µs. For each curve presented, the V_L voltage is then shifted within 1 µs by the value indicated in the legend. This voltage is maintained for a varying time t_{wait} corresponding to the x-axis of the figure. The system is finally brought back to the measurement point within 1 µs. Data obtained under application of a 100 mT magnetic field in the sample plane. **(right)** Evolution of the relaxation times extracted from the exponential decay fits of the left plot as a function of the voltage shift of the waiting position.

APPENDIX E

Spin-blockade readout in metastable position

In section 4.3, a spin readout procedure has been developed to recover the spin state of the system in the metastable configuration. It proved to be very efficient, but it is necessary to couple the system back to the electron reservoir to perform the measurement. In order to limit the number of large voltage shifts applied during an experiment, it could be interesting to readout the spin while keeping the system in the metastable position. In section 1.3.2, we have seen that the coupling to an electron reservoir is not necessary anymore if a spin-blockade procedure is used. In principle, such a measurement should be compatible with the metastable configuration.

This is investigated in the following. The experiments have been performed on the reception quantum dot, where a similar metastable double dot as for the source dot has been observed. A stability diagram showing the (2,0)-(1,1) charge degeneracy line is represented on the left part of Fig. E.1.

To achieve spin-blockade measurement, the system has to be set in a position where it is favorable for a singlet to be in a (2,0) configuration while it is favorable for triplets to be in a (1,1) configuration. This specific position is encountered close to the (1,1)-(2,0) transition, as illustrated on the energy diagram of Fig. E.1 (right plot). The corresponding position on the stability diagram is indicated by the point M_{SB}.

In order to observe such an effect in a single-shot way, the time required for a $|T^{11}\rangle$ state to relax to the ground $|S^{20}\rangle$ state must be larger than the measurement bandwidth. On the energy diagram of Fig. E.1, it can be seen that the $|S^{11}\rangle$ and $|T_0^{11}\rangle$ states are almost degenerated (this is true for relatively weak interdot tunnel coupling t_c). As was already explained, this will result in a mixing of these two states on a very fast timescale (a few 10 ns [Pet05]). Therefore, the relaxation rate from $|T_0^{11}\rangle$ to $|S^{20}\rangle$ state will scale as t_c. The value of t_c is estimated around a few 100 kHz in the measurement position. As a result, the $|S^{20}\rangle$ should be reached too fast compared to the measurement bandwidth and a (2,0) charge state will be detected.

On the contrary, the degeneracy with the $|T_+^{11}\rangle$ and $|T_-^{11}\rangle$ states is lifted thanks to the application of an 100 mT magnetic field. In this case, coupling between $|T_\pm^{11}\rangle$ and $|S^{20}\rangle$ is ensured by spin-orbit interaction. This coupling scales as $t_c a/l_{SO}$ [Dan13], where a is the distance between the two dots and l_{SO} is the spin-orbit length. Since $l_{SO} \gg a$, this

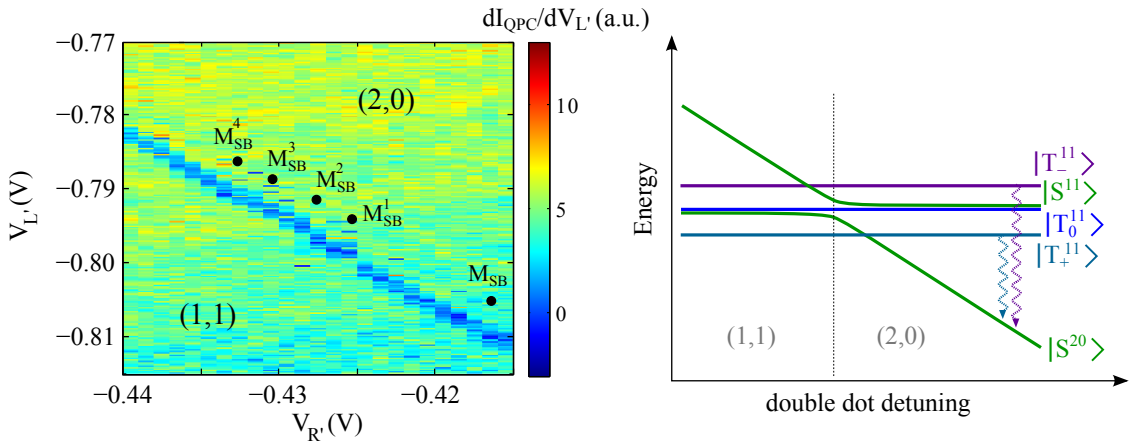

Figure E.1: (left) Stability diagram showing the (2,0)-(1,1) degeneracy line in the metastable position of the reception dot. The different positions where spin blockade has been observed are labeled on the figure. **(right)** Energy diagram of the system showing the position where spin blockade is observed. The relaxation from $|T_+^{11}\rangle$ and $|T_-^{11}\rangle$ to $|S^{20}\rangle$ seen in the measurement position is illustrated by the two arrows. Relaxation from $|S^{11}\rangle$ and $|T_0^{11}\rangle$ to $|S^{20}\rangle$ is faster than the bandwidth and therefore not detectable.

relaxation of the $|T_\pm^{11}\rangle$ should be smaller than the measurement bandwidth. In that case, a (1,1) charge state should be detected until the state finally relax to $|S^{20}\rangle$.

The different steps of the experiment that has been realized are listed below:

- The dot is coupled to its reservoir in order to load two electrons.
- It is waited in this loading position a time t_{wait} in order to vary the singlet/triplet proportion initialized.
- The system is then pulsed to the metastable position, in the (1,1) configuration. This position is held for 100 µs.
- It is finally set to the readout position (point M_{SB} on Fig. E.1) and the QPC current is recorded for a few 10 ms.

Some single-shot traces of the QPC current recorded in the readout position are shown on the top left plot of Fig. E.2. Two current levels can be distinguished, with the highest and lowest levels corresponding to the (1,1) and (2,0) charge configurations respectively. It is possible to define a current threshold between these two values (see red dotted line). If a curve passes above this threshold, it is attributed to the $|T_\pm\rangle$ states. Otherwise, it is attributed to a $|S\rangle$ or $|T_0\rangle$ state. It can be seen that at some point, the curves initially at the (1,1) current switch to the (2,0) value. These switches, that can be referred to as "quantum jumps", correspond to the relaxation from a $|T_\pm^{11}\rangle$ state to the $|S^{20}\rangle$ state.

This spin decay process at the measurement position can be analyzed directly by the average traces shown on the top right plot of Fig. E.2. The different curves have been obtained by averaging 1200 single-shot traces (as those shown on the top left plot of Fig. E.2). Each curve corresponds to a different t_{wait}, *i.e.* different singlet/triplet proportion

prepared. When a triplet is initialized, exponential decays can be seen, accounting for the $|T_{\pm}^{11}\rangle$ to $|S^{20}\rangle$ relaxation. A characteristic relaxation time of a few milliseconds is obtained. On the contrary, when a singlet is prepared, the average trace remains flat.

The maximum value I_{max} reached by the averaged curves should be proportional to the triplet probability initially prepared: the higher the probability of being in a $|T_{\pm}\rangle$ state, the more likely it is to measure a current corresponding to the (1,1) charge configuration and the higher will be I_{max}. Therefore, this should provide information about the spin decay that occurs in the loading position.

The variation of I_{max} as a function of t_{wait} has been plotted on the lower left panel of Fig. E.2 (blue curve). An exponential decay traducing the relaxation of the spin states in the loading position is observed. As a reference, a triplet to singlet relaxation curve obtained with a standard energy-selective readout is superimposed (green curve on the plot). There is a relatively good agreement between the two curves, confirming the interpretation of the data.

Finally, the same experiment has been reproduced at different measurement points (point M_{SB}^{1} to M_{SB}^{4} on the stability diagram of Fig. E.1) corresponding to different values of interdot tunnel coupling. The average current curves obtained for $t_{wait} = 0.5\,\mathrm{ms}$ and $t_{wait} = 20\,\mathrm{ms}$ are represented on the bottom right plot of Fig. E.2. The values of $V_{R'}$ for the different measurement points are indicated in the legend. The more negative is $V_{R'}$, the weaker is the interdot tunnel coupling and the longer should be the $|T_{\pm}^{11}\rangle$ to $|S^{20}\rangle$ relaxation ($\propto t_c a/l_{SO}$). This is consistent with our measurement.

In summary, these results show that spin blockade measurements can be achieved in a metastable position. This is promising to implement some readout procedure very close to the position used for the electron transfer. In our case it was only possible to differentiate between parallel and anti-parallel spin states. In principle, measurement could be done at higher interdot tunnel coupling in order to lift the degeneracy between $|S_{11}\rangle$ and $|T_{11}^{0}\rangle$ in the measurement position, and thus also be able to differentiate between these two states [Bar09]. However the measurement bandwidth of the setup was not sufficient in our case to achieve it.

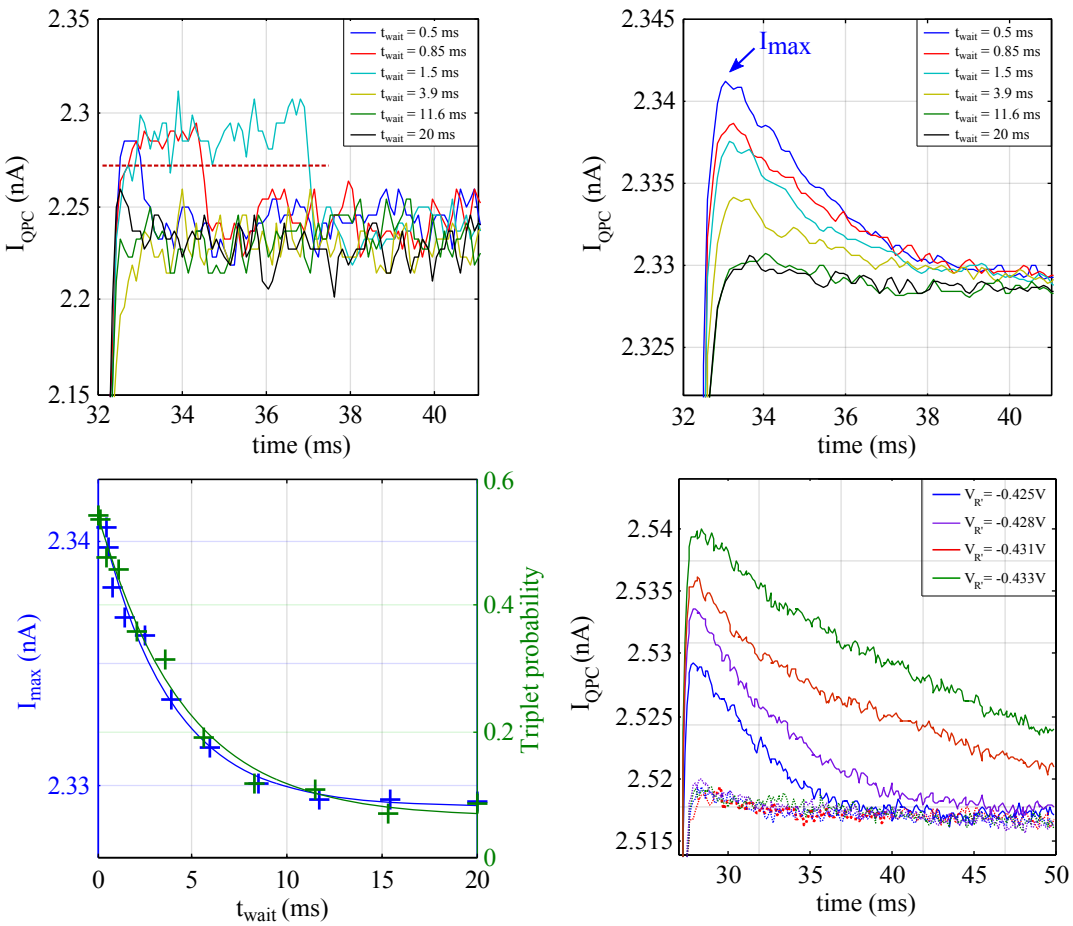

Figure E.2: (top left) Observation of quantum jumps from $|T_+\rangle$ or $|T_-\rangle$ to the S(2,0) state. The curves are single-shot traces of the QPC current after reaching the measurement position. Each one has been taken for a different waiting time t_{wait} (indicated in the legend) spent in the loading position (point L_2). A measured current around 2.29 nA corresponds to the (1,1) charge configuration whereas a current around 2.24 nA stands for the (2,0) charge configuration. **(top right)** Average over 1200 spin-blockade measurements (similar to the curves on the top left panel) for different t_{wait}. Exponential decays are observed (with 2.3 ms characteristic time), corresponding to the decay of the $|T_+\rangle$ and $|T_-\rangle$ states toward the (2,0) singlet state. **(bottom left)** The maximum value of the QPC current on the average measurement (top right figure) is plotted as a function of t_{wait} (blue curve). A standard energy-selective readout of the spin state as a function of t_{wait} is superimposed to it (green curve), and matches quite well the previous curve after scale adaptation. The curves are fitted with exponential decays of 3.7 ms (blue) and 4.5 ms (green). **(bottom right)** Similar curves as in the top left figure for different values of V_R, *i.e.* for varying tunnel coupling. For each value of V_R, the curve for $t_{wait} = 0.5$ ms (continuous) and $t_{wait} = 20$ ms (dotted lines) are shown. Small offsets between the curves have been compensated to have the $t_{wait} = 20$ ms curves superimposed. All the data were obtained under application of a 100 mT magnetic field along the sample plane.

APPENDIX F

SAW influence on the spin of the system

In the perspective of coherent spin transport in dynamical quantum dots, the impact of a SAW on the coherence of the system is of direct relevance. In this appendix, it is presented a few experiments that were realized with the objective of revealing possible detrimental effects of a SAW on the system coherence.

In a first experiment, dephasing of the separated singlet is measured (similarly to the experiment of Fig. 4.8) with a SAW burst simultaneously passing across the dot. The pulse sequence used for the dephasing experiment is depicted on the top left sketch of Fig. F.1.

- As usual, two electrons are loaded and initialized in a singlet state by waiting for relaxation.
- A microsecond voltage pulse is used to bring the system in the metastable position (point B on Fig. 4.9).
- The electron are separated by pulsing the system within a nanosecond to position C (using gate V_L, see Fig. 4.9). In this position, $J \gg g^* \mu_B \Delta B_z$ and no dephasing occurs.
- An additional nanosecond pulse (on V_R) is used to bring the system to a position where $J \ll g^* \mu_B \Delta B_z$ (point D on Fig. 4.9). This position is held for a time τ_S, before going back to point C.
- A 100 ns SAW burst is also applied in such a way to pass across the dot simultaneously with the beginning of this nanosecond pulse.
- The system is finally brought back to point B in a nanosecond timescale before performing energy-selective spin readout (point M on Fig. 4.8).

The experiment is done with a 100 mT magnetic field applied. The dephasing curves measured for different SAW powers are shown on the lower part of Fig. F.1. First of all, it can be seen that a Gaussian decay (resulting from the coupling to the nuclear spin bath) is observed for all the curves. The decay characteristic time is similar for all the SAW powers, and corresponds to the value found for the experiment without SAW applied (see Fig. 4.8).

This suggests that the spin coherence is not affected by the application of a SAW burst in this experiment.

However, the dephasing signal becomes less clear for SAW powers of 1 dBm and larger. It seems that two effects are present. First, the signal background is shifted to higher singlet probability (see the 3 dBm and 5 dBm curves). This suggest enhanced protection of the singlet state. This feature is not understood for the moment. Second, there is a reduction of the signal amplitude due to a decrease of the singlet probability (clearly seen comparing the −1 dBm and 1 dBm curves). This is attributed to mixing of the $|S\rangle$-$|T_+\rangle$ states and is described in the following.

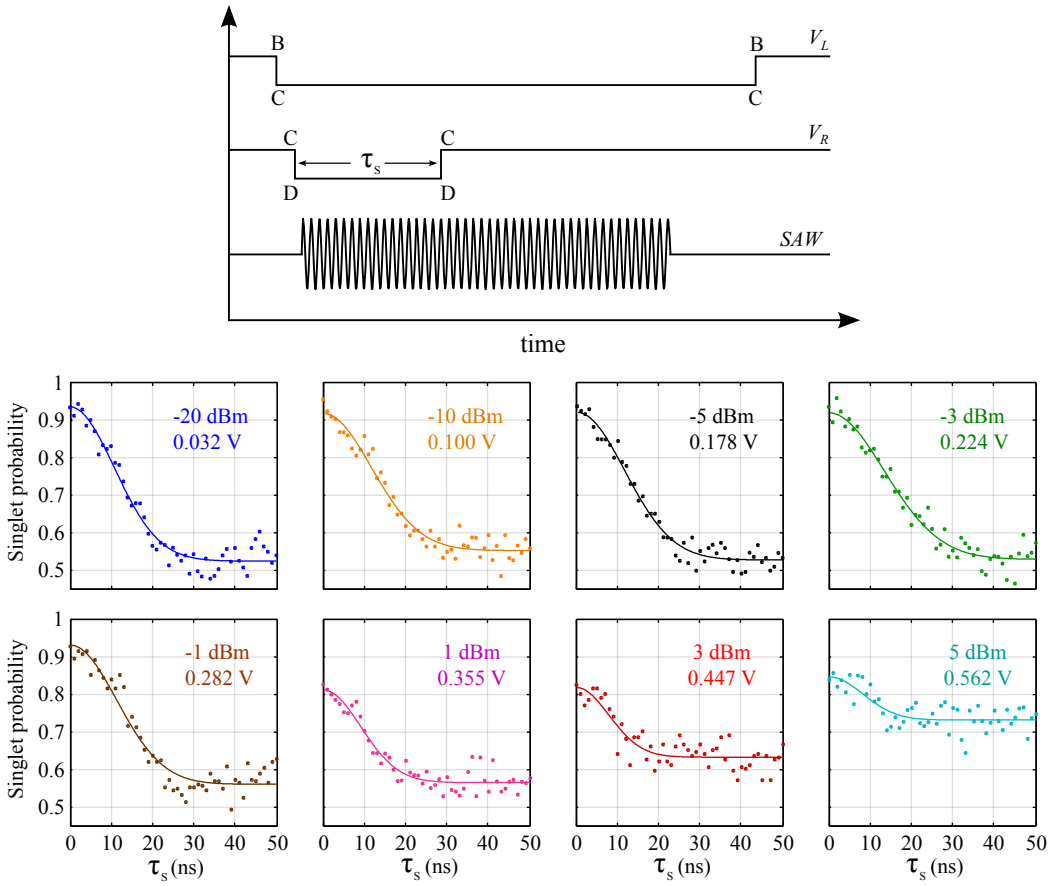

Figure F.1: Impact of SAWs on spin coherence. **(top)** Description of the pulse sequence applied on gates V_L and V_R with respect to the SAW passage time. V_L pulse duration is 150 ns. Position C corresponds to $V_L + V_{ns} = -0.725$ V and $V_R = -0.4$ V. V_R pulse duration is varied from $\tau_S = 0$ ns to 50 ns. The SAW burst duration is 100 ns. **(bottom)** Dephasing of the separated singlet as a τ_S for varying SAW power. Each data point corresponds to the average of 250 single-shot measurements.

The passage of the SAW burst on the sample is periodically modulating the static potential defined, and in particular the confining potential of the double dot. The impact of such a modulation is illustrated on the left panel of Fig. F.2. A sinusoidal potential

corresponding to the SAW influence is superimposed to a double well potential. The successive curves correspond to the shape of the potential for increasing times. It can clearly be seen that both the interdot tunnel coupling t_c and the detuning ε are affected by the wave. The impact on ε (resp. t_c) will be maximal for the curves highlighted in blue (resp. red). The modulations on each parameter are in quadrature. This means that the system will follow an elliptical path in the ε-t_c space. Two comments can be made:

- Since the wavelength of the SAW is larger compared to the size of the double dot, we expect the effect on t_c to be relatively weak. This ellipse should be more elongated on the ε direction.
- The size of the elliptical path will depend on the amplitude of the wave. The larger the amplitude, the larger is the modulation of the double dot parameters.

The expected trajectory followed by the system during the application of the SAW burst is represented on the top right panel of Fig. F.2. This is represented for two different base positions. The spiral shape illustrates the progressive rise of the wave amplitude.

For the upper base position (red trajectory), it can be seen that passage through the $|S\rangle - |T_+\rangle$ crossing can be induced. The time spent close to this degeneracy point can be sufficient to result in some mixing of the two spin states. In addition, passage through the crossing in an imperfect adiabatic or non-adiabatic way can also result in mixing of the spin states.

The following experiment has been done in order to confirm this theory:

- Similarly to previous experiments, two electrons are loaded and prepared in a singlet state by waiting for spin relaxation.
- The system is then brought to the metastable position (point B on Fig. 4.9) with the use of microsecond pulsing.
- A nanosecond pulse is used on V_L to reach the (1,1) region. In this position $J \gg g^* \mu_B \Delta B_z$, preventing mixing between the states $|S\rangle$ and $|T_0\rangle$.
- This position is held during the application of a 100 ns SAW burst.
- The system is pulsed back to point B within a nanosecond, and energy selective spin readout is performed.

The V_L value of the system during the application of the SAW burst and the SAW amplitude are varied. The measured triplet probability is represented as a function of these two parameters on the bottom right panel of Fig. F.2.

For $V_L = -0.71\,\mathrm{V}$, the system is quite close to the $|S\rangle$-$|T_+\rangle$ degeneracy during the application of the SAW burst. It can be seen that some singlets are turned into triplets even for the lowest SAW amplitude used. As V_L is shifted to more negative values, the system gets deeper into the (1,1) region and a more and more important SAW amplitude is required to observe an increase of the triplet probability. In the end, for $V_L = -0.74\,\mathrm{V}$ no triplet state is measured except for the highest SAW amplitude value. This is consistent with our expectations that SAW induced transition crossing can alter the spin states.

A line where the triplet probability is maximum (around 25 %) is observed. We attribute this line to the matching of the $|S\rangle$-$|T_+\rangle$ crossing and an extremity of the trajectory imposed by the SAW. Indeed in that case, the $|S\rangle$-$|T_+\rangle$ degeneracy line and the elliptical path followed by the system overlap maximally, allowing for a longer mixing time. Above this line, mixing occurs but is less effective since the $|S\rangle - |T_+\rangle$ crossing is passed more quickly. Below the line, a singlet is poorly affected by the wave since the transition is not reached.

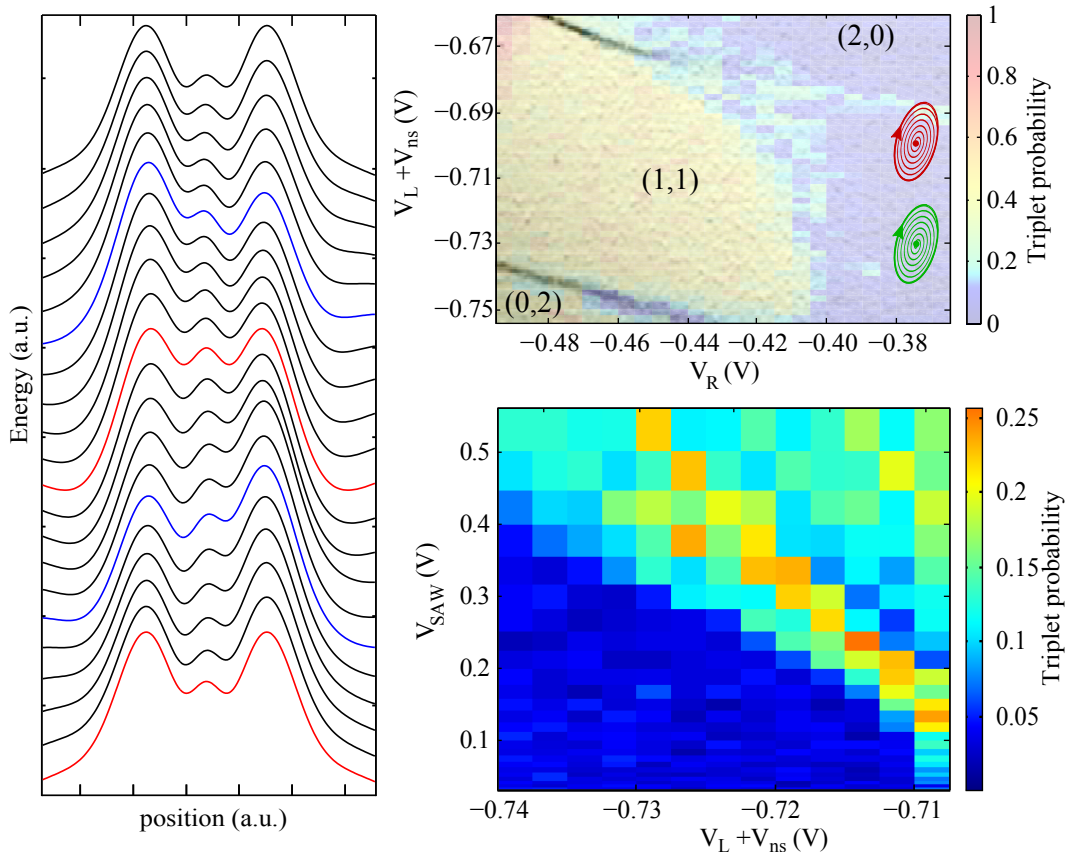

Figure F.2: SAW influence on double dot parameters and induced transition crossing. **(left)** Modification of a double dot potential with addition of a sinusoidal potential. The phase of the sin function is changed on the different curves. In blue and red are highlighted the maximum variations of detuning and interdot tunnel coupling respectively. **(top right)** Stability diagram and spin mixing mapping are superimposed. In green and red are schematized trajectories followed by the system under SAW irradiation. For the red one, the initial position of the system is too close to the (2,0)-(1,1) degeneracy and the $|S\rangle - |T_+\rangle$ mixing line can be crossed. **(bottom right)** Spin signal after SAW irradiation as a function of V_L voltage and SAW amplitude (on the source). The system is initialized in singlet, and brought within 1 ns in the (1,1) region at $V_R = -0.375$V. SAW burst duration is 100 ns. Each data point is the average of 500 single-shot measurements.

The effect of this SAW modulation of the dot parameters is therefore detrimental for preservation of a spin state. We further investigate on this effect in a last experiment. The

idea is to induce coherent oscillations through the SAW induced variation of detuning.

It has been realized with a similar gate sequence than for coherent spin rotation experiments, except that the exchange pulse is replaced by the application of a SAW burst (see left panel of Fig. F.3):

- Two electrons are loaded and prepared in a singlet state (waiting 20 ms for spin relaxation)
- A microsecond voltage pulse on gate V_L is applied to reach the metastable position (point B on Fig. 4.9).
- An additional nanosecond pulse on V_L allows to reach the (1,1) region (point C on the mapping of Fig. 4.9).
- V_R is then swept within 100 ns to reach the point D on Fig. 4.9, where $J \ll g^* \mu_B \Delta B_z$. This allows the adiabatic transformation of the singlet into the $|\uparrow\downarrow\rangle$ state.
- A 100 ns SAW burst is applied.
- The mirror sequence is finally applied to bring back the system in the (2,0) region (point B) before performing the usual energy-selective readout of the spin state.

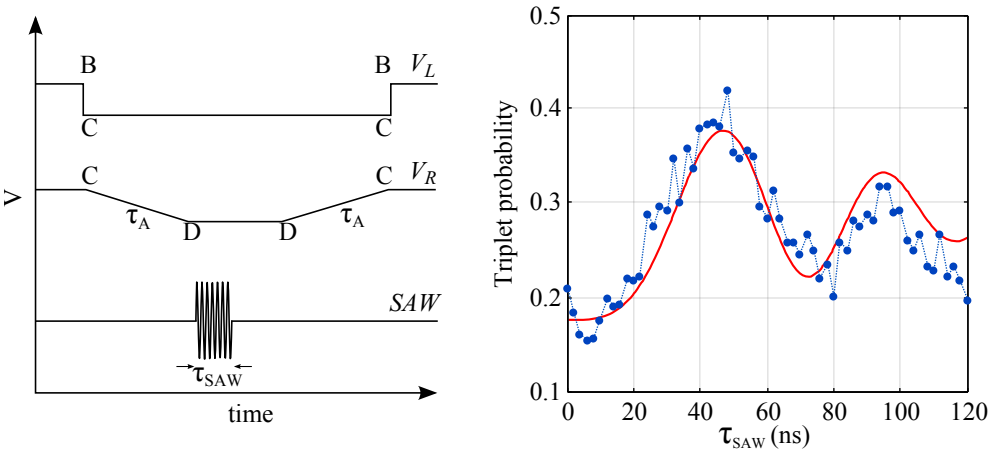

Figure F.3: SAW induced spin exchange. The system is brought in point D following the same procedure than for the previous Rabi oscillations experiments. A 0 dBm SAW is applied once in this position, with its duration varied from 0 ns to 120 ns. The red curve corresponds to a fit of an oscillation whose frequency increases with a 66 ns rise time. Each data point is the average over 500 single-shot measurements.

The final triplet probability is measured as a function of the duration of the SAW burst applied. It is represented on the right panel of Fig. F.3. Oscillations of the triplet probability are observed. The interpretation is the following. At each period of the wave, ε is modulated and so does $J(\varepsilon)$. This periodic change in J can be seen as a succession of short exchange pulses that in the end can induce coherent oscillations between $|\uparrow\downarrow\rangle$ and $|\downarrow\uparrow\rangle$. The evolution of the oscillations frequency is consistent with the expected rise time of the wave amplitude. For the shortest values of τ_{SAW}, the SAW amplitude is relatively weak

and should have a limited effect on the system. On the contrary for longer τ_{SAW} values, the SAW can reach its steady state amplitude and its impact will become larger. The red line corresponds to a fit of the expected oscillations taking into account the rise time of the SAW determined in the section 3.4. This is in relatively good agreement with the data.

These last experiments have shown that the application of a SAW burst can cause a large disturbance on the system that can affect a spin state in many different ways. In the perspective of transporting a coherent spin superposition, this can be a major issue and we need to find a way to circumvent it. A first mean to reduce the impact of a SAW burst would be to engineer very deep quantum dots. In that case, the influence of the SAW would be negligible compared to the confinement potential of the dots. The system could then be set to a position allowing the electron transfer for only a very short time (as we have seen in section 3.5). In addition, concerning coherent manipulations in a double dot, a very simple way to get around the SAW modulation of detuning has been found. It consists in designing a new sample with the two minima of the quantum dot aligned perpendicularly to the wave direction of propagation (instead of parallel as it is in our case). Indeed in that way, the SAW will modulate both parts of the double quantum dot simultaneously and therefore no change in dot tuning should be observed. Samples are currently realized with a new geometry that should be compatible with these requirements, and this is promising for future experiments of coherent spin transfer.

APPENDIX G

French summary

Introduction

Les dernières décennies ont vu une miniaturisation toujours plus importante des composants électroniques et photoniques, qui a amélioré de façon impressionnante la puissance de calcul des ordinateurs. La réalisation de composants de taille nanométrique est aujourd'hui bien maitrisée ; de récents développements de la technologie silicium atteignent même l'échelle atomique [Fue12]. À de si petites échelles l'utilisation de la mécanique quantique devient alors nécessaire pour décrire les propriétés des dispositifs utilisés. Pour certains, l'émergence de ces phénomènes quantiques constitue une difficulté supplémentaire vers une plus grande réduction d'échelle de l'électronique. Au contraire, c'est pour d'autres une formidable opportunité d'accéder à un traitement de l'information plus puissant.

L'un des premiers à introduire cette idée a été Feynman, qui posa les bases d'un modèle montrant comment effectuer des calculs en utilisant les lois de la mécanique quantique [Fey82]. Cela pourrait s'avérer particulièrement intéressant pour la simulation de systèmes quantiques. En effet, mener de telles simulations avec un ordinateur classique est rendu extrêmement difficile de par le fait que la complexité d'un système quantique croît de manière exponentielle avec le nombre de particules qu'il contient. La conjecture de Feynman fut confirmée une décennie plus tard avec la preuve que des simulateurs quantiques universels peuvent être construits à partir de systèmes quantiques [Llo96]. Cela laisse envisager un grand nombre d'applications potentielles en physique ou en chimie par exemple, pour l'étude de problèmes à plusieurs corps [Geo14].

Un autre évènement marquant dans l'essor de l'information quantique fut la découverte de l'algorithme de Shor qui permet une accélération exponentielle de la factorisation en nombres premiers [Sho94]. L'impact considérable que cet algorithme pourrait avoir sur les protocoles de cryptographie actuels a donné lieu à un énorme intérêt, s'étendant désormais bien au-delà de la communauté des physiciens. D'autres algorithmes profitant des propriétés de l'information quantique ont plus tard été proposés. Un exemple souvent cité est l'algorithme de Grover [Gro96], qui permet d'effectuer une recherche dans une base de données non triée de manière plus rapide qu'un ordinateur classique.

Le choix du système physique est un point clé pour la réalisation concrète d'un tel traitement quantique de l'information. Tout système ne convient pas forcément et à cet

égard, DiVincenzo propose un ensemble de cinq prérequis pour sa mise en œuvre [DiV00] :

1. *Un système physique et des qubits bien définis.* Un bit quantique, ou « qubit », est un système quantique à deux niveaux, comme par exemple le spin $\frac{1}{2}$ de certaines particules. Ces deux états sont généralement notés $|0\rangle$ et $|1\rangle$. La différence essentielle par rapport à un bit classique est qu'un qubit peut être préparé dans une superposition de ces deux états. On peut donc l'écrire de manière générale sous la forme $a\,|0\rangle + b\,|1\rangle$, où a et b sont des nombres complexes. Cette propriété constitue l'essence du potentiel de l'information quantique. Tous les paramètres des qubits (l'énergie des différents états et les mécanismes de couplage mis en jeu) doivent être connus avec une grande précision.
2. *La capacité d'initialiser un qubit.* Avant le début d'un calcul, le système doit être initialisé avec une valeur connue. Il doit donc être possible de préparer chaque qubit dans au moins un état déterminé. La plupart du temps, une solution simple consiste à préparer un qubit dans son état fondamental en refroidissant le système.
3. *Une faible décohérence.* La décohérence est le mécanisme conduisant à l'émergence des propriétés classiques d'un système quantique. Afin de tirer parti de ses propriétés quantiques, le temps de décohérence doit donc être aussi grand que possible par rapport au temps de calcul. On pourrait donc craindre que de longs calculs soient alors rendus impossibles. Afin de contourner ce problème, des codes de correction d'erreurs [Sho95; Ste96] ont été développés et peuvent être utilisés pour compenser l'effet de la décohérence. Une des approches les plus robustes, connue sous le nom "surface code" [Bra98; Den02; Fow12], autorise une probabilité d'erreur de l'ordre de 10^{-2}, ce qui semble expérimentalement accessible.
4. *Un ensemble universel de portes logiques quantiques.* En principe, il doit être possible d'appliquer au système des transformations unitaires impliquant un nombre arbitraire de qubits, mais un tel contrôle semble hors de portée. Cependant, il a été montré [Bar95] que n'importe quelle transformation unitaire peut être décomposée en opérations de bases impliquant un ou deux qubits, ce qui parait beaucoup plus raisonnable expérimentalement. Encore une fois, les erreurs sur ces transformations doivent être aussi faibles que possible, et au moins en-dessous du seuil de 10^{-2} nécessaire à la mise en œuvre d'un "surface code".
5. *La capacité de mesurer des qubits spécifiques.* Mesurer un qubit sans perturber le reste du système est nécessaire à la fois pour la gestion des codes de correction d'erreurs et, bien entendu, pour lire le résultat d'un calcul. La mesure d'un état $\rho = p\,|0\rangle\langle 0| + (1-p)\,|1\rangle\langle 1| + \alpha\,|0\rangle\langle 1| + \alpha^*\,|1\rangle\langle 0|$, si elle est idéale, devrait donner 0 avec une probabilité p et 1 avec une probabilité $(1-p)$ indépendamment de α, de l'état des qubits voisins ou de tout autre paramètre du système. En général, une procédure de mesure n'est pas parfaitement efficace et des erreurs peuvent se produire. Toutefois, la fiabilité de la procédure peut être augmentée en répétant le même calcul plusieurs fois.

Expérimentalement, il n'est pas facile de trouver un système répondant à toutes ces exigences. Par exemple, l'obtention de longs temps de cohérence requiert que le qubit

soit extrêmement bien isolé de son environnement ; inversement il faut aussi avoir un moyen de se coupler à ce dernier afin de manipuler l'information qu'il contient, et ces deux critères sont en général antagonistes. Dans la recherche d'un qubit "idéal" (*i.e.* qui serait à la fois facile à contrôler et peu sensible au bruit de son environnement), un grand nombre de systèmes physiques sont étudiés, chacun présentant ses propres avantages et inconvénients. Passer en revue l'ensemble de ces systèmes serait trop long. Nous pouvons citer rapidement quelques exemples comme les ions piégés [Cir95; Haf08; Roo99], les circuits supraconducteurs à base de jonctions Josephson [Jef14; Koc07; Nak99], les spins nucléaires contrôlés par résonance magnétique nucléaire (RMN) [Ger97; Jon11], les centres NV ("Nitrogen-Vacancy") du diamant [Jel04; Ken02], ou encore les spins d'électrons piégés dans des boîtes quantiques [Kop06; Los98; Pet05]. Même pour un système donné, de nombreuses implémentations différentes d'un qubit sont possibles. Dans le cas de spins d'électrons par exemple, il a été proposé d'utiliser le spin d'un unique électron [Los98; PL08], de deux électrons [Fol09; Han07b; Pet05; Tay05] ou de trois électrons [Lai10; Med13] pour définir un qubit.

Dans le cadre de cette thèse, nous allons nous intéresser au cas de spin d'électrons comme support de l'information quantique. D'impressionnants progrès ont récemment été réalisés dans ce domaine. Le confinement d'électrons uniques dans des boîtes quantiques définies par lithographie est désormais bien maîtrisé. Il est possible de contrôler précisément le couplage entre deux spins électroniques voisins, ce qui rend possible leur manipulation de manière cohérente et a permis la démonstration de l'«ensemble universel de portes quantiques" nécessaire à l'information quantique [Kop06; Pet05]. Par ailleurs, l'utilisation de matériaux isotopiquement purifiés a permis de réduire considérablement l'influence des spins nucléaires environnants, donnant lieu à des temps de cohérence très prometteurs autour de la seconde [BG13; Tyr12]. Un autre avantage de ce système réside dans sa potentielle scalabilité. En effet, la fabrication de ces boîtes quantiques nécessite une technologie très similaire à celle utilisée dans l'industrie microélectronique. Cela devient d'autant plus vrai depuis le passage récent vers des structures métal-oxyde-semiconducteur (MOS) sur silicium [Ang07; Vel14]. Par conséquent, le développement de ces qubits dans les semiconducteurs apparait comme une voie particulièrement attractive.

Étant donné la maîtrise actuelle autour de l'informatique quantique à base de spin, un champ d'investigation est maintenant la fabrication et le contrôle de dispositifs contenant un nombre de plus en plus important de qubits. Dans cette optique, une première approche est la réalisation de réseaux de boîtes quantiques couplées entre elles [Del14; Tha12], où le couplage entre spins voisins (voire au-delà [Bra13; Meh14; San14]) peut être contrôlé. Cependant, le grand nombre de paramètres de réglage et le couplage capacitif entre les différentes parties de ces dispositifs rendent leur conception et leur manipulation extrêmement complexes. Simplifier leur contrôle pourrait ainsi être un premier moyen d'accéder à de plus grands réseaux de boîtes quantiques. À cet égard, nous proposons une simplification reposant sur la suppression du couplage du système avec les réservoirs d'électrons. Le nombre d'électrons à utiliser dans un réseau de boîtes quantiques est habituellement fixe (typiquement un électron par boîte quantique) et ne doit pas varier. Cela induit de grandes contraintes sur l'ensemble de paramètres de réglage qui peut être utilisé, ce qui est préjudiciable pour le contrôle parfait du système. Comme solution, nous

avons étudié la possibilité de travailler avec des boîtes quantiques dans une configuration métastable, complètement isolé des réservoirs d'électrons. Cela assure que le nombre d'électrons dans le système ne varie pas et lève toutes les contraintes sur la gamme de paramètres utilisable.

Une deuxième approche possible pour augmenter le nombre de qubits implémentés serait d'utiliser des boîtes quantiques plus largement espacées les unes des autres. Cette approche permet en principe un contrôle beaucoup plus simple des différents qubits, mais elle requiert un couplage longue distance pour assurer l'intrication entre les différents nœuds du dispositif. Sur ce point, le très faible couplage d'un spin à son environnement, qui fait la force de ces qubits, devient alors un obstacle majeur. On pourrait imaginer des boîtes quantiques distantes interconnectées via des cavités résonnantes [Bur06; Chi04; Tri08], de façon similaire à ce qui a été développé pour coupler les qubits des circuits supraconducteurs [Maj07; Sil07]. Cette approche est étudiée dans de nombreux groupes [Del11; Fre12; Pet12], mais un couplage suffisant n'a pas encore été obtenu et semble très difficile à atteindre. D'autres propositions pour assurer le couplage de spins distants existent, comme l'utilisation d'électrodes flottantes servant d'intermédiaire pour un couplage électrostatique [Tri12] ou magnétique [Tri13]. Cependant, aucune réalisation expérimentale d'un tel système n'a été démontrée pour l'instant.

Dans notre cas, nous étudions une approche très différente s'inspirant de la recherche en spintronique. Les chercheurs de ce domaine réalisent des dispositifs visant à manipuler de l'information stockée sur le spin d'un ensemble d'électrons. Pour cela, la génération et la propagation de courants polarisés en spin dans des structures de semiconducteurs est intensivement étudiée [Bra12]. Notre objectif est d'étendre ce concept à l'échelle de l'électron unique, afin de directement déplacer des qubits de spin et de réaliser le transfert d'information quantique. Le principal avantage de cette approche est qu'elle évite d'avoir à convertir l'information de spin en une nouvelle forme pour assurer sa propagation. Cependant, un moyen de réaliser le transport cohérent du spin d'un électron unique entre deux boîtes quantiques distantes doit être mis au point. En particulier, cela implique de maintenir un électron totalement isolé au cours de son transport, afin d'empêcher tout mélange de l'information de spin avec d'autres électrons de la structure.

Bien que déplacer des électrons soit une tâche courante pour les physiciens, le contrôle du déplacement d'un électron unique constitue un véritable défi. Néanmoins, le transfert d'un électron unique entre deux boîtes quantiques distantes a été réalisé en 2011 [Her11; McN11]. Dans ces expériences, deux boîtes quantiques séparées par quelques micromètres sont reliées par un canal unidimensionnel le long duquel un électron peut se propager. Afin d'éviter la localisation de ce dernier dans le canal, une onde acoustique de surface (OAS) est excitée. La modulation du potentiel induit par l'OAS lors de son passage donne lieu à la formation de boîtes quantiques en mouvement qui assurent le transfert de l'électron entre les deux boîtes quantiques statiques. Ce processus permet de transférer des électrons uniques sur plus de quelques micromètres en une nanoseconde, un temps inférieur au temps de cohérence du spin. De plus, l'électron reste confiné pendant son transfert, ce qui accroît la longueur de cohérence de spin par rapport au cas d'un déplacement libre [Dya72; Sto05; Sto08]. Par conséquent, l'information codée sur le spin de l'électron devrait être préservée.

Au cours de ce travail de thèse, décrit dans les chapitres qui suivent, j'ai étudié la

possibilité de transporter de l'information de spin codée sur des électrons individuels en utilisant ce type de transfert assisté par OAS. Dans le chapitre 1, les bases de l'électronique à l'échelle de l'électron unique sont examinées : les moyens d'isoler un électron unique dans une boîte quantique sont d'abord expliqués ; les différentes méthodes utilisées pour la lecture du spin d'un électron ainsi que les procédures pour le manipuler de manière cohérente sont ensuite décrites ; enfin, le transfert à la demande d'un électron entre des boîtes quantiques distantes est discuté. Dans le chapitre 2, le dispositif expérimental qui a été utilisé pour les mesures est présenté. Dans le chapitre 3, le processus d'injection d'électrons depuis une boîte quantique statique vers une boîte quantique en mouvement définie par l'OAS est étudié. En particulier, nous démontrons que nous pouvons atteindre un régime où l'électron peut être injecté de manière contrôlée dans une boîte quantique en mouvement avec une probabilité unitaire. Dans le chapitre 4, la manipulation cohérente du spin d'une paire d'électron est démontrée en utilisant une double boîte quantique isolée dans une position métastable. Ce type de manipulation cohérente est immédiatement compatible avec un transfert d'électrons par OAS. Ces deux chapitres démontrent d'importants prérequis vers l'accomplissement du transfert cohérent d'un spin d'électron unique. Enfin dans le chapitre 5, les premières expériences de transfert d'information de spin utilisant des électrons individuels sont présentées.

État de l'art du contrôle d'électrons uniques et de leurs spins

Ce chapitre passe en revue l'état de l'art du contrôle d'un électron unique et de son spin, et a pour but d'introduire les concepts de base nécessaires à la compréhension du manuscrit. Dans un premier temps, les boîtes quantiques latérales réalisées à partir d'hétérostructures d'arséniure de gallium sont présentées. La variation de bande interdite des différents semiconducteurs utilisés dans ce type d'hétérostructure donne naissance à un gaz d'électron bidimensionnel situé à une centaine de nanomètres en dessous de la surface (*cf.* Fig. 1.1). Il est alors possible de dépeupler localement le gaz d'électrons en appliquant des tensions négatives sur des grilles métalliques déposées à la surface. En utilisant une géométrie de grilles adaptée, des boîtes quantiques peuvent être définies dans lesquelles un petit nombre d'électrons sont confinés (*cf.* Fig. 1.2). Le modèle à interaction constante est alors introduit [Kou97; VH92; Wan11]. Les interactions électrostatiques entre la charge contenue dans la boîte quantique et les charges des différents réservoirs et grilles sont modélisées par un réseau de capacités (*cf.* Fig. 1.3). On suppose également dans ce modèle que le spectre de la boîte quantique ne dépend pas du nombre d'électrons qu'elle contient. Ce modèle permet de décrire les propriétés de base d'une boîte quantique et donne en particulier son énergie de charge.

Pour observer ces effets expérimentalement et accéder au spin des électrons piégés, il est nécessaire de mettre en place des méthodes de détection de charge et de spin. La charge contenue dans une boîte quantique est généralement détectée en utilisant un contact ponctuel quantique formé à proximité. Le couplage capacitif entre la boîte et le contact ponctuel implique une modulation de la conductance de ce dernier en fonction du nombre de charges présentes dans la boîte (*cf.* Fig. 1.4). Afin de réaliser une mesure de spin,

l'idée est de traduire cet état de spin en une information de charge. Cela peut se faire en utilisant une différence d'énergie (*cf.* Fig. 1.5) ou de couplage tunnel (*cf.* Fig. 1.6) entre les différents états de spin.

Différentes interactions vont se coupler au spin d'un électron. Une première interaction est le couplage spin-orbite. Dans les matériaux utilisés, le déplacement d'un électron va induire un champ magnétique effectif auquel son spin va être sensible. Lorsqu'il est confiné à l'intérieur d'une boîte quantique, son déplacement est nul en moyenne et le spin est relativement bien protégé. Cependant, un traitement perturbatif met en évidence un couplage entre les différents états de spin qui est impliqué dans le phénomène de relaxation de spin. Une deuxième interaction qui entre en jeu dans la structure utilisée est l'interaction hyperfine, *i.e.* le couplage aux spins nucléaires du matériau. Cela a souvent un effet délétère sur la cohérence du système. La présence de ces deux interactions peut néanmoins s'avérer utile pour la réalisation de manipulations cohérentes de spins.

Enfin, une dernière partie traite du transport d'électrons uniques par l'intermédiaire d'ondes acoustiques de surface (OAS). Une OAS est une onde mécanique qui se propage à la surface d'un solide. Une telle onde est générée à partir d'un transducteur inter-digité. Ce dispositif est constitué de peignes d'électrodes qui s'interpénètrent (*cf.* Fig. 1.16). L'application d'une tension entre ces deux peignes va induire une déformation du matériau due aux propriétés piézoélectriques de l'arséniure de gallium. En utilisant une tension sinusoïdale, il est alors possible de générer une OAS. Par effet piézoélectrique inverse, la propagation de cette onde va s'accompagner d'une modulation du potentiel électrique qui peut être utilisée pour déplacer des électrons. En particulier, au niveau d'une constriction unidimensionnelle du gaz d'électrons vont se former des boîtes quantiques en mouvement capables de piéger un nombre donné d'électrons par période de l'onde (*cf.* Fig. 1.17). Récemment, ce mécanisme a été utilisé pour assurer le transfert d'un électron entre deux boîtes quantiques statiques [Her11; McN11] (*cf.* Fig. 1.18). L'objectif de cette thèse est d'étudier la possibilité d'appliquer ce type de transfert pour transporter de l'information de spin stockée à l'échelle de l'électron unique.

Dispositif expérimental

Comme nous avons vu au chapitre précédent, les énergies typiques associées aux boîtes quantiques latérales sont relativement faibles. Par exemple, les différences d'énergies relatives au spin que nous souhaitons mesurer sont de l'ordre de 0.1 meV, *i.e.* équivalent à une température de 1 K. Il est donc nécessaire de porter le système à une température très inférieure, au moins en dessous de 100 mK, pour observer ces effets. Une telle température peut être obtenue en se servant d'un réfrigérateur à dilution. Le principe de fonctionnement repose sur la dilution d'^{3}He dans de l'^{4}He, qui est endothermique à basse température. Pour les expériences présentées dans cette thèse, le réfrigérateur à dilution était porté à une température entre 50 mK et 60 mK. La température électronique est estimée à environ 100 mK.

L'électronique utilisée pour les expériences doit aussi être adaptée pour permettre de sonder d'aussi petites échelles d'énergies. La polarisation de l'échantillon s'effectue via des sources de tension continue (implémentées par le service électronique du laboratoire

à partir de convertisseurs numérique-analogique Linear Technology LTC2604) ayant un bruit de l'ordre de $25\,\mathrm{nV\,Hz^{-1/2}}$. Les lignes de mesures sont filtrées autour du mégahertz, permettant des fluctuations de tension au niveau de l'échantillon de l'ordre de quelques dizaines de microvolts. Un générateur arbitraire de signal (AWG Tektronix 5014) est également utilisé et permet d'appliquer des signaux au gigahertz sur certaines grilles de l'échantillon. L'excitation microonde nécessaire à la génération des pulses d'ondes acoustiques de surface est assurée par un générateur de signal (Rohde-Schwarz SMB 106A) commandé par une des sorties de l'AWG.

Les courants électriques circulant dans l'échantillon sont mesurés via des convertisseurs courant-tension (réalisés par le service électronique du laboratoire à partir d'amplificateurs opérationnels Texas Instruments TLC2201) assurant un gain variable entre $10^6\,\mathrm{V\,A^{-1}}$ et $10^9\,\mathrm{V\,A^{-1}}$. Les tensions sont ensuite enregistrées par des voltmètres Keithley K2000, ou par un oscilloscope Lecroy WaveRunner 6050A (dans ce cas, des amplificateurs réalisés à partir d'amplificateurs opérationnels Analog Devices AD620 sont ajoutés, principalement pour découpler la masse de l'expérience de celle de l'oscilloscope).

L'ensemble de l'expérience est contrôlée d'une part par un FPGA, gérant les différentes sources de tension et le déclenchement des appareils, et d'autre part depuis un programme Labview, chargé de l'initialisation des différents appareils et de la récupération des données.

Injection d'un électron unique d'une boîte quantique statique vers une boîte quantique en mouvement

Dans ce chapitre, nous étudions le mécanisme d'injection d'un électron confiné dans une boîte quantique statique vers une boîte quantique en mouvement. En effet, les pulses d'ondes acoustiques utilisés pour transférer un électron doivent durer une centaine de nanosecondes ou plus pour obtenir des taux de réussite proches de l'unité. Cela est problématique pour plusieurs raisons quant à l'application d'un tel processus pour le transfert cohérent d'un spin d'électron. Premièrement, il est souhaitable de pouvoir déterminer exactement le minimum de l'onde dans lequel est injecté l'électron, afin de contrôler le transfert plus rapidement que le temps de cohérence de spin. Deuxièmement, le grand nombre de périodes nécessaire pour capturer l'électron sous-entend la présence d'un mécanisme stochastique, impliquant probablement le passage d'une barrière tunnel. Cela pourrait potentiellement porter l'électron sur des états excités de charge, et affecter son spin par l'intermédiaire du couplage spin-orbite.

Dans un premier temps, des considérations géométriques sur la forme du potentiel statique permettent de mettre en évidence deux régimes de transfert différents (*cf.* Fig. 3.2). Le premier est le cas déjà évoqué où l'injection de l'électron nécessite le franchissement d'une barrière tunnel. Dans le second cas, l'injection se produit de manière "adiabatique", l'électron suit en permanence le minimum local de potentiel et l'injection ne nécessite en principe qu'une seule période de l'onde.

Le régime relevant est déterminé par la comparaison entre le gradient de potentiel maximal à franchir et le gradient induit par l'onde acoustique de surface. Pour atteindre le régime adiabatique, il faut donc minimiser ce gradient de potentiel statique (notamment en faisant correspondre au mieux les potentiels chimiques de la boîte quantique et du

canal) et travailler avec une amplitude d'OAS suffisamment élevée (*cf.* Fig. 3.4). Toutefois, l'amplitude de l'onde est soumise à un temps de montée relativement long, de plusieurs dizaines de nanosecondes (*cf.* Fig. 3.6), ce qui implique qu'un régime de transfert stochastique va impérativement précéder le passage à un régime adiabatique (*cf.* Fig. 3.7).

Ce problème peut néanmoins être contourné par la modulation du potentiel de la boîte quantique à la nanoseconde. L'idée est de confiner fortement l'électron pendant le temps de montée de l'onde acoustique, et ainsi empêcher son transfert. Puis, une fois que l'amplitude atteint une valeur suffisante, le potentiel de la boîte quantique est amené pendant une nanoseconde dans une configuration autorisant le transfert (*cf.* Fig. 3.8). Les résultats expérimentaux obtenus avec un tel protocole montrent qu'il est possible d'atteindre une probabilité de transfert unitaire pendant cette nanoseconde (*cf.* Fig. 3.9). Cela démontre qu'un peu plus de deux périodes de l'OAS sont suffisantes pour assurer l'injection de l'électron dans une boîte quantique en mouvement. Ces résultats sont cohérents avec une entrée dans un régime de transfert adiabatique.

Manipulations cohérentes de spin dans une double boîte quantique isolée

Nous avons vu dans le chapitre précédent que la séquence expérimentale à effectuer pour assurer le transfert d'un électron unique nécessite une variation rapide et sur une grande amplitude du potentiel de confinement. Cela permet d'alterner entre des configurations où les boîtes quantiques sont couplées ou au contraire isolées de leurs réservoirs. Cependant, il n'est pas certain qu'une telle procédure soit sans effet sur le spin de l'électron. Dans ce chapitre, nous allons montrer qu'il est possible de préparer une superposition cohérente de spin dans le régime isolé où s'effectue le transfert par onde acoustique de surface.

Des simulations du potentiel électrostatique de l'échantillon dans ce régime sont d'abord présentées et montrent l'émergence d'un comportement de double boîte quantique (*cf.* Fig. 4.1). L'étude de diagrammes de stabilité confirme expérimentalement cet effet (*cf.* Fig. 4.2). Nous montrons que le nombre d'électrons préparés dans cette double boîte quantique isolée est facilement contrôlé. L'impossibilité d'échanger des électrons avec un réservoir entraine une simplification substantielle du diagramme de stabilité et assure un contrôle parfait des paramètres de la double boîte quantique (alignement relatif ε et couplage tunnel t_c entre les deux minimums de potentiel, *cf.* Fig. 4.4). Une telle approche pourrait être bénéfique pour augmenter la taille des réseaux de boîtes quantiques couplées.

Une technique de détection de spin est ensuite mise en place. Une méthode usuelle consiste à induire l'échange d'un électron par effet tunnel avec un réservoir : dans certaines positions spécifiques, cet échange est dépendant de l'état de spin considéré (*cf.* Fig. 4.6). Nous montrons que le spin d'une paire d'électrons n'est pas affecté par une transition entre les positions couplée et isolée tant que les électrons ne sont pas séparés dans la double boîte quantique pendant la procédure (*cf.* Fig. 4.7).

Dans le cas contraire, certains états de spins peuvent être dégénérés et vont se mélanger avec un temps caractéristique de quelques dizaines de nanoseconde. Il est possible de lever cette dégénérescence, et donc d'empêcher ce mélange, en travaillant avec une valeur de t_c suffisamment importante. Une cartographie du passage entre ces différents régimes est

réalisée (*cf.* Fig. 4.9).

Enfin, nous présentons la réalisation d'oscillations de Rabi entre les états de spin $|\uparrow\downarrow\rangle$ et $|\downarrow\uparrow\rangle$. Nous montrons que ces oscillations peuvent être réalisées d'une part de manière similaire à l'état de l'art actuel, en modulant ε (*cf.* Fig. 4.12), et d'autre part en modulant t_c (*cf.* Fig. 4.13), rendu possible dans notre cas par la suppression du couplage aux réservoirs d'électrons. Cette dernière méthode permet de se placer dans une position optimale où l'influence du bruit de charge sur le paramètre ε est supprimée. Nous observons à cette position une augmentation significative lu nombre d'oscillations visibles.

Transfer de spin à l'échelle de l'électron unique

Dans ce chapitre, nous présentons les premières expériences réalisées sur le transport du spin d'électrons individuels par onde acoustique de surface. L'objectif de cette étape préliminaire est de vérifier si l'aimantation de spin est préservée lors du transfert. L'idée de base consiste à préparer un état de spin dans la boîte quantique source et mesurer cet état après transfert dans la boîte quantique de réception. Différentes proportions d'états de spin excité ou fondamental peuvent être obtenues en variant le temps laissé au système pour relaxer. On cherche donc à mesurer de manière non-locale (*i.e.* après transfert) ce phénomène de relaxation.

Dans un premier temps, une expérience a été effectuée en utilisant les états de spin d'une paire d'électron sous faible champ magnétique (100 mT). La procédure de transfert de deux électrons d'une boîte quantique à l'autre est d'abord mise en place, et un taux de réussite de 80 % est atteint. On peut cependant noter que les électrons sont transférés séquentiellement dans différents minimums de l'onde acoustique, séparés par plusieurs dizaines de nanosecondes (*cf.* Fig. 5.3). L'efficacité de la mesure est ensuite calibrée en observant les signaux de relaxation sans transfert d'électron (un contraste de 18.8 % est obtenu, *cf.* Fig. 5.4). Enfin l'expérience complète est réalisée et un signal de relaxation est mesuré avec un contraste de 5.4 % (*cf.* Fig. 5.6). Cela prouve que de l'information de spin est bien transférée. La fidélité du transfert approche 30 %.

Une explication plausible pour expliquer cette faible fidélité est l'impact de l'interaction spin-orbite. Différents régimes de champ magnétique ont alors été explorés. L'expérience précédente est d'abord reproduite à 200 mT, mais aucun changement notoire n'est observé. Nous reproduisons ensuite le même type d'expérience en utilisant un spin d'électron unique. Cela permet de travailler sous un champ magnétique plus élevé (3 T), mais là encore, une fidélité autour de 30 % est obtenue (*cf.* Fig. 5.12). Ces observations réfutent l'hypothèse d'une dépolarisation due à l'interaction spin-orbite pendant le transfert.

Un deuxième modèle proposé suppose une dépolarisation ayant lieu juste avant ou après le transfert, lorsque les électrons sont confinés dans les boîtes quantiques statiques. Nous avons vu au chapitre précédent qu'un comportement de double boîte quantique apparaissait près de la position de transfert. Les modulations de potentiel induites par le passage de l'onde acoustique de surface peuvent dans ce cas entrainer de multiples passages à travers des anti-croisements entre différents états de spin (*cf.* Fig. 5.8). Si ces passages ne sont pas parfaitement non-adiabatiques, un mélange des différents états de spin est possible.

Une expérience est alors réalisée pour mettre en évidence ce mécanisme. Un électron est

préparé dans la boîte quantique de réception placée en position de transfert. Une onde acoustique de surface est alors générée avec une durée variable. Nous observons un mélange des différents états de spin lorsque la durée de l'onde devient trop importante, ce qui est cohérent avec le modèle proposé (*cf.* Fig. 5.13).

Conclusion

L'objectif de ma thèse était d'explorer la possibilité de transférer de l'information de spin à l'échelle de l'électron unique. Il est possible de transporter sur demande des électrons individuels entre deux boîtes quantiques distantes en générant des boîtes quantiques en mouvement à partir d'ondes acoustiques de surface. Si la cohérence d'un spin d'électron s'avère préservée lors d'un tel transfert, cette approche pourrait être une avancée majeure vers la réalisation de circuits manipulant de l'information quantique codée sur des spins d'électrons.

Le travail présenté ici démontre plusieurs étapes préliminaires, en particulier la conservation de l'aimantation de spin au cours du transfert (*cf.* chapitre 5). Ce résultat a été obtenu via l'accomplissement d'une "mesure non-locale" de relaxation de spin : un état de spin donné est préparé dans une boîte quantique, et peut être varié en laissant ou non au système le temps de relaxer ; la mesure de cet état de spin est réalisée après transfert vers la seconde boîte quantique. Le signal de relaxation ainsi mesuré est une preuve du transfert d'information de spin.

Cette expérience a été réalisée en utilisant le spin d'un électron unique ou d'une paire d'électrons. Dans chaque cas, l'amplitude du signal de relaxation après transfert est inférieure aux valeurs attendues extraites des calibrations. Nous attribuons cette perte de contraste à une dépolarisation partielle des spins se produisant juste avant et après le transfert. En effet, l'émergence d'un comportement de double boîte quantique se produit pour chaque boîte quantique, près de leurs configurations utilisées lors du transfert. Le passage de l'onde acoustique de surface entraine une modulation du potentiel de ces doubles boîtes qui peut être responsable d'un mélange des différents états de spin. En évitant ce comportement de double boîte quantique, l'efficacité du transfert de spin devrait donc être améliorée.

L'objectif final n'est pas seulement d'effectuer le transfert d'aimantation de spin, mais également de s'assurer que la cohérence du spin est maintenue. Pour atteindre ce but, des développements supplémentaires sont nécessaires. En particulier, il doit être possible de contrôler le transfert d'un électron à une échelle de temps plus courte que le temps de cohérence de spin ($\sim 10\,\mathrm{ns}$). Dans cette optique, nous avons étudié le mécanisme d'injection d'un électron entre une boîte quantique statique et dynamique (*cf.* chapitre 3).

Il a été montré que la forme du potentiel statique a un impact crucial sur l'efficacité du transfert. En particulier, l'électron peut être protégé de l'influence de l'onde acoustique de surface pour un potentiel donné ou être transféré pour un potentiel légèrement différent. Un pulse de tension d'une nanoseconde peut donc être utilisé pour alterner entre ces deux configurations et permet ainsi un contrôle précis de l'instant auquel un électron est émis.

Ce contrôle à la nanoseconde de l'émission des électrons, combiné au transfert d'une paire d'électrons, laisse envisager des expériences permettant de sonder la cohérence de

spin. Pour commencer, une "mesure non-locale" du déphasage d'un singulet peut être effectuée : deux électrons sont préparés dans un état singulet dans la boîte quantique source ; les électrons sont ensuite transférés successivement avec un temps contrôlé τ_S entre l'émission de chaque électron ; l'état de spin est ensuite mesuré, et dépend en principe du temps pendant lequel les électrons ont été séparés. Pour un temps court par rapport au temps de déphasage, un état de spin singulet doit être retrouvé tandis que pour un long temps de séparation, un mélange entre états singulet et triplet se produit. Une telle observation constituerait une première preuve de cohérence du transfert d'électrons.

Pour aller plus loin dans cette étude, il pourrait être intéressant d'utiliser des doubles boîtes quantiques de part et d'autre du canal de transfert. Il serait alors possible de préparer une superposition cohérente d'états de spin d'une paire d'électrons, de transférer et finalement de mesurer cet état de spin dans la double boîte de réception, effectuant d'une certaine manière une "mesure non local" d'oscillations de Rabi. Dans le chapitre 4, une première étape a été accomplie avec la réalisation d'oscillations de Rabi dans une position isolée, compatible avec le transfert d'électrons par onde acoustique de surface. Nous avons vu que travailler avec ces doubles boîtes isolées entraine simplification considérable au niveau du contrôle de la structure, ce qui présente plusieurs avantages. Tout d'abord, cette approche devrait amplement faciliter le contrôle de systèmes plus complexes, et ouvre donc une perspective intéressante vers la réalisation de réseaux plus importants de boîtes quantiques couplées. Deuxièmement, cela permet d'effectuer les manipulations cohérentes de spin dans une position où le système n'est plus sensible à une partie du bruit de charge. Pour cela, le couplage tunnel entre les deux parties de la double boîte est modulé de façon similaire à la proposition initiale de Loss et Divincenzo [Los98]. Par conséquent, ce type de boîtes quantiques isolées est un moyen efficace pour gagner à la fois en simplicité de manipulation et sur la cohérence du système.

Néanmoins, il ne semble pas possible d'utiliser l'échantillon actuel pour aller plus loin vers la réalisation d'une mesure non local d'oscillations de Rabi. En effet, un alignement de la double boîte selon la direction de propagation de SAW est incompatible puisque qu'il va induire un mélange des différents états de spin. Un nouvel échantillon est donc en cours de préparation (*cf.* Fig. 5.14), sur lequel les doubles boîtes quantiques sont orientées de manière orthogonale à la direction de propagation de l'onde.

Si le transfert cohérent d'électrons est démontré, un tel échantillon pourrait alors permettre l'intrication de deux spins d'électrons distants. Cela serait possible de la manière suivante. Deux électrons sont préparés dans un état singulet et stockés dans la boîte quantique S (*cf.* Fig. 5.14). Un électron est également préparé dans la boîte A, et un dernier dans la boîte B. On suppose par souci de simplicité que ces électrons sont dans un état $|\uparrow\rangle$, mais le même résultat peut en principe être obtenu quel que soit l'état de spin de ces deux électrons. Le système complet s'écrit de la manière suivante :

$$|\uparrow_A\rangle \otimes |S\rangle_S \otimes |\uparrow_B\rangle = |\uparrow_A\rangle \otimes \frac{1}{\sqrt{2}} \left(|\uparrow\downarrow\rangle_S - |\downarrow\uparrow\rangle_S\right) \otimes |\uparrow_B\rangle \tag{G.1}$$

Où les indices indiquent la boîte contenant la particule. Un électron de la paire formant le

singulet est alors transféré vers la boîte R. Le système se réécrit alors sous la forme :

$$|\uparrow_A\rangle \otimes \frac{1}{\sqrt{2}}\left(|\uparrow_S\downarrow_R\rangle - |\downarrow_S\uparrow_R\rangle\right) \otimes |\uparrow_B\rangle = \frac{1}{\sqrt{2}}\left(|\uparrow_A\uparrow_S\downarrow_R\uparrow_B\rangle - |\uparrow_A\downarrow_S\uparrow_R\uparrow_B\rangle\right) \tag{G.2}$$

Il suffit alors d'effectuer une opération de SWAP ("échange") de part et d'autre du canal (entre A et S d'un côté, et R et B de l'autre). Cette opération va simplement échanger les spins de deux électrons. On obtient finalement :

$$\frac{1}{\sqrt{2}}\left(|\uparrow_A\uparrow_S\uparrow_R\downarrow_B\rangle - |\downarrow_A\uparrow_S\uparrow_R\uparrow_B\rangle\right) = \frac{1}{\sqrt{2}}\left(|\uparrow_A\downarrow_B\rangle - |\downarrow_A\uparrow_B\rangle\right) \otimes |\uparrow_S\uparrow_R\rangle \tag{G.3}$$

On peut noter que l'intrication initialement partagée par les particules en S et R est désormais induite sur les spins en A et B. Des procédures très similaires, utilisant une paire d'électrons singulet séparés, pourrait alors être employées pour réaliser des expériences de téléportation quantique [Bou97].

Toutes ces perspectives ne représentent qu'une partie des applications possibles, mais promettent déjà des recherches passionnantes pour les années à venir.

Acknowledgments

Ces années de thèse ont été pour moi une formidable aventure, tant sur le plan scientifique que personnel. Cela n'aurait pas été possible sans le soutien de nombreuses personnes, que je souhaiterai remercier ici.

Pour commencer, merci à Tristan de m'avoir fait confiance et accueilli dans l'équipe. Tu as toujours été disponible pour moi quand j'en avais besoin (malgré tous les projets que tu mènes en parallèle). C'est vraiment agréable de travailler avec quelqu'un qui a autant d'enthousiasme et de dynamisme. J'espère que tu ne va pas te mettre à recruter uniquement des célibataires à cause de moi. Merci également à Chris pour l'aide et les précieux conseils, notamment en cryogénie, et aussi pour répondre au téléphone à 2h du matin les nuits d'orage, lorsqu'il n'y a plus de courant dans le labo...

Je me dois aussi de remercier Alain Fontaine et la Fondation Nanosciences, pour avoir permis le financement de ma thèse pendant ces trois années.

Next, I am very grateful to Hendrik Bluhm and Frédéric Pierre for accepting to review my manuscript (and thank you Hendrik for the challenging question session!), to Jean-Marie George and Marc Sanquer for their kind participation in the jury, and to Thierry Ouisse, the president of the jury, who was an excellent teacher during my engineer training and made me want to learn more on mesoscopic physics.

I also acknowledge the group of Seigo Tarucha for the warm welcome I received in Tokyo. I really wish I could have stayed longer in Todai. Thank you also to Sylvain and Shintaro for providing me with a "ready-to-use" experimental setup and this amazingly robust sample. I would not have accomplished all this work without it.

Je tiens également à remercier les membres de l'institut qui m'ont apporté un soutien technique, notamment Pierre Perrier et Emilio Barria pour l'aide en cryogénie, Christophe Guttin pour les dépannages sur l'électronique, Christophe Hoarau pour l'électronique RF, l'équipe Nanofab pour l'aide en salle blanche, et enfin les membres du Liquéfacteur pour les dizaines de milliers de litres d'hélium liquide que j'ai pu récupérer sans interruption tout au long de ma thèse, y compris pendant les périodes de crise.

J'ai bien sûr une pensée spéciale pour tous mes "compagnons de galère", thésards et autres stagiaires, avec qui j'ai passé de supers moments. Danke schön Tobias pour le Grenoble-Cargèse en Bautzemobil qui m'a permis de découvrir le death metal symphonique et le

Kubb, ainsi que pour les leçons d'allemand (je ne confondrai jamais un dessert et une table de nuit grâce à toi !). Merci à Guigui, mon acolyte d'écoles d'été et de formations, Greg, pour m'avoir aidé à garder la forme sur les flancs du Néron, Étienne pour tes incroyables sujets de conversation, qui donnent des repas certes un peu longs mais animés (et c'est meilleur pour la digestion), Vivien qui supporte mes blagues dans le bureau, Olivier, Marian, Martial, Hanno, Frans, Pierre-André, Mathias, Candice, Romain, Clément, Elias, Kostas, et tous ceux que j'ai pu oublier...

En dehors du labo, un grand merci à ma famille, qui ne m'a pas beaucoup vu ces dernières années. Merci aussi à Florian de m'avoir fait prendre l'air en m'accompagnant en VTT les weekends où je ne travaillais pas, de m'attendre dans les montées un peu trop raides ou quand on passe près d'un coin à champignons, de me suivre dans les descentes un peu scabreuses, et bien sûr pour toutes les semaines B !

Enfin, comme dit le proverbe, on peut remercier mille fois une personne, mais on ne peut pas remercier mille personnes une fois, euh... Bref, mille mercis à Marie, pour n'avoir presque pas râlé pour les weekends au labo, les réveils au milieu de la nuit, le régime pâtes au pesto et l'absence de vacances. Et surtout merci pour mes deux plus beaux cadeaux : Justine, qui me remontait le moral après les dures journées de rédaction, et Arthur, qui a montré qu'il avait hérité du sens de la ponctualité de son papa en arrivant le jour de sa soutenance !